# SELF-ASSEMBLY AND PROPERTIES OF LOW BAND GAP DIKETOPYRROLOPYRROLE DERIVATIVES

**Thesis Submitted to AcSIR for the Award of the Degree of**
**DOCTOR OF PHILOSOPHY**
**in Chemical Sciences**

By

**SAMRAT GHOSH**

**Registration No: 10CC12J39004**

**Under the guidance of**

**Prof. A. AJAYAGHOSH**

**CSIR-NATIONAL INSTITUTE FOR INTERDISCIPLINARY**
**SCIENCE AND TECHNOLOGY (CSIR-NIIST)**
**THIRUVANANTHAPURAM-695019, KERALA, INDIA**

**November, 2017**

*Dedicated to*

*Maa, Baba, Kaku*

*& Teachers*

# DECLARATION

I hereby declare that the matter embodied in the thesis entitled: "**Self-Assembly and Properties of Low Band Gap Diketopyrrolopyrrole Derivatives**" is the result of the investigations carried out by me at the Photosciences and Photonics Section, Chemical Sciences and Technology Division, CSIR-National Institute for Interdisciplinary Science and Technology (CSIR-NIIST), Thiruvananthapuram, under the supervision of Prof. A. Ajayaghosh and the same has not been submitted elsewhere for any other degree.

In keeping with the general practice of reporting scientific observations, due acknowledgement has been made wherever the work described is based on the findings of other investigators.

**Samrat Ghosh**

**National Institute for Interdisciplinary Science and Technology (NIIST)**

*(Formerly Regional Research Laboratory)*

**Council of Scientific & Industrial Research (CSIR)**
**Industrial Estate P.O., Trivandrum - 695 019**
**Kerala, INDIA**

**Tel: 91-471-2490324**
**Fax: +91-471-2491 712**
**Email: ajayaghosh62@gmail.com**
**ajayaghosh@niist.res.in**

**Dr. A. Ajayaghosh FASc., FNASc., FNA., FTWAS**
**Director**

# *CERTIFICATE*

*This is to certify that the work incorporated in this Ph.D. thesis entitled* ***"Self-Assembly and Properties of Low Band Gap Diketopyrrolopyrrole Derivatives"*** *submitted by* **Mr. Samrat Ghosh** *to the Academy of Scientific and Innovative Research (AcSIR) in fulfilment of the requirements for the award of the* ***Degree of Doctor of Philosophy in Chemical Sciences*** *embodies original research work carried out by him under my supervision. I further certify that this work has not been submitted to any other University or Institution in part or full for the award of any degree or diploma. Research material obtained from other sources has been duly acknowledged in the thesis. Any text, illustration, table etc., used in the thesis from other sources, have been duly cited and acknowledged.*

Samrat Ghosh

A. Ajayaghosh
(Supervisor)

# ACKNOWLEDGEMENT

*It is with great pleasure that I extend my deep sense of gratitude to Prof. A. Ajayaghosh, my thesis supervisor, for suggesting the research problem, for his valuable guidance, support, encouragement and scientific freedom, leading to the successful completion of this work. I also want to thank him for the expression of faith in my abilities.*

*I would like to express my gratitude to Prof. M. V. George for his inspiration.*

*I thank Dr. Suresh Das (former Director) and Dr. Gangan Pratap (former acting Director) of CSIR-NIIST, Thiruvananthapuram, for providing the necessary facilities for carrying out this work.*

*My sincere thanks are also due to:*

- *Dr. Mangalam S. Nair and Dr. R. Luxmi Varma, former and present AcSIR co-ordinators.*
- *Dr. K. R. Gopidas, for his scientific discussions and valuable suggestions.*
- *Dr. D. Ramaiah, Dr. Narayanan Unni, Dr. J. D. Sudha, Dr. Joshy Joseph, Dr. K. Yoosaf, Dr. C. Vijayakumar, Dr. B. Deb and Dr. V. Karunakaran, scientists of the Photosciences and Photonics Section, Chemical Sciences and Technology Division (CSTD), for their help and support.*
- *Dr. C. H. Suresh, Dr. M. L. P. Reddy and Dr. U. S. Hareesh, the Doctoral Advisory Committee (DAC) members and the whole AcSIR faculty for the successful completion of course work.*
- *Dr. Akinori Saeki, Osaka University and Prof. Shu Seki, Kyoto University, Japan for photoconductivity measurements.*
- *Dr. C. H. Suresh, CSTD, CSIR-NIIST, for Density Functional Theory calculations.*
- *Dr. Prabha D. Nair of SCTIMST, Trivandrum for contact angle measurements.*

- *Dr. Manoj Namboothiry and Ms. Reshma Raveendran from Indian Institute of Science Education and Research, Trivandrum for OFET device fabrication and measurements.*
- *Mr. Vipi Vipin and Dr. Saju Pillai for polymer composite preparation.*
- *Dr. K. K. Maiti and Ms. Saranya Giridharan for Raman measurements.*
- *Ms. Gayathri Prabhu and Mr. Bejoymohondas K. S. for optical measurements.*
- *Dr. Sreejith Shankar and Dr. V. K. Praveen, for scientific discussions.*
- *Ms. Blessy M. Suresh and Ms. Silpa P. S., Summer Research Fellows, for their help in synthesis.*
- *All former and present group members for their help, guidance and support.*
- *All former and present members of Photosciences and Photonics Section for their cooperation and help.*
- *Mr. Robert Philip and Mr. Kiran J. S. for their general help and support.*
- *Mr. Kiran Mohan for TEM analysis, Mr. Aswin Maheshwar and Mr. Vishnu M. for AFM analysis.*
- *Ms. Saumini, Mr. Adarsh, Mr. Preethanuj, Mr. Arun, Mr. Sharan and Mr. Gokul for NMR and Ms. Viji for mass spectral analyses.*
- *Dr. T. P. D. Rajan, Dr. Ananthakumar S. and their students for the successful completion of CSIR-800 project.*
- *My roommates Mr. Satyajit Das, Mr. Ajay Kumar and Mr. Sandip Chakraborty.*
- *All my teachers for leading the way and their encouragement at different stages of my academic career.*
- *Council of Scientific and Industrial Research (CSIR) and Department of Science and Technology (DST), Government of India for financial assistance. Also Japan Society for the Promotion of Science (JSPS) for financial assistance.*

*A special word of thanks to my seniors, Dr. Seelam Prasanthkumar, Dr. Anesh Gopal, Dr. Krishnan Kartha, Dr. Sanju K. S., Dr. Adarsh N. V., Dr. Hari Shankar, Dr. Jatish Kumar, Dr. Sandeep C., Dr. Dhanya T. Jayaram, Dr. Sandeep A., Dr. Sreedevi K., Dr. Rakhi A. M., Dr. Vinayak M. V., for helping me in all ways at the early stages of my research and their support and suggestions in the research activities.*

*I am profoundly thankful to the generous help, support, discussions as well as the care rendered by my colleagues, Dr. Rahul Dev Mukhopadhyay, Dr. Divya Susan Philips and Mr. Sudheesh K. V. throughout my research in its length and breadth.*

*I am deeply and forever indebted to my family for their love, blessings and their teachings. Finally, I would like to thank all my dear friends and teachers from my school and college, my room-mates and each and every person who has made my life bright and cheerful. And above all, I place my thanks to God Almighty for every blessing that has been given to me.*

**Samrat Ghosh**

# CONTENTS

**Page**

**Declaration** i

**Certificate** ii

**Acknowledgement** iii

**Contents** vi

**List of Abbreviations** xi

**Preface** xv

**CHAPTER 1: Synthesis, Properties, Self–Assembly and Applications of Diketopyrrolopyrrole Derivatives** **01–42**

**1.1.** Abstract 1

**1.2.** Introduction 2

**1.3.** Synthesis of Diketopyrrolopyrroles (DPPs) 3

**1.4.** Optical and Electronic Properties of DPP Derivatives 5

**1.5.** DPP based Small Molecules and Their Applications 7

**1.5.1.** Organic Bulk Heterojunction (BHJ) Solar Cells 7

**1.5.1.1.** DPPs as Electron Donor 8

**1.5.1.2.** DPPs as Electron Acceptor 9

**1.5.2.** Organic Field Effect Transistors (OFETs) 11

**1.5.2.1.** DPPs as Hole Transporter 12

**1.5.2.2.** DPPs as Electron Transporter 13

**1.6.** Self–assembly of DPP Chromophores 14
**1.6.1.** Hydrogen Bonded Assemblies 15
**1.6.1.1** Latent Hydrogen Bonded Assemblies 15
**1.6.1.2.** Aqueous H–Bonded Assemblies 19
**1.6.1.3.** DPP based Organogels 21
**1.6.1.4.** H–Bonded DPP Assembly for OSCs 23
**1.6.1.5.** H–Bonded DPP Assembly for OFETs 25
**1.6.1.6.** Photoinduced Electron Transfer (PET) in DPP Assembly 28
**1.6.2.** Amphiphilic DPP Derivatives 30
**1.6.3.** π–Stacked DPP Derivatives 33
**1.6.4.** DPP based Liquid Crystal 35
**1.7.** Objectives of the Present Work 36
**1.8.** References 37

**CHAPTER 2: A Supramolecular Nanocomposite as Near Infrared Transmitting Optical Filter for Security and Forensic Applications 43–74**

**2.1.** Abstract 43
**2.2.** Introduction 44
**2.3.** Results and Discussion 51
**2.3.1.** Synthesis of **DPP–Amide** 51

**2.3.2.** Thermal Characterization 52
**2.3.3.** Gelation 52
**2.3.4.** Photophysical Characterization 53
**2.3.5.** DFT Calculations 55
**2.3.6.** Morphological Analyses 56
**2.3.7.** Nanocomposite Preparation 57
**2.3.8.** Characterization of the Nanocomposite 58
**2.3.9.** Applications of the NIR Filter 61
**2.4.** Conclusion 65
**2.5.** Experimental Section 66
**2.5.1.** Materials and Methods 66
**2.5.2.** Synthesis and Characterization 68
**2.6.** References 72
**CHAPTER 3: Modulating the Charge Carrier Polarity of a Diketopyrrolopyrrole–based Low Band Gap Semiconductor by Terminal Functionalization 75–104**
**3.1.** Abstract 75
**3.2.** Introduction 76
**3.3.** Results and Discussion 82
**3.3.1.** Synthesis of DPP Derivatives 82
**3.3.2.** Thermal Characterization 84
**3.3.3.** Photophysical Characterization 84

**3.3.4.** Frontier Molecular Orbital (FMO) Calculations 85

**3.3.5.** DFT Calculations 86

**3.3.6.** Transient Photoconductivity Studies 87

**3.3.7.** Field–Effect Transistor Characteristics 90

**3.3.8.** Morphological Analysis 92

**3.3.9.** Molecular Packing 93

**3.4.** Conclusions 95

**3.5.** Experimental Section 95

**3.5.1.** Materials and Methods 95

**3.5.2.** Synthesis and Characterization 97

**3.6.** References 102

**CHAPTER 4: Nanosheets of an Organic Molecular Assembly from Aqueous Medium : High Solid–State Emission and Anisotropic Charge–Carrier Mobility 105–140**

**4.1.** Abstract 105

**4.2.** Introduction 106

**4.3.** Results and Discussion 113

**4.3.1.** Synthesis of **PDPP–Amphi** 113

**4.3.2.** Thermal Characterization 114

**4.3.3.** Photophysical Characterization 114

**4.3.4.** Contact Angle Measurements 119

**4.3.5.** Morphological Analyses 120

**4.3.6.** Linear Dichroism (LD) 121

**4.3.7.** Frontier Molecular Orbitals (FMO) Calculations 122

**4.3.8.** Conductivity Measurements by Flash Photolysis Time Resolved Microwave Conductivity (FP–TRMC) 123

**4.3.9.** Molecular Organization 127

**4.4.** Conclusion 130

**4.5.** Experimental Section 130

**4.5.1.** Materials and Methods 130

**4.5.2.** Synthesis and Characterization 132

**4.6.** References 137

**Papers Presented at Conferences** 141

**List of Publications and Patents** 142

# List of Abbreviations

| | |
|---|---|
| 2D | Two Dimensional |
| Å | Angstrom |
| ACN | Acetonitrile |
| ADF | Amsterdam Density Functional |
| BCB | Benzocyclobutene |
| BASF | Baden Aniline and Soda Factory |
| BHJ | Bulk Herterojunction |
| BC | Bottom contact |
| BG | Bottom gate |
| °C | Degree Celsius |
| CA | Contact angle |
| CB | Cucurbituril |
| CD | Circular Dichroism |
| CGC | Critical gelation concentration |
| c.a. | Calculated approximately |
| $CDCl_3$ | Deuterated chloroform |
| COF | Covalent Organic Framework |
| CIE | International Commission on Illumination |
| $CO_2$ | Carbon dioxide |
| $C_{60}$ | Fullerene |
| $\delta$ | Chemical shift |
| DPP | Diketopyrrolopyrrole |
| D-A-D | Donor-acceptor-donor |
| DFT | Density functional theory |
| DMF | Dimethylformamide |
| DCM | Dichloromethane |
| DMSO | Dimethyl sulfoxide |
| DCB | Dichlorobenzene |
| DSC | Differential scanning calorimetry |
| *et al.* | *Et allii/alia* |

| | |
|---|---|
| $\varepsilon$ | Molar extinction coefficient |
| $\phi$ | Charge–carrier generation quantum yield |
| $\Phi_F$ | Fluorescence quantum yield |
| FT-IR | Fourier-transform infrared spectroscopy |
| FP-TRMC | Flash photolysis time resolved microwave conductivity |
| FMO | Frontier molecular orbital |
| FF | Fill factor |
| eV | Electronvolt |
| GIXD | Grazing incidence x-ray diffraction |
| G' | Elastic storage modulus |
| G" | Elastic loss modulus |
| h | Hour |
| H-bond | Hydrogen bond |
| HOPG | Highly oriented pyrolytic graphite |
| HOMO | Highest occupied molecular orbital |
| HMDS | Hexamethyldisilazane |
| HRMS | High resolution mass spectrometry |
| Hz | Hertz |
| ICT | Intramolecular charge transfer |
| IR | Infrared |
| ITC | Isothermal titration calorimetry |
| ITO | Indium tin oxide |
| I-V | Current–voltage |
| $J_{sc}$ | Short circuit current |
| K | Kelvin |
| $\lambda_{abs}$ | Wavelength of absorption |
| $\lambda_{ex}$ | Wavelength of excitation |
| $\lambda_{em}$ | Wavelength of emission |
| LUMO | Lowest unoccupied molecular orbital |
| LCST | Lower critical solution temperature |
| LD | Linear dichroism |
| M | Molar |

| | |
|---|---|
| $M^+$ | Molecular ion peak |
| MALDI-TOF | Matrix-assisted laser desorption-Time of flight |
| $\mu$ | Transition dipole moment |
| $\mu$M | micromolar |
| $\mu$m | micrometre |
| $\mu_h$ | Hole mobility |
| $\mu_e$ | Electron mobility |
| $\Sigma\mu$ | Charge carrier mobility |
| mmol | millimole |
| mL | millilitre |
| min | minutes |
| mW | milliwatt |
| mA | milliampere |
| MCH | Methyl cyclohexane |
| $\eta$ | Refractive Index |
| NIR | Near-infrared |
| nm | Nanometer |
| NMR | Nuclear magnetic resonance |
| OLED | Organic light emitting diode |
| OFET | Organic field effect transistor |
| OSC | Organic solar cell |
| ODT | 1,8-Octanedithiol |
| pH | Hydrogen ion concentration at logarithmic scale |
| $pK_a$ | Acid dissociation constant at logarithmic scale |
| PET | Photoinduced electron transfer |
| PCE | Power conversion efficiency |
| PCBM | [6,6]-Phenyl $C_{61}$ butyric acid methyl ester |
| $PC_{71}BM$ | [6,6]-Phenyl $C_{71}$ butyric acid methyl ester |
| PBI | Perylene bisimide |
| PYS | Photo yield spectroscopy |
| PDMS | Polydimethylsiloxane |

| | |
|---|---|
| ppm | Parts per million |
| ppb | Parts per billion |
| RFID | Radio-frequency identification |
| rt | Room temperature |
| s | Seconds |
| SAED | Selected area electron diffraction |
| Si | Silicon |
| $SiO_2$ | Silicon Dioxide |
| SCLC | Space charge limited current |
| SWNTs | Single walled carbon nanotubes |
| T | Temperature |
| TD-DFT | Time dependent density functional theory |
| TEM | Transmission electron microscopy |
| TPC | Transient photoconductivity |
| TGA | Thermogravimetric analysis |
| TG | Top gate |
| TC | Top contact |
| THF | Tetrahydrofuran |
| *t*-Boc | *tert*-Butyloxycarbonyl |
| UV-Vis | Ultraviolet-visible |
| V | Voltage |
| $V_T$ | Threshold voltage |
| $V_{oc}$ | Open circuit voltage |
| WAXS | Wide angle X-ray scattering |
| wt% | Weight percentage |
| XRD | X-ray diffraction |

# PREFACE

Self–assembly of π–conjugated systems started off as a curiosity driven research at the early 90s and has now grown into a full–fledged area of research at the hands of many chemists across the globe. The self–organization of chromophores under several different conditions has been extensively studied both experimentally and theoretically by various research groups. Our group had also been actively contributing to the area of molecular self–assembly and fine tuning of their optoelectronic properties for over a decade.[1] When I started off my research at CSIR–NIIST, I was assigned the task of design and development of a few low band gap π–conjugated organic molecules for organic electronics. To serve this purpose, we chose π–conjugated electron donor–acceptor (D–A) systems bearing a relatively new acceptor unit diketopyrrolopyrrole (DPP). The rationale behind choosing DPP is briefly described in **Chapter 1**. DPP based systems have opened up a fascinating research arena because of their highly promising optical features, thermal and photostability which can be understood from the sudden upsurge in the number of publications based on them. However, until 2013, there was very few literature precedence on the self–assembly of DPP after which a number of self–assembled DPP systems were reported for various optoelectronic applications which is also summarized in this chapter.

Inspired from the brilliant pieces of work in this area, we have designed and synthesized an amide functionalized π–conjugated D–A molecule based on a DPP chromophore (**DPP–Amide**) in **Chapter 2** with the aim of developing a low bandgap organogel that is capable of absorbing completely in the visible region while transmitting the NIR light. This resulted in a completely black organogel and the “blackness” arises from the molecular self–assembly of the π–conjugated D–A–D system. In order to create a free standing NIR transmitting elastomeric black filter for suitable applications, the nanoscopic molecular aggregates of **DPP–Amide** were embedded in a polydimethylsiloxane (PDMS) matrix. We have demonstrated the use of the developed material for NIR photography, security and forensic related applications.[2]

Then we attempted to tune the band gap of DPP derivatives by increasing the acceptor strength *via* simple synthetic modifications which is explained in **Chapter 3**. Also, changing the acceptor strength led to the switching of charge carrier mobility as estimated from the field effect transistor (FET) devices.[3] This study established that terminal functional modification approach is a simple and efficient method to alter the charge carrier polarity of organic semiconductors.

In **Chapter 4**, we discuss the design and synthesis of a DPP amphiphile (**PDPP–Amphi**) which can form two dimensional (2D) supramolecular assembly in aqueous as well as in non–polar medium. Nanosheets obtained under aqueous conditions exhibited a remarkably high solid state emission quantum yield of 54% and an anisotropic charge carrier mobility of 0.33 $cm^2/Vs$ as estimated from flash photolysis time resolved microwave conductivity (FP–TRMC) measurements.[4] The ability to develop highly fluorescent and crystalline 2D nanosheets with high anisotropic charge–carrier mobility is expected to be useful in designing molecular systems for device applications.

## References

1. The chemistry and applications of π–gels. **S. Ghosh**, V. K Praveen, A. Ajayaghosh. *Annu. Rev. Mater. Res.* **2016**, *46,* 235.
2. A Supramolecular Nanocomposite as Near Infrared Transmitting Optical Filter for Security and Forensic Applications. **S. Ghosh**, S. Cherumukkil, C. H. Suresh, A. Ajayaghosh.
   *Adv. Mater.*, **2017**, 1703783.

3. Modulating the Charge Carrier Polarity of a Diketopyrrolopyrrole–based Low Band Gap Semiconductor by Terminal Functionalization. **S. Ghosh**, R. Raveendran, M. Namboothiry, A. Saeki, S. Seki, A. Ajayaghosh.
   (Manuscript under preparation)

4. Nanosheets of Organic Molecular Assembly from Aqueous Medium Exhibit High Solid–State Emission and Anisotropic Charge–Carrier Mobility. **S. Ghosh**, D. S. Philips, A. Saeki, A. Ajayaghosh.
   *Adv. Mater.*, **2017**, *29*, 1605408.

# Chapter 1

# Synthesis, Properties, Self–Assembly and Applications of Diketopyrrolopyrrole Derivatives

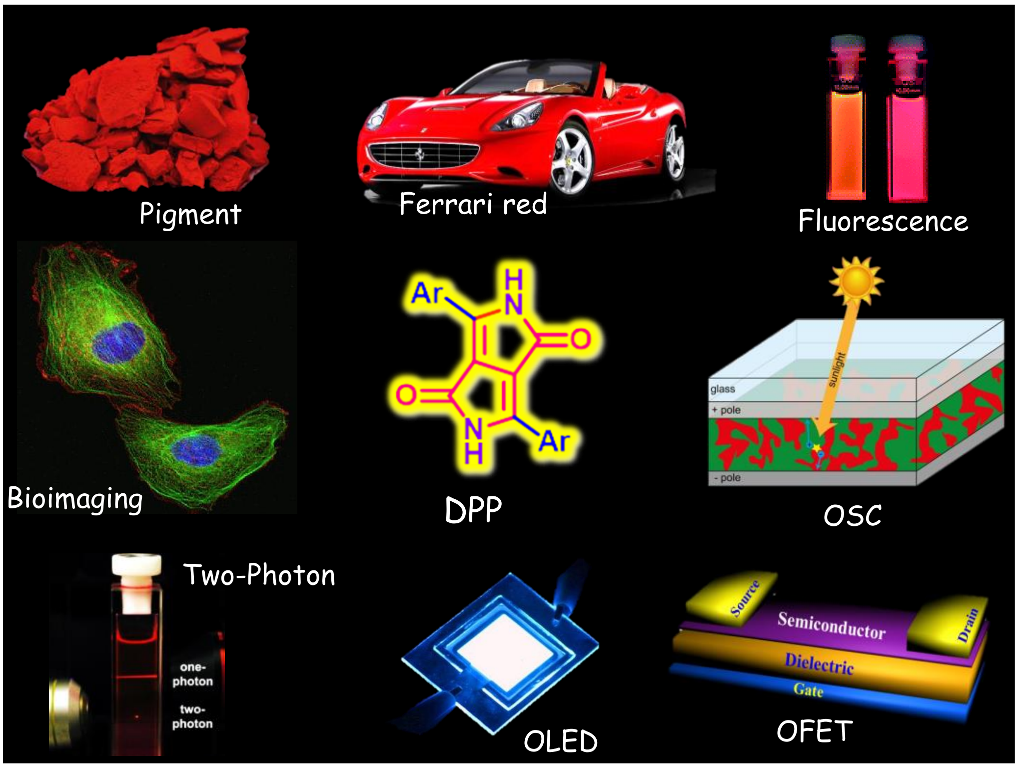

## 1.1. Abstract

*The very concept of dye and pigment chemistry that was long known to the industrial world underwent a radical revision following the discovery and commercialization of dyes such as mauveine, indigo etc. Apart from their conventional role as coloring agents, organic dyes and pigments have been identified as indispensible sources for high–end technological applications that include optical and electronic devices. Out of all the major pigments, diketopyrrolopyrrole (DPP) better known as the "Ferrari Pigment" has emerged as a major class of organic functional dyes that find varied applications in fields such as industrial pigments, organic solar cells, organic field effect transistors and*

*bioimaging. Since its discovery in 1974 by Farnum et al., DPP derived dyes gained rapid attention because of its attractive color, synthetic feasibility, ease of functionalization and tunable optical and electronic properties. In this chapter, the recent development in the synthesis, self–assembly and applications of DPP derivatives are discussed.*

## 1.2. Introduction

In the early nineteenth century, chemists realized the importance of synthetic dyes in mimicking natural colors to produce colorful garments for the civilized society. The very first organic synthetic dye, mauveine was accidentally discovered by Sir William Henry Perkin in 1856.[1] Since then, a large library of synthetic organic dyes and pigments were developed for color and paint industries. Among them, hydrogen–bonded (H–bonded) organic pigments are highly desirable because of their applicability in textiles, paints, plastics, food and cosmetics as powdered microcrystalline colorant.[2] A new H–bonded organic pigment diketopyrrolopyrrole (DPP) was discovered in early 1970s, got attention in the mid–eighties and later commercialized as '*Ferrari pigments*'.[3] This red pigment has an intense characteristic color, high thermal and photochemical stability. The intense color of the DPP originates from the extended π–conjugation between its electron rich and electron deficient units.[4] In the early 1990s, DPP was predicted to be one of the potential dyes for optoelectronic applications after a close observation of their optical properties and crystal structures.[5] Soon after, tremendous interest in DPP derived dyes emerged as seen in a large volume of literature reporting their application as semiconductors in organic solar cells (OSCs)[6], organic field effect transistors (OFETs)[7] and organic light emitting diodes (OLEDs).[8] Also, the fluorescence properties and large two–photon absorption cross–section of DPP derivatives make them potential material for application in sensing, bio–imaging and related techniques.[9–12] Most of the reported DPP derivatives are either small molecules or polymers and used in OSC or OFET applications with excellent power conversion efficiency (PCE) or high charge carrier mobility.[13–17]

Molecular self–assembly offers a unique strategy to enhance or tune the optical and electronic properties of π–conjugated systems.[18–20] Further, the optoelectronic efficiency can be enhanced by controlling the crystallinity of nano– or mesoscale assembly of the π–chromophores. By virtue of various non–covalent interactions (ionic, van der Waals, solvophobic, hydrogen and coordination bonds), 1D, 2D or 3D supramolecular architectures can be constructed out of π–conjugated systems.[21,22] 'Bottom up' approach and the dynamic nature of aggregates give an opportunity to control the size and shape in the nano– and mesoscopic regimes.[23] In fact, the molecular self–assembly involving DPP derivatives had been shown to enhance their optical as well as electronic properties.

In this chapter, we discuss the recent reports on DPP–based systems and their synthesis, self–assembly and applications in optoelectronics. An overview of the synthesis and brilliant optical properties of DPP, with special emphasis on the most efficient small molecules and self–assembled DPPs for OSCs and OFETs reported till date are discussed.

## 1.3. Synthesis of Diketopyrrolopyrroles (DPPs)

In 1974, Mehta *et. al.* made an attempt to synthesize an unsaturated *β*–lactam under the Reformatsky condition by reacting ethylbromoacetate with benzonitrile in presence of zinc (**Figure 1.1a**).[24] However, instead of obtaining the desired product, a highly insoluble brilliant red organic pigment having a dilactum structure was isolated and named as Diketopyrrolopyrrole **(**DPP). It did not receive much attention until 1986, when Iqbal *et al.* from Ciba–Geigy AG (currently a subsidiary of BASF) found structural similarity of DPP with other H–bonded organic pigments such as indigo, quinacridone and epindolindione.[3] The retrosynthetic analysis by Iqbal and his colleagues revealed that DPP can be obtained in better yield through Stobbe condensation between benzonitrile and succinic acid ester (**Figure 1.1b, c**).[4] This was a turning point and indeed DPP derivatives could now be obtained in high yields by reaction of any aromatic carbonitrile with diethyl succinate in the presence of strong bases such as alkali metal alkoxides.[25]

As mentioned earlier, DPP is an organic pigment due to very less solubility in common organic solvents unlike organic dyes that are highly soluble in non–polar organic solvents. Strong intermolecular complementory H–bonding between amide groups and π–stacking interactions are mainly responsible for its insolubility.[13] However, for practical applications, good solubility is highly desirable. One of the possible strategies to increase the solubility of DPP derivatives involves the *N*–alkylation of the amide of DPP that hinders possibility of intermolecular H–bonding. This *N*–alkylation is generally achieved in polar solvents such as DMF in presence of an alkyl halide and a base at 100 °C (**Figure 1.1d**).[25]

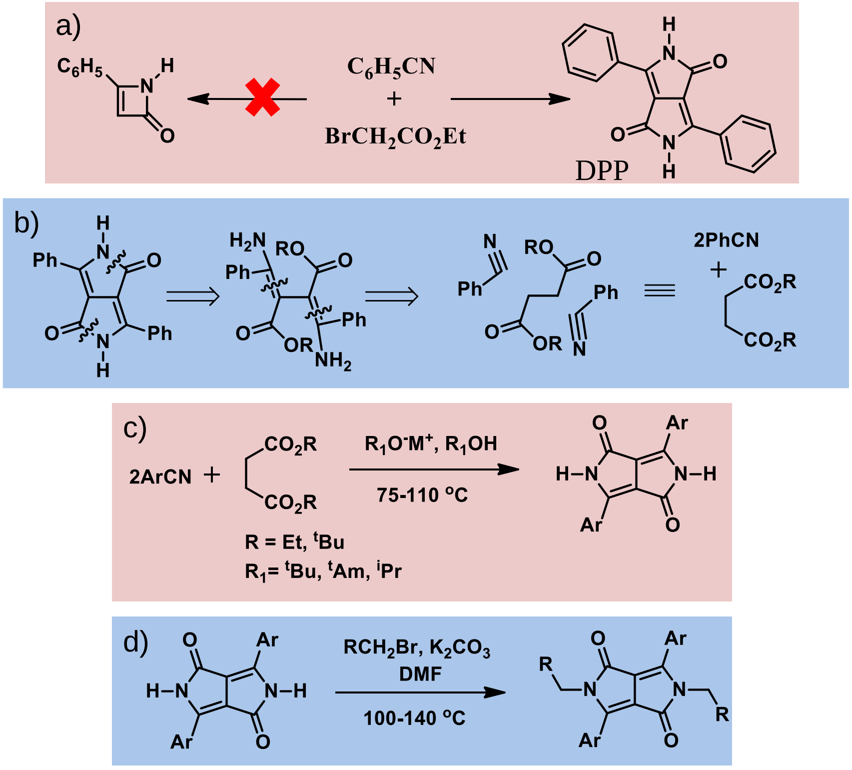

**Figure 1.1. a)** Serendipitous discovery of DPP. **b)** Retrosynthetic analysis of DPP. **c)** Presently used synthetic scheme for DPP. **d)** *N*–alkylation of DPP.

## 1.4. Optical and Electronic Properties of DPP Derivatives

π–Conjugated donor–acceptor (D–A) systems have distinct optical and electronic properties due to intramolecular charge transfer (ICT) from the donor to the acceptor.[26] The band gap of D–A semiconductors can be tuned by changing the strength of acceptor or donor. Thus, low band gap semiconductors can be designed by conjugating suitable donors with acceptors (**Figure 1.2a**). Basically, in a conjugated D–A system, highest occupied molecular orbital (HOMO) of the donor interact with the HOMO of the acceptor leading to two new HOMOs. Similarly, the lowest unoccupied molecular orbital (LUMO) of the donor and acceptor interact with each other resulting in two new LUMOs. The energy difference between the newly formed hybrid HOMO and LUMO is much smaller than those of the individual donor and acceptor, leading to an effective reduction of the optical bandgap (**Figure 1.2b**).

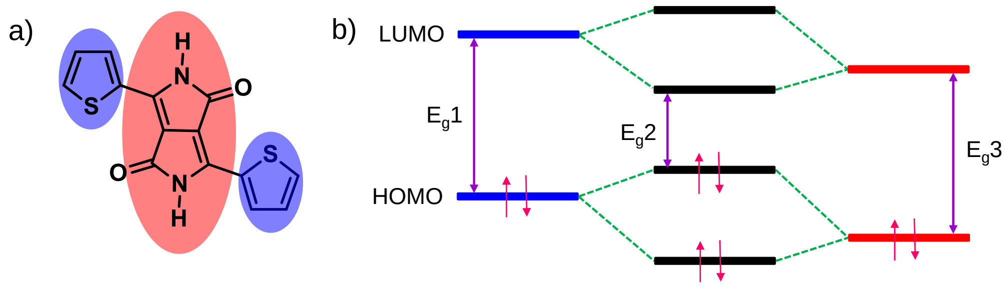

**Figure 1.2. a)** Chemical structure of a thiophene derivative of DPP showing donor (blue) and acceptor (red). **b)** Schematic representation of bandgap lowering in a π–conjugated donor–acceptor system *via* the interaction of corresponding molecular orbitals.

DPP is an excellent electron acceptor and by its chemical conjugation to a suitable electron donor (D–A–D), gives an opportunity to fine tune the optical properties and the band gap. Almost all DPP based D–A–D systems exhibit dual band in their absorption spectra. The lower wavelength (high energy) band corresponds to the π–π* transition whereas broad band at higher wavelength (low energy) originates due to ICT from the donor to the acceptor unit.[25] Majority of the DPP derivatives in the monomeric state, exhibit high fluorescence. Patil and co–workers have reported three DPP derivatives **1**–**3**, containing different donor groups with varying electron donating strengths (selenophene> thiophene> phenyl) (**Figure 1.3a**).[27] With the increase in the donor strength bathochromic shift in absorption as well as emission was observed (**Figure 1.3b, c**) along with the increment in molar absorption co–efficient ($\varepsilon$). The optical properties and band gaps can be even tuned by introducing electron–donating and electron–withdrawing groups on the same aromatic substituents **4–9**, as shown by Würthner and co–workers.[28] Here also, increasing the strength of electron–donating groups in these DPP derivatives induced a red shift in their absorption and emission with the corresponding enhancement of the $\varepsilon$ value (**Figure 1.3e**). In addition, broad absoption range and comparable low band gaps makes them suitable candidate for OSCs.

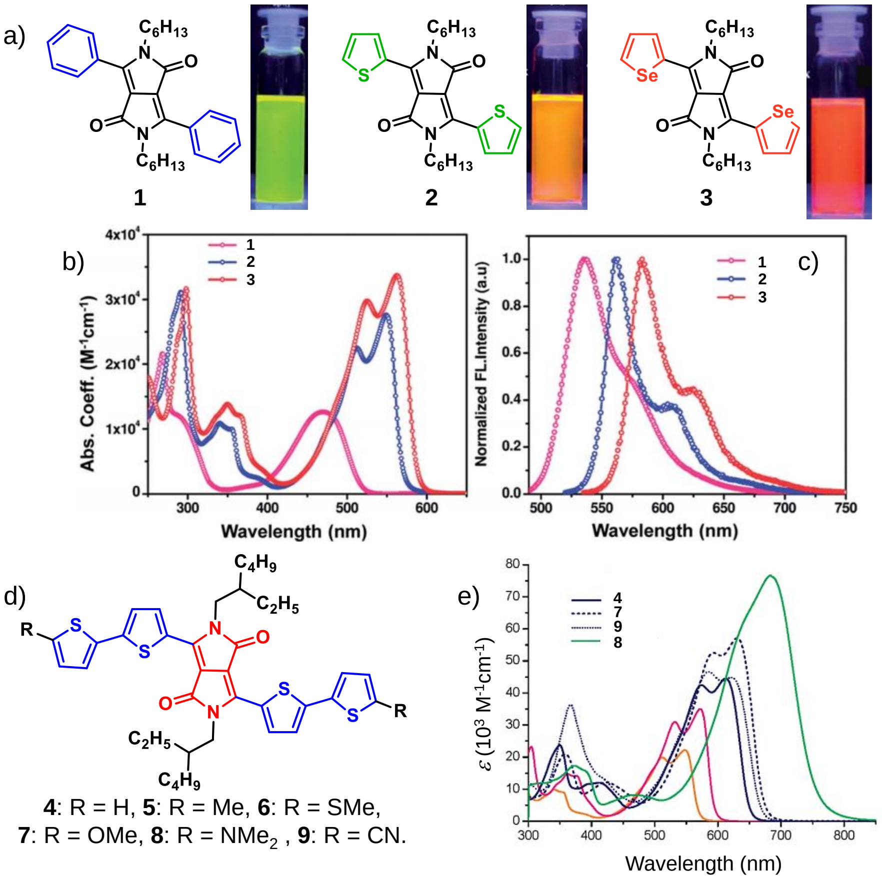

**Figure 1.3. a)** Chemical structures and the photographs of the DPP derivatives **1–3** in the solution state under UV light. **b)** Absorption and **c)** Emission profile of **1–3**. **d)** Molecular structures of the DPP derivatives **4–9** and **e)** the corresponding absorption spectra.

## 1.5. DPP based Small Molecules and Their Applications

Over the years, small molecule based organic semiconductors have gained a lot of attention due to their synthetic ease, possibility of functional modification, low–cost, light–weight, and flexible nature.[29] As a result, a large number of small molecules are reported to improve the optoelectronic performance of OSCs and OFETs. However, most of them have weak absorption in the visible and NIR region, low charge carrier mobility and comparably large band gap. In 2008, Nguyen and coworkers demonstrated for the first time that DPP based small molecules could be promising candidates for optoelectronic applications, devoid of aforementioned limitations.[6] Since then, there has been a sudden leap in the number of reports on the optoelectronic applications of DPP. A large number of structural modifications had been done to modulate the optical and electronic properties.[17] In this section, selected ‘champion’ small molecules with exceptional efficiency in OSCs as well as superior charge carrier mobility in OFETs, will be discussed.

### 1.5.1. Organic Bulk Heterojunction (BHJ) Solar Cells

Accelerated depletion of fossil fuels has prompted the human community to harvest energy from renewable sources. Amongst the alternative sources of energy, solar energy is highly preferred because of its abundance and conversion possibilities. In this context, organic solar cells (OSCs) got tremendous attention during last two decades owing to the low–cost fabrication techniques when compared to the silicon based solar cells.[30] The first organic photovoltaic device was reported by Tang, in 1986, with an efficiency of 1%, using vacuum–deposited CuPc/perylene derivatives respectively as donor/acceptor in a bilayer architecture.[31] Subsequently, Heeger and coworkers discovered an ultrafast electron transfer from a conjugated polymer to $C_{60}$ with an enhancement in charge photogeneration yield.[32] Thus, the concept of BHJ was introduced by using conjugated polymers as electron donors and $C_{60}$ or its derivatives as electron acceptors.[33] In a typical BHJ structure, phase separated active layers of donor and acceptor is sandwiched between two electrodes (**Figure 1.4a**).[34] Key steps involved in the working mechanism of BHJ solar cells are (i) photoexcitation of the donor leading to the generation of excitons, (ii) diffusion of excitons to the D–A interface, (iii) exciton dissociation, i.e. transfer of electron from donor to acceptor and (iv) charge transport to the respective electrodes (**Figure 1.4b**). Although a large number of DPP based small molecules are reported as active layer in BHJ solar cells, functioning both as acceptor as well as donors, we limit our discussion to some selected systems that are highly efficient.

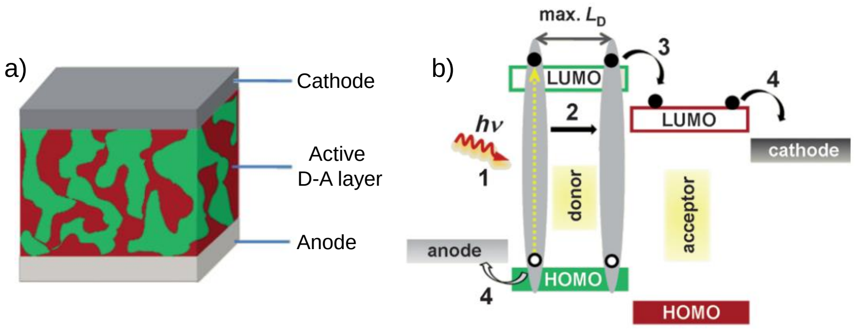

**Figure 1.4. a)** Typical device structure of a BHJ solar cell and **b)** key stages after photoexcitation.

### 1.5.1.1. DPPs as Electron Donor

Most of the DPP based small molecules are D–A type. Depending on the comparative donor or acceptor strength, they can either act as an electron donor or an electron acceptor. Recently, Peng and coworkers have reported a molecular system **10** where a central porphyrin was attached to two DPP units through ethynylene bridges (**Figure 1.5a**).[35] This molecule exhibited a broad absorption spectrum up to 907 nm with a low band gap of 1.37 eV because of extended $\pi$–conjugation (**Figure 1.5b**). Solution–processed OSCs were fabricated using **10** as a donor and $PC_{61}BM$ as an acceptor with an optimized ratio of 1:1.2, with a device structure of ITO/PEDOT: PSS/active layer/PFN/Al. Devices fabricated without solvent additives displayed a maximum PCE of 5.53% and upon annealing at 120°C for 10 min, the PCE increased to 5.89%. Further improvement in efficiency was observed when device was fabricated in presence of 1% pyridine as an additive followed by thermal annealing. The optimized solar cell exhibited a remarkable PCE of 8.08% with an external quantum efficiency and short circuit current ($J_{sc}$) of 65% and 16.76 mA/cm$^2$, respectively (**Figure 1.5c**). More interestingly, the best performing device showed an open–circuit voltage ($V_{oc}$) of 0.78 V with an energy loss of 0.59 eV, the lowest reported for a small molecule based solar cell. Nano phase segregation in these solar cells was confirmed via TEM and grazing incidence X–ray diffraction (GIXD) analyses (**Figure 1.5d, e**).

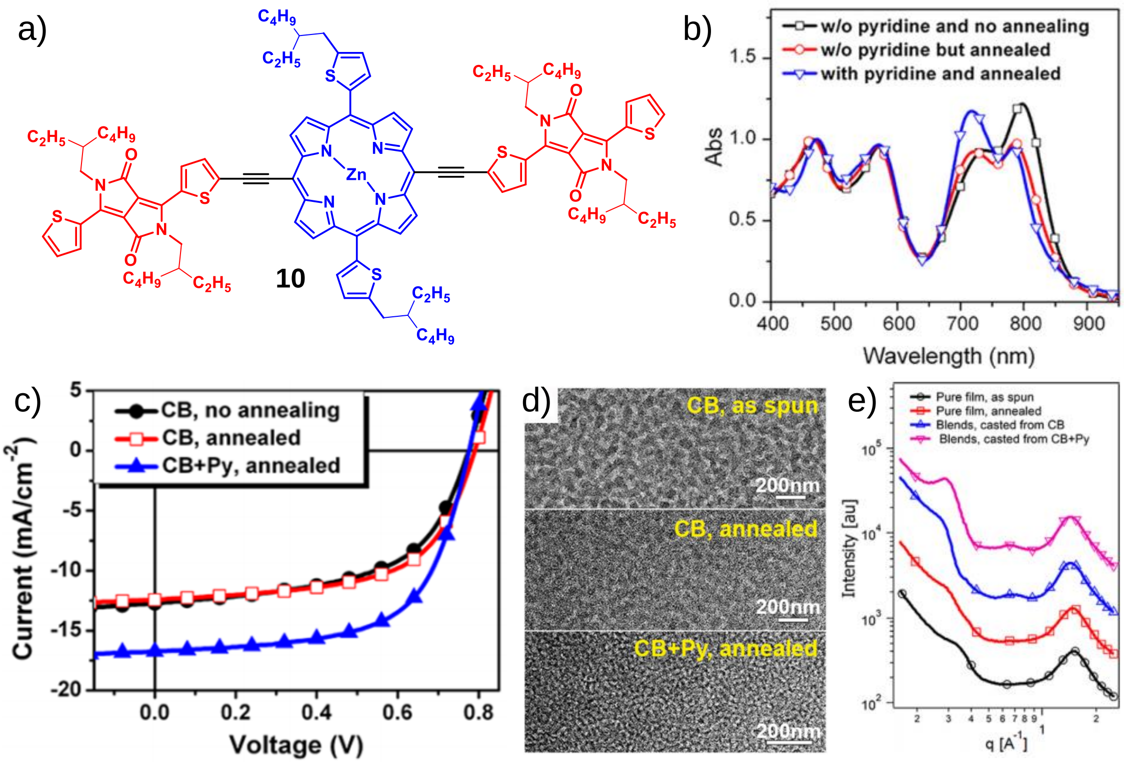

**Figure 1.5. a)** Chemical structure of **10**. **b)** Film state absorption spectra. **c)** *I*–*V* curves of OSCs having an active layer of **10**: PC$_{61}$BM (1:1.2) and **d)** the corresponding morphology from TEM. **e)** Out–of–plane XRD profiles of the active layer.

## 1.5.1.2. DPPs as Electron Acceptor

Most of the DPP based small molecules are electron donors, however by increasing the acceptor strength it is possible to develop DPP based electron acceptors for organic solar cells. Considerable attention in the last few years has been focused on the development of non–fullerene based D–A small molecule acceptors.[36] General strategy for the design of such electron acceptor involves the introduction of several electron accepting units in the π–conjugated backbone. By using the same analogy, Sharma and coworkers have designed and synthesized two carbazole–based diketopyrrolopyrroles **12** and **13** with tetracyanobutadiene as the non–fullerene acceptor (**Figure 1.6a**).[37] An A–D–A–D polymer **11** was chosen as the electron donor. BHJ solar cells were fabricated by using **11** as donor, with **12** and **13** as acceptor in a ratio of 1:2 having a conventional device structure ITO/ PEDOT: PSS/ active layer/ PFN/ Al.

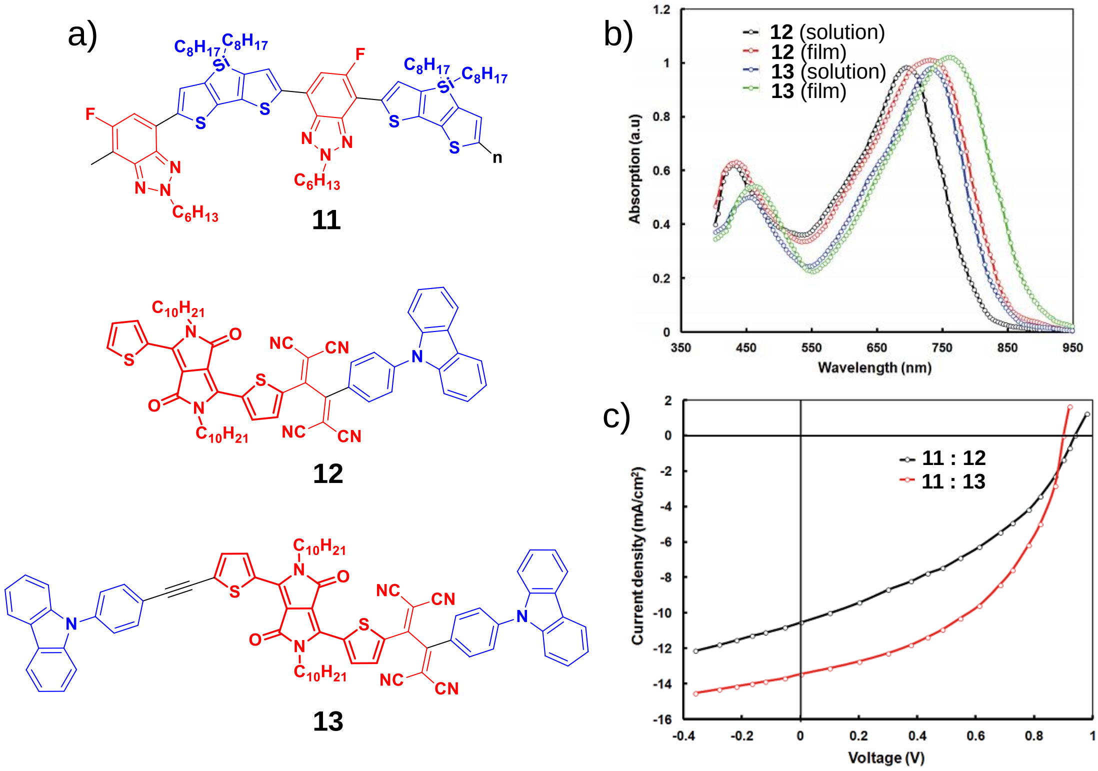

**Figure 1.6. a)** Chemical structure of polymeric donor **11** and acceptors **12** and **13**. **b)** Absorption spectra of **12** and **13** in the solution and film state. **c)** *I–V* curves of OSCs upon illumination of active layers.

Upon solvent vapor annealing of the active layer consisting of **11**:**12** (1:2), the cell showed an efficiency of 4.86% ($J_{sc}$ = 10.56 mA $cm^{-2}$, $V_{oc}$ = 0.94, and FF = 0.49) whereas **11**:**13** (1:2) exhibited an efficiency of 7.19% ($J_{sc}$ = 13.78 mA $cm^{-2}$, $V_{oc}$ =

0.90, and FF = 0.58) (**Figure 1.6c**). These values correspond to the highest reported efficiencies till date for an organic solar cell using a DPP–based non–fullerene acceptor. The high PCE arises probably due to the very broad absorption, high $J_{sc}$ and FF with a strong phase separation as supported by TEM and XRD analysis (**Figure 1.6b**).

## 1.5.2. Organic Field Effect Transistors (OFETs)

Over the last couple of decades, OFETs have attracted significant attention because of their potential application in radio frequency identification (RFID) tags, device chips, and sensors.[38] Due to the lower costs, light weight and flexibility, organic semiconductors are preferred over silicon counterpart for applications in field effect transistors.[39] Solution processable π–conjugated small molecules rendered promise as material of choice in OFETs but they suffer from poor mobility and stability. Typically, an OFET comprises of three electrodes where the two electrodes– source and drain are placed over a semiconductor layer which is deposited over a dielectric material and the third electrode, gate is situated on the other side of the dielectric.[40] Depending on the position of the gate, two types of device architectures are possible top–gate and bottom–gate configuration. A schematic of the top–contact/bottom–gate FET device structure is shown in **Figure 1.7**. The application of an electric field at gate electrode causes the flow of charges in the conducting channel at the dielectric/semiconductor interfaces. The key performance parameters of an OFET include the charge carrier mobility ($\mu$), the threshold voltage ($V_T$) and the on/off current ratio ($I_{ON}/I_{OFF}$). Majority of the organic semiconductors are hole transporting (p–type) material whereas a few exhibit electron transporting (n–type) or ambipolar behavior. DPP based π–conjugated D–A oligomers are reported to have impressively high charge carrier mobilities due to the delocalization of electron density and strong π–π interaction. Also, depending on the donor or acceptor strength, they either exhibit p–type or n–type or ambipolar characteristics.[17]

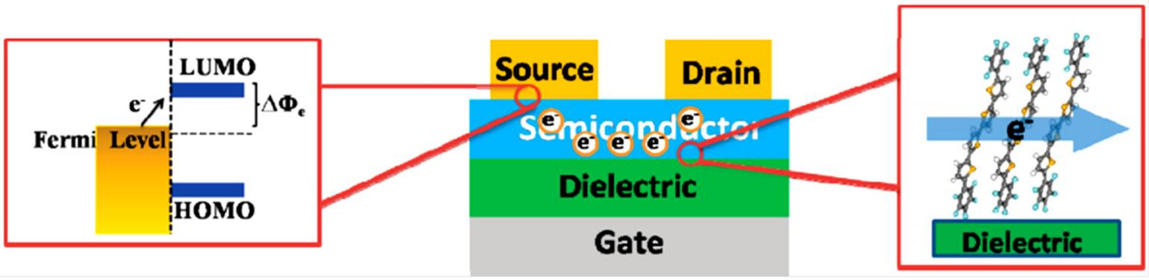

**Figure 1.7.** Schematic representation of top–contact/bottom–gate FET showing the charge–injection process and the preferred direction for electron transport.

#### 1.5.2.1. DPPs as Hole Transporter

Recently, Noh and coworkers have designed and synthesized D–A type small molecules **14** and **15** for OFET applications (**Figure 1.8a**).[41] A well–studied donor silaindacenodithiophene was placed between two DPP units and octylrhodanine was attached to the terminals as the electron–acceptor. In order to investigate the effect of side chains in OFET performance, branched alkyl chains were introduced in **14** and bulky siloxane–terminated hybrid alkyl chains in **15**. Both molecules showed similar absorption profiles in solution and solid states, but **15** in its film state had a red–shifted absorption when compared to that of **14**, pointing towards the stronger π–stacking interaction in **15**. The OFETs were fabricated by spin coating the solution of the semiconductors over a dielectric in a top gate/bottom contact (TGBC) configuration. Maximum hole mobility of 3.04 $cm^2\ V^{-1}s^{-1}$ was observed for **15** upon annealing at 100°C whereas **14** showed only 0.47 $cm^2V^{-1}s^{-1}$ under identical conditions (**Figure 1.8b, c**). This enhancement in hole mobility can be ascribed to the higher degree of crystallinity in **15** and hence smaller π–stacking distance as supported by GIXD.

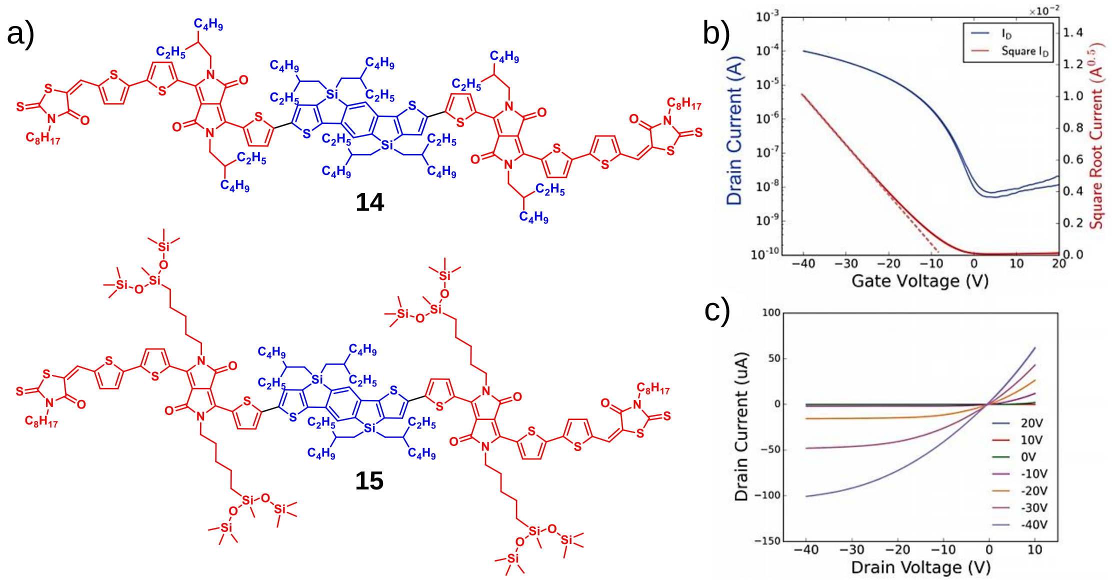

**Figure 1.8. a)** Molecular structures of the DPP derivatives **14** and **15**. **b)** Typical transfer and **c)** output characteristics of the OFET based on **15**.

### 1.5.2.2. DPPs as Electron Transporter

As mentioned earlier, most of the DPP based small molecules are p–type in nature and a very few exhibit n–type characteristics. Although significant efforts were made to increase the electron mobility of the DPP derivatives, due to their low–lying LUMO, these have less stability under ambient conditions.[17] The first major breakthrough came in 2012, when Zhu and co–workers came up with two quinoidal DPP–derivatives, **16** and **17** with dicyanomethylene terminals (**Figure 1.9a**).[42] Interestingly, these derivatives were found to be air stable and displayed excellent electron mobility up to 0.55 $cm^2V^{-1}s^{-1}$ (**16**) and 0.35 $cm^2V^{-1}s^{-1}$ (**17**). However, quinoidal structures have less aromaticity and are difficult to synthesize. Subsequently, Park and co–workers introduced a strong electron accepting dicyanovinyl group in the aromatic backbone of a similar π–conjugated derivative **18**.[43] The low–lying LUMO of **18** got substantial stabilization through extended delocalization. For OFET fabrication, single crystals of **18** were grown over $SiO_2$/Si substrates using slow solvent evaporation (**Figure 1.9b**). Interestingly, these single crystals exhibited very high electron mobility up to 0.96 $cm^2V^{-1}s^{-1}$ which is one of the highest value reported for DPP (**Figure 1.9c**). Wide–angle X–

ray scattering (WAXS) indicated strong intermolecular π–π stacking (3.6 Å) between D–A chromophores resulting in such high electron mobility.

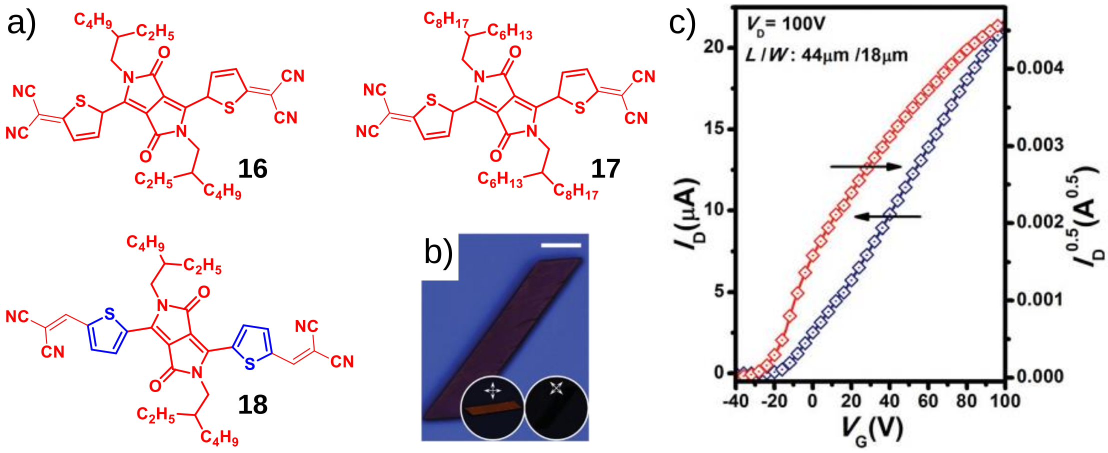

**Figure 1.9. a)** Chemical structures of **16–18**. **b)** Optical microscope images of a single crystal of **18** grown on $SiO_2$/Si and **c)** transfer characteristics of a single crystal of **18**.

## 1.6. Self–assembly of DPP Chromophores

Till now we have mainly discussed the design, synthesis, optical and electronic properties of DPP based small molecules with high performance in optoelectronic devices. The significance of morphological control and molecular packing of DPP based organic semiconductors in defining the efficiency of the fabricated devices has already been detailed. To further improve the performance of organic semiconductors, control over molecular organization and morphology is a prerequisite. In this context, supramolecular polymers of π–conjugated systems are potential candidates as efficient organic semiconductors due to their ability to form highly directional and dynamic molecular assemblies.[19] Unlike in classical polymers, the building blocks in supramolecular polymers are held together through various non–covalent interactions (e.g., hydrogen bonding, aromatic π–stacking, host–guest interactions, metal coordination etc.) that enable the possibility for the self–rectification of packing defects during their formation.[21] Moreover, these individually weak supramolecular forces are collectively strong, thereby inducing robustness to these materials. Hence, researchers made attempts to enhance or tune the optical and electronic properties of DPP *via* self–organization which is an interesting strategy towards better organic semiconductors. Therefore, in the forthcoming sections, we will focus on the self–assembling properties of some selected DPP based systems that were studied for their charge transporting behavior.

### 1.6.1. Hydrogen Bonded Assemblies

Among various non–covalent interactions, hydrogen bonding (H–bonding) is mostly used to construct supramolecular architectures due to its high selectivity and directional nature.[22] Generally, H–bonds are formed when a donor with an available acidic hydrogen atom interacts with an acceptor having available nonbonding electron lone pairs. Several reports have demonstrated that H–bonded supramolecular assembly of $\pi$–conjugated systems exhibit better charge transporting property because of continuous charge percolation path.[19] Here, we will be discussing a few reports to show the importance of H–bonding for organizing DPP chromophores.

#### 1.6.1.1. Latent Hydrogen Bonded Assemblies

DPP has high propensity towards intermolecular H–bonding due to the presence of complementary H–bonding unit that makes it insoluble in common organic solvents. Although DPP has brilliant optical and electronic properties, their insolubility is the bottle neck for practical applications. In 1997, Iqbal and co–workers made an attempt to convert this pigment into a 'latent' pigment which is readily soluble in common organic solvents, similar to a dye and upon thermal treatment it gets transformed to the parent pigment.[51] A synthetic modification of DPP involved protection of the amide nitrogen with *t*–butoxycarbonyl (*t*–Boc) to get **20** which enhances its solubility in organic solvents. Upon annealing at 180 °C, the protecting group got eliminated as $CO_2$ and the parent pigment **19** was regenerated (**Figure 1.10a**). This unique chemistry prompted several research groups for application in devices since DPP based molecules have excellent charge transporting property.

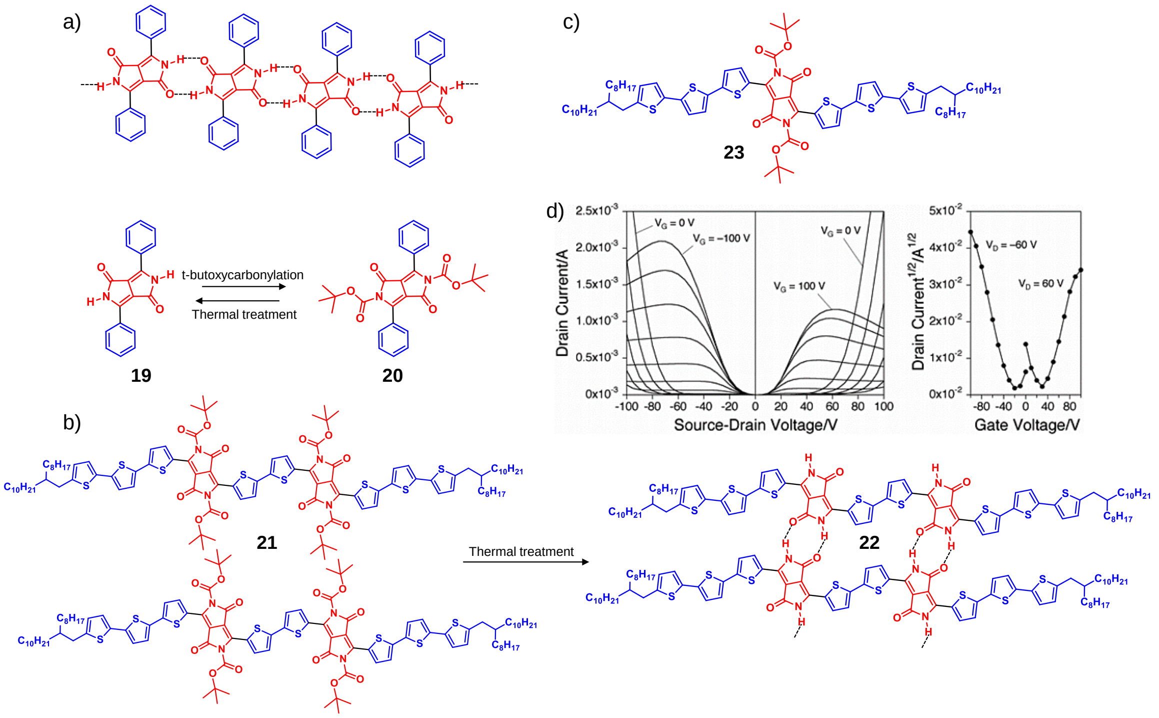

**Figure 1.10. a–c)** Chemical structures of the oligomers **19–23**. **a–b)** Activation of latent H–bond *via* thermal treatment. **d**) Output and transfer characteristics of **22**.

The first report came from the group of Sakai who demonstrated that *t*–Boc protected DPP as a latent pigment can be used in OFET applications, however only an order less hole mobility was observed.[52] Later, Yamashita and co–workers synthesized oligomers **21** and **23**, having thiophenes attached with branched alkyl chains and the DPP substituted with *t*–Boc (**Figure 1.10b, c**).[53] These molecules were shown to have high solubility and good film forming property. Also, intermolecular interaction was improved through thermal regeneration of the H–bonding network. The thermal cleavage of the *t*–Boc group was confirmed from differential scanning calorimetry (DSC) measurements. Bottom–gate/bottom–contact (BGBC) FET devices were fabricated *via* drop–casting a chloroform solution of **21** and **23** that exhibited low hole mobilities of $8.3 \times 10^{-6}$ $cm^2V^{-1}s^{-1}$ and $2.3 \times 10^{-5}$ $cm^2V^{-1}s^{-1}$, respectively. Interestingly, thermal annealing not only increased the hole mobility but also facilitated electron mobility leading to ambipolar behavior. For instance, the oligomer **22** regenerated upon thermal treatment exhibited balanced hole and electron mobilities of 6.7 × $10^{-3}$ $cm^2V^{-1}s^{-1}$ and 5.6 × $10^{-3}$ $cm^2V^{-1}s^{-1}$, respectively (**Figure 1.10d**). The high charge carrier mobility can probably be attributed to the extended H–bonding interactions leading to high crystallinity.

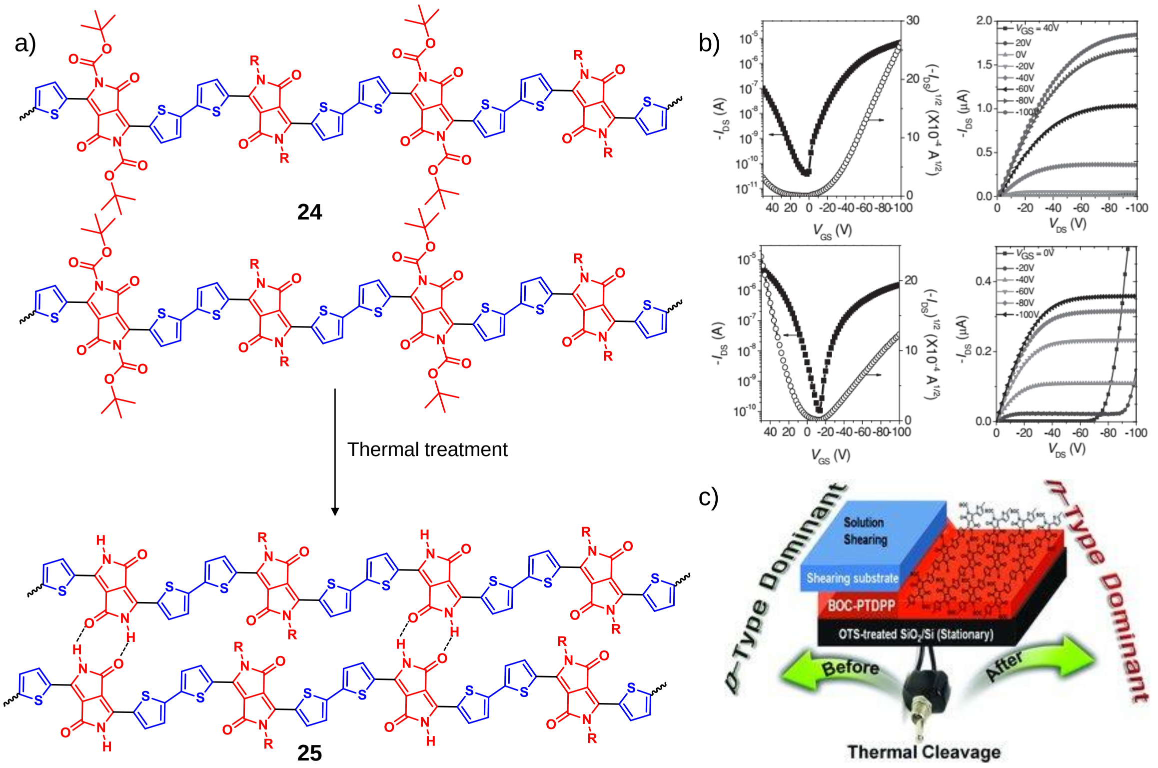

**Figure 1.11. a)** Molecular structures of the thermocleavable polymer **24** (before thermal treatment) and **25** (after thermal treatment). **b)** Transfer and output characteristics of **24** (top) and **25** (bottom) in a bottom–gate/top–contact (BGTC) OFET. **c)** Schematic representation showing the inversion of polarity upon thermal annealing.

In pursuit of further improving the hole as well as electron mobilities, Yang and co–workers prepared a solution processable polymer **24** with each alternating DPP protected with *t*–Boc (**Figure 1.11a**).[54] Annealing removes the *t*–Boc group and the resulting change in molecular packing was confirmed by thermogravimetric analysis (TGA), Fourier transform infrared (FT–IR) spectroscopy, and X–ray diffraction (XRD) analysis. All the OFETs were prepared through solution–shearing process because it provides better crystallinity and superior mobilities when compared to those prepared by the drop–cast method. The polymer **24** was used as an active layer in a bottom–gate/top–contact (BGTC) OFET that exhibited higher hole mobilities ($1.32 \times 10^{-2}$ $cm^2V^{-1}s^{-1}$) and lower electron mobilities (2.63 $\times 10^{-3}$ $cm^2V^{-1}s^{-1}$) (**Figure 1.11b**). Interestingly, upon thermal treatment at 200 °C under nitrogen atmosphere, **24** was converted into the parent polymer **25** and a switching in polarity was observed with increased electron mobility ($4.60 \times 10^{-2}$ $cm^2V^{-1}s^{-1}$) and lower hole mobility ($4.30 \times 10^{-3}$ $cm^2V^{-1}s^{-1}$) (**Figure 1.11c**). The polymer **25** possessed a more delocalized LUMO and greater crystallinity that provided better percolation path for the electrons.

Recently, Zhang and co–workers have used a very similar chemistry for sensing and detection of ammonia using OFETs.[55] Instead of directly protecting the amide with a *t*–Boc group, a *tert*–butyl carboxylate was attached (**26**) for better solubility (**Figure 1.12a**). A bottom–gate/bottom–contact (BGBC) FET fabricated by using **26**, exhibited a hole mobility of $1.5 \times 10^{-3}$ $cm^2V^{-1}s^{-1}$. However, a decrease in hole mobility was observed upon thermal annealing above 240 °C due to thermal elimination of *t*–Boc, forming **27** which led to packing disorder and rough morphology as concluded from XRD and AFM characterizations. Interestingly, a reduction in current was observed for **27**, when the FET was exposed to ammonia vapor due to the salt formation with the free –COOH. Also, this FET has the unique ability to signal the presence of ammonia as low as 10 ppb.

The chemistry of latent pigment is not only applied in OFETs but also applied in BHJ solar cells. Brovelli and co–workers attempted to obtain an optimum phase separation for preferential percolation of electrons and holes.[56] A solution processable *t*–Boc protected DPP oligomer **28** was mixed with PCBM to form a good film (**Figure 1.12b**). The active layer was fabricated by spin coating a mixture of **28**:PCBM (70:30 wt%) over an ITO/PEDOT:PSS anode. The thermal cleavage of the electron donor **28** led to the restoration of intermolecular H–

bonding to create stable **29**, crystalline and phase–separated molecular aggregates. As a result, over 20–fold increase of the PCE was observed due to superior exciton mobility in the crystalline domain. Hence, this can be an efficient strategy to improve the PCE of a BHJ solar cell.

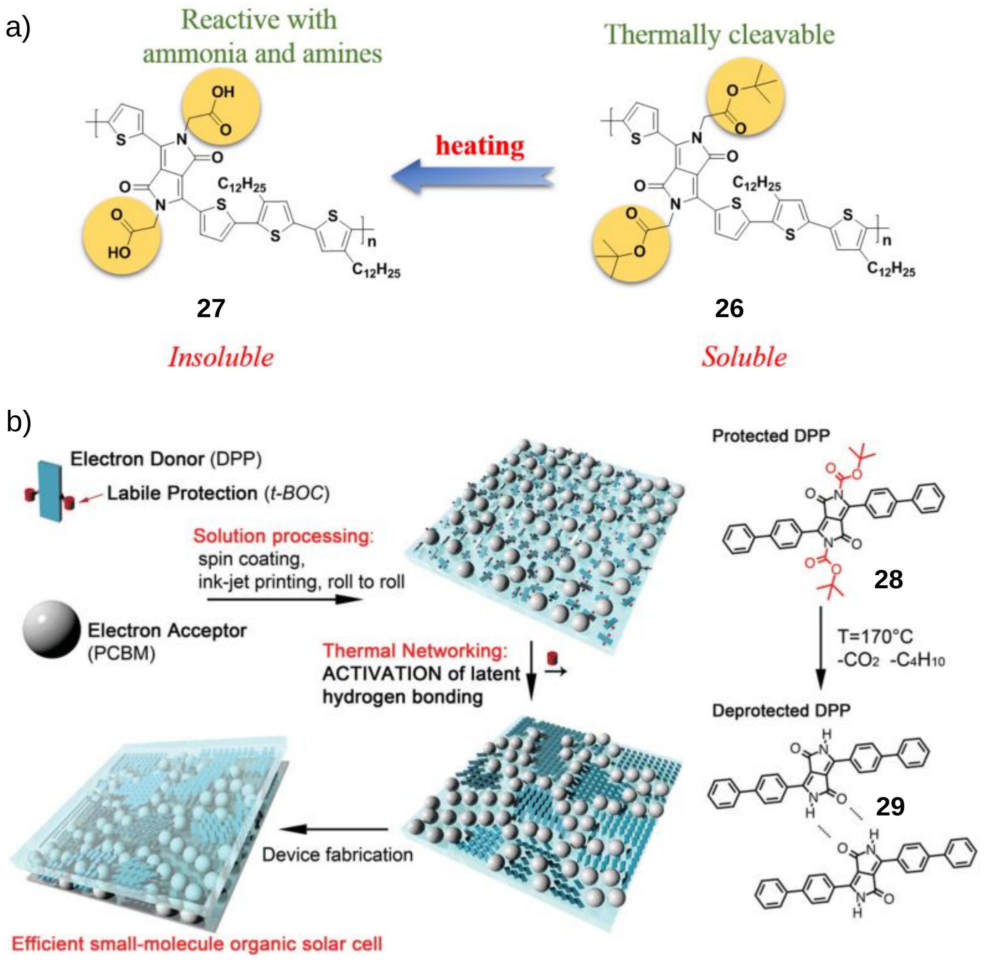

**Figure 1.12. a)** Chemical structures of the polymers **26** and **27**, along with the design rationale for ammonia sensing. **b)** Schematic representation and chemical structures of **28** and **29** showing the activation of latent H–bond upon thermal treatment.

#### 1.6.1.2. Aqueous H–Bonded Assemblies

Although, latent H–bonding provides better molecular organization it brings extra thermal budget. Hence, an alternative strategy involves the introduction of H–bonding motifs in the side chain or in the π–backbone without hampering the solution processability. Moreover, H–bonding imparts directionality to the supramolecular polymer of π–conjugated chromophores. Zhang and co–workers have designed and synthesized a DPP derivative **30** having two carboxylic acid groups at each terminus of the side chain, with the aim of creating aqueous supramolecular polymer (**Figure 1.13a**).[57]

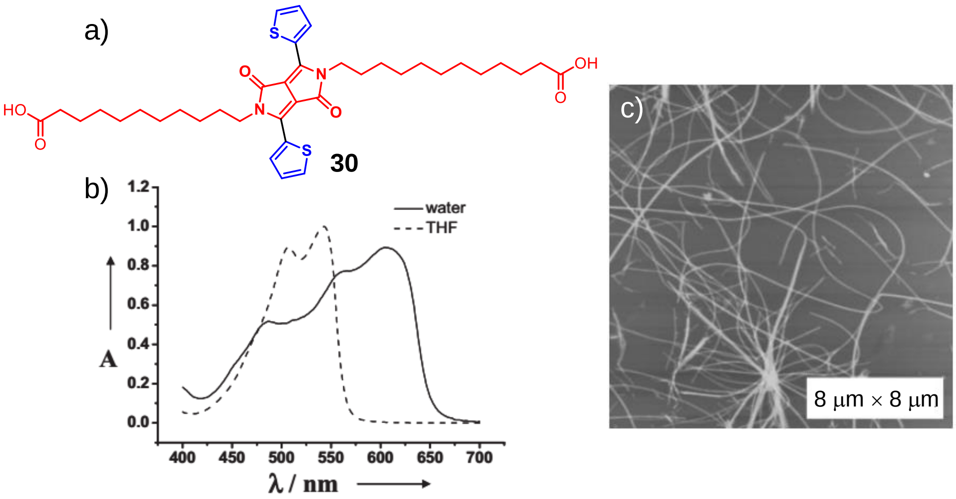

**Figure 1.13. a)** Molecular structure of the diacid **30**. **b)** UV–Vis absorption spectra of **30** in THF (dashed line) and water (solid line). **c)** TEM image of the nanofibers of **30** in water.

The formation of supramolecular polymers were observed when a THF solution of the diacid **30** was added drop wise into water leading to a change in color from orange to purple with a concomitant red shift in absorption (**Figure 1.13b**). AFM and TEM analysis confirmed the formation of supramolecular nanofibers of ~30 nm width and several micrometers in length (**Figure 1.13c**). This supramolecular nanofibers exhibited anisotropic fluorescence spectra when measured from a parallel or a perpendicular direction of the polarizations. Molecule **30** is soluble in THF and it does not form nanofiber even after slow evaporation of the solvent, as supported by AFM study. To understand the contribution of carboxyl group towards the formation of nanofibers, the diacid **30** was converted into the potassium salt. As expected, the salt formed ill–defined aggregates in water without any trace of fiber like structures. FT–IR studies further confirmed the presence of H–bonding (peak at 1724 cm$^{-1}$) for **30** which is absent for its potassium salt, indicating the indispensable role of H–bonding in the formation of supramolecular nanofibers. However, the practical applications of these DPP based supramolecular nanofibers were not explored.

#### 1.6.1.3. DPP based Organogels

Often H–bonding in chromophoric systems leads to the gelation of solvents owing to the formation of extended supramolecular nanostructures that can entrap solvent in a three dimensional matrix. Organogels and hydrogels have attracted tremendous attention of the scientific community due to their characteristic properties including the continuity of the network structure, solid–like rheology, absence of steady state flow, tunable transparency, low processing temperature and reversibility.[21] In this context, $\pi$–gels are a promising class of functional soft materials formed out of short $\pi$–conjugated molecules.[19] The application oriented research on $\pi$–gels was centered mainly around their promising electronic properties, such as tunable emission, energy and electron transfer, charge transport, and electrical conductivity.[20] These electronic properties are amenable to modulation through size and shape control of molecular assemblies. Although, a large number of $\pi$–gels are reported, only a few of them are DPP based. In a very recent report, Adams and co–workers prepared an L–phenylalanine attached DPP **31**, that formed a hydrogel (**Figure 1.14a**).[58] To a solution of **31**, glucono $\delta$–lactone was added to trigger the gelation by decreasing the pH to 3.3. Rheological measurements showed that storage modulus ($G'$) is much greater than loss modulus ($G''$) confirming the formation of the hydrogel. The xerogel of **31** exhibited a blue shift in the absorption maximum with respect to the monomer, indicating the predominant presence of H–aggregates (**Figure 1.14b**). As a result, the xerogel of **31** exhibited better ohmic contact than the solution dried sample of **31** as evident from the corresponding *I–V* curves (**Figure 1.14c**). Further increase in conductivity was observed when the xerogel was doped with iodine vapor for 20 min (**Figure 1.14d** and **e**). It is well established that self–sorted assemblies of electron–donor and electron–acceptor molecules provide ample scope for facilitating photocurrent generation. An attempt in this direction was made by adding perylenebisimide (PBI) derivative, which is an n–type material to a solution of **31**. The formation of self–sorted assemblies was established from UV–Vis absorption, rheology and NMR studies. However, the self–sorted assembly was found to produce less current as compared to PBI film. This report showed the importance of H–bonding in aligning the DPP chromophores for achieving high conductivity.

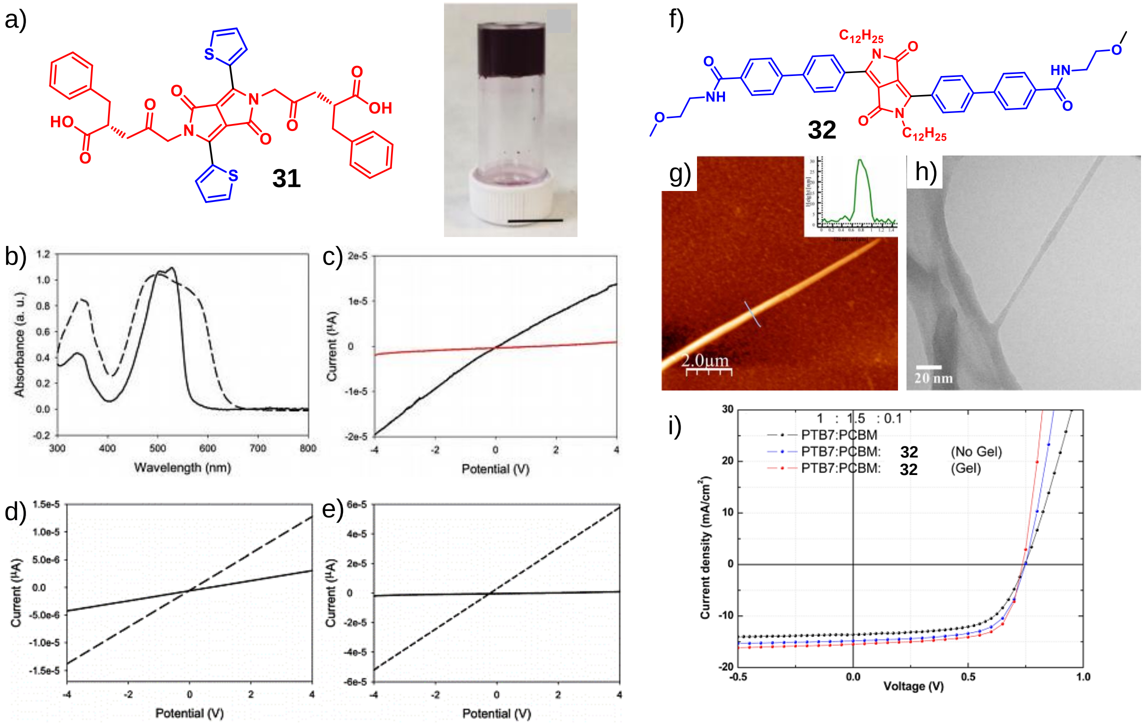

**Figure 1.14.** **a)** Molecular structure of **31** and photograph of the corresponding gel, **b)** UV–Vis absorption spectra of **31** in the solution and xerogel state. *I–V* curves of **c)** dried solution (red) and xerogel (black); after exposing to the iodine vapor *I–V* curves of **d)** dried solution and **e)** xerogel of **31**. **f)** Chemical structure of amide functionalized DPP derivative, **32**. **g)** AFM and **h)** TEM images of the nanofibers of **32**. **i)** *I–V* characteristics of optimized device comprising of an active layer of PTB7:PCBM:**32**.

Singh and co–workers reported the fabrication of solar cells from a DPP based organogel derived from the diamide **32** with an efficiency of 7.9% and this was the first demonstration of using a DPP based organogel for solar cell application (**Figure 1.14f**).[59] The molecular structure of **32** consists of amide groups in the backbone that drives the hydrogen bonding interactions supported by additional π–stacking and van der Waals interactions. The diamide **32** has the ability to form gel in DCM, DMSO, DMF, ethylacetate, and chlorobenzene. **32** exhibited a red shifted broad absorption when compared to its monomer, indicating the existence of J–type aggregates. AFM and TEM analyses supported the formation of 1D supramolecular nanofibers when the organogel of **32** was spin coated over a silicon substrate (**Figure 1.14g, h**). Powder XRD pattern confirmed that these nanofibers had a lamellar organization with a π–stacking distance of 3.8 Å. 1D supramolecular nanofibers generally have high charge transporting property and are highly desirable for device applications. To check their charge transporting property, OSCs were fabricated with the active layer of PTB7/$PC_{71}BM$/**32** (1:1.5:0.1). Maximum PCE of 7.85% was obtained when the gel of **32** was used as an additive (**Figure 1.14i**). Thus, supramolecular assembly of **32** favored energy transfer to suitable acceptors by providing a better percolation path for charge transport.

### 1.6.1.4. H–bonded DPP Assembly for OSCs

As discussed previously, the performance of an OSC depends considerably on the active layer morphology that can be controlled *via* self–assembly, in particular by H–bonding. Stupp and co–workers have reported a hairpin–shaped donor molecule **33** comprising of a *trans*–1,2–diamidocyclohexane core and two arms of DPP conjugated segments attached through amide groups (**Figure 1.15a**).[60] Utilizing the synergistic effects of H–bonding and π–stacking, the donor molecule self–assembles in non–polar solvents, leading to the formation of long supramolecular nanowires. The active layer of the BHJ solar cell was fabricated by spin coating a stirred mixture of the donor **33** and $PC_{71}BM$ in (toluene : chlorobenzene) at 80 °C for 12 hours to avoid possible clustering. However, these devices showed very poor PCE of <0.0014% due to the absence of 1D supramolecular nanostructures. To improve the PCE, a stepwise procedure was followed to prepare the active layer where the donor molecules were first allowed to self–assemble and then

$PC_{71}BM$ was added into it. UV–Vis absorption revealed the simultaneous formation of both H– and J–type aggregates that eventually formed nanowires as evident from the AFM and cryo–TEM analyses (**Figure 1.15b**). The active layer consisting of **33**:$PC_{71}BM$ (1:1) exhibited maximum device efficiency of 0.53% which is almost 400 times higher than that of the previous device, pointing towards the better charge transporting property of 1D self–assembled nanofibers.

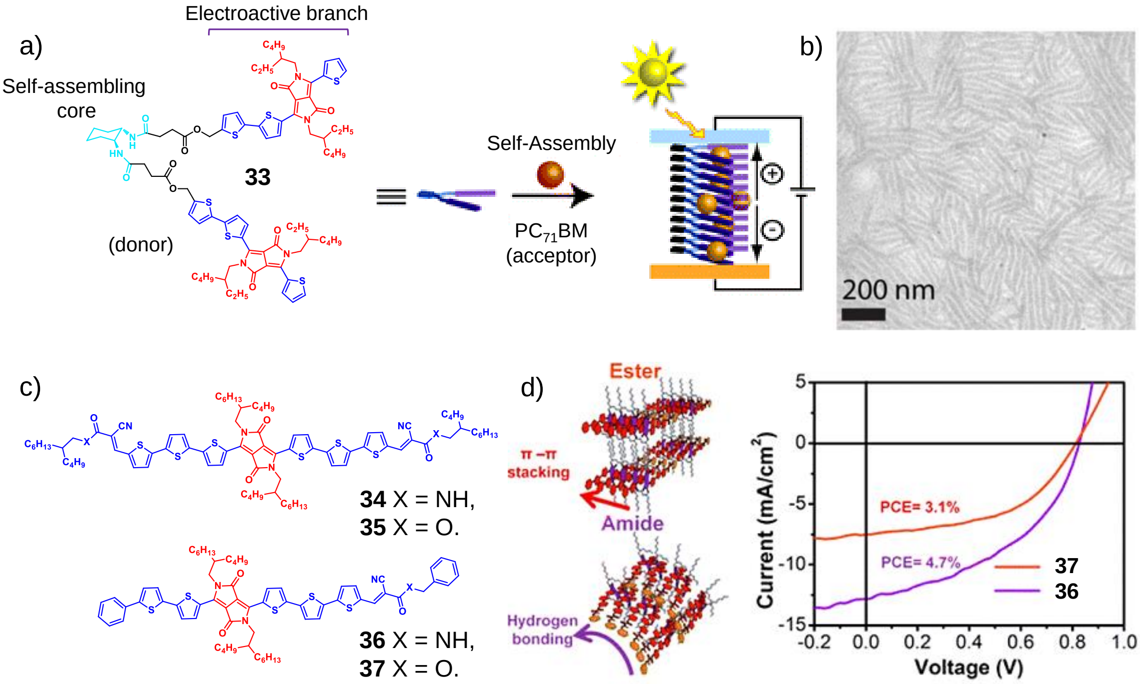

**Figure 1.15. a)** Chemical structure of the hairpin–shaped donor **33** and the schematic representation of its self–assembly with $PC_{71}BM$. **b)** Cryo–TEM images of the nanofibers obtained by the self–assembly of **33** with $PC_{71}BM$. **c)** Molecular structures of **34–37**. **d)** Pictorial representation of the self–assembly and *I–V* characteristics of **36** and **37**.

Later, the same group modified the system and developed a series of molecules with and without H–bonding units to control the degree of aggregation. Highly conjugated DPP based oligomers (**34** and **35**) were prepared with extremely low band gap capable of acting as a donor (**Figure 1.15c**).[61] The derivatives **34** and **35** exhibited very similar absorption profile in solution and solid states. Aggregated films of both **34** and **35** showed very broad and red–shifted absorption due to the combined effect of H–bonding and π–stacking, leading to strong aggregation.

OSCs fabricated using **34** and **35** as donor and $PC_{71}BM$ as acceptor (1:1) showed a poor PCE efficiency of 0.37% and 0.15%, respectively. The low PCE was attributed to the strong phase segregation that in turn leads to low exciton generation as deduced from the morphological analysis. In order to obtain nanophase segregation, the derivative **36** and **37** were synthesized which have less aggregation property. The device with the derivative **36** exhibited a PCE of 3.65% when the active layer was prepared by mixing with $PC_{71}BM$, whereas that with the derivative **37** reached only 1.45%. Further increase in PCE up to 4.57% was obtained for the device with **36** when nitrobenzene was used as an additive (**Figure 1.15d**). Although the molecule **36** and **37** had very similar optical properties, better PCE was observed for the former. These results underpin the synergistic effects of H–bonding and π–stacking in providing better nanophase segregation and charge percolation pathway.

### 1.6.1.5. H–Bonded DPP Assembly for OFETs

Unidirectional charge transporting materials are highly desirable for OFETs and the directionality of H–bonding can be used as a driving force to create such materials with enhanced charge carrier mobility. Commonly, dialkylation increase the solubility of DPP derivatives, however during the purification of the reaction mixture, Patil and co–workers obtained a highly crystalline mono alkylated DPP.[62] Two benzene appended (**38**, **39)** and two thiophene appended (**40**, **41**) DPP derivatives were thus obtained (**Figure 1.16a.**). Monoalkylated (**38**, **40**) and dialkylated (**39**, **41**) derivatives exhibited very similar absorption and emission profiles in the solution and solid states. Interestingly, the dialkylated derivatives **39** and **41** preferred herringbone packing, whereas the monoalkylated derivatives **38** and **40** formed cofacial layered structures due to complementary intermolecular H–bonding. Bottom–gate/bottom–contact (BGBC) OFET devices were fabricated over $SiO_2$ wherein a solution of the respective organic material was drop cast and evaporated slowly to grow the crystals between the source and the drain electrodes. The crystals of **38** and **40** showed hole mobility of $1.6 \times 10^{-2}$ and 0.3 $cm^2V^{-1}s^{-1}$

respectively, whereas dialkylated DPP crystals exhibited considerably less mobility (**Figure 1.16b**). The best optimized device showed a maximum hole mobility of 2 cm$^2$V$^{-1}$s$^{-1}$ for **40**, confirming the importance of H–bonding in inducing the formation of cofacial layered structures with a $\pi$–stacking distance of 3.45 Å.

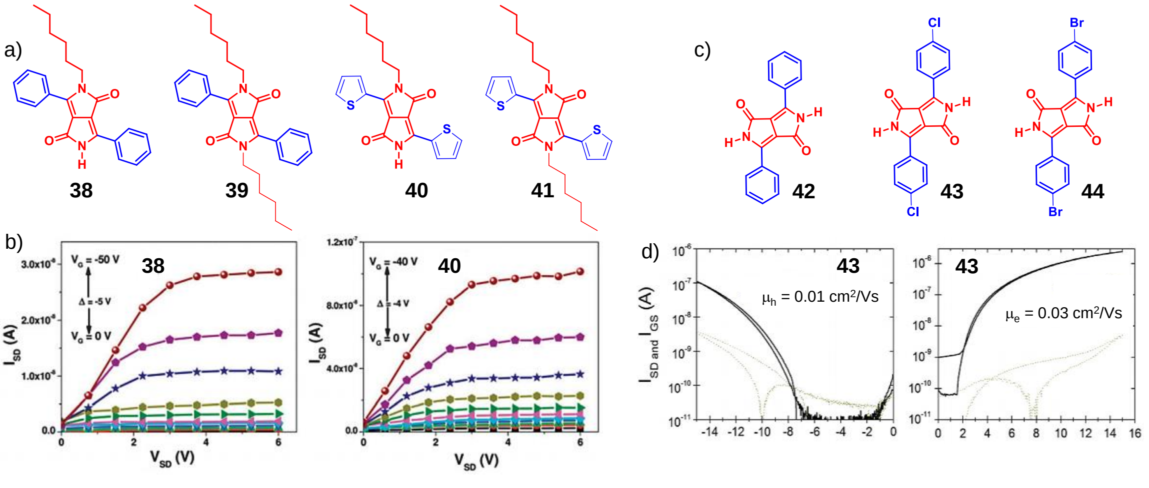

**Figure 1.16. a)** Molecular structures of the mono– and dialkylated DPP derivatives **38–41** and **b)** output characteristics of **38** and **40**. **c)** Chemical structures of the DPP derivatives **42–44** and **d)** OFET output characteristics of **43**.

In another report, Głowacki and co–workers used three pigments, **42**–**44** to fabricate OFETs for understanding their charge carrier mobility (**Figure 1.16c**).[63] Bottom–gate/top–contact (BGTC) OFETs were fabricated by vacuum deposition because these derivatives are not solution processable. All these derivatives were found to exhibit ambipolar charge carrier mobilities in the range 0.01–0.06 cm$^2$V$^{-1}$s$^{-1}$ (**Figure 1.16d**). From the single crystal analysis, it was proven beyond doubt that the H–bonding aligns well with the strong co–facial $\pi$ stacking, resulting an increase in the charge transfer integral.

Zhang and co–workers have reported DPP–quaterthiophene conjugated polymers **45**–**48**, where most of the DPP units were appended with branched alkyl chains for achieving better solubility and the remaining side chains appended with urea moiety (**Figure 1.17a**).[64] The rationale behind choosing the urea moiety was to increase the inter–chain interactions though H–bonding would enhance the formation of self–assembled crystalline domains. Moreover, in a mixture of donor and acceptor, the H–bonding interactions between the polymer chains would lead to better nanophase segregation. In order to control the aggregate size and degree of aggregation, polymers **45**–**47** were investigated by varying the mole ratio of x and y from 1:30 to 1:20 and 1:10, respectively. For comparison, the derivative **48** was synthesized devoid of urea groups in the alkyl side chains. FT–IR and $^1$H–NMR of the polymer **46** indicated the existence of inter–chain hydrogen–bonding. All the polymers showed similar absorption spectral profile absorption spectra in the solution and solid states.

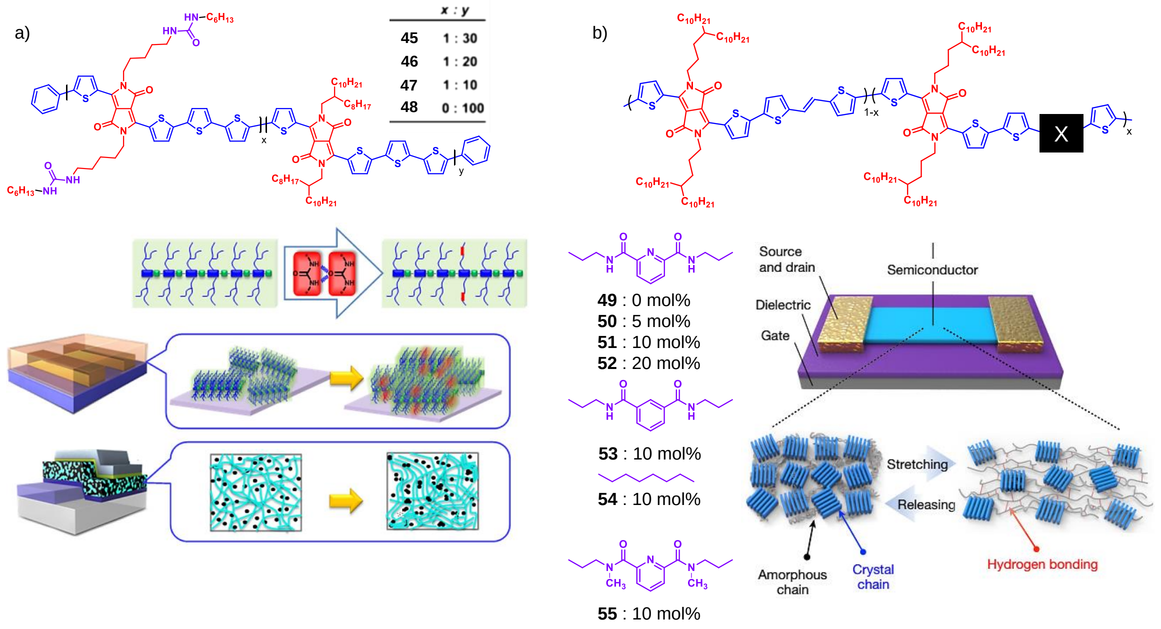

**Figure 1.17. a)** Chemical structures of the polymers **45–48** and schematic representation of the H–bonded assembly in the active layer of the device. **b)** Molecular structure of the polymer **49–55** and the plausible mechanism showing the role of H–bond in retaining the molecular packing upon stretching and releasing.

Bottom–gate/bottom–contact (BGBC) FETs were fabricated to understand the effect of H–bonding on charge carrier mobility. The polymers **45**, **46** and **47** exhibited average charge carrier mobility of 5.1, 7.1, and 11.4 cm$^2$V$^{-1}$s$^{-1}$, respectively, much higher than that for the polymer **48**. Remarkably, high hole mobility of 13.1 $cm^2V^{-1}s^{-1}$ was obtained for the polymer **47** after thermal annealing at 100 °C for an hour. From GXRD, it is evident that optimum H–bonding facilitates lamellar organization with strong π–stacking. Due to the high hole mobility of all these polymers, they were used as donor units in OSCs while $PC_{71}BM$ was selected as the acceptor. A maximum PCE of 6.8% was obtained for **45** : $PC_{71}BM$, whereas **46** : $PC_{71}BM$ and **47** : $PC_{71}BM$ exhibited PCE of 6.7% and 6%, respectively. All these reports corroborate the fact that H–bonding facilitates the improvement of charge carrier mobility as well as photovoltaic performance in oligomers as well as polymers.

Another interesting report came from Bao and co–workers where a H–bonding unit incorporated into the polymer backbone provided dynamic crystalline domains. To understand the effect of H–bonding, several polymers **49**–**55** were prepared with different mole percentage of H–bonding and non H–bonding motifs (**Figure 1.17b**).[65] A gradual decrease in mobility was observed with increasing number of H–bonding units due to reduction in conjugation. Among the different polymers studied, only **51** maintained a mobility of > 1 $cm^2V^{-1}s^{-1}$ even on applying 100% strain. Also, the nanocracks generated upon stretching were healed completely through solvent annealing and heating. Experimental results suggest that extensive H–bonding was responsible for the high stretchability and self–healing property of the polymer **51** which was also studied for its application as a stretchable (like the human skin) electronic wearable device.

### 1.6.1.6. Photoinduced Electron Transfer (PET) in DPP Assembly

From natural photosynthesis to organic solar cells, photoinduced electron transfer (PET) is the fundamental process that converts light to chemical energy.[66] Efficiency of a PET depends on the energy levels of the donor and acceptor, and the distance between them. By proper positioning of the donor and the acceptor, one can obtain long lifetime photoinduced charge–separated states, a requirement for harvesting maximum light.[67] Supramolecular polymers are known to provide such spatial organization for efficient charge separation. Braunschweig and co–workers reported a combination of 2,6–pyridine dicarboxamide attached DPP, **56** and bay substituted PBI **57** for complementary H–bonding (**Figure 1.18a**).[68] Initial studies directed towards the possibility for homo– and heteroaggregate formation involving **56** and **57** through H–bonding and π–stacking. The DPP derivative **56** alone formed disordered aggregates, whereas ordered heteroaggregates were formed when **56** and **57** were mixed in a 2:1 ratio. Upon slow cooling of the mixture from 30 °C to 13 °C, emergence of a red–shifted band was observed in UV–Vis spectra along with an exciton coupled CD, indicating the formation of J–type helical superstructures.

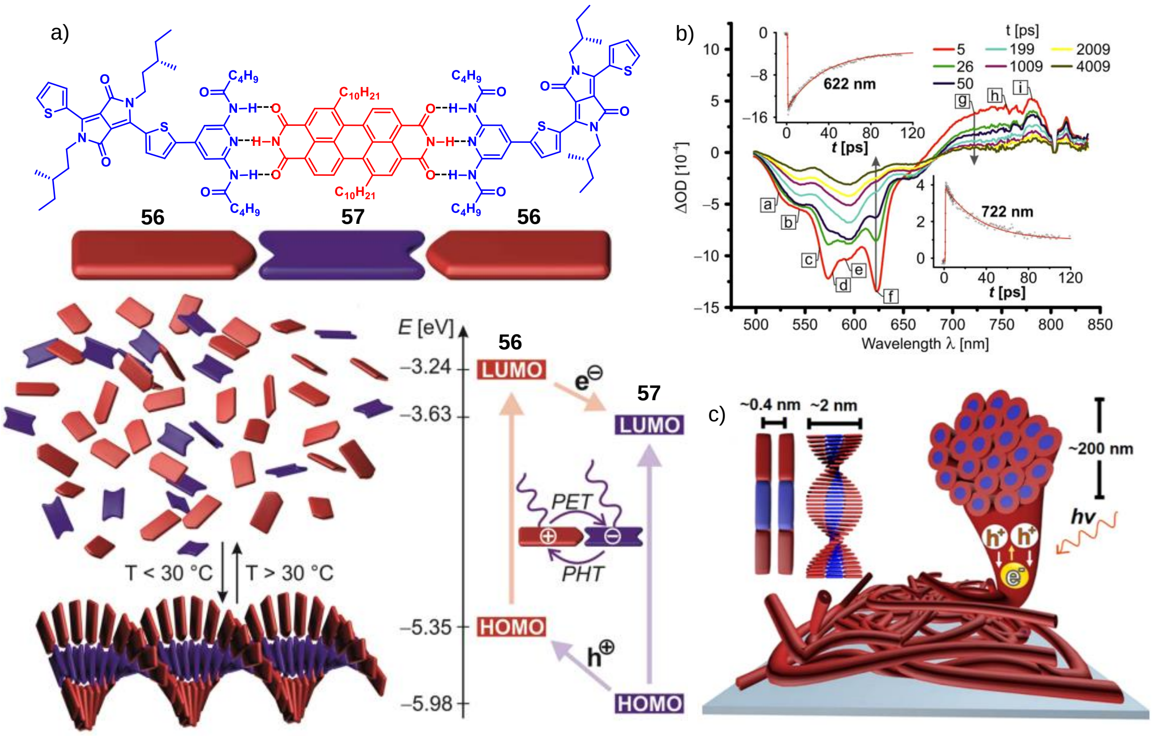

**Figure 1.18. a)** Chemical structure of **56** and **57** with schematic representation showing the formation of superstructure upon cooling. **b)** Femtosecond transient absorption spectra of 2:1 (**56**:**57**). **c)** A schematic representation of the H–bonded hierarchical superstructures with π–channels for photoinduced charge separation and transport.

Authors also made an attempt to understand the PET process upon photoexcitation of the donor DPP derivative.[69] The energy levels of the donor **56** and the acceptor

**57** were estimated from cyclic voltammetry (CV) measurements, indicating the thermodynamic feasibility of electron transfer (**Figure 1.18a**). Helical supramolecular superstructures of **56** and **57** were created in a similar fashion as discussed earlier. Photoexcitation was performed at 365 nm since donor **56** has three times higher absorption than the acceptor **57** at that particular wavelength. Upon cooling the mixture below 40 °C, a decrease in fluorescence intensity was observed for **56** due to the electron transfer from donor **56** to acceptor **57**. At higher temperatures, electron transfer was not observed because of increased distance between the donor and acceptor moieties. Moreover, a ground state bleaching in absorption was observed with a broad positive feature in the 722 nm region from the femtosecond transient absorption study of the superstructures (**Figure 1.18b**). The anion radical (**57**$^{\bullet-}$) is known to exhibit this kind of broad absorption as explained in the previous literature. Thus, supramolecular self–assembly provides a unique strategy to obtain long lived charge separated states. Subsequently, the same group has shown that these superstructures were less prone to charge recombination in their film state than in the solution state. This might be due to the fact that supramolecular hierarchical structures tend to provide long range photoconductivity due to defect free ordered arrangement (**Figure 1.18c**).

### 1.6.2. Amphiphilic DPP Derivatives

Amphiphilic π–conjugated molecular building blocks are potential candidates for creating functional supramolecular polymers of different shape and dimensionality by means of solvophilic and solvophobic interactions.[70] Zhang and co–workers have reported a DPP based bolaamphiphile **58** by attaching a pyridinium moiety at the end of the alkyl chain **(Figure 1.19a)**.[71] Above the critical micelle concentration, the DPP derivative **58** self–organize *via* π–stacking as manifested from the changes in NMR and UV–Vis spectra **(Figure 1.19b)**. Dynamic J–type aggregate formation was confirmed from time and temperature dependent absorption studies. Moreover, AFM studies revealed the presence of disk like monolayered micelles which can overlap to form bilayered or multilayered structures **(Figure 1.19c)**.

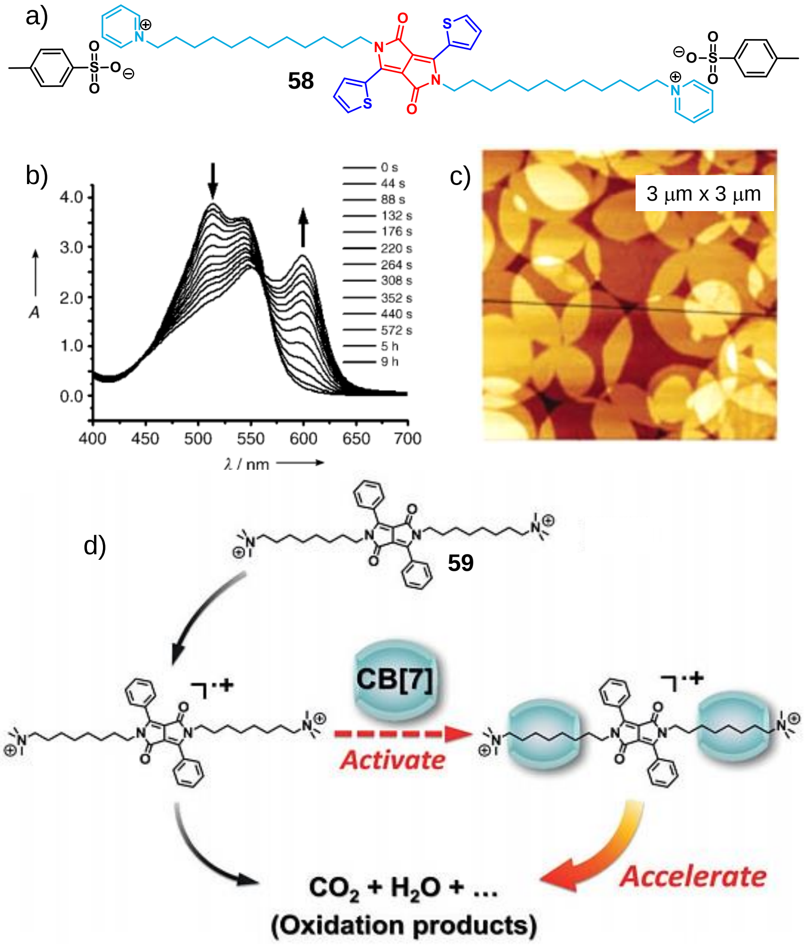

**Figure 1.19. a)** Chemical structure of the bolaamphiphile **58**. **b)** Change in the absorption spectrum of **58** with time in water. **c)** AFM images of the micellar structures. **d)** Molecular structure of the amphiphile **59** and possible mechanism of accelerated Fenton oxidation.

The same group have reported another DPP based bolaamphiphile **59** with a tertiary amine group at the end of the alkyl chain that formed host–guest complex with the cucurbit[7]uril (CB[7]) as evident from NMR and isothermal titration calorimetry (ITC) studies **(Figure 1.19d)**.[72] The derivative **59** was used as a model dye for Fenton oxidation that degrades pollutant dyes in water. The mechanism involves the CB[7] mediated activation of DPP cation radical through electrostatically negative carbonyl groups which in turn accelerates the Fenton reaction. This system has a potential to be applied as a supramolecular catalyst to purify water by oxidizing the organic pollutants.

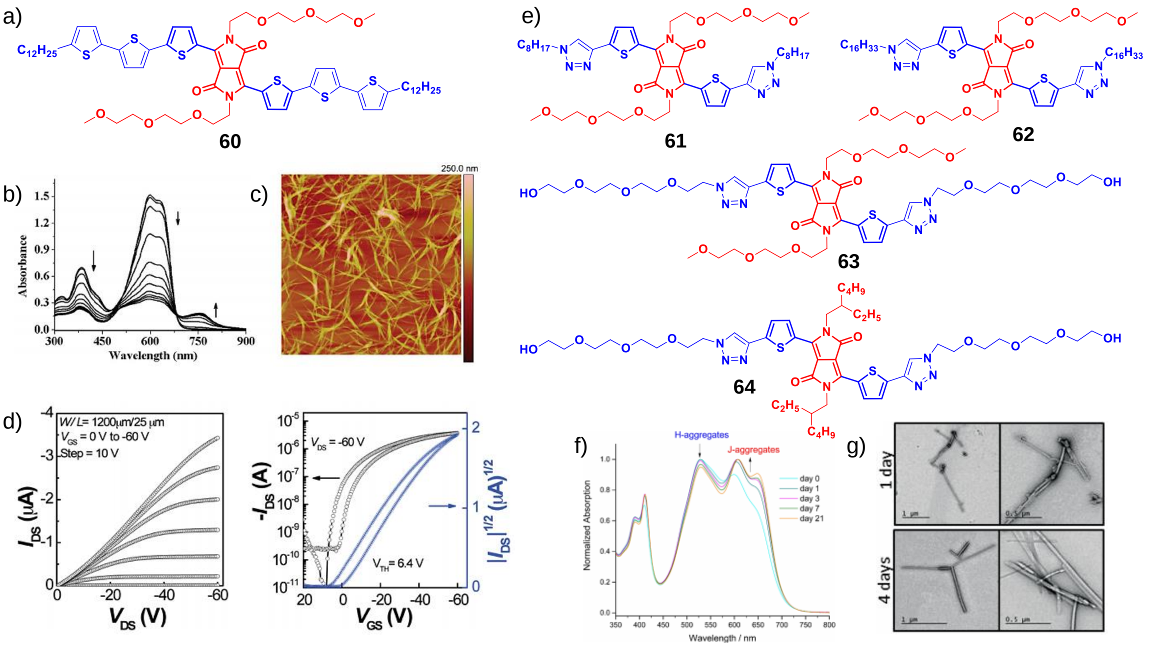

**Figure 1.20. a)** Chemical structure of the amphiphile **60. b)** Temperature dependent UV–Vis absorption of **60** in methylcyclohexane. **c)** AFM images of the nanofibers and **d)** Output and transfer characteristic of the OFET obtained from **60**. **e)** Molecular structures of the DPP derivatives **61–64**. Time dependent **f)** absorption and **g)** morphology of **61**.

Instead of using cationic group, Reynolds and co–workers attached lipophilic paraffinic chains and hydrophilic triglyme chains orthogonal to each other to a highly conjugated D–A low band gap molecule **60** (**Figure 1.20a**).[73] UV–Vis absorption study revealed that the DPP derivative **60** formed J–aggregates in methylcyclohexane (MCH) through intermolecular excitonic interactions (**Figure 1.20b**). From AFM analysis it was observed that **60** formed supramolecular nanofibers in THF–Hexane mixture (**Figure 1.20c**). The self–assembled supramolecular system exhibited a moderate hole mobility of $3.4 \times 10^{-3}$ $cm^2V^{-1}s^{-1}$ as estimated from OFET (**Figure 1.20d**), with a maximum PCE of 0.43% (**60**:$PC_{61}BM$ as active layer). By adopting a similar design strategy Farinola and co–workers have synthesized the molecules **61**–**64** with hydrophilic and hydrophobic side chains (**Figure 1.20e**) and investigated in detail their optical and aggregation properties.[74] Except molecule **63,** all other derivatives were water insoluble and the derivatives **61** and **62** formed nanostructures in polar solvents. Molecule **61** initially formed H–aggregates that were gradually transformed to J–aggregates over a period of time. These nanoparticles exhibited a broad absorption and NIR emission that is important for many biological applications. TEM images confirmed that both compounds **61** and **62** formed 1D structures with time.

### 1.6.3. π–Stacked DPP Derivatives

In 2008, Nguyen and co–workers reported the self–assembly properties of a number of oligothiophene derivatives (**65**–**66**) with a diketopyrrolopyrrole core (**Figure 1.21a**).[75] To understand the self–assembly, the conjugation as well as the alkyl side chains were systematically varied and all the derivatives were found to have tunable absorption and electrochemical band gap in the range of 2.25 to 1.80 eV. AFM analysis inferred that straight alkyl chains led to rod–like or needle–like morphologies whereas molecules with branched alkyl chains exhibited low solid state ordering (**Figure 1.21b, c**). π–Stacking is the major driving force behind this self–assembly and this was disrupted by the sterically crowded branched chains. Molecules **65** and **66** were able to form typical nanofibers over silicon substrates with excellent charge transporting properties due to ordered molecular organization. To have a deeper understanding, Nowakowski and co–workers made an attempt to envision the molecular organization of these types of molecules over different substrates.[76] A monolayer of this system over HOPG resulted 2D supramolecular assembly. Scanning tunneling microscopy (STM) revealed that all the molecules are arranged face–to–face and alkyl chain provides the intermolecular separation.

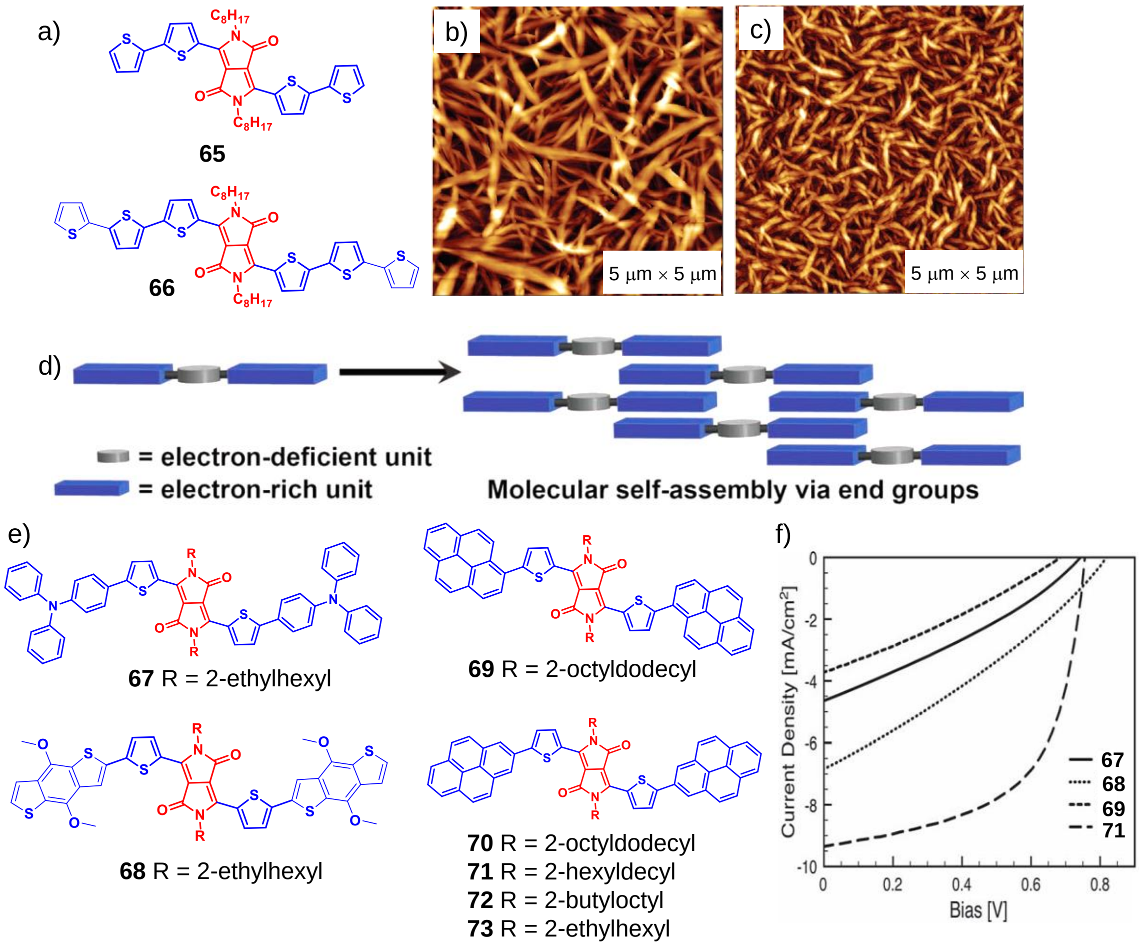

**Figure 1.21. a)** Chemical structure of the DPP derivatives **65** and **66**, and AFM images of **b) 65** and **c) 66** over a Si/SiO$_2$ substrate. **d)** Schematic representation of the self–assembly through π–stacking. **e)** Molecular structures of the DPP derivative **67–73** and **f)** characteristic *I*–*V* curves of OSCs.

In another report, Miao and co–workers have reported that π–stacking is assisted by intermolecular H···O=C hydrogen bonds between the hydrogen of thiophene rings and C=O of the DPP units of neighboring molecules. Fréchet and co–workers have introduced π–stacking motifs at the terminals of small molecules **67–73** to have an end–to–end self–assembly (**Figure 1.21e**).[77] Among different π–stacking motifs, pyrene is known to have the maximum propensity to π–stack. All the derivatives (**67**–**73**) exhibited broad absorption in the film state and hence can be used as a donor in BHJ solar cells. Active layer of the OSCs were fabricated by using PC$_{71}$BM as an acceptor in different blend ratio and maximum PCE of 4.1%

was obtained for the derivative **71** (**Figure 1.21f**). High PCE is attributed to the high $J_{SC}$ value arising from end group promoted highly crystalline assembly.

### 1.6.4. DPP based Liquid Crystals

$\pi$–Conjugated liquid crystalline molecules got tremendous attention as flexible electronic materials because of their potential applications in OLEDs, OSCs and OFETs. Till date, there are very few reports on DPP based liquid crystalline derivatives. To impart liquid crystallinity, Wong and co–workers have reported DPP attached hexabenzocoronene derivatives **74**–**76** with different solubilizing groups (**Figure 1.22a**).[78] Dyes **75** and **76** exhibited broad absorption due to extended $\pi$–conjugation as compared to **74**. Shift in $^1$H–NMR signals with the increase in concentration revealed the aggregation in all these derivatives (**74**, **75** and **76**). **74** formed columnar assembly, whereas **75** and **76** formed lamellar structures as evident from 2D–WAXS. Charge carrier mobility of all the derivatives were estimated from space–charge limited current (SCLC) and OFET and the highest was determined to be $1 \times 10^{-4}$ cm$^2$V$^{-1}$s$^{-1}$ for **74**. BHJ solar cells were fabricated by using PC$_{71}$BM as an acceptor and a maximum PCE of 1.59% was obtained for **74**. The columnar packing in the superstructures of **74** provides a better vertical charge percolation path as compared to others, resulting in the high PCE.

To further enhance PCE, Adachi and co–workers have reported a few small molecules **77**–**78** based on DPP, exhibiting liquid–crystalline properties (**Figure 1.22b**).[79] **77** showed an endothermic peak at 117 °C which corresponds to the liquid–crystalline mesophase. OSCs were fabricated with a typical device structure: ITO/PEDOT:PSS/**77**:PC$_{71}$BM/LiF/Al and a maximum PCE of 4.3% was obtained for the optimized device upon annealing at 140 °C. Thermal treatment led to the formation of mesogen as evident from the OPM studies (**Figure 1.22c**). UV–Vis spectral data suggested the transformation of J–aggregates to H–aggregates which has better charge transporting property. SCLC and OFET measurements further confirmed the increase in hole mobility up to 4.2 × $10^{-3}$ $cm^2V^{-1}s^{-1}$ upon thermal annealing.

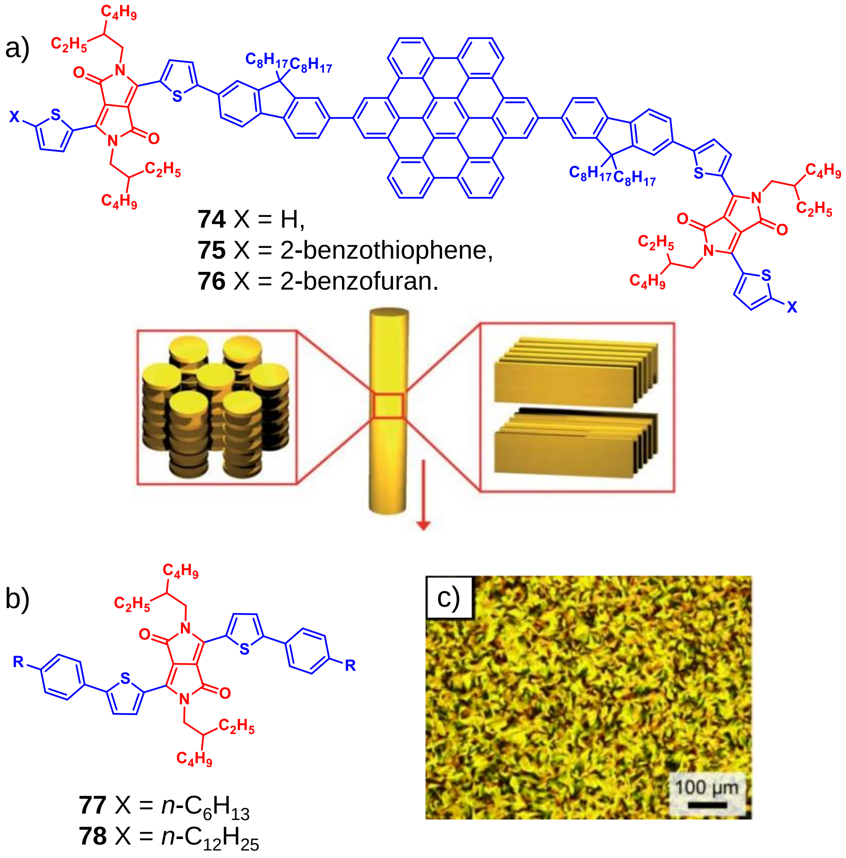

**74** X = H,
**75** X = 2-benzothiophene,
**76** X = 2-benzofuran.

**77** X = *n*-$C_6H_{13}$
**78** X = *n*-$C_{12}H_{25}$

**Figure 1.22.** **a)** Chemical structures of the DPP derivatives **74–76** and probable molecular organization inside extruded fiber. **b)** Molecular structures of **77–78** and **c)** polarized optical microscope image of the mesophase of **77** upon thermal annealing at 140 °C.

## 1.7. Objectives of the Present Work

A survey of the recent literature on DPP derivatives indicates their important role in various optoelectronic applications. In this context, we decided to design and synthesize a few DPP derivatives, mainly to look for their self–assembly and electronic properties. Also, we thought of tuning their morphology at nanoscale through various supramolecular interactions for device applications. For this purpose, we envisaged the synthesis of a few DPP derivatives flanked with different self–assembling motifs and to study their optical and electronic properties in the monomer as well as in the self–assembled states.

With the above objectives, we designed and synthesized an amide functionalized π–conjugated donor–acceptor (D–A) molecule based on a diketopyrrolopyrrole (DPP) chromophore with an expectation to develop low bandgap organogels capable of absorbing complete visible light and transmit NIR light. Such NIR transmitting materials find application in photography, security and forensic fields as described in **Chapter 2**. Then we attempted to tune the band gap by increasing the acceptor strength *via* simple synthetic modifications as explained in **Chapter 3**. Also, changing acceptor strength can lead to the switching of charge carrier mobility as estimated from the FP–TRMC and FET measurements. Finally, we have synthesized a DPP based amphiphile that forms aggregates in polar as well as in non–polar solvents *via* solvophobic interactions as described in **Chapter 4**. Thus the present thesis is a detailed and systematic study on the synthesis, self–assembly and electronic properties of a few rationally designed DPP derivatives.

## 1.8. References

[1] W. H. Perkin, *J. Chem. Soc., Trans.* **1879**, *35*, 717.

[2] W. Herbst, K. G. Hunger, In Industrial Organic Pigments, 3rd ed.; WILEY–VCH: Weinheim, Germany **2004**.

[3] A. Iqbal, M. Jost, R. Kirchmayr, J. Pfenninger, A. Rochat, O. Wallquist, *Bull. Soc. Chim. Belg.* **1988**, *97*, 615.

[4] Z. Hao, A. Iqbal, *Chem. Soc. Rev.* **1997**, *26*, 203.

[5] J. Mizuguchi, *J. Phys. Chem. A* **2000**, *104*, 1817.

[6] A. B. Tamayo, B. Walker, T–Q Nguyen, *J. Phys. Chem. C* **2008**, *112*, 11545.

[7] M. Tantiwiwat, A. Tamayo, N. Luu, X–D Dang, T–Q Nguyen, *J. Phys. Chem. C* **2008**, *112*, 17402.

[8] A. L. Kanibolotsky, F. Vilela, J. C. Forgie, S. E. T. Elmasly, P. J. Skabara, K. Zhang, B. Tieke, J. McGurk, C. R. Belton, P. N. Stavrinou, D. D. C. Bradley, *Adv. Mater.* **2011**, *23*, 2093.

[9] M. Kaur, D. H. Choi, *Chem. Soc. Rev.* **2015**, *44*, 58.

[10] X. Zhang, Y. Hang, W. Qu, Y. Yan, P. Zhao, J. Hua, *RSC Adv.* **2016**, *6*, 20014.

[11] Y. Gao, G. Feng, T. Jiang, C. Goh, L. Ng, B. Liu, B. Li, L. Yang, J. Hua, H. Tian, *Adv. Funct. Mater.* **2015**, *25*, 2857.

[12] M. Grzybowski, E. Glodkowska–Mrowka, V. Hugues, W. Brutkowski, M. Blanchard–Desce, D. T. Gryko, *Chem. Eur. J.* **2015**, *21*, 9101.

[13] S. Qu, H. Tian, *Chem. Commun.* **2012**, *48*, 3039.

[14] C. B. Nielsen, M. Turbiez, I. McCulloch, *Adv. Mater.* **2012**, *25*, 1859.

[15] Y. Li, P. Sonar, L. Murphya, W. Hong, *Energy Environ. Sci.* **2013**, *6*, 1684.

[16] W. Li, K. H. Hendriks, M. M. Wienk, R. A. J. Janssen, *Acc. Chem. Res.* **2016**, *49*, 78.

[17] A. Tang, C. Zhan, J. Yao, E. Zhou, *Adv. Mater.* **2017**, *29*, 1600013.

[18] A. Ajayaghosh, V. K. Praveen, *Acc. Chem. Res.* **2007**, 40,644.

[19] S. Ghosh, V. K. Praveen, A. Ajayaghosh, *Annu. Rev. Mater. Res.* **2016**, *46*, 235.

[20] S. S. Babu, S. Prasanthkumar, A. Ajayaghosh, *Angew. Chem. Int. Ed.* **2012**, *51*, 1766.

[21] S. S. Babu, V. K. Praveen, A. Ajayaghosh, *Chem. Rev.* **2014**, *114*, 1973.

[22] E. Busseron, Y. Ruff, E. Moulin, N. Giuseppone, *Nanoscale* **2013**, *5*, 7098.

[23] H–J. Kim, T. Kim, M. Lee, *Acc. Chem. Res.* **2010**, *44*, 72.

[24] D. G. Farnum, G. Mehta, G. G. I. Moore, F. P. Siegal, *Tetrahedron Lett.* **1974**, *29*, 2549.

[25] M. Grzybowski, D. T. Gryko, *Adv. Optical Mater.* **2015**, *3*, 280.

[26] L. Dou, Y. Liu, Z. Hong, G. Li, Y. Yang, *Chem. Rev.* **2015**, *115*, 12633.

[27] J. Dhar, N. Venkatramaiah, A. Anitha, S. Patil, *J. Mater. Chem. C* **2014**, *2*, 3457.

[28] H. Bürckstümmer, A. Weissenstein, D. Bialas, Frank Würthner, *J. Org. Chem.* **2011**, *76*, 2426.

[29] Y. Lin, Y. Lia, X. Zhan, *Chem. Soc. Rev.* **2012**, *41*, 4245.

[30] K. A. Mazzio, C. K. Luscombe, *Chem. Soc. Rev.* **2015**, *44*, 78.

[31] C. W. Tang, *Appl. Phys. Lett.* **1986**, *48*, 183.

[32] N. S. Sariciftci, L. Smilowitz, A. J. Heeger, F. Wudl, *Science* **1992**, *258*, 1474.

[33] G. Yu, J. Gao, J. C. Hummelen, F. Wudl, A. J. Heeger, *Science* **1995**, *270*, 1789.

[34] A. Mishra, Peter Büerle, *Angew. Chem. Int. Ed.* **2012**, *51*, 2020.

[35] K. Gao, L. Li, T. Lai, L. Xiao, Y. Huang, F. Huang, J. Peng, Y. Cao, F. Liu, T. P. Russell, R. A. J. Janssen, X. Peng, *J. Am. Chem. Soc.* **2015**, *137*, 7282.

[36] Y. Lin, X. Zhan, *Mater. Horiz.* **2014**, *1*, 470.

[37] Y. Patil, R. Misra, M. L. Keshtovb, G. D. Sharma, *J. Mater. Chem. A* **2017**, *5*, 3311.

[38] C. Wang, H. Dong, W. Hu, Y. Liu, D. Zhu, *Chem. Rev.* **2012**, *112*, 2208.

[39] H. Sirringhaus, *Adv. Mater.* **2014**, *26*, 1319.

[40] H. Usta, A. facchetti, T. J. Marks, *Acc. Chem. Res.* **2011**, *44*, 501.

[41] B. Lim, H. Sun, J. Lee, Y–Y Noh, *Sci. Rep.* **2017**, *7*, 164.

[42] Y. Qiao, Y. Guo, C. Yu, F. Zhang, W. Xu, Y. Liu, D. Zhu, *J. Am. Chem. Soc.* **2012**, *134*, 4084.

[43] W. S. Yoon, S. K. Park, I. Cho, J–A Oh, J. H. Kim, S. Y. Park, *Adv. Funct. Mater.* **2013**, *23*, 3519.

[44] G. Li, R. Zhu, Y. Yang, *Nat. Photonics* **2012**, *6*, 153.

[45] W. Li, K. H. Hendriks, W. S. C. Roelofs, Y. Kim, M. M. Wienk, R. A. J. Janssen, *Adv. Mater.* **2013**, *25*, 3182.

[46] H. Choi, S–Jin Ko, T. Kim, P–O Morin, B. Walker, B. Hoon Lee, M. Leclerc, J. Y. Kim, A. J. Heeger, *Adv. Mater.* **2015**, *27*, 3318.

[47] W. Li, W. S. C. Roelofs, M. Turbiez, M. M. Wienk, R. A. J. Janssen, *Adv. Mater.* **2014**, *26*, 3304.

[48] I. Kang, H–J Yun, D. S. Chung, S–K Kwon, Y–H Kim, *J. Am. Chem. Soc.* **2013**, *135*, 14896.

[49] B. Sun, W. Hong, Z. Yan, H. Aziz, Y. Li, *Adv. Mater.* **2014**, *26*, 2636.

[50] J. Lee, A–R Han, H. Yu, T. J. Shin, C. Yang, J. H. Oh, *J. Am. Chem. Soc.* **2013**, *135*, 9540.

[51] J. S. Zambounis, Z. Hao, A. Iqbal, Nature **1997**, *388*, 131.

[52] H. Yanagisawa, J. Mizuguchi, S. Aramaki, Y. Sakai, *Jpn. J. Appl. Phys.* **2008**, *47*, 4728.

[53] Y. Suna, J–I Nishida, Y. Fujisaki, Y. Yamashita, *Org. Lett.* **2012**, *14*, 3356.

[54] J. Lee, A–R Han, J. Hong, J. H. Seo, J. H. Oh, C. Yang, *Adv. Funct. Mater.* **2012**, *22*, 4128.

[55] Y. Yang, G. Zhang, H. Luo, J. Yao, Z. Liu, D. Zhang, *ACS Appl. Mater. Interfaces* **2016**, *8*, 3635.

[56] F. Bruni, M. Sassi, M. Campione, U. Giovanella, R. Ruffo, S. Luzzati, F. Meinardi, L. Beverina, S. Brovelli, *Adv. Funct. Mater.* **2014**, *24*, 7410.

[57] B. Song, H. Wei, Z. Wang, X. Zhang, M. Smet, W. Dehaen, *Adv. Mater.* **2007**, *19*, 416.

[58] E. R. Draper, B. Dietrich, D. J. Adams, *Chem. Commun.* **2017**, *53*, 1864.

[59] G. S. Thool, K. Narayanaswamy, A. Venkateswararao, S. Naqvi, V. Gupta, S. Chand, V. Vivekananthan, R. R. Koner, V. Krishnan, S. P. Singh, *Langmuir* **2016**, *32*, 4346.

[60] A. Ruiz–Carretero, T. Aytun, C. J. Bruns, C. J. Newcomb, W–W Tsaia, S. I. Stupp, *J. Mater. Chem. A* **2013**, *1*, 11674.

[61] T. Aytun, L. Barreda, A. Ruiz–Carretero, J. A. Lehrman, S. I. Stupp, *Chem. Mater.* **2015**, *27*, 1201.

[62] J. Dhar, D. P. Karothu, S. Patil, *Chem. Commun.* **2015**, *51*, 97.

[63] E. D. Głowacki, H. Coskun, M. A. Blood–Forsythe, U. Monkowius, L. Leonat, M. Grzybowski, D. Gryko, M. Schuette White, A. Aspuru–Guzik, N. S. Sariciftci, *Org. Electron.* **2014**, *15*, 3521.

[64] J. Yao, C. Yu, Z. Liu, H. Luo, Y. Yang, G. Zhang, D. Zhang, *J. Am. Chem. Soc.* **2016**, *138*, 173.

[65] J. Y. Oh, S. Rondeau–Gagné, Y.–C. Chiu, A. Chortos, F. Lissel, G.–J. N. Wang, B. C. Schroeder, T. Kurosawa, J. Lopez, T. Katsumata, J. Xu, C. Zhu, X. Gu, W.–G. Bae, Y. Kim, L. Jin, J. W. Chung, J. B. H. Tok, Z. Bao, *Nature* **2016**, *539*, 411.

[66] M. R. Wasielewski, *Chem. Rev.* **1992**, *92*, 435.

[67] G. D. Scholes, G. R. Fleming, A. Olaya–Castro, R. van Gron–delle, *Nat. Chem.* **2011**, *3*, 763.

[68] D. Ley, C. X. Guzman, K. H. Adolfsson, A. M. Scott, A. B. Braunschweig, *J. Am. Chem. Soc.* **2014**, *136*, 7809.

[69] C. X. Guzman, R. M. K. Calderon, Z. Li, S. Yamazaki, S. R. Peurifoy, C. Guo, S. K. Davidowski, M. M. A. Mazza, X. Han, G. Holland, A. M. Scott, A. B. Braunschweig, *J. Phys. Chem. C* **2015**, *119*, 19584.

[70] H–J. Kim, T. Kim, M. Lee, *Acc. Chem. Res.* **2010**, *44*, 72.

[71] B. Song, Z. Wang, S. Chen, X. Zhang, Y. Fu, M. Smet, W. Dehaen, *Angew. Chem. Int. Ed.* **2005**, *44*, 4731.

[72] Y. Jiao, W–L Li, J–F Xu, G. Wang, J. Li, Z. Wang, X. Zhang, *Angew. Chem. Int. Ed.* **2016**, *55*, 8933.

[73] J. Mei, K. R. Graham, R. Stalder, S. P. Tiwari, H. Cheun, J. Shim, M. Yoshio, C. Nuckolls, B. Kippelen, R. K. Castellano, John R. Reynolds, *Chem. Mater.* **2011**, *23*, 2285.

[74] A. Punzi, E. Maiorano, F. Nicoletta, D. Blasi, A. Ardizzone, N. Ventosa, I. Ratera, J. Veciana, G. M. Farinola, *Eur. J. Org. Chem.* **2016**, 2617.

[75] A. B. Tamayo, M. Tantiwiwat, B. Walker, T–Q Nguyen, *J. Phys. Chem. C* **2008**, *112*, 15543.

[76] T. Jaroch, A. Maranda–Niedbała, M. Góra, J. Mieczkowski, M. Zagórska, M. Salamonczyk, E. Górecka, R. Nowakowski, *Synthetic Metals* **2015**, *204*, 133.

[77] O. P. Lee, A. T. Yiu, P. M. Beaujuge, C. H. Woo, T. W. Holcombe, J. E. Millstone, J. D. Douglas, M. S. Chen, J. M. J. Fréchet, *Adv. Mater.* **2011**, *23*, 5359.

[78] W. W. H. Wong, J. Subbiah, S. R. Puniredd, B. Purushothaman, W. Pisula, N. Kirby, Klaus Müllen, D. J. Jones, A. B. Holmes, *J. Mater. Chem.* **2012**, *22*, 21131.

[79] W. Shin, T. Yasuda, G. Watanabe, Y. S. Yang, C. Adachi, *Chem. Mater.* **2013**, *25*, 2549.

# Chapter 2

## A Supramolecular Nanocomposite as Near Infrared Transmitting Optical Filter for Security and Forensic Applications

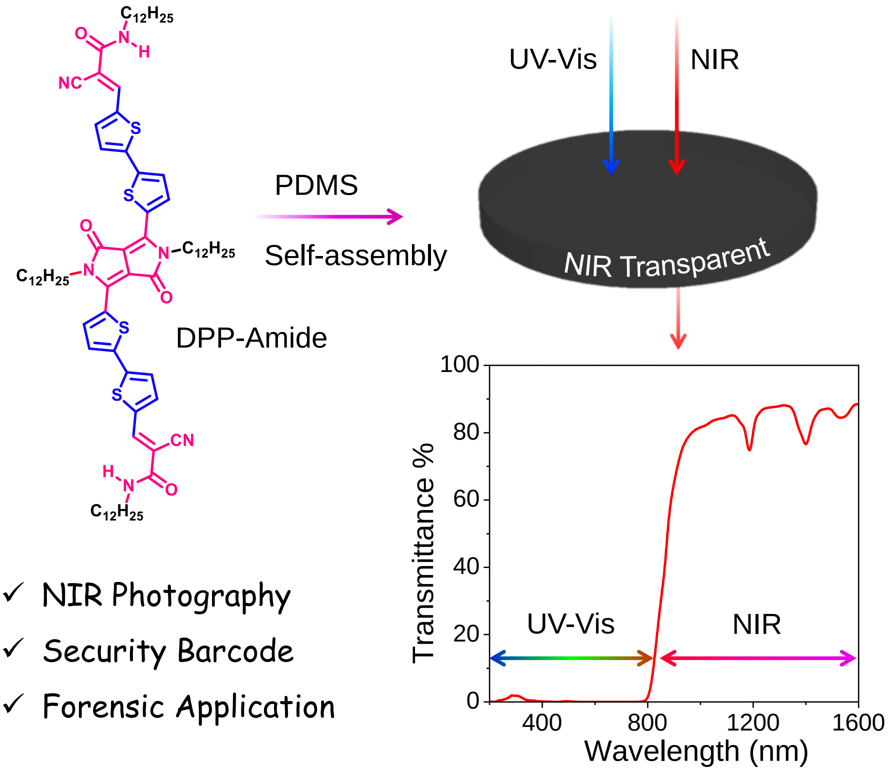

### 2.1. Abstract

*Visibly opaque but NIR transparent materials are essential components for night vision photography, security imaging and forensic applications. Herein, we describe the development of a novel supramolecular black dye from a diketopyrrolopyrrole (DPP) based low molecular weight organogelator. In solution state, the monomer of* ***DPP–Amide*** *exhibits deep green colour with a broad absorption in the visible region due to firm intramolecular charge transfer from the donor to acceptor unit. Interestingly, due to synergistic effect of H–bonding and π–stacking,* ***DPP–Amide*** *can form a black organogel in toluene with complete*

*spectral coverage from 300–800 nm and transmits beyond 850 nm. Complete visible spectral coverage was achieved in the gel state due to the simultaneous formation of both H– and J– type aggregates, as confirmed by UV-Vis-NIR studies. To create a free standing NIR transmitting elastomeric black filter, we have embedded the nanoscopic molecular aggregates of* ***DPP–Amide*** *(0.15 wt %) into a polydimethylsiloxane (****PDMS****) matrix. This nanocomposite possesses high NIR transparency with good thermal and photostability for practical applications. Finally, we demonstrate the use of the developed material for NIR photography, security and forensic related applications.*

## 2.2. Introduction

The field of molecular assembly which is an off–shoot of the broad area of supramolecular chemistry has been gradually transforming from curiosity driven to application oriented research that spans across materials and biological world.[1–3] Over the years, many exciting research on the concept, structures, properties and applications has occurred in this exciting field of research.[4–6] In this context, molecular gel chemistry has been in the forefront, with respect to the development of new generation soft materials for a wide range of applications including organic electronics and solar energy conversion.[7,8] However, chemists still need to go a long way to achieve a major breakthrough as far as applications are concerned. This needs aggressive thinking and massive input on new ways of exploring self–assembled materials.[9,10] Though potential use of fluorescent gels for security inks, sensor platforms and energy conversion has been demonstrated, they are yet to see commercial use.[11,12] This state of the affair of soft materials research has motivated us to think on new applications of molecular assemblies and organogels.

Among different organogels, π–gels are an interesting class of functional soft materials composed of fluorescent molecular systems.[4] Fine tuning the structure, morphologies and the type of interactions can result in gels with distinct photophysical properties including emission at different wavelengths.[13] Majority of these soft gels absorb and emit in the UV–Vis range. Gels which absorb and emit in the near–IR region are very rare, however, they have many applications, especially in the areas of imaging and security.[4] Organic molecules or organogels that absorb UV–Vis light, while allowing the passage of NIR radiation in the electromagnetic spectrum are rare. Such exclusively NIR transparent materials are required for night vision photography, security imaging and forensic applications.[14–15]

A domain of societal and strategical relevance wherein NIR technology has been put into use is the anti–counterfeiting segment and in the pharmaceutical industries. The stupendous rise in crime rate, counterfeiting of currencies and valuable documents, fabrication of unauthentic barcodes etc. serve as major threats to social and economic growth across the globe. Food items and drugs forged by anti–social elements using deceptive packaging and faked barcodes are threats to national health and revenue. Similarly, illegal activities and crimes occurring at night have increased at an alarming rate which can be curtailed by night surveillance using NIR cameras. NIR reflecting materials having high visible light transparency is an integral part of any camera to produce true color images because camera is sensitive to both visible and NIR light.[16] For NIR photography, a filter with complete visible light absorption and high NIR transmission is a prerequisite. Compared to their inorganic counterparts, organic molecules with the above properties have certain advantages such as easy processing and flexibility, but are little known.

Commonly, inorganic materials such as metal oxides, chalcogenide glasses, germanium or silicon semiconductors have been used as NIR transparent materials due to their high refractive indices and minimal losses in the wavelength range of 1–10 μm.[17,18] However, these materials are expensive, brittle, toxic and require high temperature for their synthesis and fabrication. To solve these problems, Pyun and co–workers developed a high refractive index thermoplastic copolymer for IR optics.[19] These copolymers were synthesized by reacting molten sulphur with 1,3–diisopropenylbenzene *via* inverse vulcanization (**Figure 2.1a**).

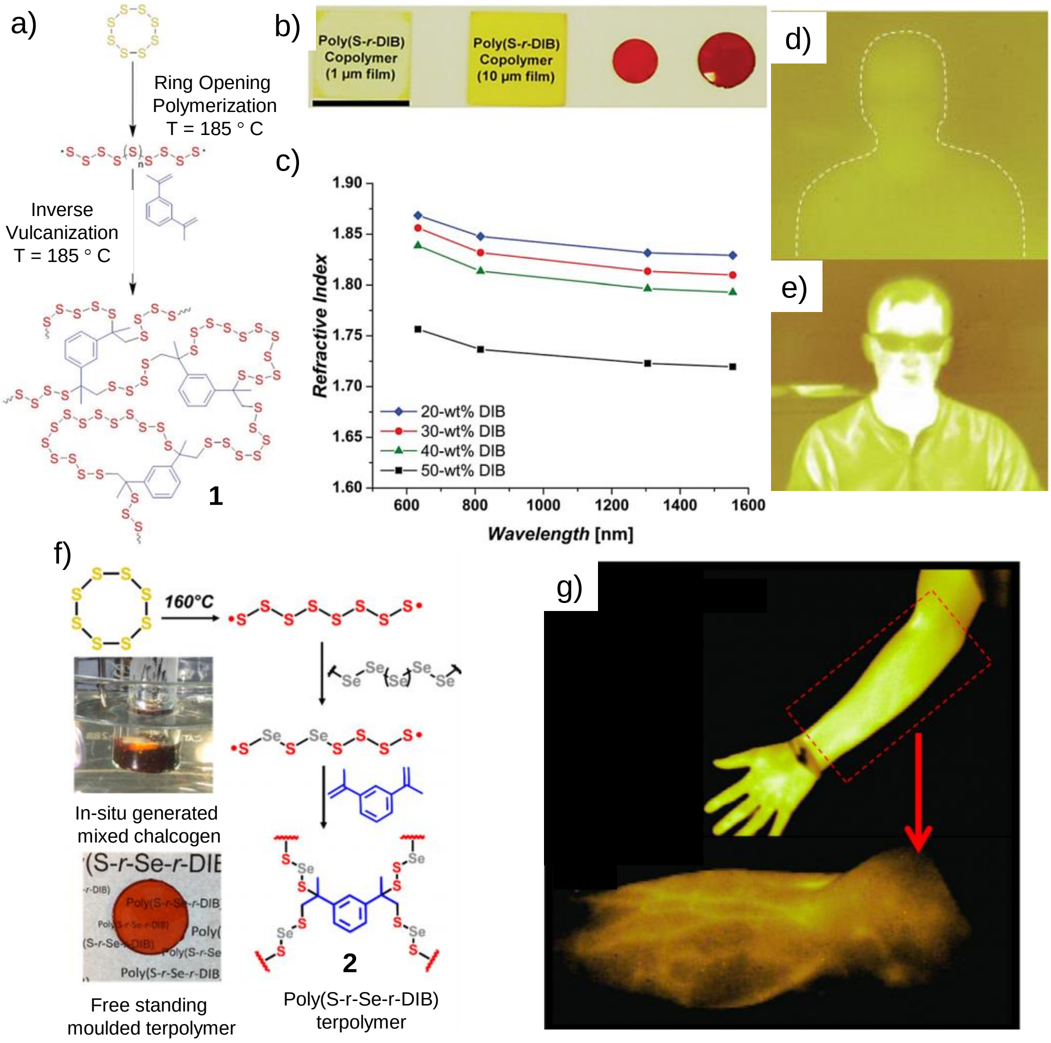

**Figure 2.1.** Synthetic scheme of the copolymers **a) 1** and **f) 2**. **b)** Photograph of the films of copolymer **1** at different thickness (left to right; 1 μm and 10 μm film over glass, 200 μm free–standing film, and 2 mm free–standing lens) **c)** A plot of refractive indices versus wavelength for the composite consisting of different wt% of the copolymer **1**. Thermal imaging of a human subject at **d)** ~37 °C and **e)** ~24 °C through an optical filter consisting of 80 wt% of copolymer **1** film (~1 mm) in the mid–IR (3–5 μm) regime. **g)** IR thermal image of a human arm, and high resolution image of a human forearm obtained using a mid–IR camera, operating at 3−5 μm consisting of a film of copolymer **2** (1 mm thick, 25 mm wide).

High optical transparency was achieved for all these materials in the near and mid–infrared regime since S–S bond is IR inactive as evident from FT–IR and UV–Vis absorption studies (**Figure 2.1b**). Also, these copolymers exhibited high refractive index (n ~ 1.8) in the spectral regime of 600–1600 nm (**Figure 2.1c**). The use of these polymeric materials as lens for mid IR imaging was also demonstrated (**Figure 2.1d,e**). To further increase the refractive index, a few inorganic/organic chalcogenide hybrid polymers were employed. These mid–IR transparent polymers were obtained *via* the inverse vulcanization of elemental sulfur, selenium, and 1,3–diisopropenylbenzene (**Figure 2.1f**).[20] Controlled incorporation of selenium resulted in very high refractive index (n ~ 2), comparable to the chalcogenide glasses. As a result, these materials found promising applications in imaging the human vasculature (**Figure 2.1g**).

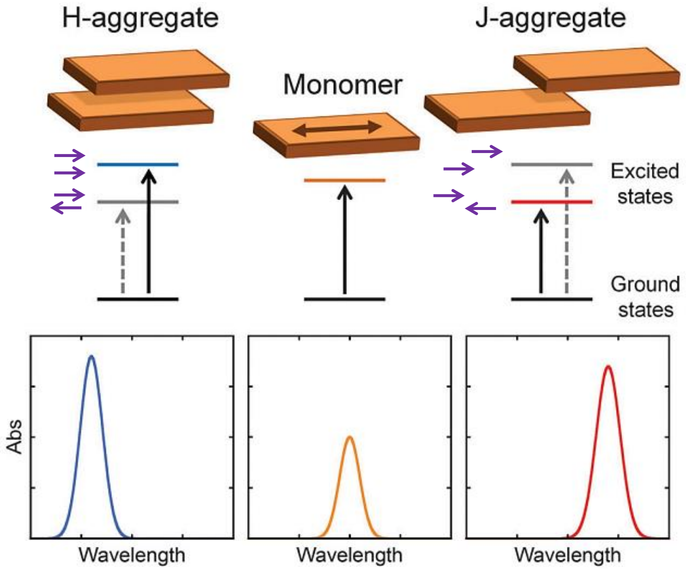

**Figure 2.2.** Schematic representation of typical H– and J–type dimers for a π–conjugated molecule (monomer) and corresponding effects in the UV–Vis absorption spectra. Allowed transitions are depicted in solid arrows (transition dipole moment μ > 0), and dashed arrows represent the forbidden ones (μ = 0).

There are a few reports on metal–free organic panchromatic dyes, especially organic black dyes, useful in solar cells, ink formulation, electrophotographic recording, and infrared photography.[21–23] However, developing a single component metal free organic black dye is highly challenging. In this context, π–conjugated D–A systems are ideal candidate due to their broad absorption in the visible region *via* intramolecular charge transfer (ICT).[24] Nevertheless, most of these dyes do not exhibit black color due to unequal absorption intensity at each wavelength in the visible range. The required full spectrum coverage may be achieved through specific molecular organization of the D–A dyes *via* H– or J–type or oblique dipolar arrangements (**Figure 2.2**). According to Kasha's exciton theory, these dipolar organization can provide either blue (H–type) or red (J–type) or both blue and red shift in absorption (oblique).[25–27] In H–aggregates, two or more monomers are arranged one on the top of each other (face–to–face), whereas for J–aggregates, the monomers adopt a slipped parallel arrangement (end–to–end). However, for both H– and J– aggregates transition dipole moments are aligned parallel to each other.

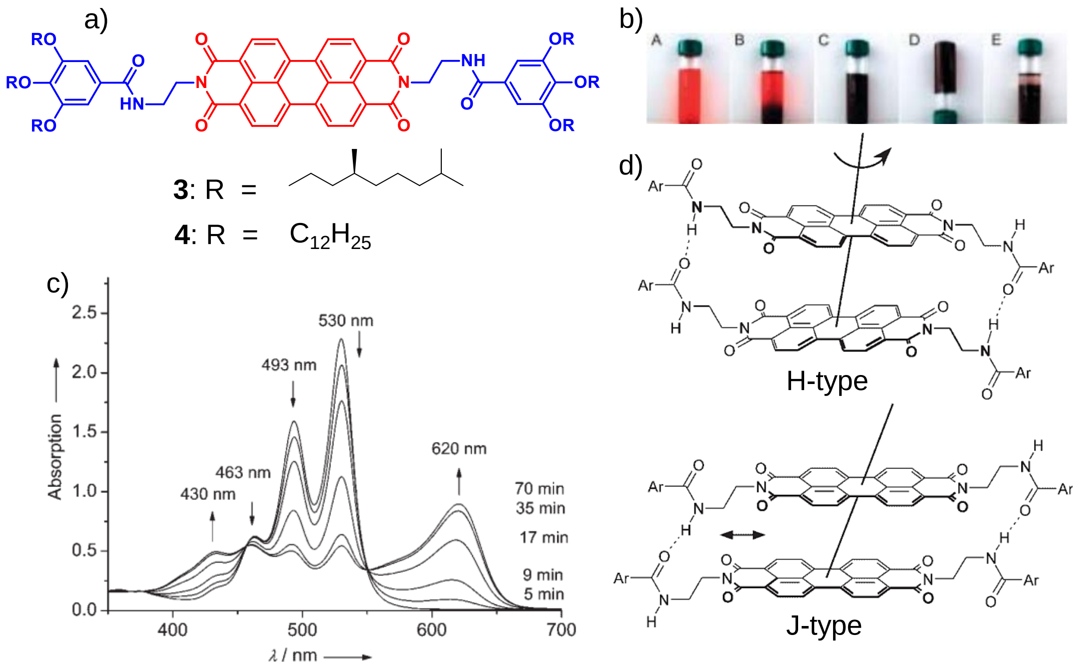

**Figure 2.3. a)** Molecular structure of the PBI organogelators **3** and **4**. **b)** Images showing the time dependent gelation of PBI **3** in S–limonene (0.3 mM). **c)** Time–dependent absorption spectra monitoring the gelation of a $4 \times 10^4$ M toluene solution of **3** after dissolution at 80°C and cooling to 48°C in a 1 mm cell. **d)** Packing model for H–type (**4,** top) and J–type (**3,** bottom) aggregates.

A large number of π–conjugated supramolecular systems are capable of forming either H–type or J–type aggregates, however, the controlled formation of a mixture of H– and J–type aggregates is a challenge.[28] Würthner *et al.* have reported a 'serendipitous discovery of a dark green to almost black' perylene bisimide (PBI) organogel when linear alkyl chains were substituted with branched ones (**Figure 2.3a**).[29] Due to the presence of the amide groups and large π– surface, **3** has a high propensity to form gels in most of the common organic solvents (**Figure 2.3b**). Well defined nanofibers were observed under AFM over a highly oriented pyrolytic graphite (HOPG) substrate. From the concentration, temperature, and solvent–dependent UV–Vis absorption studies it was evident that **3** formed preferentially J–type aggregates (**Figure 2.3c**). Interestingly, in the film state, these J–type aggregates were transformed into H–type aggregates upon thermal treatment. However, **4** spontaneously formed a red color gel comprised of H–type aggregates. It was observed that while the red gel has the perylene cores stacked on top of each other with a very small longitudinal displacement, the black one showed a longitudinal displacement of about 3.3 Å (**Figure 2.3d**). Later, a library of PBI derivatives was reported based on the same molecular structure, having different alkyl chains. But none of them formed simultaneous H– and J– type aggregates. Also, BASF has reported a product based on PBI that is black in its crystalline state.[30]

Meskers and co–workers have reported that diketopyrrolopyrrole derivatives are capable of forming both H– and J–type aggregates in the solid state.[31] A number of DPP derivatives **5**–**14,** with different alkyl substituents were investigated for their characteristics optical properties (**Figure 2.4a**). Most of these derivatives showed simultaneous blue and red shifts in absorption spectra in solid state as compared to the monomer (**Figure 2.4b, c**). This result points towards the co–existence of H– and J– aggregates in the unit cell which was further supported by Quantum–chemical calculations. Substantial Davydov splitting was observed for molecules with linear alkyl chains on the nitrogen atom, whereas derivatives with branched alkyl side chains exhibited almost zero Davydov splitting. These findings prompted us to design a DPP derivative that can simultaneously form both H– and J– aggregates resulting in a panchromatically absorbing supramolecular organogel.

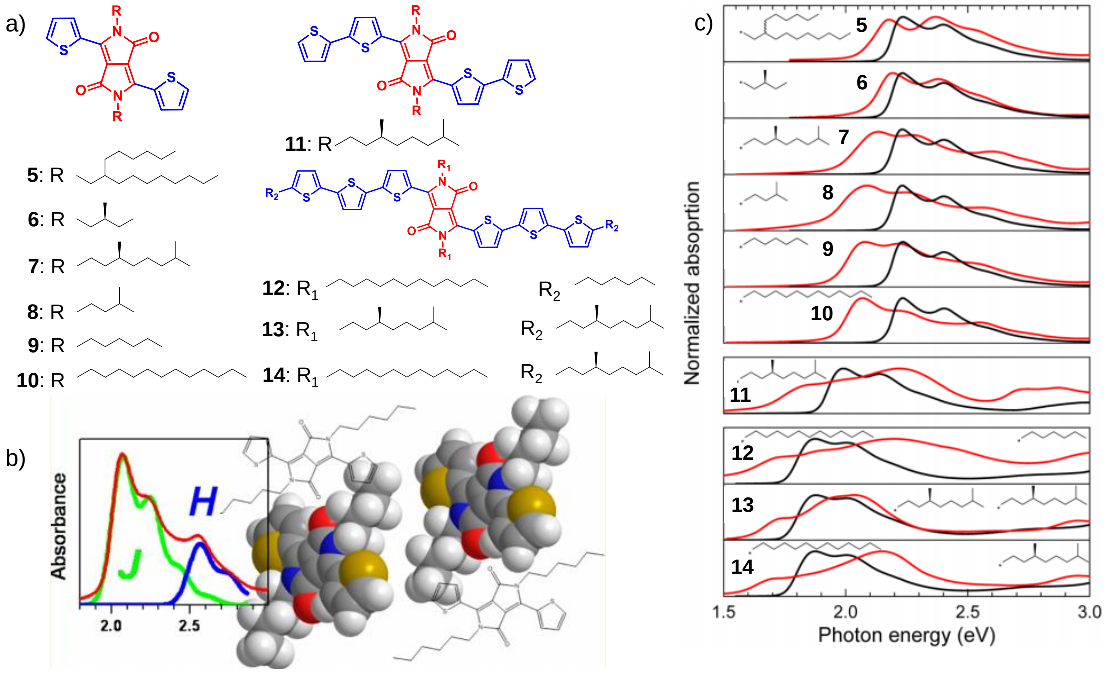

**Figure 2.4. a)** Chemical structure of DPP–based oligothiophenes **5**–**14**. **b)** Deconvolution of the absorption spectrum showing the contribution of J– and H– aggregates. **c)** Solution (black lines) and solid state (red lines) absorption spectra of DPP oligothiophenes **5**–**14**.

Herein, we report a π–conjugated donor–acceptor (D–A) molecule based on a diketopyrrolopyrrole (DPP) chromophore[32,33] that self–assembles to form a black gel (**DPP–Amide**, **22**). The monomer of **DPP–Amide** exhibited a dark green colour with a broad absorption in the visible region due to strong internal charge transfer (ICT) from the donor to the acceptor unit. The color of the dye turned black upon aggregation, covering a broad spectral region from 300–800 nm. The co–existence of H– and J–type aggregates resulting from the synergistic effect of H–bonding and π–stacking led to a supramolecular organogel comprising of nanofibers. Incorporation of the self–assembled **DPP–Amide** aggregate into a polydimethylsiloxane (**PDMS**) elastomer resulted in a black nanocomposite that could exclusively filter out the broad UV–Vis wavelength range thereby transmitting NIR light. The high extinction coefficient of the **DPP–Amide** renders the use of a very low weight% of the dye (0.15 wt%) to create an NIR filter with a minimum thickness of 1.27 mm.

## 2.3. Results and Discussion

### 2.3.1. Synthesis of DPP–Amide (22)

The π–extended A–D–A–D–A type diketopyrrolopyrrole **22** (**DPP–Amide**) has been synthesized by a multistep synthetic procedure using condensation, alkylation and Suzuki coupling reactions (**Scheme 2.1**). The final product **22** was obtained via Knoevenagel condensation between **19** and **21**.

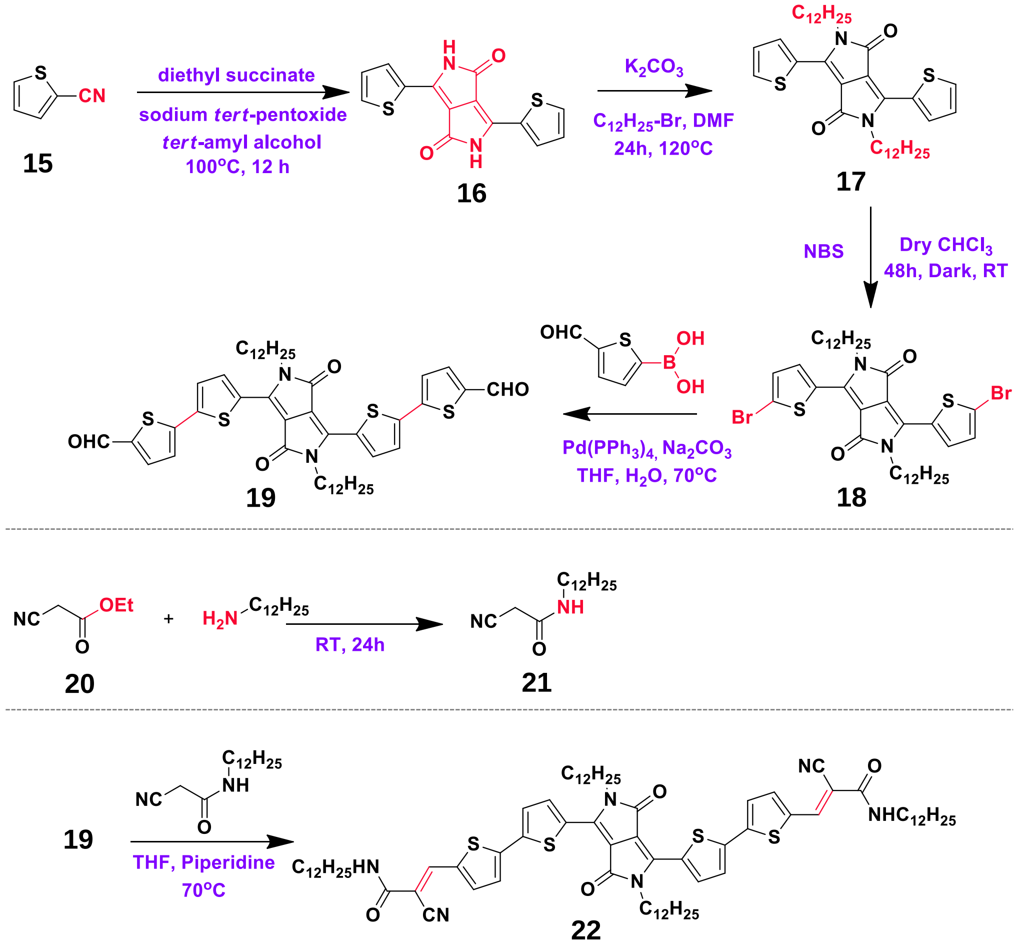

**Scheme. 2.1.** Synthetic protocol adopted for the synthesis of the **DPP–Amide** (**22**).

All the purified intermediates and the final compound were characterized by nuclear magnetic resonance spectroscopy (NMR), high–resolution mass spectroscopy (HRMS), and matrix assisted laser desorption/ionization–time of flight (MALDI–TOF) mass spectrometry.

### 2.3.2. Thermal Characterization

Generally, DPP derivatives have high photo and thermal stability which are additional advantages for practical applications. Thermo gravimetric analysis (TGA) (**Figure 2.5a**) of the **DPP–Amide** revealed high thermal stability exhibiting only 5% decomposition at 340°C under nitrogen atmosphere. **DPP–Amide** did not show any phase change except melting and crystallization as seen from differential scanning calorimetry (DSC) (**Figure 2.5b**).

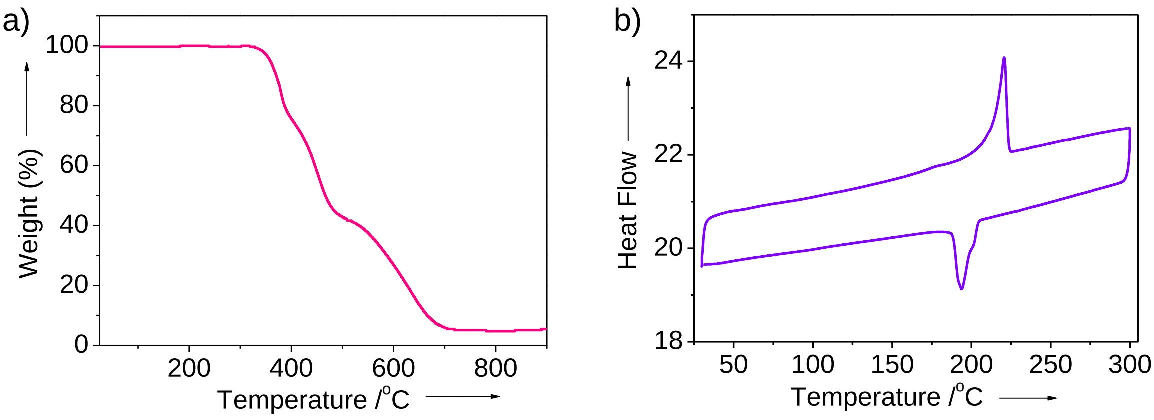

**Figure 2.5. a)** TGA and **b)** DSC of **DPP–Amide**.

### 2.3.3. Gelation

**DPP–Amide** appeared green in the monomeric solution (**Figure 2.6b**). However, it has a high propensity towards molecular aggregation due to the presence of the amide units and extended π–surface. We, therefore, performed the gelation studies in different solvents and it was found to form a stable black color gel only in toluene with a critical gelator concentration (CGC) of $3\times10^{-3}$ M at 298 K (**Figure 2.6b**) aided by H–bonding and π–π stacking interactions. Gel–like behavior of

**DPP–Amide** was confirmed from rheological analysis, where the value of elastic storage modulus (G′) was found to be invariant with the applied frequency and was higher than that of elastic loss modulus (G″) (**Figure 2.6c**). Fourier transform infrared (FT–IR) transmission measurements revealed broad N–H stretching at 3290 cm$^{-1}$ indicative of H–bonding along with C=O stretching (amide I) and N–H bending (amide II) peak at 1672 cm$^{-1}$ and 1574 cm$^{-1}$, respectively (**Figure 2.6d, e**).[34]

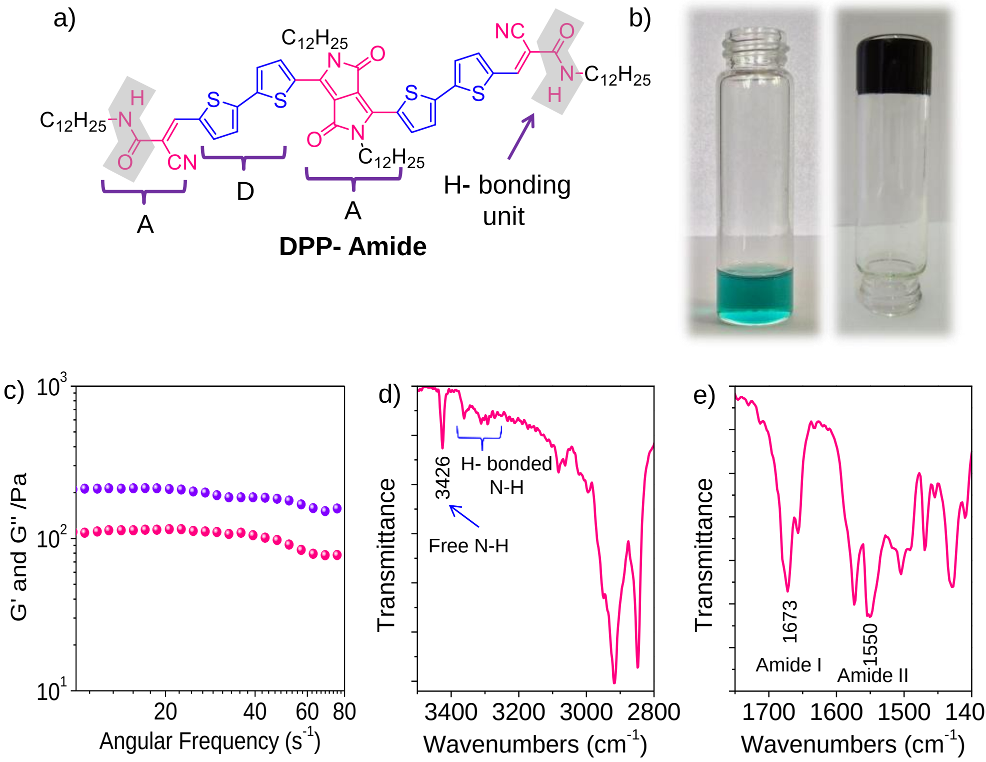

**Figure 2.6. a)** Chemical structure of **DPP–Amide**. **b)** Photographs of **DPP–Amide** in monomeric state (chloroform, left) and in the self–assembled state leading to the formation of gel (toluene, right).**c)** Rheological behavior of **DPP–Amide** gel. **d, e)** FT–IR of **DPP–Amide** xerogel.

## 2.3.4. Photophysical Characterization

The normalized absorption spectra of **DPP–Amide** in its monomer and aggregated states are shown in **Figure 2.7a**. At a very low concentration ($c = 1 \times 10^{-5}$ M), it remains as monomer in chloroform as well as in toluene, where **DPP–Amide** exhibited two distinct absorption bands, one at 428 nm, corresponding to π–π* transition and an intense broad absorption with a maximum at 628 nm due to ICT from the donor to the acceptor unit. As a result, **DPP–Amide** exhibits a high extinction coefficient of ~$10^5$ L $mol^{-1}cm^{-1}$ which is desirable for any optoelectronic application.

To understand the nature of aggregation during gelation, we dispersed a very small amount of the **DPP–Amide** gel (10 μL) in 6.8 mL toluene (*via* vortex motion or gentle sonication) and recorded the absorption spectrum. The spectrum showed several new bands that are hypsochromically and bathochromically shifted with respect to the monomer, confirming the formation of both H– and J–aggregates as shown in **Figure 2.7a**.[31] The major absorption peaks for the aggregates appeared at 388, 451, 607 (H–band), 694 and 768 (J–band) nm, with an excellent spectral coverage in the visible region. The blue and red shifts in absorption of **DPP–Amide** aggregates with respect to the monomeric **DPP–Amide** possibly arise from the positive as well as negative interaction energy between the transition charge density.[27] Also, a substantial Davydov splitting (the photon energy difference between the two allowed transitions) of 0.42 eV was obtained for **DPP–Amide**.[31]

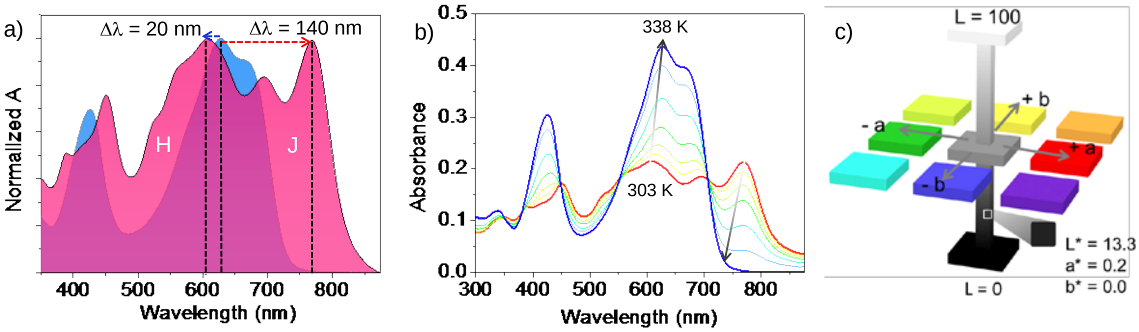

**Figure 2.7.** **a)** Normalized absorption spectra of **DPP–Amide** in monomeric (blue) and gel state (pink). **b)** Temperature dependent absorption of **DPP–Amide** aggregates from 303 to 338 K. **c)** CIE 1976 three–dimensional L*a*b* plot of values measured for the color of **DPP–Amide** gel.

Heating from 303 to 338 K led to an attenuation of aggregation bands and the appearance of monomer bands with isosbestic points at 707, 552, 449 and 348 nm, revealing the dynamic nature of the aggregates (**Figure 2.7b**). Color of the gel was estimated by chromaticity coordinates, L*a*b*, where L* indicates lightness measurement parameter (0 = black, 100 = white), a* represents red–green balance (+a* = red and –a* = green), and b* represents yellow–blue balance (+b* = yellow and –b* = blue) in a 3D color space (CIELAB) defined by the CIE in 1976. From the reflectance spectra of **DPP–Amide** gel, we found L* = 13.3, a* = 0.2 and b* = 0, affirming the "blackness" of the gel (**Figure 2.7c**).

## 2.3.5. DFT Calculations

To have a theoretical support for the observed aggregation induced optical property changes, we optimized the geometries of the **DPP–Amide** dimer which is the smallest unit of an aggregate, *via* M06L/6–31G* density functional theory (DFT) using *Gaussian09* suite of programs.[35] The most stable structure of the dimer (H–type) showed stacked arrangement of the monomers with their dipoles aligned parallel at a π–π distance of 3.50 Å (**Figure 2.8a**). Structural optimization was performed with slipped parallel π–π stacked arrangement of J–type dimers which were also found to be stable (**Figure 2.8.a**). The H–type dimer is stabilized by a high binding energy of 60 kcal/mol which starts decreasing with increase in slipping distances ($\Delta x$) (**Figure 2.8.b**). Even two monomer units of **DPP–Amide** were stabilized by 23.5 kcal/mol when placed side by side with only two H–bonding interactions in the absence of any π–π interaction. To model the spectroscopic observations, excitation energies were calculated for the monomer and different dimer structures of **DPP–Amide** using time–dependent DFT (TD–DFT) at the PBE1PBE/6–31G*//M06L/6–31G* level.[36] The H–type dimer exhibited blue shift in absorption as compared to the monomer whereas gradual red shift was observed for the slipped dimers, in support of our experimental observation of the co–existence of H– and J– type aggregates (**Figure 2.8.c**).[37]

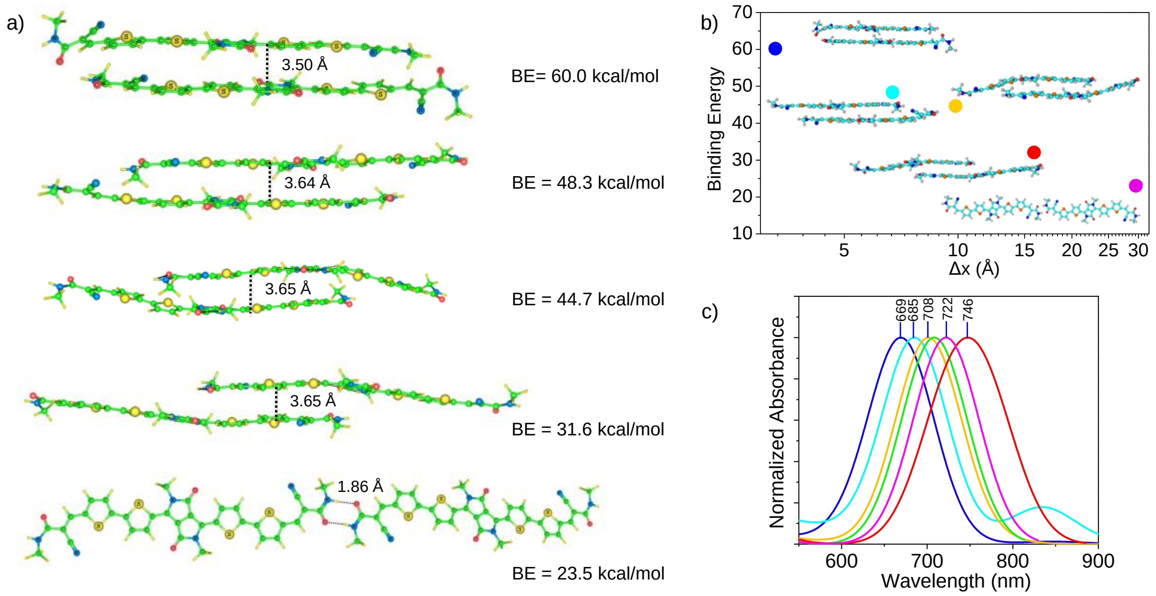

**Figure 2.8. a)** Optimized structures of **DPP–Amide** dimer having different binding energies. **b)** Decrease in binding energies with slipping distance. **c)** Simulated absorption spectra of different dimers of **DPP–Amide**.

## 2.3.6. Morphological Analyses

Scanning electron microscopy (SEM) image of the xerogel of **DPP–Amide** revealed the presence of the typically entangled network of the fibrous assembly (**Figure 2.9a**). It appears that the initially formed nanofibres are interwined and bundled to form large fibers having approximate diameter of 400–500 nm. Branched nanofibers were observed under transmission electron microscope (TEM) when an aggregated dilute solution of **DPP–Amide** ($c$ = $5\times10^{-5}$ M in toluene) was placed over a carbon coated copper grid (**Figure 2.9b**). Atomic force microscopy (AFM) image further confirmed the formation of thin nanofibers having an average height of 25 ± 5 nm and diameter of 200 ± 50 nm (**Figure 2.9.c**), upon drop casting an aggregated solution of **DPP–Amide** over a freshly cleaved mica. Since such large fibers may facilitate scattering of light, we downsized the aggregates by controlled self–assembly using lower concentration of **DPP–Amide** (0.15 wt%), followed by entrapping the resultant fibers in a polydimethylsiloxane (**PDMS**) film to develop a free standing NIR transparent filter.

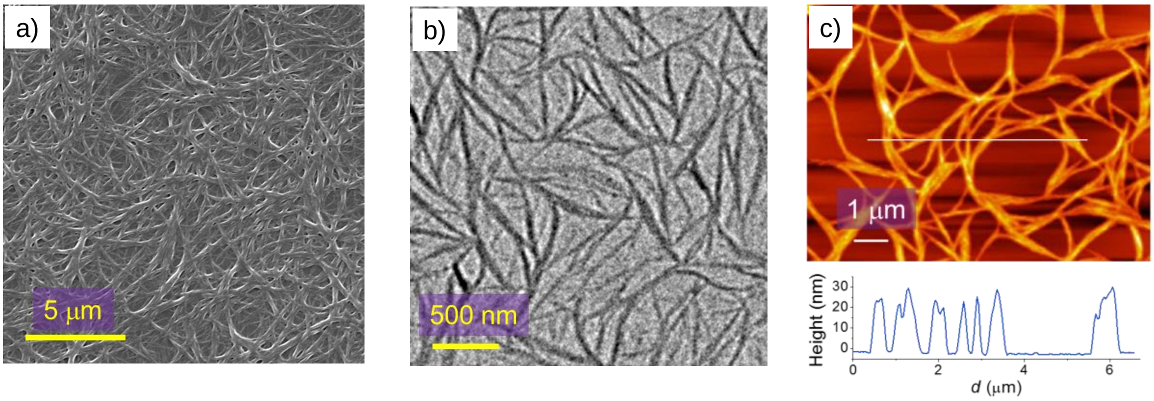

**Figure 2.9. a)** SEM image of **DPP–Amide** xerogel. **b)** TEM and **c)** AFM images of **DPP–Amide** aggregates with height profile (below) along the solid line in image **c)**.

### 2.3.7. Nanocomposite Preparation

In order to achieve an optimum NIR transparency, the thickness and the percentage of the dye loading were varied. It was observed that the visible transparency decreased dramatically for the nanocomposite with the increase in weight percentage (wt%) of **DPP–Amide** (**Figure 2.10a**). Interestingly, even with a very small amount of dye doping (0.15 wt%), we could achieve high NIR transmittance with a minimum visible light transmittance. **PDMS** alone showed a consistent transmittance (T ≈ 90%) in the visible region except for two weak absorption bands in the NIR region (1180 nm and 1400 nm) (**Figure 2.10b**). A drastic decrease in transmittance was observed after loading a 0.15 wt% of **DPP–Amide** into **PDMS** with a thickness of 1.46 mm. It maintained a transmittance below 1% in the UV–Vis region with a sharp recovery in transmittance after 850 nm that reached up to 70% at 900 nm (**Figure 2.10b**) which is a prerequisite for an NIR filter. To standardize the optimum thickness of the composite we made filters of different thickness with a fixed dye loading of 0.15 wt% (**Figure 2.10c**) and a thickness of 1.27–1.46 mm was found to be optimum for the effective transmittance of NIR radiation (**Figure 2.10d**).

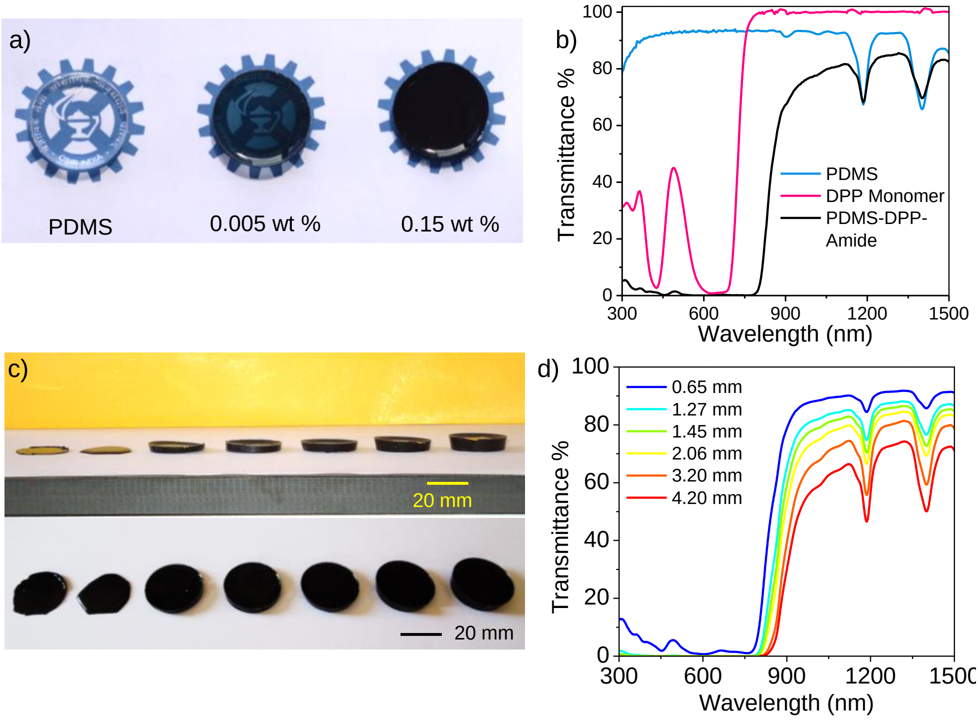

**Figure 2.10. a)** Photograph showing the change in transparency with a loading of 0, 0.005 and 0.15 wt% of **DPP–Amide** in a **PDMS** matrix. **b)** Transmittance of **PDMS**, **DPP–Amide** monomer and **PDMS–DPP–Amide** composite. **c)** Photograph of **PDMS–DPP–Amide** composite with different thickness and **d)** their transmittance spectra.

## 2.3.8. Characterization of the Nanocomposite

In order to confirm that the aggregates are not perturbed inside the polymer matrix, we performed spectroscopic, morphological and X–ray diffraction analyses. The absorption profile of the **PDMS–DPP–Amide** composite matched well with that of the **DPP–Amide**, establishing the formation of both H– and J–aggregates as in the gel state (**Figure 2.11a**). The polymer matrix caused a broadening of the aggregation bands, with a slight shift in peak positions. Morphology of the nanocomposite was investigated by TEM analysis and we observed nanofibers of different lengths with an average diameter of 100 ± 50 nm (**Figure 2.11.b**) which further supported our assumption.

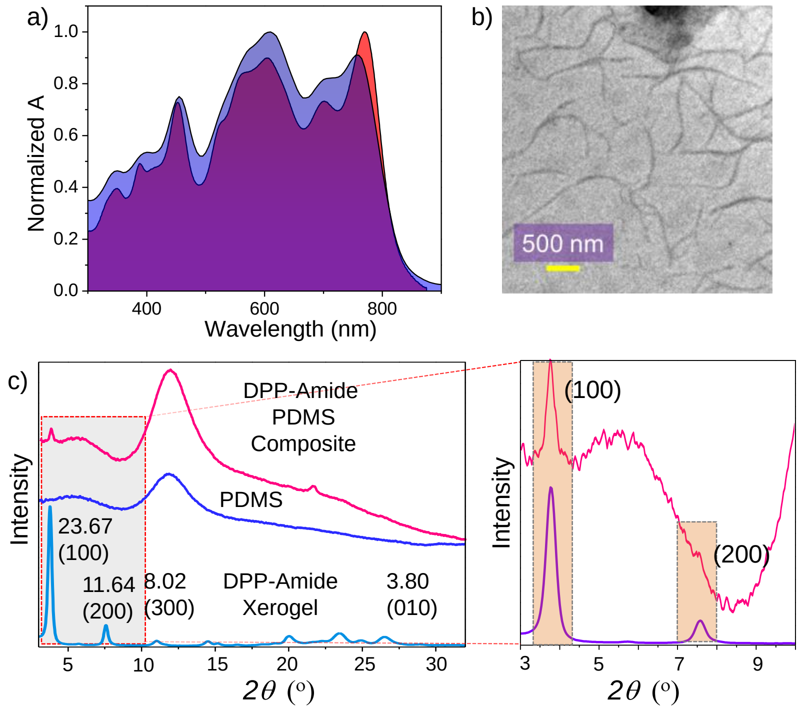

**Figure 2.11. a)** Absorption spectra of **DPP–Amide** aggregate (red) and **PDMS–DPP–Amide** composite (blue). **b)** TEM image of **PDMS–DPP–Amide** nanocomposite**. c)** WAXS of **DPP–Amide** xerogel, **PDMS** and **PDMS–DPP–Amide** composite.

Wide angle X–ray scattering (WAXS) showed sharp diffraction peaks for the **DPP–Amide** xerogel with a reciprocal *d*–spacing ratio of 1:2:3:4, indicating lamellar domains having a π–stacking distance of 3.8 Å.[38–39] On the other hand, **PDMS** exhibited diffused peaks ($2\theta$ = 10–15°) due to its amorphous nature (**Figure 2.11c**). Along with the broad diffraction peaks of **PDMS**, a few small sharp peaks were obtained for **PDMS–DPP–Amide** composite which are characteristic peaks of **DPP–Amide** (zoomed **Figure 2.11c**). These results further revealed that the lamellar molecular organization remains unaffected inside the **PDMS** matrix. However, the intensities of the diffraction peaks were low in the composite owing to the extremely low loading of the **DPP–Amide** (~1 wt %) in the matrix. This observation indicates the inherent nature of aggregation of **DPP–Amide** irrespective of the medium. The absorption studies, morphological analysis and the WAXS measurements are indicative of the fact that the molecules are dispersed as nanosized aggregates in the polymer matrix. As a result, the composite appears black in color as in the case of the gel and the degree of blackness computed using CIE 1976 L*a*b* where L* = 16.12, a* = 0.47 and b* = 0.07.

Raman spectrum of **DPP–Amide** showed three intense peaks at 1657 cm$^{-1}$ (amide C=O of **DPP**), 1574 cm$^{-1}$ (C=C stretching of thiophene) and 1515 cm$^{-1}$ (C=C stretching of DPP) (**Figure 2.12a**). **PDMS** exhibited main Raman peaks at 670 cm$^{-1}$, 791 cm$^{-1}$ (Si–C symmetric stretching), 880 cm$^{-1}$ (symmetric rocking of $CH_3$), 1266 cm$^{-1}$ (symmetric bending of $CH_3$), and 1441 cm$^{-1}$ (asymmetric bending of $CH_3$), analogous to the literature reports (**Figure 2.12b**).[40] In the **PDMS–DPP–Amide**, both **DPP–Amide** and **PDMS** retained their individual peaks affirming that all components are chemically intact. Moreover, we have performed $^1H$ NMR by dissolving the **DPP–Amide**, **PDMS** and **PDMS–DPP–Amide** in $CDCl_3$ separately. We found **PDMS–DPP–Amide** showed peaks corresponding to protons of pristine **DPP–Amide** with the corresponding chemical shift ($\delta$) values which further proves that **DPP–Amide** aggregates and **PDMS** are phase segregated (**Figure 2.12c**).

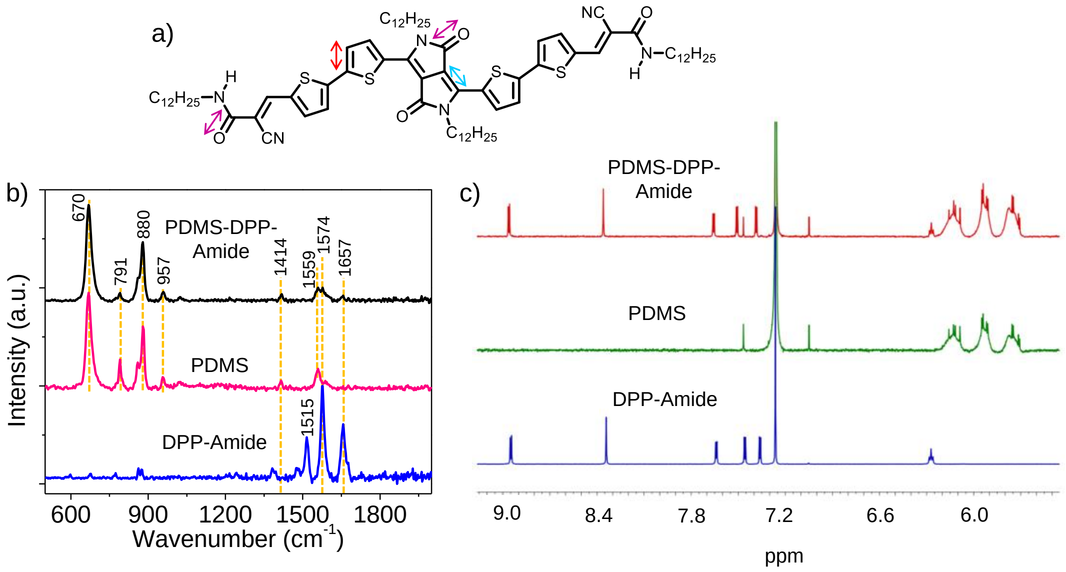

**Figure 2.12. a)** Structure of **DPP–Amide** with a diagram showing the major Raman active vibrational modes. **b)** Raman spectra of **DPP–Amide**, **PDMS** and **PDMS–DPP–Amide** in the film state. **c)** Solution state $^1H$ NMR by dissolving the compound and the composite in $CDCl_3$.

In order to understand the ambient stability of the composite for practical applications, we have exposed the filter to outdoor environment for about 6 months (**Figure 2.13a**). Transmittance was measured at different time intervals which revealed very little change in transmittance at the end, confirming the high stability of the **PDMS–DPP–Amide** composite (**Figure 2.13b**).

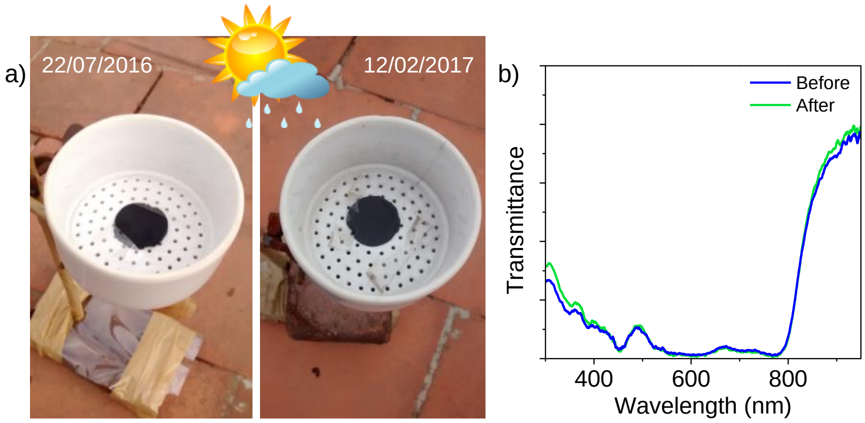

**Figure 2.13. a)** Setup on the terrace for aging the **PDMS–DPP–Amide** composite under real outdoor atmospheric conditions. **b)** Transmittance of the composite before and after exposing to the outdoor atmosphere for six months.

### 2.3.9. Applications of the NIR Filter

In order to understand the potential use of the new nanocomposite for NIR photography, we have modified an ordinary digital camera with the new **DPP–Amide** derived NIR filter. Normally, a digital camera detector is sensitive to both visible and NIR light and therefore, for true color photography, an NIR cut off filter is placed in front of the detector. A normal digital camera can be converted into an NIR camera by replacing the NIR reflecting filter with a visibly opaque and NIR transmitting one. A schematic illustration of the design concept with the nano–phase segregated supramolecular structures of **DPP–Amide** is described in **Figure 2.14**. Installation of the **PDMS–DPP–Amide** nanocomposite based NIR transmitting filter in a digital camera is shown in **Figure 2.14**.

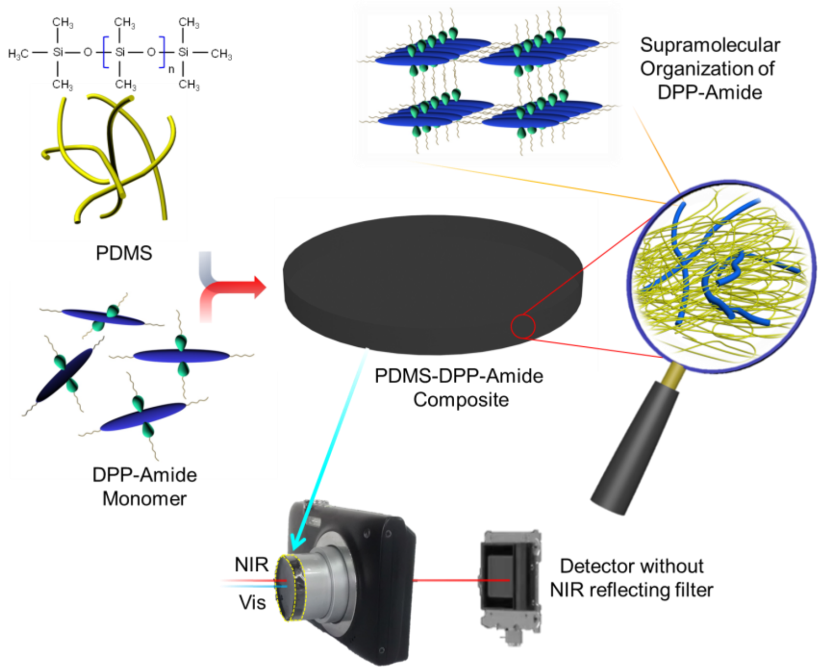

**Figure 2.14.** Schematic illustration of the construction of an NIR camera describing the preparation of NIR filter by mixing **PDMS** and **DPP–Amide** leading to phase separated nano–domain formation through highly ordered fibrous assembling.

To validate the spectral response of the modified NIR camera, letters N, I, R written in pure blue, green and red ink, respectively, and the words ‘DPP’ and ‘BLACK’ written in black ink were viewed through the camera (**Figure 2.15b**). Photograph of **PDMS–DPP–Amide** nanocomposite as NIR filter and a digital camera fitted with this filter shown in **Figure 2.15a**. A commercially available NIR reflecting filter was placed over the word ‘DPP’ and an NIR transmitting filter was placed over the word ‘BLACK’. It was possible to see the letters DPP and N, I and R but the word BLACK was not visible to naked eyes or through a normal camera. Interestingly, when viewed through the camera mounted with the **DPP–Amide** based NIR filter, only the word BLACK which was covered with the NIR transmitting filter could be seen (**Figure 2.15c**). The word DPP covered with the NIR reflecting filter of the letters N I R were not visible. Thus, it was clear that the camera fitted with the **PDMS–DPP–Amide** filter is responsive only to NIR light.

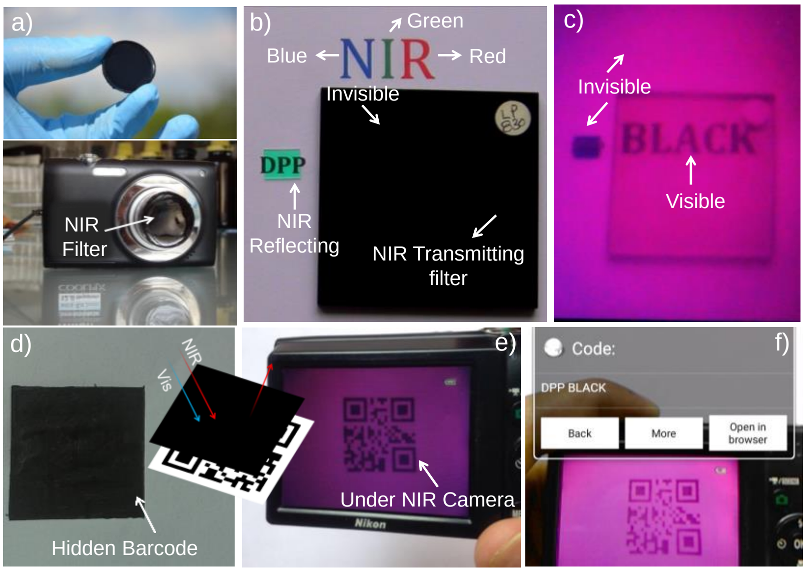

**Figure 2.15.** Security applications**. a)** Photograph of **PDMS–DPP–Amide** composite as an NIR filter. **b)** Image under a normal camera showing N, I, R written in pure blue, green and red inks, respectively and the writings DPP (left, visible) and BLACK (right, not visible). The word DPP is covered with an NIR reflecting lens and BLACK with an NIR transmitting filter. **c)** The image **b** seen through camera fitted with the **PDMS–DPP–Amide** as an NIR transmitting filter. **d)** Hidden barcode which is viewed under normal camera and **e)** the same viewed under the NIR camera. **f)** Barcode under the modified NIR camera was readable using a mobile application.

To take a step further, we made a hidden barcode by the combination of two commercial black inks. Initially, we generated a two dimensional barcode written as ‘DPP BLACK’ using an online barcode generator. This barcode was then printed over a normal white paper and covered with an NIR transparent black ink (**Figure 2.15d**). A schematic diagram of a hidden barcode reading is shown in inset **Figure 2.15d**. When a normal barcode reader is used, it appears as a black square due to the lack of visible optical contrast. However, when the barcode is seen with the camera fitted with the **PDMS–DPP–Amide** NIR filter (**Figure 2.15e**), the barcode becomes visible, which can then be read through a smartphone having barcode reader application (**Figure 2.15f**). This will allow reading hidden barcodes to authenticate genuine currencies, valuable documents, and commercial products using smartphones having an NIR camera fitted with such a filter in combination with a barcode reader app. This would enable a person to verify the authenticity of any document or product using a smartphone at the point of care. In addition, manipulation of bank cheques, and documents with a different ink can be distinguished by a camera fitted with NIR transparent filters. To demonstrate this, we have deliberately faked a bank cheque for the transaction of four thousand rupees (**Figure 2.16a**) which was originally issued for one thousand rupees, by using two different black inks. When viewed under NIR camera fitted with the **PDMS–DPP–Amide** filter, it was clear that the cheque was manipulated since the two black inks have different NIR transparencies (**Figure 2.16b**).

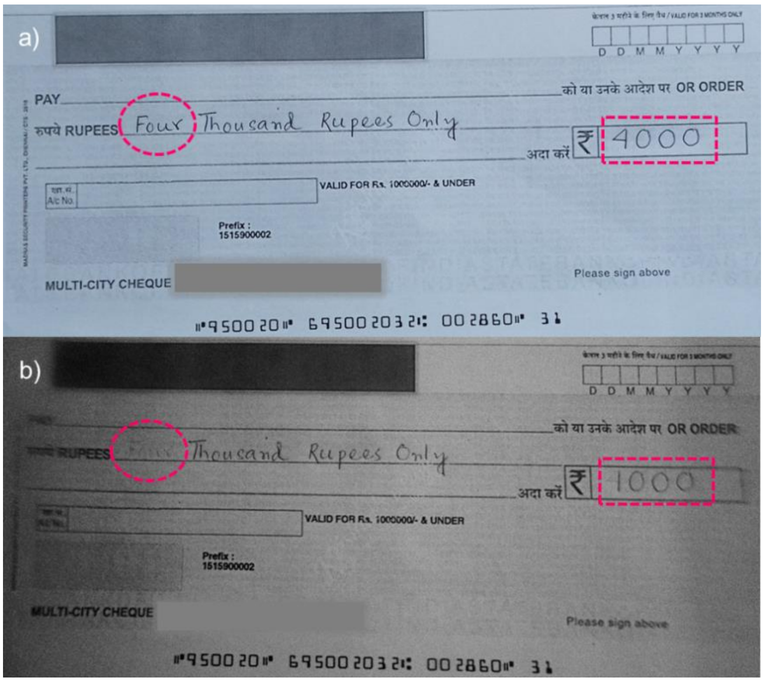

**Figure 2.16.** Photographs of the faked bank cheque under **a)** normal camera and **b)** an NIR camera fitted with **PDMS–DPP–Amide** filter.

NIR photography also has an important role in the field of forensic sciences because it can capture latent evidences of crime which are not visible to human eye or normal camera.[41,42] In forensic science, detection of blood stain over dark and dirty cloths is a challenge. NIR camera does not have any spectral response towards visible light. Hence, NIR photography is capable of identifying the blood stain over any dark color cloth owing to difference in contrast from the background material. In order to prove this, a black fabric cloth was stained with blood (**Figure 2.17a**) and allowed to dry under sunlight for 6 hours. After drying there was no difference in color or contrast with respect to the black background that made it invisible to human eye (**Figure 2.17b**). However, a clear difference in contrast was detected under NIR camera due to higher NIR reflectance from the cloth than the blood stain (**Figure 2.17c**). Finally, in order to understand the full potential of the **PDMS–DPP–Amide** as an NIR filter for night surveillance, we attempted the photography of objects in the dark. For this purpose our laboratory was photographed in the dark using the camera fitted with the **PDMS–DPP–Amide** filter, while illuminating with a NIR light source ($\lambda$ >850 nm) a clear image of the laboratory was obtained (**Figure 2.17d**).

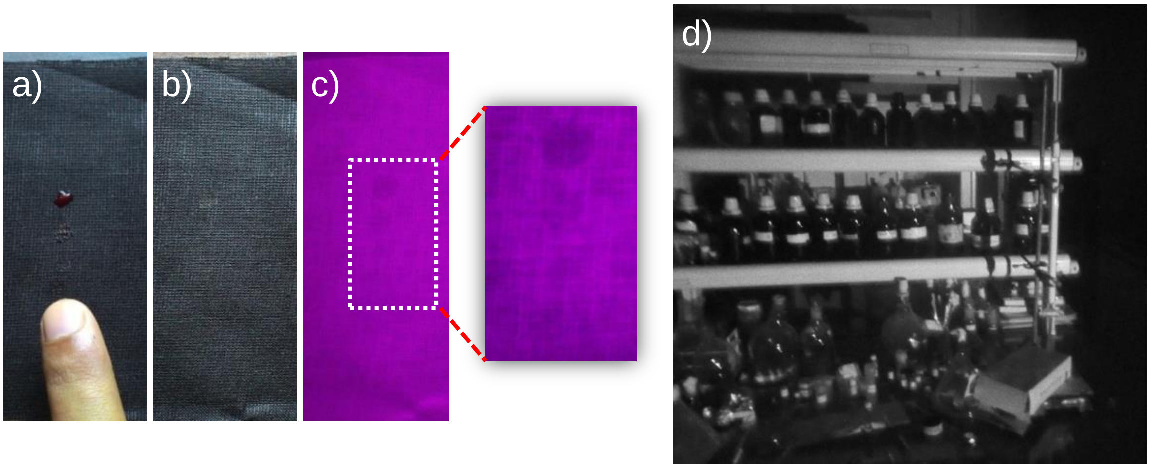

**Figure 2.17.** Forensic application and surveillance. **a)** Fresh blood stain over a black cloth; **b)** dried blood stain under visible camera and **c)** under NIR camera. **d)** The NIR photograph of the laboratory under NIR light.

## 2.4. Conclusion

In conclusion, we have described here a UV–Vis cut–off filter for selective transmission of NIR light, based on the self–assembly of a $\pi$–extended DPP dye. Due to the presence of H–bonding and $\pi$–stacking unit, **DPP–Amide** formed a supramolecular polymer in toluene, resulting a black organogel. Photophysical studies revealed that the self–assembled nano–aggregates of the **DPP–Amide** exhibited a broad absorption with almost equal intensity from 300–800 nm due to the formation of both H– and J–type aggregates. Formation of nanofibers were confirmed from the morphological analysis such as SEM, TEM and AFM. These self–assembled **DPP–Amide** nano–aggregates (0.15 wt%) was entrapped in **PDMS** resulting in an all organic, flexible, photostable and free–standing filter with high NIR transmittance. Detailed charecterisation of the nanocomposite revealed that the molecualr assembly was chemically intact inside the polymer matrix. Finally, we have used the nanocomposite for NIR photography, security and forensic applications.

## 2.5. Experimental Section

### 2.5.1. Materials and Methods

#### General procedures

Reagents and solvents obtained from commercial suppliers (Sigma Aldrich, Alfa Aesar, Merck and TCI) were used without further purification. Moisture and oxygen sensitive reactions were carried out under dry argon/nitrogen atmosphere. All organic extracts were dried over anhydrous sodium sulfate ($Na_2SO_4$) powder, and solvents were removed under reduced pressure with a rotary evaporator BUCHI R–210. Solvents required were dried according to standard literature procedure. Column chromatography was performed by using 100–200 mesh silica gel. HPLC grade solvents were used for precipitation and optical studies.

$^{1}H$ and $^{13}C$ NMR spectra were obtained in $CDCl_3$, using TMS (0 ppm for $^{1}H$ and 77 ppm for $^{13}C$) as an internal standard on a Bruker Avance 500 ($^{1}H$: 500 MHz; $^{13}C$: 125 MHz) spectrometer. Elemental analyses were performed with a Perkin–Elmer Series–2 Elemental Analyzer 2400. Matrix–assisted laser desorption ionization time–of–flight (MALDI–TOF) mass spectra were obtained on an AXIMA–CFR PLUS (SHIMADZU) MALDI–TOF mass spectrometer. High–

resolution mass spectra were recorded on a JEOL JSM 600 fast atom bombardment (FAB) high resolution mass spectrometer (HRMS–FAB).

### UV–Vis Electronic Absorption and Emission Spectral Measurement

Electronic absorption spectra were recorded on a Shimadzu UV–2600 Spectrophotometer and emission spectra were recorded on a SPEX–Fluorolog FL–1039 Spectrofluorimeter. Temperature dependent studies were carried out either in a 0.1 cm or 1 cm quartz cuvette with a thermistor directly attached to the wall of the cuvette holder.

### Scanning Electron Microscopy (SEM)

SEM images were obtained using a Zeiss EVO 18 cryo SEM Special Edn. with variable pressure detector working at 20–30 kV. The images were obtained by drop–casting **DPP–Amide** organogel ($c = 3 \times 10^{-3}$ M) in toluene over a freshly cleaved mica substrate, attached to the SEM stub followed by drying under vacuum.

### Transmission Electron Microscopy (TEM)

TEM and HR–TEM images were obtained on a FEI Tecnai G2 30 EDAX microscope with an accelerating voltage of 100 kV and 300 kV, respectively. The samples were prepared by drop casting **DPP–Amide** and **PDMS–DPP–Amide** composite aggregates over a formvar coated copper grid. TEM images were obtained without staining.

### Atomic Force Microscopy (AFM)

Atomic Force Microscopy images were recorded under ambient conditions using a Multimode SPM (Bruker Nanoscope V) operating with a tapping mode regime. Micro–fabricated TiN cantilever tips (NSG10) with a resonance frequency of 299 kHz and a spring constant of 20–80 $\mathrm{Nm^{-1}}$ were used. AFM section analysis was done offline. Samples for the imaging were prepared by drop casting the solution over freshly cleaved mica surface and silicon wafer at the required concentrations.

### Wide–angle X–ray Scattering (WAXS)

Wide–angle X–ray Scattering measurements were obtained on a XEUSS 2D SAXS/WAXS system using a Genix microsource from Xenocs operated at 50 kV and 0.3 mA. The Cu Kα radiation ($\lambda$ = 1.54 Å) was collimated with a FOX2D mirror and two pairs of scatterless slits from Xenocs. Xerogel of **DPP–Amide** and **PDMS–DPP–Amide** composite was placed directly in the sample holder.

## 2.5.2. Synthesis and Characterization

### Synthesis of 3,6–Di(thiophen–2–yl)pyrrolo[3,4–c]pyrrole 1,4(2H, 5H)–dione (16)

A 250 mL two–neck flask connected to a condenser was charged with a stir bar. Sodium *tert*–pentoxide (20 g, 182 mmol) and *tert*–amyl alcohol (30 mL) were added under argon atmosphere and the mixture was heated at 100 °C until the mixture became homogeneous (~ 1 h). The mixture was then cooled to 60°C and thiophene–2–carbonitrile (**15**) (10 g, 91.61 mmol) was added. From a pressure equalizer diethyl succinate (7.9 g, 45.77 mmol) in *tert*–amyl alcohol (10 mL) was added dropwise to the reaction mixture over 2 h, and the solution turned dark purple. The reaction mixture was vigorously stirred at 100 °C for 10 h, and then acidic MeOH (40 mL MeOH and 20 mL glacial acetic acid) was added at room temperature to neutralise the reaction mixture. Again the reaction mixture was heated at 70°C and was vacuum filtered through a Buchner funnel (Whatman filter paper). A dark red solid cake of **16** (15g) was obtained and dried inside a vacuum oven at 100 °C, which was used in subsequent reactions without further purification.

### Synthesis of 2,5–Didodecyl–3,6–di(thiophen–2–yl)pyrrolo[3,4–c]pyrrole–1,4(2H,5H)–dione (17)

In a two–necked 250 mL round bottom flask, **16** (3 g, 10 mmol) and anhydrous activated $K_2CO_3$ (8.28 g, 60 mmol) were added and the mixture was degassed thrice, then degassed anhydrous *N,N*–dimethylformamide (DMF, 50 mL) was injected into the mixture and heated at 120°C under argon for 1 h. Dodecyl bromide (6.23 mL, 25 mmol) was added drop–wise using a syringe for a period of 2 h, and the reaction was proceeded further for 24 h at 120°C. The reaction mixture was allowed to cool down to room temperature, poured into ice cold water (150 mL) and stirred for 30 minutes. The mixture was extracted with $CHCl_3$ and dried over anhydrous $Na_2SO_4$ and the solvent was removed under reduced pressure. The crude product was purified by column chromatography using chloroform as eluent, and the solvent was evaporated under reduced pressure to obtain **17** as a purple–brown powder (yield 4.2 g, 66%). $^1H$–NMR (500 MHz, $CDCl_3$, δ): 8.94 (d, *J* = 8 Hz, 2H, Ar–H), 7.64 (d, *J* = 4.5 Hz, 2H, Ar–H), 7.30 (t, *J* = 4.5 Hz, 2H, Ar–H), 4.08 (t, *J* = 8.0 Hz, 4H, $–NCH_2–$), 1.77 (quintet, *J* = 8 Hz, *J* = 7.5 Hz, 4H, $–N–CH_2–CH_2–$), 1.40–1.42 (m, 4H, $–N–CH_2–CH_2–CH_2–$), 1.13–1.45 (m, 32H, $–CH_2–$), 0.87 (t, *J* = 6.5 Hz, 6H, $–CH_3$). $^{13}C$–NMR (125 MHz, $CDCl_3$, δ): 157.4, 136.0, 131.3, 126.7, 125.8, 124.6, 103.7, 38.2, 27.9, 26.0, 25.7, 25.6, 25.6, 25.4, 25.3, 22.9, 18.7, 10.2, 10.1. MALDI–TOF: m/z 638.85 (100%). Calculated Mass: 637.0.

### Synthesis of 3,6–Bis(5–bromothiophen–2–yl)–2,5–didodecyl pyrrolo[3,4–c]pyrrole 1,4(2H,5H)–dione (18)

**17** (1.0 equiv., 2 g, 3.13 mmol) was dissolved in dry chloroform (100 mL) inside a 250 mL two–neck flask in the dark, then *N*–bromosuccinimide (2.2 equiv., 1.23 g, 6.91 mmol) was added in small portions over 30 min. After stirring at room temperature for 48 h, the reaction mixture was poured into ice cold water (200 mL) and extracted with chloroform (3 × 60 mL). The organic phase was washed with brine (2 × 100 mL), dried over anhydrous $Na_2SO_4$ and the solvent was evaporated under reduced pressure. The dark–red residue was purified by column chromatography using chloroform as eluent to obtain **18** (yield 1.80 g, 72%). $^1$H–NMR (500 MHz, $CDCl_3$, δ): δ 8.67 (d, *J* = 3 Hz, 2H, Ar–H), 7.24 (d, *J* = 7 Hz, 2H, Ar–H), 3.97 (t, *J* = 8.0 Hz, 4H, $–NCH_2–$), 1.74–1.65 (m, 4H, $–N–CH_2–CH_2–$), 1.44–1.13 (m, 36H), 0.85–0.89 (m, 6H). $^{13}$C–NMR (125 MHz, $CDCl_3$, δ): δ 161.0, 138.9, 135.1, 131.5, 131.2, 118.9, 108.0, 42.2, 31.8, 29.9, 29.5, 29.4, 29.4, 29.2, 29.1, 29.0, 26.7, 22.5, 13.9. MALDI–TOF: m/z 796.35 (100%). Calculated Mass: 794.79.

### Synthesis of 5',5''–(2,5–didodecyl–3,6–dioxo–2,3,5,6–tetrahydro pyrrolo[3,4–c]pyrrole–1,4–diyl)di–2,2'–bithiophene–5–carbaldehyde (19)

In a 100 mL two neck round bottom flask, **18** (0.50 g, 0.63 mmol), $Pd^0(PPh_3)_4$ (50 mg, 0.01 mmol), and $Na_2CO_3$ (2.66 g, 25.16 mmol) was mixed under argon atmosphere inside a glove bag and the system was sealed with a condenser. Then deoxygenated THF (10 mL) and $H_2O$ (5 mL) were added to the mixture and heated at 45°C under an argon atmosphere for 30 min. A solution of 5–formylthiophen–2–yl boronic acid (0.4 g, 2.52 mmol) in deoxygenated THF (25 mL) was added slowly, and the mixture was refluxed for another 12 h, until a blue color was observed. After cooling to room temperature, the mixture was extracted with 100 mL of $CH_2Cl_2$ (100 mL) and dried over anhydrous $Na_2SO_4$. The organic extract was collected and concentrated by rotary evaporation. The residue was purified by column chromatography on silica ($CH_2Cl_2$/ethyl acetate 1/70, v/v) to give **19** as a black solid (yield: 0.3 g 55%). $^1$H–NMR (500 MHz, $CDCl_3$, δ): 9.90 (s, 2H, Ar–CHO), 8.94 (d, *J* = 6.5 Hz, 2H, Ar–H), 7.73 (d, *J* = 6.5 Hz, 2H, Ar–H), 7.49 (d, *J* = 7 Hz, 2H, Ar–H), 7.41 (d, *J* = 7 Hz, 2H, Ar–H), 4.12 (t, *J* = 8 Hz, 4H, $–NCH_2–$), 1.77–1.68 (m, 4H, $–N–CH_2–CH_2–$), 1.44–1.13 (m, 36H), 0.85–0.89 (m, 6H). $^{13}$C–NMR (125 MHz, $CDCl_3$, δ): δ 182.3, 161.0, 145.0, 143.1, 140.9, 138.9, 137.0, 130.4, 128.1, 127.1, 125.5, 109.0, 42.2, 31.8, 29.9, 29.5, 29.4, 29.4, 29.2, 29.1, 29.2, 26.7, 22.5, 13.9. MALDI–TOF: m/z 858.36 (100%). Calculated Mass: 857.26.

## Synthesis of *N*–Dodecylcyanoacetamide (21)

*n*–Dodecylamine (6.13 g, 33.1 mmol) was mixed with ethyl cyanoacetate (**20**) (23.0 mL, 216 mmol) by slightly warming in a round bottom flask. Formation of a precipitate was observed upon stirring for 1 h at room temperature. After 17 h, this precipitate was filtered off, washed with ethanol and diethyl ether and recrystallized from ethanol to yield a colorless solid (4.2 g). Concentration of the mother liquor and recrystallization of the residue from ethanol gave further pure product **21** (yield: 5.4 g , 64%), m.p. 82–83°C. $^1$H–NMR (500 MHz, $CDCl_3$, δ): 6.15 (s, 1H, N–H), 3.37 (s, 2H, CN–$CH_2$), 3.30 (d, *J* = 7.2 Hz, 2 H, –NH–$CH_2$–), 1.54–1.59 (m, 2H, –NH–$CH_2$–$CH_2$), 1.2–1.4 (m, 18 H, –$(CH_2)_9CH_3$), 0.88 ppm (t, *J*= 6.9 Hz, 3H, –$CH_3$).

## Synthesis of (2E,2'E)–3,3'–(5',5''–(2,5–didodecyl–3,6–dioxo–2,3,5,6–tetrahydropyrrolo[3,4–c]pyrrole–1,4–diyl)bis(2,2'–bithiophene–5',5–diyl))bis(2–cyano–*N*–dodecylacrylamide) (DPP–Amide, 22)

**19** (0.10 g, 0.12 mmol) and **21** (0.15 g, 0.60 mmol) were taken in a 100 mL two–neck round bottom flask under argon atmosphere. Freshly distilled dry THF (20 mL) and piperidine (1 mL) were added to this mixture and heated to reflux under argon atmosphere for 6 h. A green colouration was observed. After cooling to room temperature, THF was removed *via* rotary evaporation. The residue was extracted with $CHCl_3$ (100 mL) and the solvent was removed by rotary evaporation. The residue was purified by column chromatography on silica ($CHCl_3$:ethyl acetate 10:1, v:v) followed by precipitation in $CHCl_3$/MeOH mixture to give **22** as a black solid (yield: 0.12 g 73%). $^1$H–NMR (500 MHz, $CDCl_3$, δ): 8.95 (d, *J* = 4 Hz, 2H, Ar–H), 8.34 (s, 2H, –C=CH–), 7.64 (d, *J* = 4.5 Hz, 2H, Ar–H), 7.46 (d, *J* = 4 Hz, 2H, Ar–H), 7.36 (d, *J* = 7 Hz, 2H, Ar–H), 6.27 (t, *J* = 6 Hz, 2H, –NH–), 4.09 (t, *J* = 8 Hz, 4H, –$NCH_2$–), 3.42 (t, *J* = 7 Hz, 4H, –NH–$CH_2$–), 1.73–1.79 (m, *J* = 7 Hz, 4H, –N–$CH_2$–$CH_2$–), 1.44–1.13 (m, 36H), 0.85–0.89 (m, 6H). $^{13}$C–NMR (125 MHz, $CDCl_3$, δ): 161.0, 160.2, 143.9, 143.6, 140.9, 138.8, 136.4, 130.4, 127.1, 125.7, 117.1, 109.1, 100.5, 42.2, 31.8, 29.9, 29.5, 29.4, 29.4, 29.2, 29.1, 29.0, 26.7, 22.5, 13.9. MALDI–TOF: m/z calculated for $C_{78}H_{112}N_6O_4S_4$ 1326.02 and found 1327.48. CHN Analysis: calculated for $C_{78}H_{112}N_6O_4S_4$ C, 70.65; H, 8.51; N, 6.34; O, 4.83; S, 9.67 found: C, 70.45; H, 8.78; N, 6.70.

## 2.6. References

[1] K. Ariga, J. P. Hill, M. V. Lee, A. Vinu, R. Charvet, S. Acharya, *Sci. Technol. Adv. Mater.* **2008**, *9*, 014109.

[2] F. J. M. Hoeben, P. Jonkheijm, E. W. Meijer, A. P. H. J. Schenning *Chem. Rev.* **2005**, *105*, 1491.

[3] T. Aida, E. W. Meijer, S. I. Stupp, *Science* **2012**, *335*, 813.

[4] S. S. Babu, V. K. Praveen, A. Ajayaghosh, *Chem. Rev.* **2014,** *114*, 1973.

[5] N. M. Sangeetha, U. Maitra, *Chem. Soc. Rev.* **2005**, *34*, 821.

[6] J.–F. Lutz, J.–M. Lehn, E. W. Meijer, K. Matyjaszewski, *Nat. Rev. Mater.* **2016**, *1*, 16024.

[7] S. S. Babu, S. Prasanthkumar, A. Ajayaghosh, *Angew. Chem. Int. Ed.* **2012**, *51*, 1766.

[8] S. Ghosh, V. K. Praveen, A. Ajayaghosh, *Annu. Rev. Mater. Res.* **2016**, *46*, 235.

[9] E. Busseron, Y. Ruff, E. Moulin, N. Giuseppone, *Nanoscale* **2013**, *5*, 7098.

[10] M. J. Webber, E. A. Appel, E. W. Meijer, R. Langer, *Nat. Mater.* **2016**, *15*, 13.

[11] S. Srinivasan, P. A. Babu, A. Mahesh, A. Ajayaghosh, *J. Am. Chem. Soc.* **2009**, *131*, 15122.

[12] A. Ajayaghosh, V. K. Praveen, C. Vijayakumar, *Chem. Soc. Rev.* **2008**, *37*, 109.

[13] S. S. Babu, K. K. Kartha, A. Ajayaghosh, *J. Phys. Chem. Lett.* **2010**, *1*, 3413.

[14] S. T. Debroux, K. K. McCaul, S. Shimamoto, Infrared Photography, http://www.crime–scene–invetigator.net/Infrared_Photography_research_paper.pdf (accessed: January, 2017).

[15] R&D and industrial applications for Near Infrared (NIR) cameras http://support.flir.com/appstories/AppStories/R&D/Near_Infrared_(NIR)_cameras_EN.pdf (accessed: January, 2017).

[16] X. Zhang, B. Bureau, P. Lucas, C. Boussard–Pledel, J. Lucas, *Chem. Eur. J.* **2008**, *14*, 432.

[17] B. J. Eggleton, B. Luther–Davies, K. Richardson, *Nat. Photonics* **2011**, *5*, 141.

[18] A. Llordes, G. Garcia, J. Gazquez, D. J. Milliron, *Nature* **2013**, *500*, 323.

[19] J. J. Griebel, S. Namnabat, E. T. Kim, R. Himmelhuber, D. H. Moronta, W. J. Chung, A. G. Simmonds, K. J. Kim, J. van der Laan, N. A. Nguyen, E. L. Dereniak, M. E. Mackay, K. Char, R. S. Glass, R. A. Norwood, J. Pyun, *Adv. Mater.* **2014**, *26*, 3014.

[20] L. E. Anderson, T. S. Kleine, Y. Zhang, D. D. Phan, S. Namnabat, E. A. LaVilla, K. M. Konopka, L. Ruiz Diaz, M. S. Manchester, J. Schwiegerling, R. S. Glass, M. E. Mackay, K. Char, R. A. Norwood, J. Pyun, *ACS Macro Letters* **2017**, *6*, 500.

[21] H. Khandelwal, A. P. H. J. Schenning, M. G. Debije *Adv. Energy Mater.* **2017**, 1602209.

[22] J. Fabian, H. Nakazumi, M. Matsuoka, *Chem. Rev.* **1992**, *92*, 1197.

[23] M. İ. Özkut, M. P. Algi, Z. Öztaş, F. Algi, A. M. Önal, A. Cihaner, *Macromolecules* **2012**, *45*, 729.

[24] L. Dou, Y. Liu, Z. Hong, G. Li, Y. Yang, *Chem. Rev.* **2015**, *115*, 12633.

[25] M. Kasha, *Radiat. Res.* **1963**, *20*, 55.

[26] F. C. Spano, *Acc. Chem. Res.* **2010**, *43*, 429.

[27] F. C. Spano, C. Silva, *Annu. Rev. Phys. Chem.* **2014**, *65*, 477.

[28] S. Ghosh, X. Q. Li, V. Stepanenko, F. Wurthner, *Chem. Eur. J.* **2008**, *14*, 11343.

[29] F. Würthner, C. Bauer, V. Stepanenko, S. Yagai, *Adv. Mater.* **2008**, *20*, 1695.

[30] F. Graser, E. Hädicke, *Liebigs Ann. Chem.* **1980**, 1994.

[31] M. Kirkus, L. Wang, S. Mothy, D. Beljonne, J. Cornil, R. A. Janssen, S. C. Meskers, *J. Phys. Chem. A* **2012**, *116*, 7927.

[32] S. Qu, H. Tian, *Chem. Commun.* **2012**, *48*, 3039.

[33] M. Grzybowski, D. T. Gryko, *Adv. Opt. Mater.* **2015**, *3*, 280.

[34] T. Aytun, L. Barreda, A. Ruiz–Carretero, J. A. Lehrman, S. I. Stupp, *Chem. Mater.* **2015**, *27*, 1201.

[35] Y. Zhao, D. G. Truhlar, *Theor. Chem. Acc*. **2008**, *120*, 215.

[36] T. Matsui, Y. Imamura, I. Osaka, K. Takimiya, T. Nakajima, *J. Mater. Chem. C* **2016**, *120*, 8305.

[37] G. Han, X. Shen, R. Duan, H. Geng, Y. Yi, *J. Mater. Chem. C* **2016**, *4*, 4654.

[38] S. Yagai, S. Okamura, Y. Nakano, M. Yamauchi, K. Kishikawa, T. Karatsu, A. Kitamura, A. Ueno, D. Kuzuhara, H. Yamada, T. Seki, H. Ito, *Nat. Commun.* **2014**, *5*, 4013.

[39] S. Ghosh, D. S. Philips, A. Saeki, A. Ajayaghosh, *Adv. Mater.* **2017**, *29*, 1605408.

[40] A. Riano, P. M. Burrezo, M. J. Mancheno, A. Timalsina, J. Smith, A. Facchetti, T. J. Marks, J. T. L. Navarrete, J. L. Segura, J. Casadob, R. P. Ortiz, *J. Mater. Chem. C* **2014**, *2*, 6376.

[41] J. Albanese, R. Montes, *J. Forensic Sci.* **2011**, *56*, 1601.

[42] A. C. Lin, H. M. Hsieh, L. C. Tsai, A. Linacre, J. C. Lee, *J. Forensic Sci.* **2007**, *52*, 1148.

# Chapter 3

## Modulating the Charge Carrier Polarity of a Diketopyrrolopyrrole–based Low Band Gap Semiconductors by Terminal Functionalization

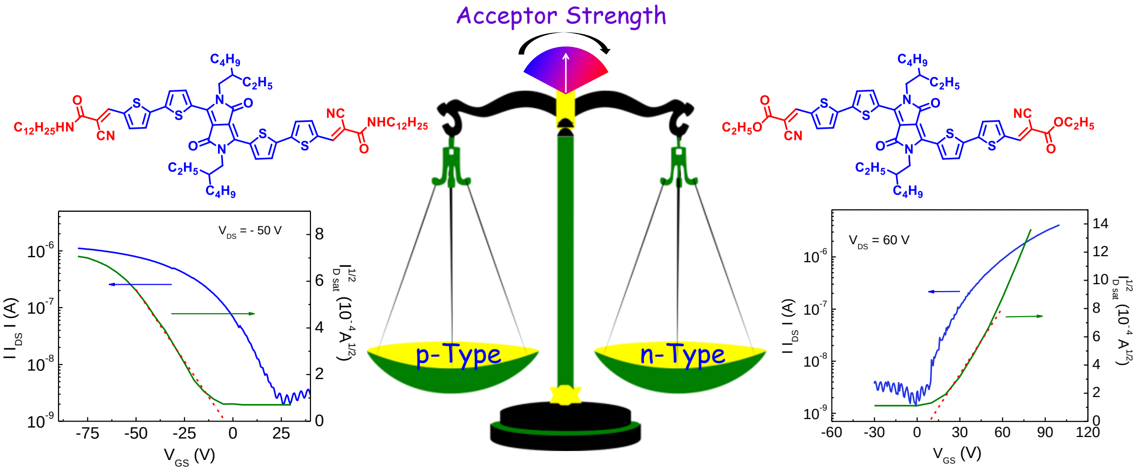

## 3.1. Abstract

*Organic semiconductors with variable charge carrier polarity are required for optoelectronic applications. In this chapter, we have synthesized three diketopyrrolopyrrole (DPP) based D–A molecules with a subtle variation in their terminal groups (amide, ester and cyano). They exhibited broad absorption and low band gaps. FP–TRMC and FET measurements confirmed that a small increase in acceptor strength resulted in a complete change in the charge transport properties from p– to n–type.* ***DPP–Amide*** *exhibited a moderate p–type mobility* ($0.9 \times 10^{-2}$ $cm^2V^{-1}s^{-1}$)*, whereas good n–type mobilities were observed for* ***DPP–Ester*** ($1.45 \times 10^{-2}$ $cm^2V^{-1}s^{-1}$) *and* ***DPP–DCV*** ($1 \times 10^{-2}$ $cm^2V^{-1}s^{-1}$)*. Detailed AFM and WAXS analyses of the films of the new molecules revealed the formation of uniform morphology of the molecular aggregates. The terminal functional*

*modification approach presented here is a simple and efficient method to alter the charge carrier polarity of organic semiconductors.*

## 3.2. Introduction

Organic semiconductors, in comparison to their inorganic counterparts, have generated significant interest for more than a decade due to their potential as promising candidates in thin, flexible and light weight organic field–effect transistors (OFETs).[1–3] Unlike inorganic semiconductors, band gap tuning and engineering is quite feasible in organic semiconductors *via* synthetic modifications.[4,5] Therefore, organic small molecules and polymers have attracted significant attention in semiconductor research although their advantages *vs* disadvantages in terms of synthesis, solution processability, film formation, crystallinity etc. are still matters of debate in the scientific community.[6,7] Over the past few years, a large number of small molecules and polymers were designed and synthesized for FET applications.[3] Majority of these semiconductors are hole transporting (p–type) in nature, while a few of them exhibit electron transporting (n–type) or ambipolar characteristics.[8,9] Generally, electron rich motifs like benzothiophene, tetrathiafulvalene, fluorine, thienothiophene etc. are used in the design of p–type semiconductors,[10] whereas n–type semiconductors are largely based on electron deficient cores such as naphthalenediimide, perylenediimide, fullerene etc.[11] A few π–conjugated D–A oligomers and polymers are reported to exhibit p–type or n–type or ambipolar characteristics depending on the nature of the attached substituents.[12,13] However, cost effective realization of these semiconductor materials with tunable transport properties is still challenging. Moreover, it is mandatory to understand the structure–property relationships behind organic semiconductors for further improvement in device performance. Recent reports have demonstrated the switching in polarity for a few π–conjugated systems upon application of an external stimulus, *via* small synthetic modifications or by changing the metal center.

Seki and co–workers have reported two polymers **1**–**2**, based on the same D–A π–conjugated backbone, differing only in the position of the side chain at the thiophene unit (**Figure 3.1a**).[14] Flash–photolysis time–resolved microwave conductivity (FP–TRMC) measurement revealed that polymer **1** has better photoconductivity when compared to **2**, in presence of a small amount of 1,8–octanedithiol (ODT) as additive (**Figure 3.1b**). It was also observed that **1** exhibited both electron and hole mobilities as obtained from space–charge–limited current (SCLC) measurements.

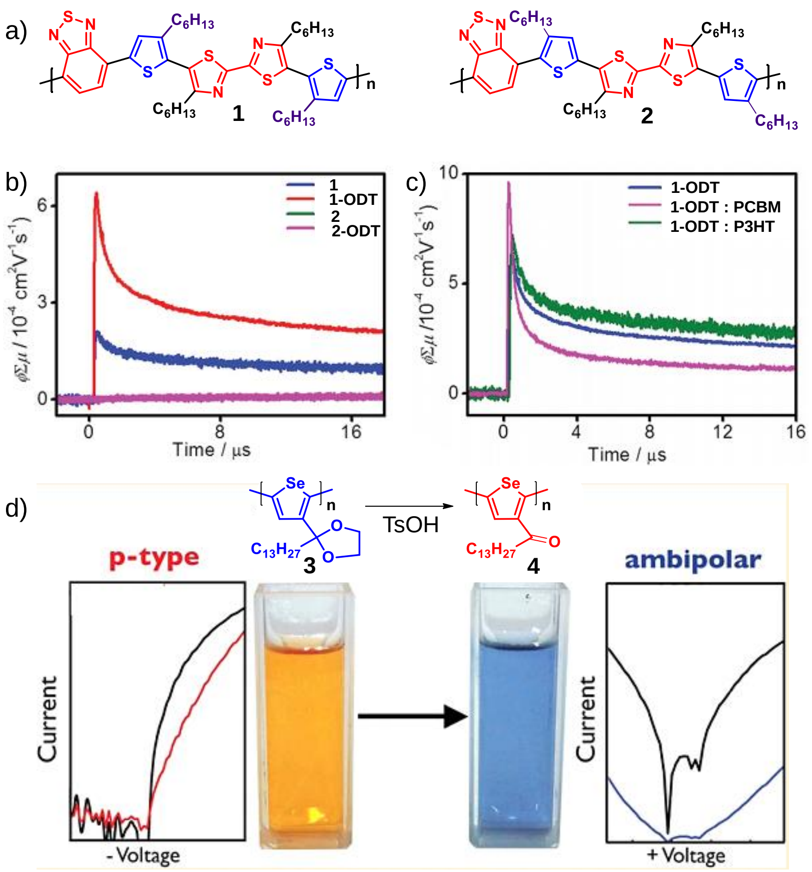

**Figure 3.1. a)** Molecular structures of the polymers **1**–**2**. **b)** Comparison of the FP–TRMC transients of the polymer films of **1** and **2** with and without **ODT**; **c) ODT** processed polymer films of polymer **1** (**1**:**PCBM**, and **1**:**P3HT**). **d)** Chemical structure of ketal polymer **3** and its conversion into **4** along with corresponding color change and transfer characteristics of the OFET devices.

Hence, it was expected that polymer **1** can act as an electron donor for phenyl–$C_{61}$–butyric acid methyl ester (**PCBM)** and an electron acceptor for poly–3–

hexylthiophene (**P3HT**). FP–TRMC results indicated that **1** showed an increase in photoconductivity when mixed with same weight of **P3HT** (**Figure 3.1c**). However, a 1:1 blend of **1** and **PCBM** exhibited a decrease in photoconductivity in the absence of additive ODT, probably due to macroscopic phase segregation. However, in presence of the additive, the blend of **1** and **PCBM** showed an increase in photoconductivity (**Figure 3.1c**). Thus, it was shown that polymer **1** can behave as both p– and n–type material in presence of an additive with an ability to switch its charge carrier polarity.

Seferos and co–workers reported a stimuli responsive polymer capable of switching charge carrier polarity upon chemical treatment.[15] A polyselenophene **3** containing *α*–ketal side–chains was prepared and the *α*–ketal side–chains were then converted into the corresponding *α*–ketone (**4**) in presence of *para*–toluenesulfonic acid. A red shift in absorption consistent with the lowering of band gap was observed, and was attributed to the electron withdrawing ability of the *α*–keto moiety (**Figure 3.1d**). These observations were further supported by the DFT calculations, indicating the delocalization of LUMO and predicted low lying energy levels for **4**. Finally, bottom–gate/bottom–contact (BGBC) OFETs were fabricated with the *α*–ketal polymer **3** and *α*–ketone polymer **4**. While **3** exhibited p–type characteristics with a hole mobility ($\mu_h = 1.6 \times 10^{-5}$ cm$^2$V$^{-1}$s$^{-1}$), **4** showed an ambipolar behavior with both hole ($\mu_h = 4.9 \times 10^{-4}$ cm$^2$V$^{-1}$s$^{-1}$) and electron ($\mu_e = 1.0 \times 10^{-4}$ cm$^2$V$^{-1}$s$^{-1}$) mobility. Thus, the chemical modification of functional groups was demonstrated to switch the charge transport properties of a polymeric material.

Jiang and co–workers have demonstrated the switching in charge carrier polarity in 2D polymers which was till then reported only for linear polymers.[16] 2D covalent organic frameworks (COFs) of π–conjugated molecules have unique structural and electronic properties due to their highly organized structure. Charge transport properties of three porphyrin based COFs, two of them bearing a metal center – Zn (ZnP–COF) and Cu (CuP–COF) and the third metal–free ($H_2$P–COF) (**Figure**

**3.2a**) were investigated. FP–TRMC measurements indicated that $H_2P$–COF exhibited only hole mobility, whereas CuP–COF exhibited more of an electron transporting nature and ZnP–COF exhibited a balanced hole and electron mobility (**Figure 3.2c**). All the COFs possessed high photoconductivity and charge carrier mobilities due to the favorable layered structure with columnar porphyrin paths, macrocycle–on–macrocycle and metal–on–metal channels, through which holes and electrons could readily be transported (**Figure 3.2b**).

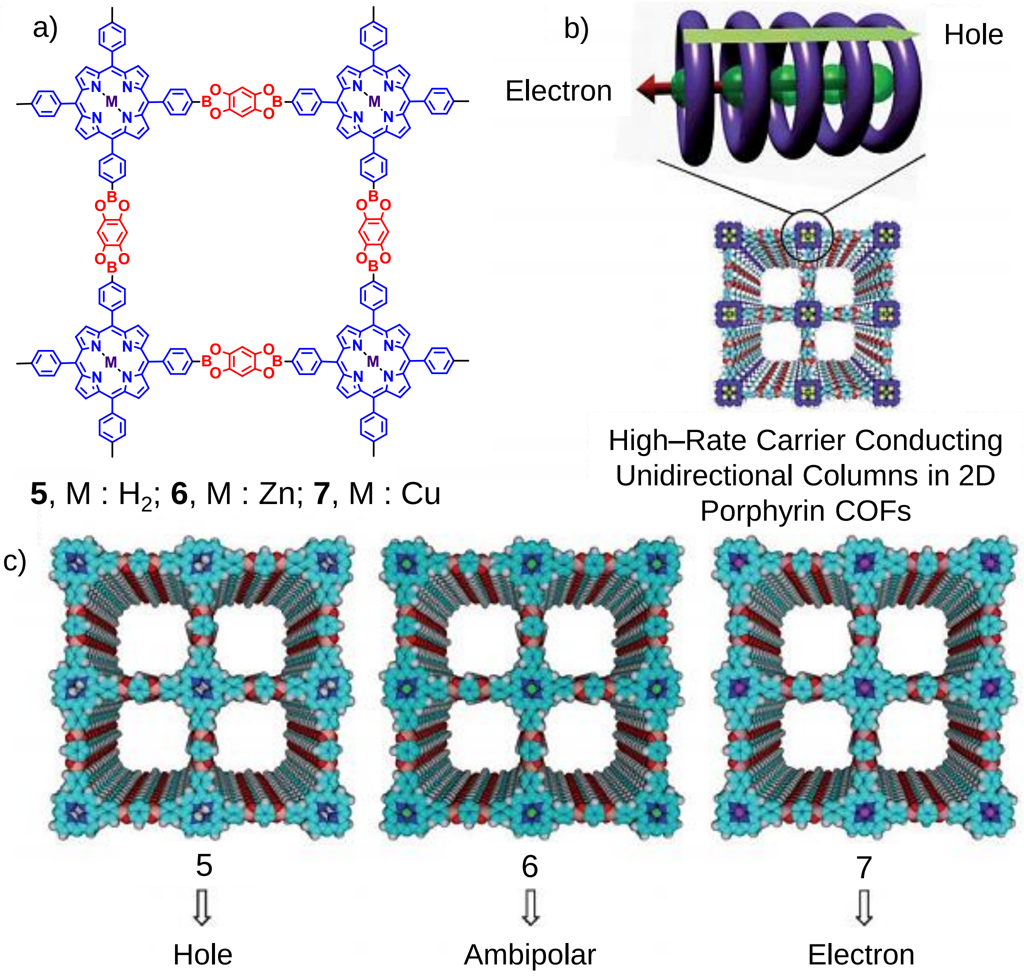

**Figure 3.2. a)** Molecular structures of the 2D COFs of **5–7**. **b)** Graphical representation of the metal–on–metal and macrocycle–on–macrocycle channels for respective electron and hole transport inside the stacked porphyrin column. **c)** Schematic representations of the stacked COF assemblies of **5–7**.

Kloc and co–workers have reported a few metal phthalocyanines **8**–**15** (fluorinated and non–flourinated, **Figure 3.3a**) and tuned their charge transporting property from p–type to n–type *via* molecular crystal engineering.[17] The rationale behind introducing the fluorine atoms was to increase the electron injection into these materials. Charge carrier mobilities of these materials were estimated in single–crystal field–effect transistors over the $SiO_2$/Si substrate. Very high hole mobilities were obtained for **8** ($\mu_h$ = 2.35 $cm^2V^{-1}s^{-1}$) and **9** ($\mu_h$ = 2.31 $cm^2V^{-1}s^{-1}$, **Figure 3.3b**). With the increase in the number of fluorine atoms, the hole mobilities decreased rapidly with concomitant rise in electron mobilities ($\mu_e$ for **14** = 0.75 $cm^2V^{-1}s^{-1}$, ($\mu_e$ for **15** = 1.24 $cm^2V^{-1}s^{-1}$, **Figure 3.3c**). Other derivatives exhibited ambipolar charge transport properties. DFT calculations indicated an increase in electron transfer integral with increase in fluorine substitution leading to the observed switching in polarity from p– to n–type.

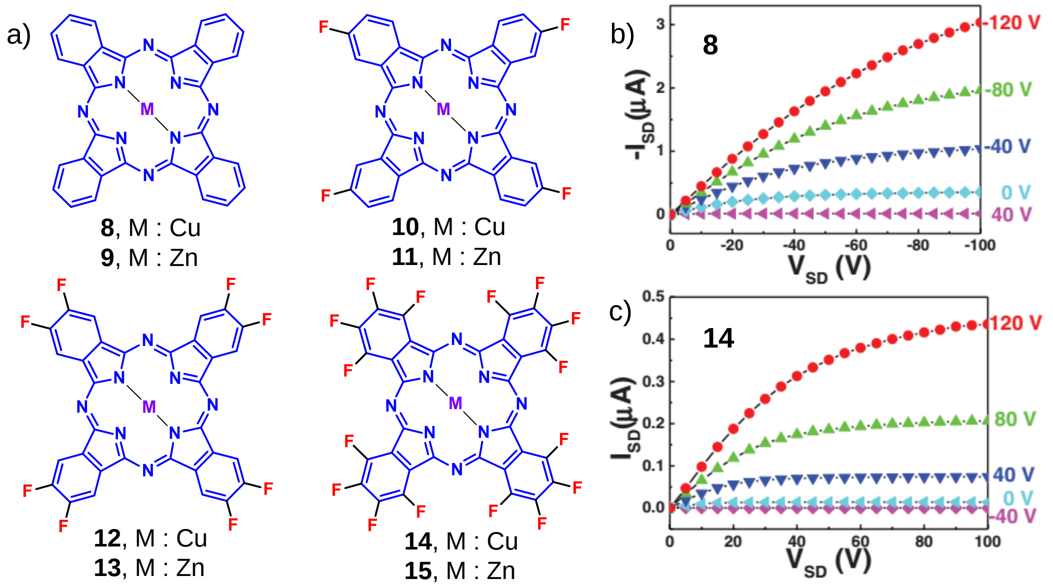

**Figure 3.3. a)** Molecular structures of the metallophthalocyanines **8–15**. Output characteristics of the OFET devices fabricated from **b)** copper phthalocyanine **8** and **c)** fluorinated copper phthalocyanine **14**.

Wang and co–workers have reported two diketopyrrolopyrrole (DPP)–based oligomers appended with 3–ethylrhodanine (**16**) and dicyano–2–vinyl (**17**) (**Figure**

**3.4a**).[18] Optical and electrochemical band gaps of both derivatives were calculated from the UV–Vis absorption and cyclic voltammetry (CV) studies. It was found that oligomer **16** has suitable HOMO and LUMO for the injection of holes and electrons from the Au electrode, whereas the low lying LUMO of **17** favored only electron injection (**Figure 3.4b**). The charge transport properties of **16** and **17** were investigated by using bottom–gate/top–contact (BGTC) OFET devices. As expected, **17** exhibited only electron transporting property ($\mu_e$ = 1.8 × $10^{-2}$ $cm^2V^{-1}s^{-1}$) and a balanced hole ($\mu_h$ = 2.1 × $10^{-2}$ $cm^2V^{-1}s^{-1}$) and electron ($\mu_e$ = 7.2 × $10^{-2}$ $cm^2V^{-1}s^{-1}$) mobility was observed for **16** (**Figure 3.4c–d**). Furthermore, a film of **17** possessed a better lattice orientation and a larger crystalline domain for efficient charge transport as compared to **16**.

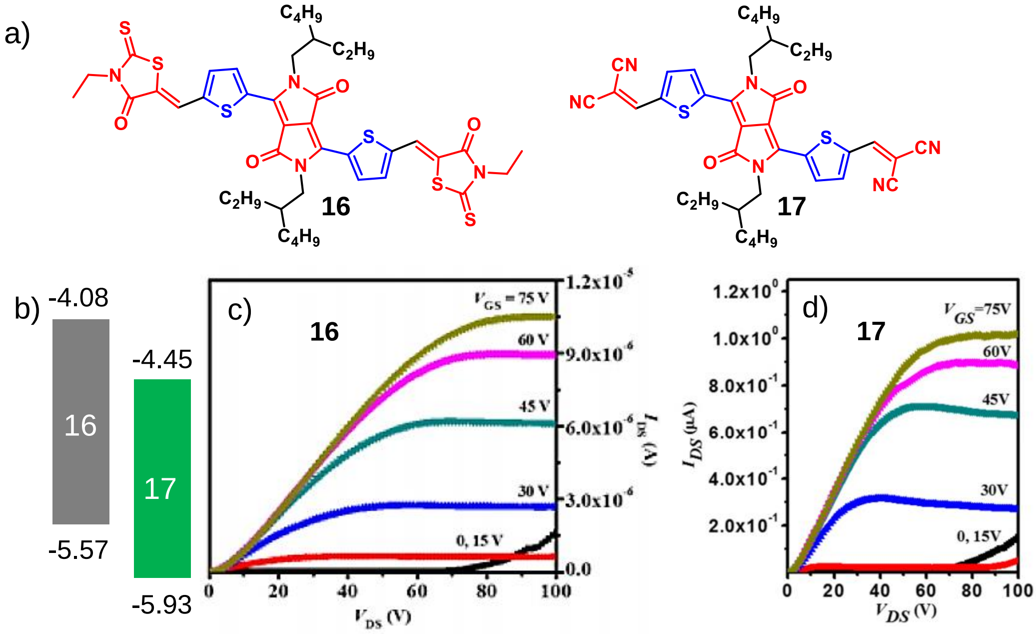

**Figure 3.4. a)** Chemical structures of 3–ethylrhodanine (**16**) and dicyano–2–vinyl (**17**) attached DPP derivatives. **b)** HOMO/LUMO energy levels of **16** and **17.** Output characteristics of the oligomer **c) 16** and **d) 17**.

With the above literature precedence, we have decided to study the charge carrier polarity modulation in small organic semiconductors by introducing different functional groups at the terminus of the molecule. For this purpose, we designed a

$\pi$–conjugated D–A oligomer with DPP as the acceptor and bithiophene as the donor.[19–21] Among different electron–accepting moieties, DPP has been intensively investigated due to several characteristic features including planarity, high crystallinity, excellent photostability, enhanced charge carrier mobility, etc.[22–24] A number of DPP based oligomers and polymers are reported with high unipolar and ambipolar charge carrier mobilities.[25–29] However, switching the charge carrier mobility in oligomers *via* small synthetic modifications is by far less explored.[30,31] With this objective in mind, we designed an aldehyde containing D–A system that would give rise to either a p–type or n–type semiconductor upon careful terminal substitution. Three derivatives, **DPP–Amide** (**27**), **DPP–Ester** (**28**) and **DPP–DCV** (**29**) were obtained *via* simple Knoevenagel condensation of the corresponding precursors with the aldehyde **DPP–CHO**. All three derivatives are low band gap semiconductors capable of facile injection of both electrons and holes. FP–TRMC measurements confirmed that the n–type charge carrier mobility of these derivatives increased with the increase in acceptor strength. Further, FET characteristics confirmed the switching in polarity from p– to n–type *via* fine tuning of the acceptor strength.

## 3.3. Results and Discussion

### 3.3.1. Synthesis of DPP Derivatives

**DPP–CHO** (**22**) was synthesized by a multistep synthetic procedure as represented in **Scheme 3.1**.[32] **DPP–Amide** (**27**), **DPP–Ester** (**28**) and **DPP–DCV** (**29**) were obtained *via* simple Knoevenagel condensation reaction of **DPP–CHO** (**22**) with 2–cyano–*N*–dodecylacetamide (**25**), ethyl cyanoacetate (**23**) and malononitrile (**26**), respectively, in good yields (**Scheme 3.1**). All the molecules after purification, were characterized by various analytical techniques such as $^{1}$H NMR, $^{13}$C NMR, IR and HRMS. Excellent photostability and solubility in most of the common organic solvents were also confirmed for all these derivatives.

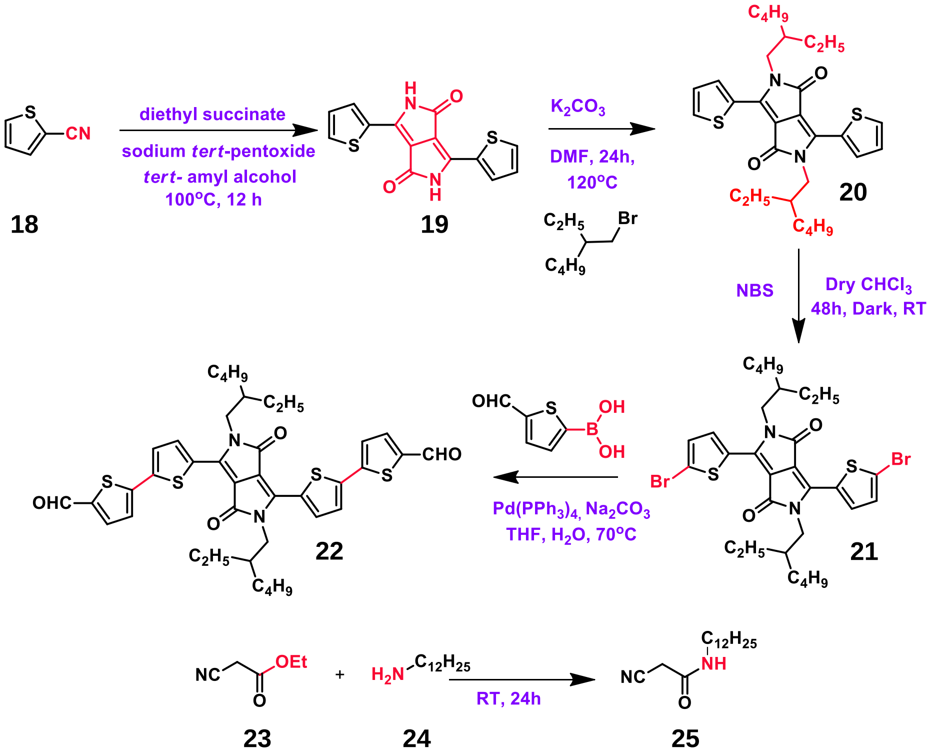

**Scheme. 3.1.** Synthetic protocol adopted for the synthesis of the **DPP–CHO** (**22**).

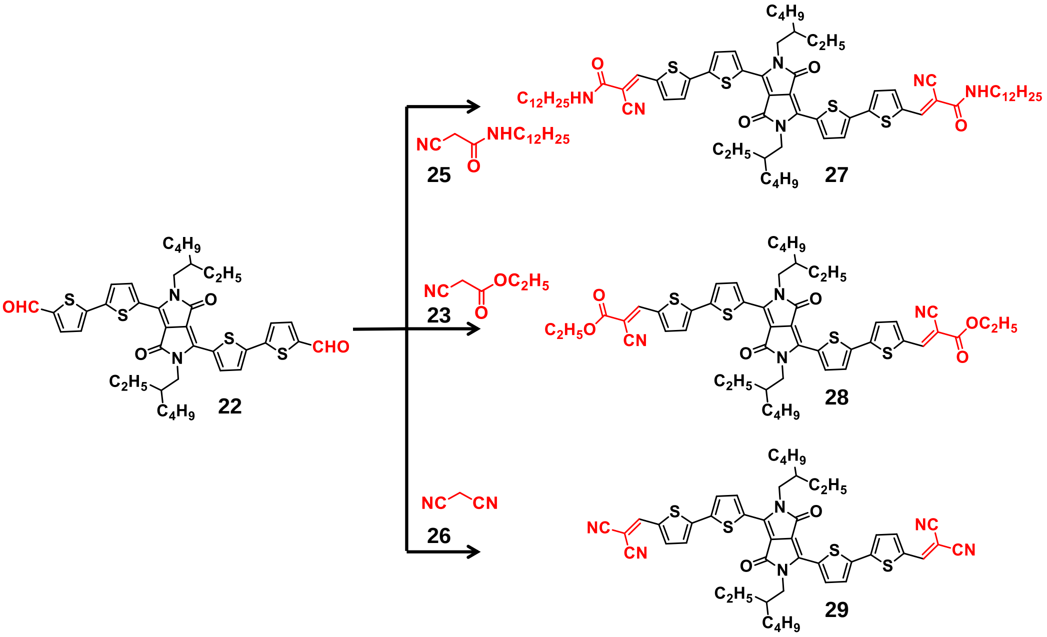

**Scheme. 3.2.** Synthesis of the DPP–derivatives **27–29** *via* Knoevenagel condensation reaction in presence of piperidine as a base.

## 3.3.2. Thermal Characterization

The thermal properties of the three derivatives were investigated by thermogravimetric analysis (TGA) and differential scanning calorimetry (DSC). It was found that **DPP–Amide**, **DPP–Ester** and **DPP–DCV** have high thermal stabilities with a decomposition temperature of 350°C, 320°C and 355°C, respectively, under nitrogen atmosphere (**Figure 3.5a**). Despite of having the same π– conjugated backbone, these derivatives exhibited different thermal behavior in DSC. **DPP–Ester** melts at 255°C that is much higher than the melting points for **DPP–Amide** (214°C) and **DPP–DCV** (234°C), with a sharp exothermic recrystallization peak (**Figure 3.5b**). Unlike **DPP–Amide** and **DPP–Ester**, **DPP–DCV** showed an endothermic peak at 203°C and an exothermic peak at 193°C in addition to melting and crystallization, indicating the possibilities for a phase transition. However, no mesogen formation was observed under polarized optical microscope (POM) upon heating or cooling.

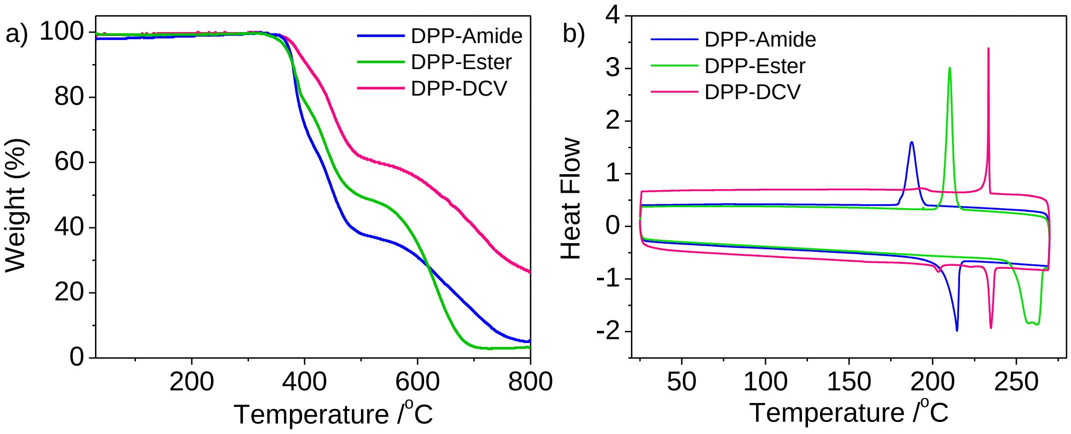

**Figure 3.5. a)** TGA and **b)** DSC of **DPP–Amide**, **DPP–Ester** and **DPP–DCV**.

## 3.3.3. Photophysical Characterization

The UV–visible absorption spectra of the oligomers were recorded in solution as well as in the film state (**Figure 3.6a**). In solution (chloroform), all the derivatives exhibited similar absorption profiles with a relatively less intense absorption band at 400–500 nm corresponding to π–π* transition and an intense and broad internal charge transfer (ICT) band at 600–700 nm.[33] A gradual red shift in absorption maximum was observed with the increase in acceptor strength from amide to ester to cyano side chains.[34] Solid state samples were prepared by spin coating a chloroform solution (4 mg/mL) of the respective derivative. **DPP–Amide** and **DPP–Ester** exhibited almost similar absorption profile as in solution with a small red shift and broadening, whereas a highly red shifted strong aggregation band was observed at 811 nm for **DPP–DCV** (**Figure 3.6b**). This observation can be attributed to the formation of strong J–type aggregation in the condensed solid state for **DPP–DCV** with respect to **DPP–Amide** and **DPP–Ester**.[35] The optical band gaps were estimated for all the derivatives from the absorption onset and a decrease in optical band gap was observed with increase in acceptor strength.

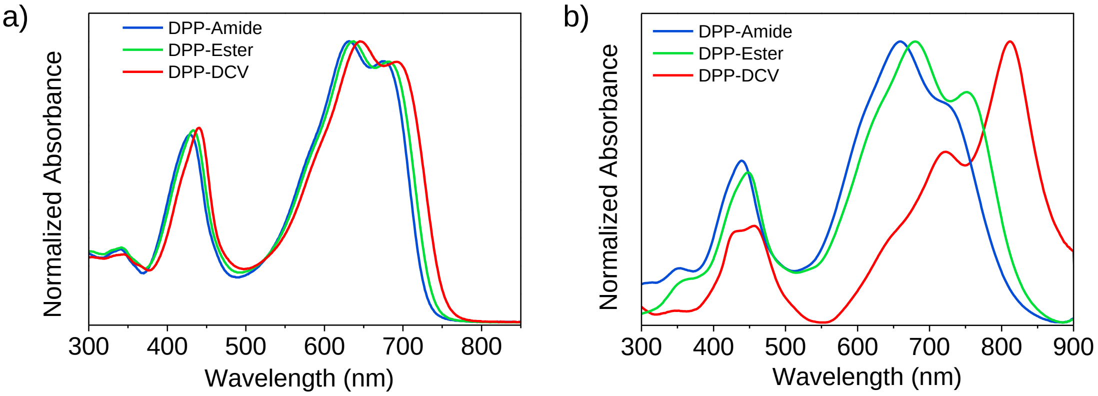

**Figure 3.6.** Normalized absorption of the **DPP–Amide**, **DPP–Ester** and **DPP–DCV** in the **a)** solution (chloroform) and **b)** film state.

### 3.3.4. Frontier Molecular Orbital (FMO) Calculations

Frontier molecular orbital (FMO) energies of **DPP–Amide**, **DPP–Ester**, **DPP–DCV**, **P3HT** and **PC$_{71}$BM** were estimated by using photoelectron yield spectroscopy (PYS) and absorption spectroscopy (**Figure 3.7a**).[36] It was observed that the highest occupied molecular orbital (HOMO) estimated from PYS decreased gradually with increase in acceptor strength. The HOMO for **DPP–Amide** and **DPP–Ester** were estimated to be –5.62 eV and –5.64 eV, respectively, however for **DPP–DCV** it was found to be much lower at –5.81 eV (**Figure 3.7b**).

From the optical band gap, the lowest unoccupied molecular orbitals (LUMO) for all the derivatives were calculated and similar trends as in the HOMO were observed. The lowest value for LUMO was estimated for **DPP–DCV** due to the high electron withdrawing effects of dicyanovinyl unit.[32] Similarly, the energy levels of **P3HT** (donor) and **PC$_{71}$BM** (acceptor) were also estimated. **P3HT** and **PC$_{71}$BM** are well known for their respective p–type or n–type charge transporting properties. We incurred that it may be possible to predict the charge carrier polarities of **DPP–Amide**, **DPP–Ester** and **DPP–DVC** from the photoconductivity measurement by mixing them with **P3HT** or **PC$_{71}$BM**.

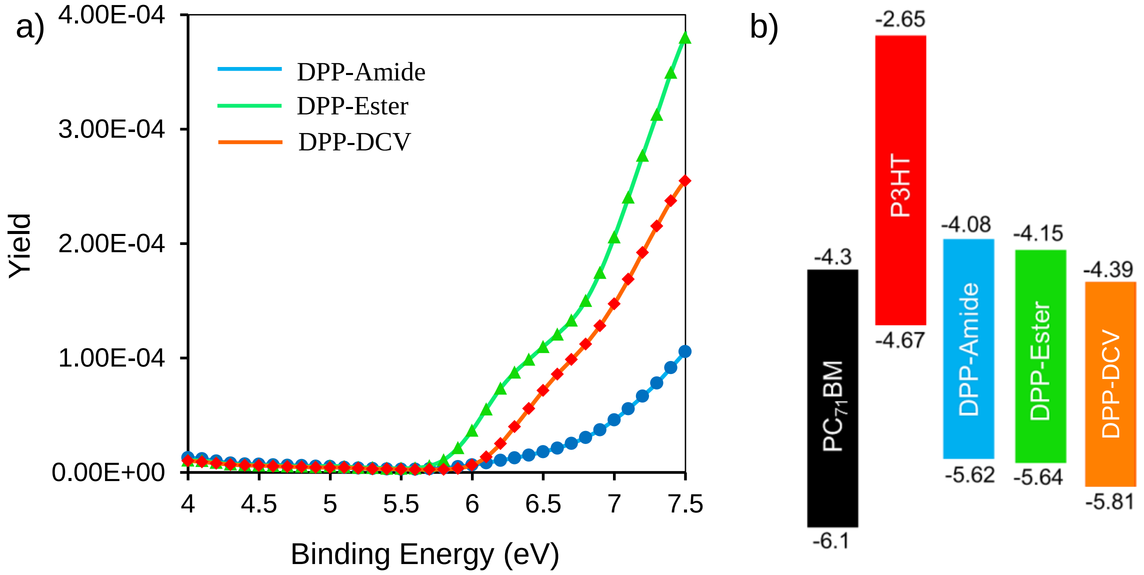

**Figure 3.7. a)** Photo yield spectra of **DPP–Amide**, **DPP–Ester** and **DPP–DCV** in their film state. **b)** Energy level diagram of all the DPP derivatives, **P3HT** and **PC$_{71}$BM**.

### 3.3.5. DFT Calculations

Before going to the estimation of photoconductivity for all the derivatives, we have performed time dependent density functional theory (TD–DFT) calculations for all the derivatives in order to gain more insights into their electronic properties. For reasons related to computational time and costs, the branched and long alkyl chains were replaced with methyl groups. All molecules under study were found to be almost planar and their HOMO and LUMO wave functions were completely delocalized over the π–surface (**Figure 3.8**). The HOMO of all the derivatives was centered mostly over the DPP and the adjacent thiophene units. Compared to **DPP–Amide** and **DPP–Ester**, the LUMO of **DPP–DCV** was found to be more delocalized over the π–surface, in agreement with the strong electron withdrawing nature of the dicyanovinyl units. Hence, **DPP–DCV** may be expected to possess better electron transport properties.

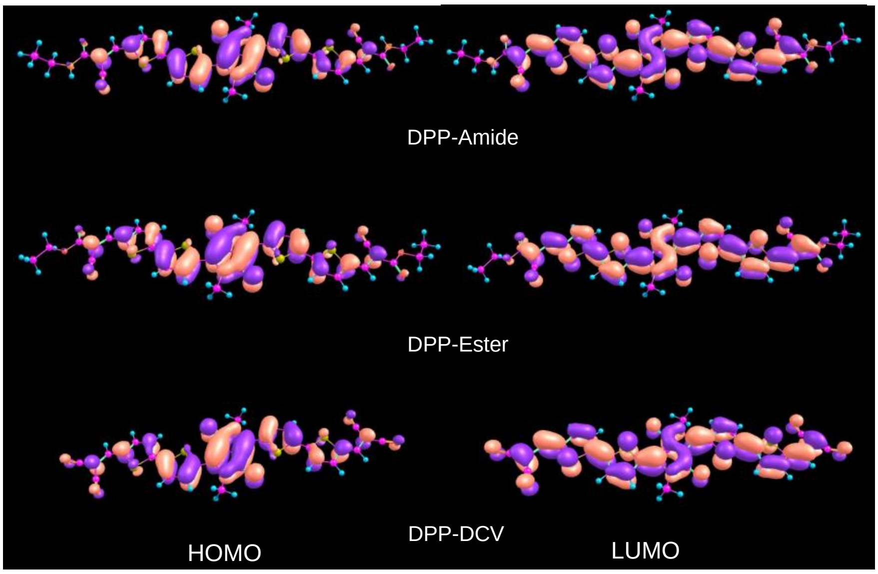

**Figure 3.8.** Energy minimized structures of **DPP–Amide**, **DPP–Ester** and **DPP–DCV** with their corresponding HOMO and LUMO levels. Alkyl side chains were replaced by methyl group for simplicity.

### 3.3.6. Transient Photoconductivity Studies

Prior to the fabrication of the OFETs, intrinsic charge carrier mobility of the synthesized DPP derivatives was estimated by FP–TRMC, using a 355 nm laser as the excitation source. FP–TRMC is a fast and reliable electrodeless technique, which provides a measure of photoconductivity as $\phi\sum\mu$, where $\phi$ is the charge carrier generation quantum yield and $\sum\mu$ is the sum of charge carrier mobilities, i.e., the sum of electron and hole mobilities ($\mu_e$ and $\mu_h$, respectively).[37–39] The photoconductivities of the pristine **DPP–Amide**, **DPP–Ester** and **DPP–DCV** in their film state were determined by FP–TRMC. A film of **DPP–Amide** processed from toluene exhibited higher $\phi\sum\mu$ with respect to a film processed from chloroform, indicating the significance of amide H–bonding in intrinsic charge carrier mobility. To estimate the hole mobility of all the DPP derivatives, three films were prepared by mixing them with **$PC_{71}BM$** (1:1 weight ratio) in chloroform. The blend of **$PC_{71}BM$** with **DPP–Amide** and **DPP–Ester** showed enhancement in $\phi\sum\mu$ with respect to pristine **DPP–Amide** and **DPP–Ester** (**Figure 3.9a, b**). Although both of them have similar LUMO, the increase in $\phi\sum\mu$ is rather significant for **DPP–Amide** than **DPP–Ester**, probably due to its better hole mobility of **DPP–Amide**. In contrast, the blend of **DPP–DCV** and **$PC_{71}BM$** showed a decrease in $\phi\sum\mu$ when compared to pristine **DPP–DCV** (**Figure 3.9c**), most likely a result of restricted electron transfer from its low lying LUMO to **$PC_{71}BM$** due to unfavorable energetics.

In order to understand the electron transport properties of all the DPP derivatives, three films were prepared by mixing them with an electron donor (**P3HT**, 1:1 weight ratio) in chlorobenzene. All the films exhibited an increase in photoconductivity with respect to the corresponding DPP derivatives, as electron transfer is highly energetically favored from **P3HT** to DPP derivatives. Also, **P3HT** is known to have high hole transporting property. Maximum photoconductivity was observed for the blend of **DPP–DCV**:**P3HT** ($5.3 \times 10^{-3}$ $cm^2V^{-1}s^{-1}$, **Figure 3.9c**) followed by **DPP–Ester**:**P3HT** ($2.3 \times 10^{-3}$ $cm^2V^{-1}s^{-1}$, **Figure 3.9b**) and **DPP–Amide**:**P3HT** ($7.5 \times 10^{-4}$ $cm^2V^{-1}s^{-1}$, **Figure 3.9a**). Since, all the DPP derivatives have very low lying LUMO as compared to that of **P3HT**, one can expect that the extent of electron transfer would be almost the same for all the derivatives. Hence, the enhancement in $\phi\sum\mu$ is attributed mainly to the increase in hole and electron mobilities. To summarize this data, we have plotted the values of $\phi\sum\mu$ for all the DPP derivatives (**Figure 3.9d**). With respect to **P3HT**, all the DPP derivatives behaved as n–type material and **DPP–DCV** had the highest electron mobility among all the three derivatives. Both **DPP–Amide** and **DPP–Ester** showed enhancement in $\phi\sum\mu$, in presence of **$PC_{71}BM$** as well as **P3HT**, suggesting that these derivatives have the ability to transport both electrons and holes. However, a closer look into the data revealed that **DPP–Amide** has more of a p–type character than **DPP–Ester**, as **DPP–Ester** exhibited a 3–fold increase in $\phi\sum\mu$ as compared to **DPP–Amide** in presence of **P3HT**.

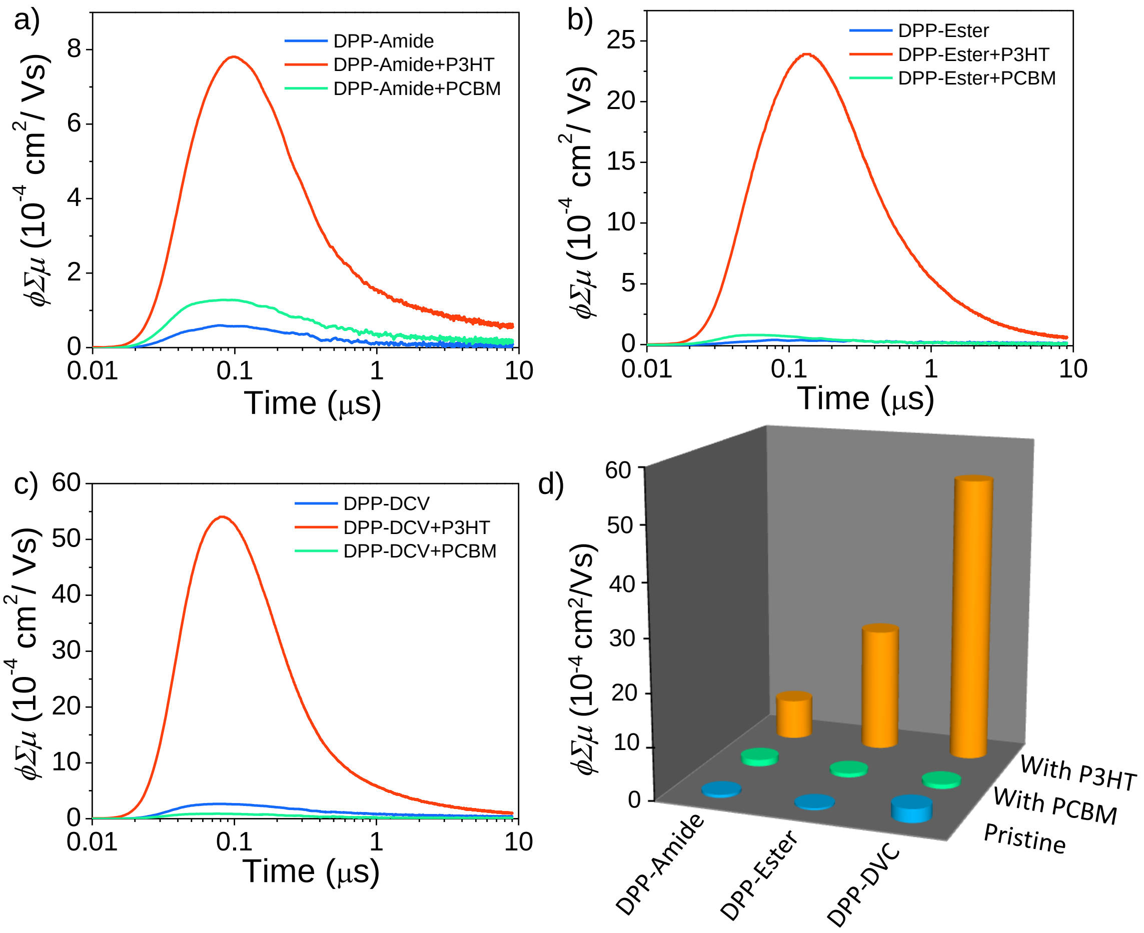

**Figure 3.9.** FP–TRMC transients of **a) DPP–Amide**, **DPP–Amide:P3HT** and **DPP–Amide:PC$_{71}$BM**, **b) DPP–Ester**, **DPP–Ester:P3HT** and **DPP–Ester:PC$_{71}$BM**, and **c) DPP–DCV**, **DPP–DCV:P3HT** and **DPP–DCV:PC$_{71}$BM**. **d)** Comparison of $\phi\sum\mu$ values of all the DPP derivatives in presence and absence of **P3HT** and **PC$_{71}$BM**.

### 3.3.7. Field–Effect Transistor Characteristics

In order to estimate the exact charge carrier mobilities of all the DPP derivatives, we fabricated bottom–gate/top–contact (BGTC) OFETs with the architecture: Al/benzocyclobutene(BCB)/hexamethyldisilazane(HMDS)/oligomer/Au.

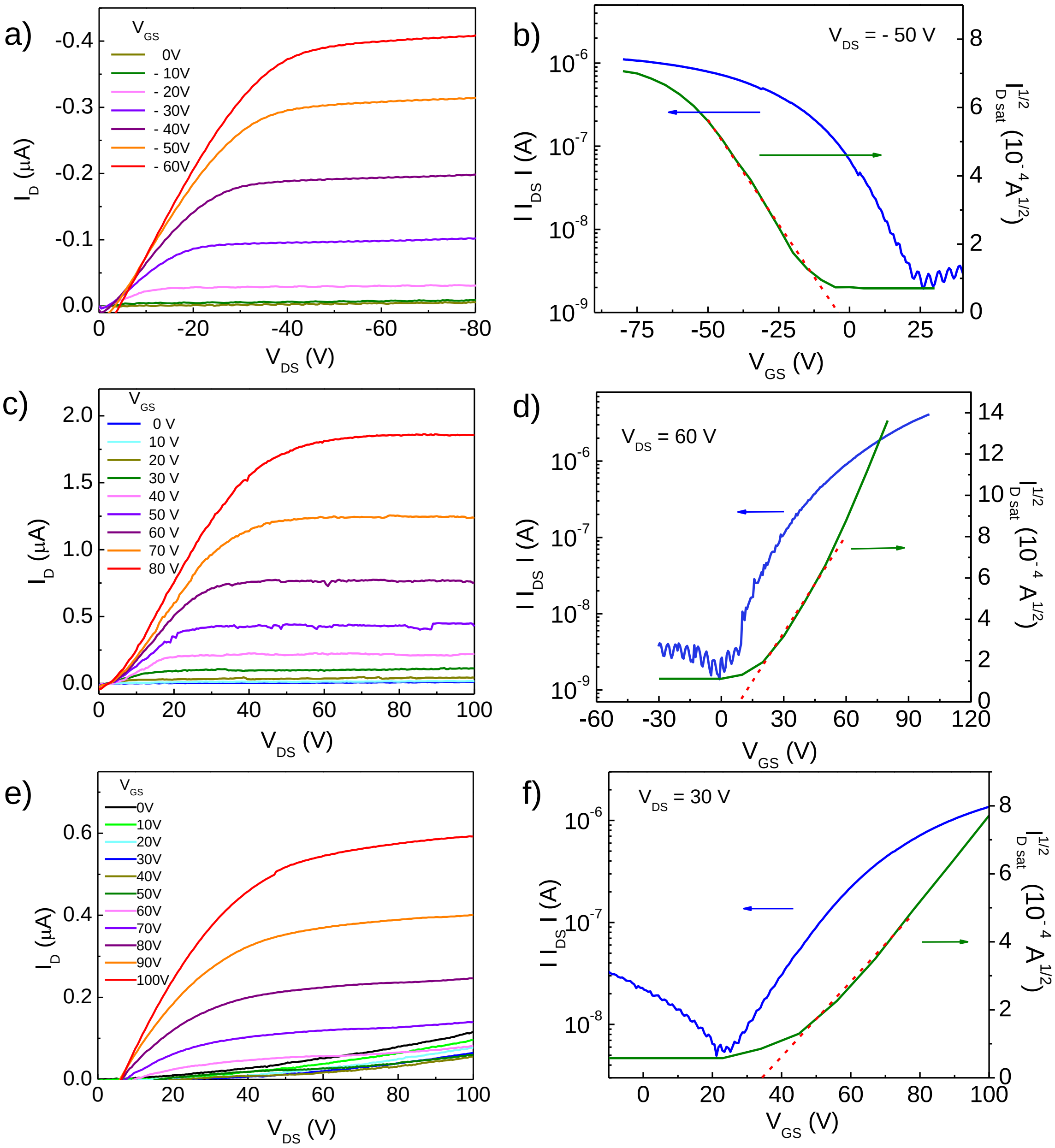

**Figure 3.10.** Output (left) and transfer (right) characteristics of the OFETs based on HMDS–modified substrates upon thermal annealing at 120 °C. Output characteristics of **a) DPP–Amide**, **c) DPP–Ester** and **e) DPP–DCV** and transfer characteristics of the **b) DPP–Amide**, **d) DPP–Ester** and **f) DPP–DCV**.

Aluminium was deposited over a cleaned glass substrate (gate electrode) and benzocyclobutene (BCB) was used as the dielectric material. The BCB surface was further modified by a self–assembled monolayer of hexamethyldisilazane (HMDS). The semiconductor layers were deposited by spin–coating a solution of the corresponding DPP derivative (**DPP–Ester** and **DPP–DCV** in chloroform and **DPP–Amide** in toluene) over the HMDS modified substrate. Finally, Au source and drain electrodes were deposited and the channel length ($L$) and width ($W$) of the devices were estimated as 50 µm and 2 mm, respectively. The charge carrier mobilities of all the devices were estimated in the linear as well as in the saturation current regimes. Maximum mobilities were obtained for all the devices upon thermal annealing at 120 °C and the corresponding output and transfer characteristics are presented in **Figure 3.10**.

**DPP–Amide** exhibited only p–type transport behavior with a maximum hole mobility of $0.9 \times 10^{-2}$ $cm^2V^{-1}s^{-1}$ (**Figure 3.10a,b**). From the output and transfer characteristics, it was evident that both **DPP–Ester** and **DPP–DCV** exhibited an n–type character (**Figure 3.10c–f**). Better electron transport properties were observed for **DPP–Ester** ($1.45 \times 10^{-2}$ $cm^2V^{-1}s^{-1}$) as compared to **DPP–DCV** ($1 \times 10^{-2}$ $cm^2V^{-1}s^{-1}$). Also, the threshold voltage was higher for **DPP–DCV** ($V_T = 40$ V) with respect to the other two derivatives, probably due to the larger roughness of the **DPP–DCV** film. The charge carrier mobilities ($\mu$), threshold voltage ($V_T$) and current on/off ratios for the different derivatives are summarized in **Table 3.1**. These results confirm that switching the charge carrier polarity of the DPP derivatives was achieved *via* simple chemical modification of the terminal functional groups.

| Sl. No. | Molecule | Polarity | Mobility ($cm^2$ / V s ) | | $I_{ON}$ / $I_{OFF}$ | Threshold voltage |
|---|---|---|---|---|---|---|
| | | | Saturation regime | Linear regime | | |
| 1 | DPP– Amide | p–type | $0.91 \times 10^{-2}$ | $0.89 \times 10^{-2}$ | $1.19 \times 10^{3}$ | 4.35 V |
| 2 | DPP– Ester | n–type | $1.48 \times 10^{-2}$ | $3.72 \times 10^{-2}$ | $3.35 \times 10^{3}$ | 8.6 V |
| 3 | DPP–DCV | n–type | $1.05 \times 10^{-2}$ | $3.32 \times 10^{-2}$ | $0.43 \times 10^{3}$ | 40 V |

**Table 3.1.** Summary of the OFET device characteristics for **DPP–Amide**, **DPP–Ester** and **DPP–DCV**.

### 3.3.8. Morphological Analysis

Morphological analysis of the active layer of the semiconductor molecules were performed in order to understand the effect of annealing on molecular organization before and after annealing using atomic force microscopy (AFM). Fiber like morphology was obtained for **DPP–Amide** (**Figure 3.11a**) which did not change even after annealing at 120 °C (**Figure 3.11d**). These types of aggregates are known to have better charge transport properties due to the presence of continuous charge percolation pathways. **DPP–Ester** formed a uniform film with very low roughness (**Figure 3.11b**) and negligible changes in morphology was observed upon thermal annealing (**Figure 3.11e**). In contrast, **DPP–DCV** initially formed ill–defined structures with very high roughness (**Figure 3.11c**), which were converted to lower sized aggregates upon thermal annealing (**Figure 3.11f**). Morphological analysis corroborates the results obtained from FET measurements.

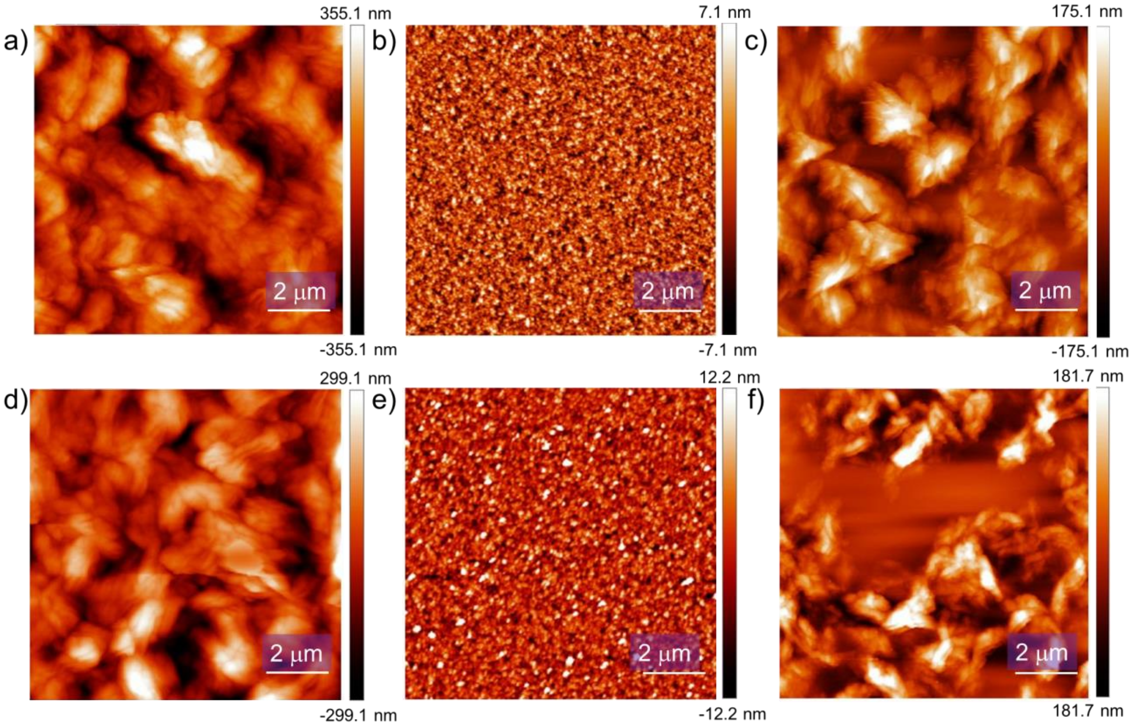

**Figure 3.11.** AFM images of **a) DPP–Amide**, **b) DPP–Ester** and **c) DPP–DCV** active layers before thermal annealing and **d) DPP–Amide**, **e) DPP–Ester** and **f) DPP–DCV** active layers after thermal annealing.

### 3.3.9. Molecular Packing

To investigate molecular packing of the DPP derivatives in their film states, wide angle X–ray scattering (WAXS) measurements were performed. For **DPP–Amide,** a sharp peak was observed at a lower $2\theta$ with a *d*–spacing of 19.36 Å (100) along with a few smaller peaks having reciprocal *d*–spacing ratio of 1:2:3, indicating a lamellar organization (**Figure 3.12a**).[33] A broad peak at higher $2\theta$ (~25°) confirmed the presence of strong $\pi$–stacking (010) interactions between the chromophores with a distance of 3.57 Å. All these interactions were retained after annealing at 120 °C, indicating the excellent thermal stability of the molecular organization. Similarly, **DPP–Ester** also formed lamellar organization as calculated from the reciprocal *d*–spacing ratio, however a broad peak at $2\theta \sim 4°$ (100) indicated a rather poor long range ordering. **DPP–Ester** exhibited better $\pi$–stacking (3.47 Å) than **DPP–Amide** and thermal annealing led to only slight changes in the diffraction pattern (**Figure 3.12a**). Based on the information gathered from the WAXS analysis, a plausible molecular packing of **DPP–Amide** and **DPP–Ester** are presented in **Figure 3.12b** and **c**. In line with morphological analysis, **DPP–DCV** showed a drastic change in molecular packing upon thermal annealing. Annealing resulted in the sharpening of certain diffraction peaks at lower $2\theta$ (*d*–spacing 11.6 Å). The change in the peak intensities as well as disappearance of certain peaks can be corroborated to temperature induced variations in molecular packing. In fact, a conversion of the initially less ordered aggregates into more ordered crystalline packing, upon annealing, was evident (**Figure 3.12a**). However, from these diffractograms, it is difficult to define the molecular packing of **DPP–DCV** before and after thermal annealing.

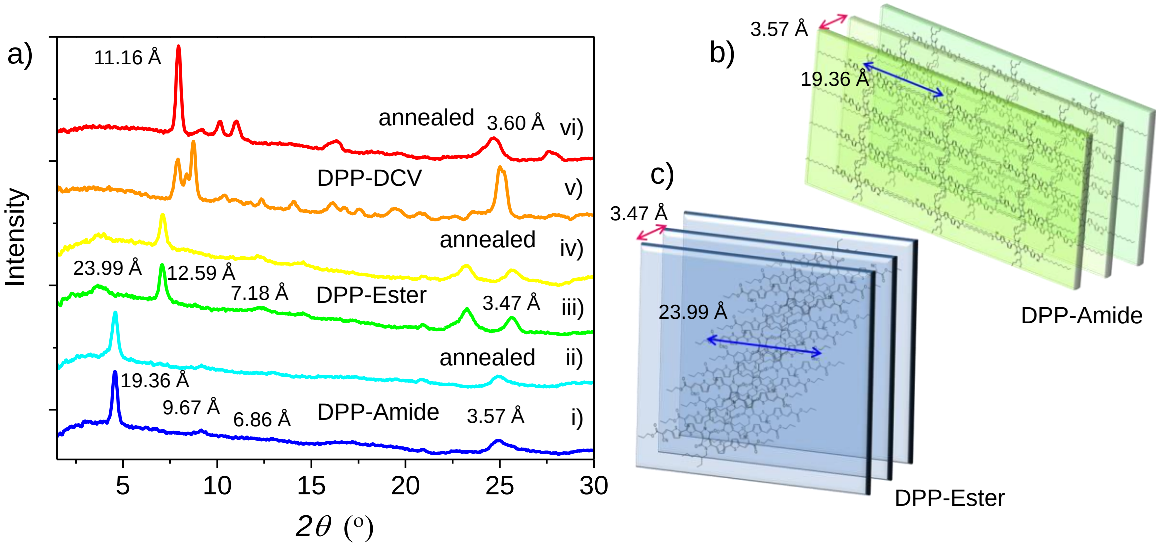

**Figure 3.12. a)** WAXS of **i) DPP–Amide**, **iii) DPP–Ester** and **v) DPP–DCV** films before and **ii) DPP–Amide**, **iv) DPP–Ester** and **vi) DPP–DCV** films after thermal annealing. Probable molecular organization in **b) DPP–Amide** and **c) DPP–Ester**.

## 3.4. Conclusion

In conclusion, we have demonstrated the change in the charge carrier polarity of diketopyrrolopyrrole (DPP)–based D–A molecules that differ only in their terminal functional groups. These molecules exhibited very broad absorption and low optical band gaps. FP–TRMC measurements of these derivatives upon mixing with

**P3HT** and **PC$_{71}$BM** confirmed that a small increase in acceptor strength is sufficient to modulate the charge transport properties from p– to n–type. These results were further supported by FET measurements and it was found that **DPP–Amide** exhibited a moderate p–type mobility ($0.9 \times 10^{-2}$ cm$^2$V$^{-1}$s$^{-1}$), whereas good n–type mobilities were observed for **DPP–Ester** ($1.45 \times 10^{-2}$ cm$^2$V$^{-1}$s$^{-1}$) and **DPP–DCV** ($1 \times 10^{-2}$ cm$^2$V$^{-1}$s$^{-1}$). These high charge carrier mobilities were the results of the uniform packing of the molecules and the resultant morphology as confirmed by AFM and WAXS analyses. The terminal functionalization approach presented here is a simple method to alter the charge carrier polarity of the molecules.

## 3.5. Experimental Section

### 3.5.1. Materials and Methods

### UV Photoelectron Yield Spectroscopy (PYS)

PYS measurements were performed on a Sumitomo Heavy Industry Co. PCR–202. For this measurement, DPP derivatives were spin–coated on an ITO–coated glass surface from a chloroform solution. The solvent was completely removed under vacuum before mounting on to the spectrometer. Photoelectrons emitted from the film was detected after illuminating the film with UV irradiation. The photoelectron counts were measured with a systematic increase in photon energy at intervals of 0.1 eV.

### Flash–Photolysis Time Resolved Microwave Conductivity (FP–TRMC)

A resonant cavity was used to obtain a high degree of sensitivity in the conductivity measurements. The resonant frequency and microwave power were set at ~ 9.1 GHz and 3 mW, respectively, so that the electric field of the microwave was sufficiently small to not disturb the motion of charge carriers. The third harmonic generation (THG; 355nm) of a Nd:YAG laser (Continuum Inc., Surelite II, 5 −8 ns pulse duration, 10 Hz) was used as an excitation source. The laser power was fixed at 2.5 mJ $cm^{-2}$ $pulse^{-1}$ for all excitation wavelengths (incident photon density, $I_0 = 4.6 \times 10^{15}$ photons $cm^{-2}$ $pulse^{-1}$). An in–house–built Xe–flash lamp (10 μs pulse duration, 10 Hz) with a power of 0.3 mJ $cm^{-2}$ $pulse^{-1}$ was used for the Xe–flash TRMC experiments. For the attenuation of excitation light energy, neutral density filters were used for both Xe–flash and laser–flash TRMC. In the case of laser–flash TRMC, the photoconductivity transient $\Delta\sigma$ is converted to the product of the quantum efficiency: $\phi$ and the sum of charge carrier mobilities, $\Sigma\mu$, by $\phi\Sigma\mu = \Delta\sigma\ (eI_0F_{light})^{-1}$, where e and $F_{light}$ are the unit charge of a single electron and a correction (or filling) factor.

## OFET Fabrication and Characterization

Bottom–gate/ top–contact (BGTC) configuration was adopted for device fabrication. A glass substrate was cleaned ultrasonically in deionized water, acetone, and isopropyl alcohol for 10 min, blown dry by nitrogen gas, and coated with aluminium as the gate electrode. Benzocyclobutene (BCB) was used as the dielectric material and the surface was further modified with a self–assembled monolayer of hexamethyldisilazane (HMDS). The molecules were dissolved in chloroform (**28** and **29**) and toluene (**27**) to form solutions with a concentration of 5 mg/mL. Uniform thin films were obtained over a substrate upon spin coating at 800 rpm for 1 minute followed by annealing at 120 °C for 10 minutes on a hot plate under nitrogen atmosphere. The source/ drain gold contacts were thermally evaporated onto the thin film with a transistor channel of length (L) of 50 μm and width (W) of 2 mm using a shadow mask. All the electrical characteristics of the OFET were measured by using the Keithley SCS 4200 parameter analyzer in vacuum.

### 3.5.2. Synthesis and Characterization

#### Synthesis of 3,6–Di(thiophen–2–yl)pyrrolo[3,4–c]pyrrole–1,4(2H,5H)–dione (19)

A 250 mL two–necked flask connected to a condenser was charged with a stir bar. Sodium *tert*–pentoxide (20.0 g, 182 mmol) and *tert*–amyl alcohol (30.0 mL) were added under an argon atmosphere and was heated at 100 °C until the mixture became homogeneous (~1 h.). The mixture was then cooled to 60 °C and thiophene–2–carbonitrile **18** (10.0 g, 91.61 mmol) was added. Diethyl succinate (7.9 g, 45.77 mmol) in *tert*–amyl alcohol (10.0 mL) was added dropwise to the reaction mixture over 2 h, leading the solution to turn dark purple. The reaction contents were vigorously stirred at 100 °C for 10 h, and then acidic MeOH (40.0 mL MeOH and 20.0 mL glacial acetic acid) was added at room temperature to neutralize the reaction mixture. Again the reaction mixture was heated to 70 °C and filtered when hot through a Buchner funnel (Whatman filter paper). A dark red solid cake of **19** (15.0 g) was obtained which was dried in a vacuum oven at 100 °C, and was used in the next step without further purification.

#### Synthesis of 2,5–bis(2–ethylhexyl)–3,6–di(thiophen–2 yl)pyrrolo [3,4–c]pyrrole–1,4(2H,5H)–dione (20)

In a two–necked 250 mL round bottom flask, **19** (3.0 g, 10 mmol) and anhydrous activated $K_2CO_3$ (8.28 g, 60 mmol) were added and the mixture was degassed three times. Degassed anhydrous *N*,*N*–dimethylformamide (DMF, 50.0 mL) was injected into the mixture and heated to 120 °C under argon for 1 h. 2–Ethylhexyl bromide (4.8 mL, 25 mmol) was added dropwise over a period of 2 h using a syringe, and stirred for 24 h at 120 °C. The reaction mixture was then allowed to cool down to room temperature, poured into ice cold water (150 mL) and stirred for 30 min. The aqueous mixture was then extracted with $CHCl_3$ and dried over anhydrous $Na_2SO_4$ and the solvent was removed under reduced pressure. The crude product was purified by column chromatography (chloroform as eluent), to obtain **20** as a purple–brown powder (4.2 g, 66%). $^1$H–NMR (500 MHz, $CDCl_3$) δ:

8.89 (d, $J$ = 8 Hz, 2H, Ar–H), 7.63 (d, $J$ = 4.5 Hz, 2H, Ar–H), 7.26 (t, $J$ = 4.5 Hz, 2H, Ar–H), 4.12–4.06 (m, 4H, $–NCH_2–$), 1.86 (t, $J$ = 8 Hz, 2H, $–N–CH_2–CH–$), 1.36–1.22 (m, 16H), 1.45–1.13 (m, 32H, $–CH_2–$), 0.93–0.86 (m, 12H, $–CH_3$). $^{13}$C–NMR (125 MHz, $CDCl_3$) δ: 157.4, 136.0, 131.3, 126.7, 125.8, 124.6, 103.7, 45.9, 39.2, 30.3, 28.4, 23.6, 23.2, 14.1, 10.6. MALDI–TOF: m/z 524.67 (100%). Exact Mass: 524.25.

### Synthesis of 3,6–Bis(5–bromothiophen–2–yl)–2,5–bis(2ethyl hexyl) [3,4–c]pyrrole 1,4(2H,5H)–dione (21)

The molecule **20** (2.0 g, 3.8 mmol) was dissolved in dry chloroform (100 mL) in a 250 mL two–necked flask in the dark. *N*–bromosuccinimide (1.5 g, 8.38 mmol) was added in small portions over 30 min. After stirring at room temperature for 48 h, the reaction mixture was poured into ice cold water (200 mL) and extracted with chloroform (3 × 60 mL). The organic phase was washed with brine (2 × 100 mL), dried over anhydrous $Na_2SO_4$ and the solvent was evaporated under reduced pressure. The dark–red residue was purified by column chromatography using (chloroform as eluent) to yield **21** as a red solid (1.80 g, 72%). $^1$H–NMR (500 MHz, $CDCl_3$) δ: 8.67 (d, $J$ = 3 Hz, 2H, Ar–H), 7.24 (d, $J$ = 7 Hz, 2H, Ar–H), 3.92–3.86 (m, 4H, $–NCH_2–$), 1.92–1.88 (m, 2H, $–N–CH_2–CH–$), 1.36–1.25 (m, 16H), 0.93–0.87 (m, 12H). $^{13}$C–NMR (125 MHz, $CDCl_3$) δ: 161.0, 138.9, 135.1, 131.5, 131.2, 118.9, 108.0, 46.1, 39.2, 30.3, 28.4, 23.7, 23.2, 14.2, 10.6. MALDI–TOF: m/z 682.63 (100%). Exact Mass: 680.07.

### Synthesis of 5',5'''–(2,5–bis(2–ethylhexyl)–3,6–dioxo–2,3,5,6 tetrahydropyrrolo[3,4–c]pyrrole–1,4–diyl)bis(([2,2'–bithiophene] –5–carbaldehyde)) (22)

To a 100 mL two–necked round bottom flask, **21** (0.50 g, 0.73 mmol), $Pd^0(PPh_3)_4$ (50.0 mg, 0.01 mmol), and $Na_2CO_3$ (2.66 g, 25.16 mmol) were added under inert atmosphere inside a glove box and the system was sealed with a condenser. Then degassed THF (10 mL) and degassed water (5 mL) were added to the reaction mixture and heated to 45 °C for 30 min. A solution of 5–formylthiophen–2–yl boronic acid (0.4 g, 2.52 mmol) in degassed THF (25 mL) was added slowly, and the mixture was refluxed for another 12 h, till a blue coloration was observed. After cooling to room temperature, the mixture was extracted with $CH_2Cl_2$ (100 mL) and dried over anhydrous $Na_2SO_4$. The organic extracts were combined and the solvent was removed in vacuo. The residue was purified by column chromatography on silica ($CH_2Cl_2$/ethyl acetate 1/70, v/v) to give **22** as a black solid (0.3 g, 55%). $^1$H–NMR (500 MHz, $CDCl_3$) δ: 9.90 (s, 2H, Ar–CHO), 8.94 (d, *J* = 6.5 Hz, 2H, Ar–H), 7.73 (d, *J* = 6.5 Hz, 2H, Ar–H), 7.49 (d, *J* = 7 Hz, 2H, Ar–H), 7.40 (d, *J* = 7 Hz, 2H, Ar–H), 4.06 (t, *J* = 8.0 Hz, 4H, –$NCH_2$–), 1.92–1.88 (m, 2H, –N–$CH_2$–CH–), 1.36–1.25 (m, 16H), 0.93–0.86 (m, 12H). $^{13}$C–NMR (125 MHz, $CDCl_3$) δ: 182.3, 161.0, 145.0, 143.1, 140.9, 138.9, 137.0, 130.4, 128.1, 127.1, 125.5, 109.0, 46.0, 39.1, 30.3, 28.2, 23.7, 23.1, 14.2, 10.6. MALDI–TOF: m/z 745.79 (100%). Exact Mass: 744.22.

## Synthesis of *N*–Dodecylcyanoacetamide (25)

*n*–Dodecylamine (6.13 g, 33.1 mmol) was added to ethyl cyanoacetate (23.0 mL, 216 mmol) in a two–necked stoppered round bottom flask and warmed slightly. Upon stirring the mixture for 1 h at room temperature, formation of a white precipitate was observed. After 17 h, the precipitate was filtered off, washed with ethanol and diethyl ether and recrystallized from ethanol to yield a colorless solid. Concentration of the mother liquor and recrystallization of the residue from ethanol gave the pure product **25** (5.4 g, 64%), m.p. 82–83°C. $^1$H–NMR (500 MHz, $CDCl_3$) δ: 6.15 (s, 1H, N–H), 3.37 (s, 2H, CN–$CH_2$), 3.30 (d, *J* = 7.2 Hz, 2 H, –NH–$CH_2$–), 1.60–1.54 (m, 2H, –NH–$CH_2$–$CH_2$), 1.40–1.20 (m, 18 H, –$(CH_2)_9CH_3$), 0.88 ppm (t, *J* = 6.9 Hz, 3H, –$CH_3$).

### Synthesis of (2E,2'E)–3,3'–(5',5'''–(2,5–bis(2–ethylhexyl)–3,6–dioxo–2,3,5,6–tetrahydropyrrolo[3,4–c]pyrrole–1,4–diyl)bis(2,2'–bithiophene–5',5–diyl))bis(2–cyano–N–dodecylacrylamide) (27)

The molecules **22** (0.10 g, 0.13 mmol) and **25** (0.15 g, 0.60 mmol) were added to a 100 mL two–necked round bottom flask under argon atmosphere. Freshly distilled dry THF (20 mL) and piperidine (1.0 mL) were then added to the above mixture and heated at reflux under argon atmosphere for 6 h, when a green coloration was observed. After cooling to room temperature, THF was removed under reduced pressure. Then the residue was extracted with $CHCl_3$ (100 mL) and the solvent was removed in vacuo. The residue was purified by column chromatography on silica ($CHCl_3$:ethyl acetate 10:1, v:v) followed by precipitation in $CHCl_3$/MeOH to give **27** as a black solid (0.10 g, 70%). $^1$H–NMR (500 MHz, $CDCl_3$) δ: 8.93 (d, *J* = 4 Hz, 2H, Ar–H), 8.34 (s, 2H, –C=CH–), 7.65 (d, *J* = 4.5 Hz, 2H, Ar–H), 7.45 (d, *J* = 4 Hz, 2H, Ar–H), 7.35 (d, *J* = 7 Hz, 2H, Ar–H), 6.29 (t, *J* = 6 Hz, 2H, –NH–), 4.09–3.99 (m, 4H, –$NCH_2$–), 3.50–3.43 (m, 4H, –NH–$CH_2$–), 1.92–1.87 (m, 2H, –N–$CH_2$–CH–), 1.45–1.38 (m, 18H), 1.13–1.30 (m, 38H), 0.92 (t, *J* = , 6H), 0.89–0.85 (m, 12H). $^{13}$C–NMR (125 MHz, $CDCl_3$) δ: 161.0, 160.2, 143.9, 143.5, 140.9, 138.8, 136.4, 130.4, 127.1, 125.7, 117.1, 109.1, 100.5, 46.0, 42.2, 31.8, 30.3, 29.9, 29.5, 29.4, 29.4, 29.2, 29.1, 29.0, 28.2, 26.7, 23.7, 23.1, 22.5, 14.2, 13.9. MALDI–TOF: m/z calculated for $C_{70}H_{96}N_6O_4S_4$ 1212.64 and found 1213.50.

### Synthesis of (2E,2'E)–diethyl 3,3'–(5',5'''–(2,5–bis(2–ethylhexyl) 3,6–dioxo–2,3,5,6–tetrahydropyrrolo[3,4–c]pyrrole–1,4 diyl)bis(( [2,2'–bithiophene]–5',5–diyl)))bis(2–cyanoacrylate) (28)

The compounds **22** (0.10 g, 0.13 mmol) and **26** (0.05 g, 0.75 mmol) were added to a 100 mL two–necked round bottom flask under argon atmosphere. Freshly distilled dry THF (20 mL) and piperidine (1.0 mL) were added and heated at 60 °C to reflux under argon atmosphere for 6 h. The green colored solution obtained was cooled to room temperature and THF was removed under reduced pressure. Then the residue was extracted with $CHCl_3$ (100 mL) and the solvent was removed in vacuo. The residue was purified by column chromatography on silica ($CHCl_3$:ethyl acetate 10:1, v:v) followed by precipitation in $CHCl_3$/MeOH to give **28** as a black solid (0.12 g, 80%). $^1$H–NMR (500 MHz, $CDCl_3$) δ: 8.94 (d, *J* = 4 Hz, 2H, Ar–H), 7.80 (s, 2H, –C=CH–), 7.71 (d, *J* = 3.5 Hz, 2H, Ar–H), 7.55 (d, *J* = 4 Hz, 2H, Ar–H), 7.43 (d, *J* = 7 Hz, 2H, Ar–H), 4.10–4.01 (m, 4H, –$NCH_2$–), 1.96–1.90 (m, 2H, –N–$CH_2$–CH–), 1.40–1.27 (m, 18H), 0.94–0.86 (m, 12H). $^{13}$C–NMR (125 MHz, $CDCl_3$) δ: 160.9, 160.1, 143.8, 143.5, 140.9, 138.82, 136.3, 130.3, 127.1, 125.6, 117.1, 109.1, 100.5, 46.2, 39.1, 31.8, 30.3, 29.5, 29.4, 28.2, 26.7, 23.1, 22.5, 14.2. MALDI–TOF: m/z calculated for $C_{50}H_{54}N_4O_6S_4$ 935.25 and found 936.7.

### Synthesis of 2,2'–((5',5'''–(2,5–bis(2–ethylhexyl)–3,6–dioxo 2,3, 5,6–tetrahydropyrrolo[3,4–c]pyrrole–1,4–diyl)bis([2,2'–bithio phene] 5',5–diyl))bis(methanylylidene))dimalononitrile (29)

Compound **22** (0.10 g, 0.13 mmol) and **23** (0.10 g, 0.88 mmol) were added to a 100 mL two–necked round bottom flask under argon atmosphere. Freshly distilled dry THF (20 mL) and piperidine (1.0 mL) were added and heated to reflux under argon atmosphere for 6 h, resulting in a green colored solution. After cooling to room temperature, THF was removed under reduced pressure. Then the residue was extracted with $CHCl_3$ (100 mL) and the solvent was removed in vacuo. The residue was purified by column chromatography on silica ($CHCl_3$:ethyl acetate 10:1, v:v) followed by precipitation in $CHCl_3$/MeOH to give **29** as a black solid (0.12 g, 75%). $^1$H–NMR (500 MHz, $CDCl_3$) δ: 8.94 (d, *J* = 4 Hz, 2H, Ar–H), 8.28 (s, 2H, –C=CH–), 7.40 (d, *J* = 3.5 Hz, 2H, Ar–H), 7.50 (d, *J* = 4 Hz, 2H, Ar–H), 7.39 (d, *J* = 7 Hz, 2H, Ar–H), 4.41–4.36 (q, *J* = 6 Hz, 4H, –O–$CH_2$), 4.10–4.01 (m, 4H, –$NCH_2$–), 1.96–1.90 (m, 2H, –N–$CH_2$–CH–), 1.42–1.37 (m, 4H), 1.36–1.28 (m, 18H), 0.94–0.86 (m, 12H). $^{13}$C–NMR (125 MHz, $CDCl_3$) δ: 160.9, 160.1, 143.8, 143.5, 140.9, 138.8, 136.3, 130.3, 127.1, 125.6, 117.1, 109.1, 100.5, 46.2, 39.1, 30.3, 28.2, 23.7, 23.1, 14.2, 10.6. MALDI–TOF: m/z calculated for $C_{46}H_{44}N_6O_2S_4$ 841.14 and found 842.4.

## 3.6. References

[1] H. Sirringhaus, *Adv. Mater.* **2014**, *26*, 1319.

[2] X. Huang, C. Tan, Z. Yin, H. Zhang, *Adv. Mater.* **2013**, *25*, 6158.

[3] C. Wang, H. Dong, W. Hu, Y. Liu, D. Zhu, *Chem. Rev.* **2012**, *112*, 2208.

[4] S. Allard, M. Forster, B. Souharce, H. Thiem, U. Scherf, *Angew. Chem. Int. Ed.* **2008**, *47*, 4070.

[5] J. Mei, Y. Diao, A. L. Appleton, L. Fang, Z. Bao, *J. Am. Chem. Soc.* **2013**, *135*, 6724.

[6] P. M. Beaujuge, J. M. J. Fréchet, *J. Am. Chem. Soc.* **2011**, *133*, 20009.

[7] C. B. Nielsen, M. Turbiez, I. McCulloch, *Adv. Mater.* **2013**, *25*, 1859.

[8] K. Takimiya, I. Osaka, M. Nakano, *Chem. Mater.* **2014**, *26*, 587.

[9] J. E. Anthony, A. Facchetti, M. Heeney, Seth R. Marder, X. Zhan, *Adv. Mater.* **2010**, *22*, 3876.

[10] K. Takimiya, S. Shinamura, I. Osaka, E. Miyazaki, *Adv. Mater.* **2011**, *23*, 4347.

[11] J. T. E. Quinn, J. Zhu, X. Li, J. Wang, Y. Li, *J. Mater. Chem. C* **2017**, 5, 8654.

[12] S. Ando, J–I Nishida, E. Fujiwara, H. Tada, Y. Inoue, S. Tokito, Y. Yamashita, *Chem. Mater.* **2005**, *17*, 1261.

[13] K. Zhou, H. Dong, H–L Zhang, W. Hu, *Phys. Chem. Chem. Phys.* **2014**, *16*, 22448.

[14] B. Balan, C. Vijayakumar, A. Saeki, Y. Koizumi, Shu Seki, *Macromolecules* **2012**, *45*, 2709.

[15] C. R. Bridges, C. Guo, H. Yan, M. B. Miltenburg, P. Li, Y. Li, D. S. Seferos, *Macromolecules* **2015**, *48*, 5587.

[16] X. Feng, L. Liu, Y. Honsho, A. Saeki, S. Seki, S. Irle, Y. Dong, A. Nagai, D. Jiang, *Angew. Chem. Int. Ed.* **2012**, *51*, 2618.

[17] H. Jiang, P. Hu, J. Ye, Y. Li, H. Li, X. Zhang, R. Li, H. Dong, W. Hu, C. Kloc, *Adv. Mater.* **2017**, 1605053.

[18] S–L Wu, Y–F Huang, C–T Hsieh, B–H Lai, P–S Tseng, J–T Ou, S–T Liao, S–Y Chou, K–Y Wu, C–L Wang, *ACS Appl. Mater. Interfaces* **2017**, *9*, 14967.

[19] M. Tantiwiwat, A. Tamayo, N. Luu, X–D Dang, T–Q Nguyen, *J. Phys. Chem. C* **2008**, *112*, 17402.

[20] H. Bürckstümmer, A. Weissenstein, D. Bialas, Frank Würthner, *J. Org. Chem.* **2011**, *76*, 2426.

[21] S. Ghosh, S. Cherumukkil, C. H. Suresh, A. Ajayaghosh, *Adv. Mater.* **2017**, 1703783.

[22] S. Qu, H. Tian, *Chem. Commun.* **2012**, *48*, 3039.

[23] M. Grzybowski, D. T. Gryko, *Adv. Optical Mater.* **2015**, *3*, 280.

[24] A. Tang, C. Zhan, J. Yao, E. Zhou, *Adv. Mater.* **2017**, *29*, 1600013.

[25] B. Lim, H. Sun, J. Lee, Y–Y Noh, *Sci. Rep.* **2017**, *7*, 164.

[26] W. S. Yoon, S. K. Park, I. Cho, J–A Oh, J. H. Kim, S. Y. Park, *Adv. Funct. Mater.* **2013**, *23*, 3519.

[27] B. Sun, W. Hong, Z. Yan, H. Aziz, Y. Li, *Adv. Mater.* **2014**, *26*, 2636.

[28] V. S. Nair, J. Sun, P. Qi, S. Yang, Z. Liu, D. Zhang, A. Ajayaghosh, *Macromolecules* **2016**, 49, 6334.

[29] J. Yao, C. Yu, Z. Liu, H. Luo, Y. Yang, G. Zhang, D. Zhang, *J. Am. Chem. Soc.* **2016**, *138*, 173.

[30] J. Lee, A–R Han, J. Hong, J. H. Seo, J. H. Oh, C. Yang, *Adv. Funct. Mater.* **2012**, *22*, 4128.

[31] C. Yu, C. He, Y. Yang, Z. Cai, H. Luo, W. Li, Q. Peng, G. Zhang, Z. Liu, D. Zhang, *Chem. Asian J.* **2014**, *9*, 1570.

[32] G. Lin, Y. Qin, J. Zhang, Y–S Guan, H. Xu, W. Xu, D. Zhu, *J. Mater. Chem. C*, **2016**, *4*, 4470.

[33] S. Ghosh, D. S. Philips, A. Saeki, A. Ajayaghosh, *Adv. Mater.* **2017**, *29*, 1605408.

[34] S. Furukawa, H. Komiyama, T. Yasuda, *J. Phys. Chem. C* **2016**, *120*, 21235.

[35] T. Aytun, L. Barreda, A. Ruiz–Carretero, J. A. Lehrman, S. I. Stupp, *Chem. Mater*. **2015**, *27*, 1201.

[36] A. Gopal, A. Saeki, M. Ide, S. Seki, *ACS Sustainable Chem. Eng.* **2014**, *2*, 2613.

[37] S. Seki, A. Saeki, T. Sakurai, D. Sakamaki, *Phys. Chem. Chem. Phys.* **2014**, *16*, 11093.

[38] S. Prasanthkumar, A. Saeki, S. Seki, A. Ajayaghosh, *J. Am. Chem. Soc.* **2010**, *132*, 8866.

[39] S. Prasanthkumar, S. Ghosh, V. C Nair, A. Saeki, S. Seki, A. Ajayaghosh, *Angew. Chem. Int. Ed.* **2015**, *54*, 946.

# Chapter 4

## Nanosheets of an Organic Molecular Assembly from Aqueous Medium : High Solid–State Emission and Anisotropic Charge–Carrier Mobility

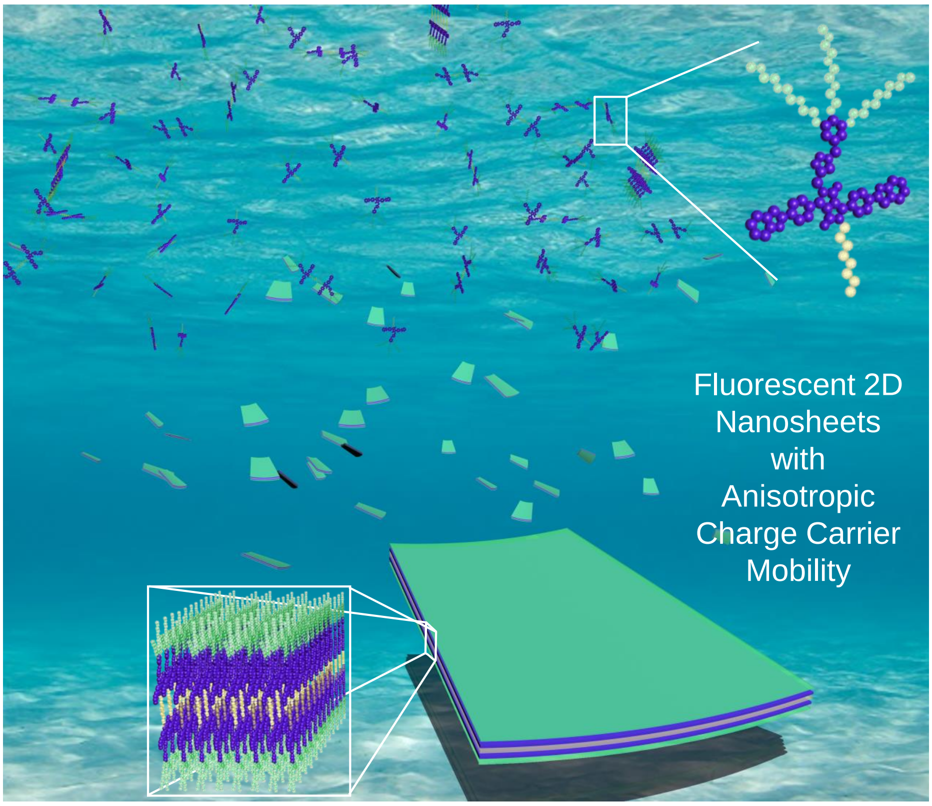

### 4.1. Abstract

*Nature has most of its beautiful assemblies stabilized in water and are highly functional, be it the DNA or the photosystems, both of which sustain life on earth. Thus, water being inexpensive, ubiquitous and environmentally benign, forms the most ideal choice of solvent for self–assembly. In this chapter, we present the self–assembly of a diketopyrrolopyrrole (DPP) oligomer in water to semiconducting nanosheets. The amphiphilic DPP molecule is designed in such a way to have a water loving and water hating side chains, leading to highly anisotropic molecular*

*arrangements. They exhibit high solid state fluorescence quantum yield ($\phi_f$ = 0.54) with superior anisotropic charge carrier mobility of 0.33 $cm^2/Vs$. This value is among the highest reported for various supramolecular assemblies and the observed anisotropy is attributed to the preferential edge–on orientation of the molecule as concluded from the linear dichroism and grazing incidence X–ray diffraction measurements.*

## 4.2. Introduction

The most widely studied 2D nanosheet is graphene, whereas covalent organic frameworks (COFs) and hexagonal boron nitride are the recent additions to this family of nanomaterials.[1–3] These ultrathin, atomic, or sub–nanometer layers of 2D materials are in demand owing to their exceptional electronic, optical, thermal, and mechanical properties with high degree of anisotropy for applications in flexible optoelectronics, catalysis, bioimaging, and energy storage.[4–6] During the past two decades, supramolecular chemistry has been judiciously exploited for the creation of a variety of 0D, 1D, 2D, and 3D nanomaterials.[7–15] In most of the cases, spontaneous self–assembly of organic molecules leads to 1D structures, but preparation of the corresponding 2D nanosheets of a few layer thickness is a challenge.[16–19] 2D sheets of fluorescent molecules are required for display and sensing applications, however, organic 2D nanosheets having high fluorescence quantum yield is difficult to achieve due to the fluorescence self–quenching.[20,21] Another prerequisite for organic 2D and 3D materials is high anisotropic charge–carrier mobility for applications in organic field–effect transistors (OFETs) and organic solar cells.[22,23] Therefore, for flexible organic electronics, it is necessary to have a few layered 2D nanosheets with high fluorescence quantum yield and superior anisotropic charge–carrier properties.

In order to meet the above requirements, creation of oriented, a few layered 2D crystalline organic nanosheets of small $\pi$–conjugated systems engineered *via* non–covalent interactions under aqueous processing conditions is of great demand.[24]

Water mediated self–assembly of amphiphilic π–conjugated molecular building blocks has the potential to create functional supramolecular polymers of defined size, shape, and dimensionality by means of solvophilic and solvophobic interactions.[25–28] In the literature, a few examples have been reported on π–extended donor (D) or acceptor (A) molecules, decorated with hydrophilic groups that form 2D nanosheets in water, exhibiting either p–type or n–type charge transport and light harvesting properties.

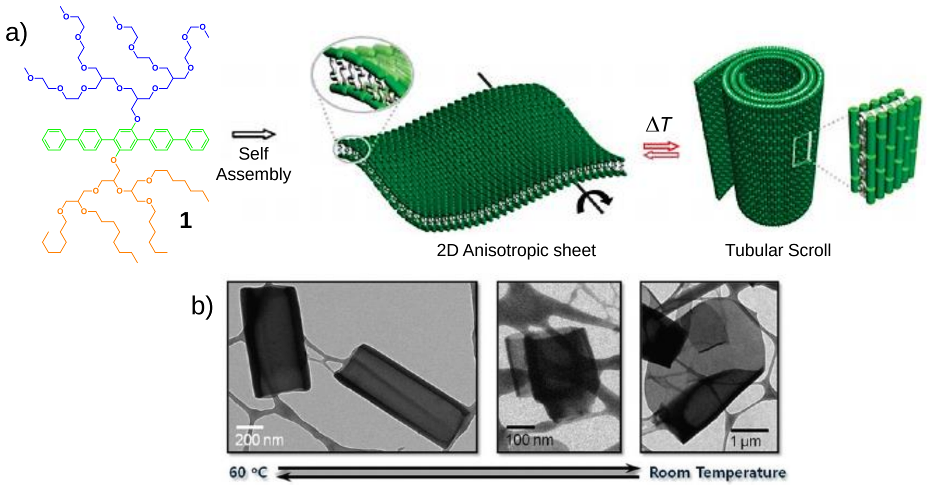

**Figure 4.1. a)** Molecular structure of the amphiphile **1** with schematic representation showing the reversible scrolling of the nanosheet and **b)** the corresponding TEM images.

Lee and co–workers have reported a π–conjugated rod like amphiphile, **1** capable of forming 2D assembly in aqueous medium (**Figure 4.1a**).[29] Aggregate formation was confirmed from the corresponding emission spectra and dynamic light scattering (DLS) experiments. 2D aggregates were observed under the cryo–TEM and AFM, with an average thickness of ~6 nm. Interestingly, these nanosheets rolled up on heating the aqueous solution above a lower critical solution temperature (LCST) of 60°C as evident from SEM and cryo–TEM images (**Figure 4.1b**). Heating causes the dehydration of oligoether chains which eventually decreases the effective hydrophilic volume leading to scrolling of the nanosheets. Upon cooling, the oligoether chains recapture water molecules resulting in the conversion of the tubular aggregates back to nanosheets and the cycles were repeated multiple times. Thus, proper molecular design provides unprecedented opportunities to modulate unique structural transformations in 2D nanomaterials.

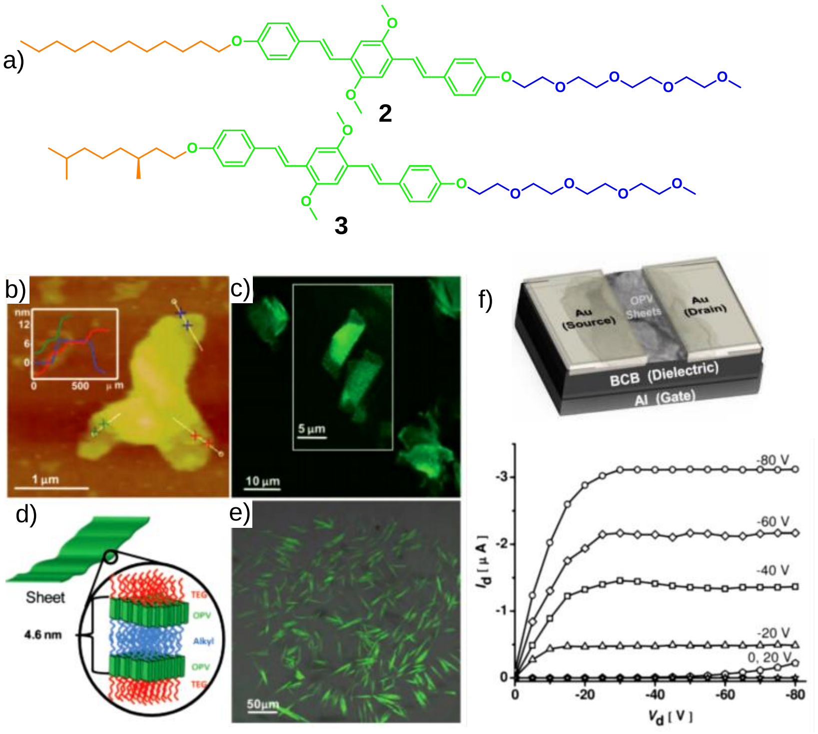

**Figure 4.2. a)** Chemical structures of the amphiphilic OPV **2** and **3**. Morphology of **2** observed under **b)** AFM, **c)** and **e)** confocal microscope, **d)** schematic representation of the probable molecular organization and **f)** OFET output characteristics obtained from a device fabricated by using the nanosheets of **2**.

By adopting a similar design strategy, George and co–workers synthesized amphiphilic oligo(*p*–phenylenevinylene) (OPV) derivatives **2** and **3** which formed free standing nanosheets in water with enhanced hole mobility (**Figure 4.2.a**).[30] The OPV derivative **2** spontaneously formed free standing 2D assemblies in water as confirmed from the confocal microscopy images and the bilayer structure was confirmed from the AFM height profile (**Figure 4.2b–e**). Aggregate formation was monitored from the temperature dependent UV–Vis absorption and circular dichroism (CD) spectroscopies. Mobility was estimated by fabricating OFETs and the maximum hole mobility was obtained for **2** and was estimated to be $8 \times 10^{-3}$ $cm^2V^{-1}s^{-1}$ (**Figure 4.2f**). Thus, amphiphiles are capable of forming ordered supramolecular organization that can facilitate improved charge transporting behavior in molecular assemblies.

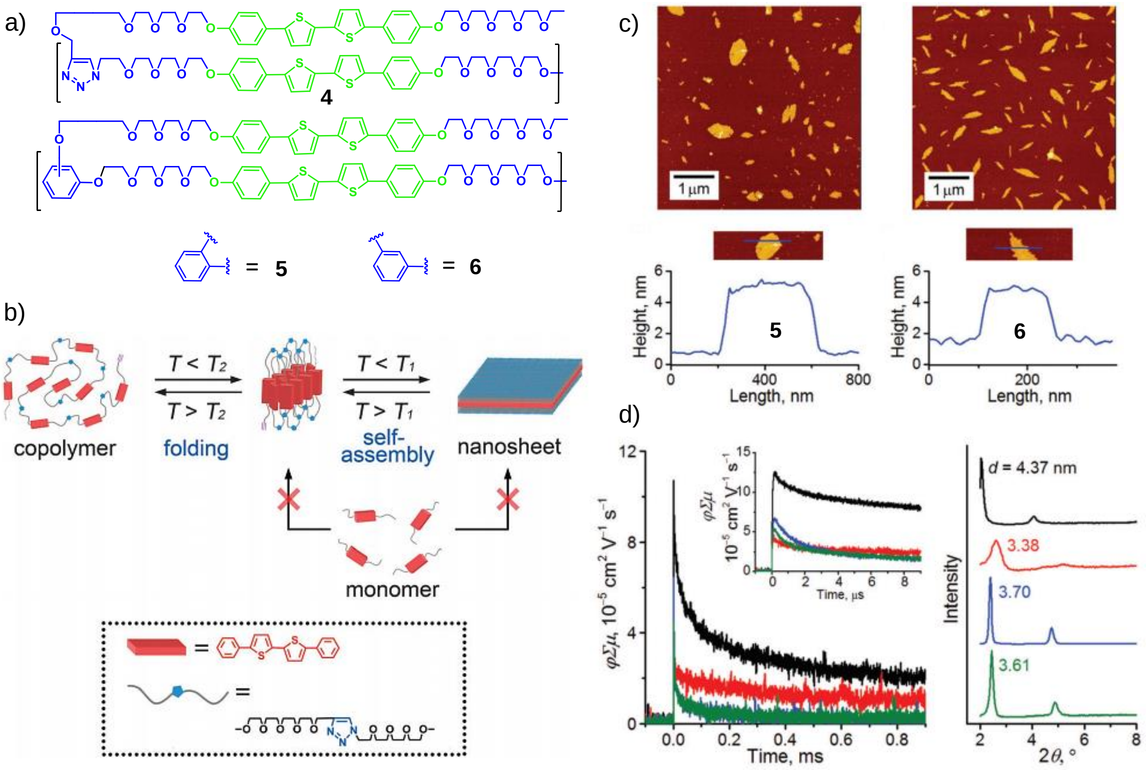

**Figure 4.3.** **a)** Molecular structures of the polymers **4–6** and **b)** schematic representation of the steps involved in the formation of thiophene nanosheet. **c)** AFM images of the nanosheets obtained from the polymers **5** and **6**. **d)** Photoconductivity kinetic traces upon photoexcitation at 355 nm and XRD pattern of the nanosheets obtained from **5** (black) and **6** (red), and drop–cast films of **5** (blue) and **6** (green).

To impart better electroactive characters, Ikeda and coworkers came up with the idea of preparing a supramolecular thiophene nanosheet.[31] An amphiphilic polymer **4** was prepared *via* a copper(I) catalyzed azide–alkyne Huisgen cycloaddition (**Figure 4.3a**). The polymer **4** had high propensity to form aggregates in DCB, DMF, and DMSO as evident from UV–Vis absorption and $^1$H NMR studies. AFM and TEM images showed the presence of micrometer sized nanosheets with a uniform height of 3.5 nm. The steps involved in the formation of supramolecular thiophene nanosheets in the solution is shown in **Figure 4.3b**. These nanosheets were found to possess long as well as short range molecular ordering thereby providing an efficient percolation path for charge transport. Also, surface functionalization mediated by the presence of free acetylene groups present over the surface was possible without disturbing the nanostructures. In a subsequent work, the triazole moiety was replaced with catechol (**5**) and resorcinol (**6)** units, to control the folding as well as molecular packing by inducing changes in the folding angle (**Figure 4.3a**).[32] The polymer **5** showed considerably blue shifted absorption due to the vertical arrangement of the chromophores with respect to the lateral orientation of the nanosheets, whereas the polymer **6** adopted a tilted orientation. Both **5** and **6** formed nanosheets in *o*–dichlorobenzene as evident from AFM images (**Figure 4.3c**). The nanosheets obtained from the polymer **5** had preferential crystalline molecular organization as evident from the XRD analysis (**Figure 4.3d**) and theoretical calculations. As a result, the nanosheets of **5** exhibited maximum intrinsic charge carrier mobility of 1.2 × $10^{-4}$ $cm^2V^{-1}s^{-1}$ as estimated from FP–TRMC.

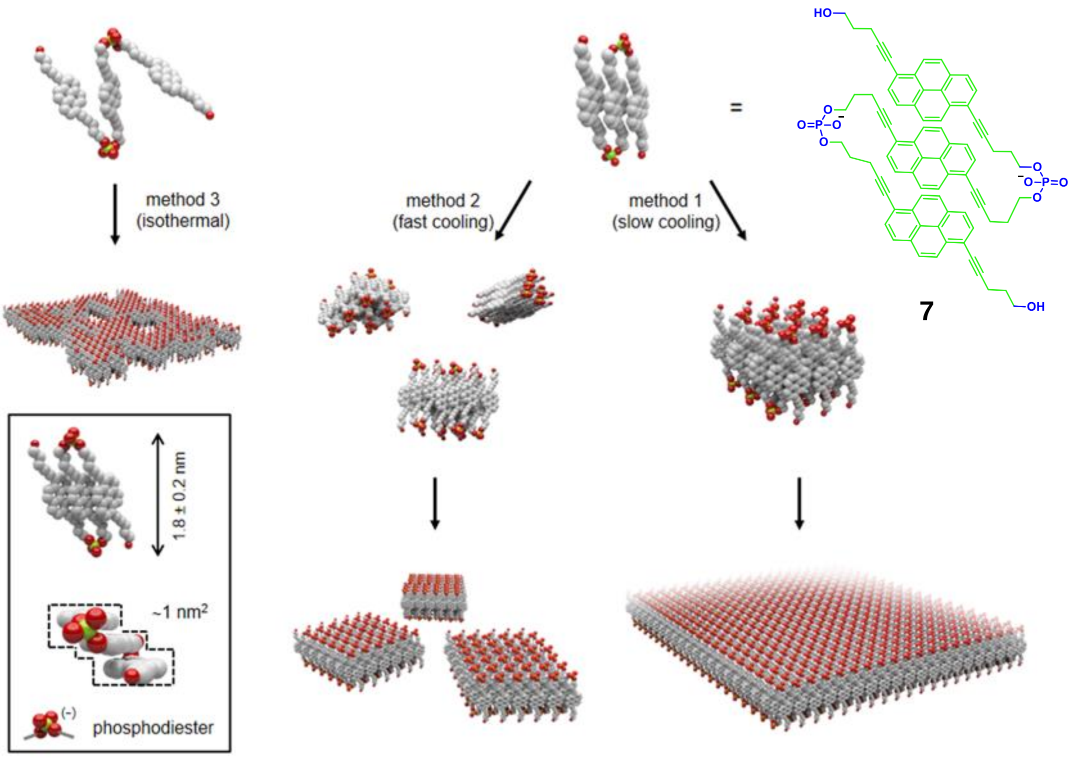

**Figure 4.4.** Structure of the foldamer **7** and the schematic representation of supramolecular nanosheet formation.

Häner and co–workers have reported a very similar pyrene based foldamer **7** where the folding angle is determined by the phosphodiester–linker (**Figure 4.4.**).[33] This amphiphilic oligomer **7** formed 2D supramolecular assemblies in water, with the hydrophobic pyrene unit sandwiched between hydrophilic phosphodiester as seen under AFM. Simultaneous formation of H– and J– aggregates lead to supramolecular polymers as evident from blue and red shifted absorption spectra. Temperature dependent absorption and emission studies confirmed the thermal reversibility of these aggregates. Strong excimer emission was observed at higher temperature which was quenched upon cooling, due to the formation of aggregates. Recently, the same group was successful in creating supramolecular nanosheets with very high aspect ratio by using the same precursor, **7**.[34]

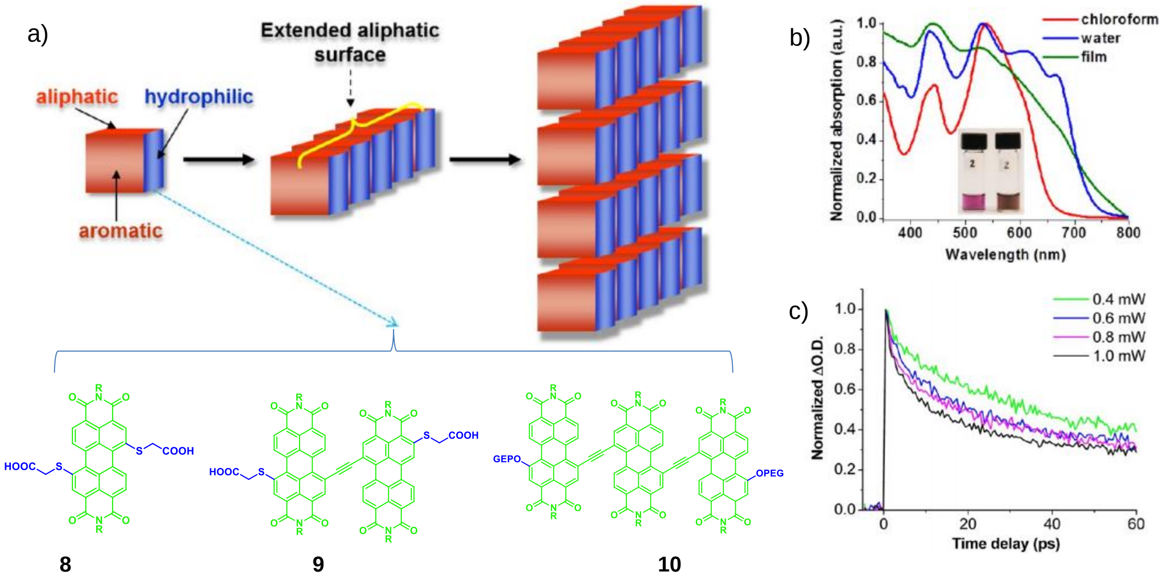

**Figure 4.5. a)** Chemical structures of **8–10** and schematic representation of the assembly formation. **b)** UV–Vis absorption spectra of **9** in the monomer, aggregated and film states. **c)** Transient absorption decay kinetics (probed at 745 nm, normalized) at different laser powers.

Self–assembly of electron accepting molecules are important due to their potential as n–type semiconductors. Rybtchinski and co–workers have reported the preparation of crystalline light harvesting 2D assembly of perylene diimides (PDI).[35] Three amphiphiles (**8**–**10**) bearing one, two and three perylene diimide chromophoric units (**Figure 4.5a**) were synthesized for this purpose. Morphological analyses using cryo–TEM and AFM revealed that all the derivatives formed crystalline 2D assemblies. These nanosheets exhibited broad absorption (**Figure 4.5b**) in the visible region and hence can be used as light harvesting material. The exciton transporting property of the 2D assembly was investigated using femtosecond transient absorption spectroscopy. The 2D supramolecular assembly of **9** exhibited the maximum light harvesting property and the highest exciton diffusion length of 120±10 nm when compared to the other derivatives (**Figure 4.5c**).

These results motivated us to suitably design and develop semiconducting 2D supramolecular nanomaterials based on an efficient chromophoric backbone such as diketopyrrolopyrrole (DPP).[36] Herein, we describe the preparation of 2D nanosheets of a novel amphiphilic D–A–D π–system (**PDPP–Amphi**) that exhibits excellent fluorescence quantum yields and high charge–carrier mobility when self–assembled in aqueous medium. For this purpose, the well–known acceptor, DPP was integrated with two π–bridged benzofuran donor moieties, which provide greater electron delocalization. Janus type substitution by hydrophilic and hydrophobic solubilizing groups in the DPP unit makes it an amphiphile. Due to the amphiphilic nature of the molecule, we were able to grow 2D sheets under organic as well as aqueous conditions. The strong solvophobic interaction facilitates planarization of the molecule, which in turn facilitates the spontaneous formation of lamellar assembly. The water grown 2D assembly of **PDPP–Amphi** is highly emissive ($\Phi_f$ = 0.54) with a high anisotropic intrinsic charge–carrier (electron + hole) mobility of 0.33 $cm^2V^{-1}s^{-1}$, measured by the combination of flash photolysis time–resolved microwave conductivity (FP–TRMC) and transient photocurrent measurements (TPC). Although a few DPP based bola–amphiphiles are reported, none of these systems are known to form strongly emissive 2D nanosheets with such high charge–carrier mobility.

## 4.3. Results and Discussion

### 4.3.1. Synthesis of PDPP–Amphi

We have adopted a multistep synthetic strategy to synthesize the target molecule **PDPP–Amphi** (**18**) (**Scheme 4.1**).[37] The final compound **18** was obtained through click reaction involving the alkyne **15** and the azide **17** under an inert atmosphere in DMF with an yield of 87%. All intermediates and final compound were purified and characterized by nuclear magnetic resonance spectroscopy (NMR), high–resolution mass spectrometry (HRMS), and matrix assisted laser desorption/ionization–time of flight (MALDI–TOF) mass spectrometry.

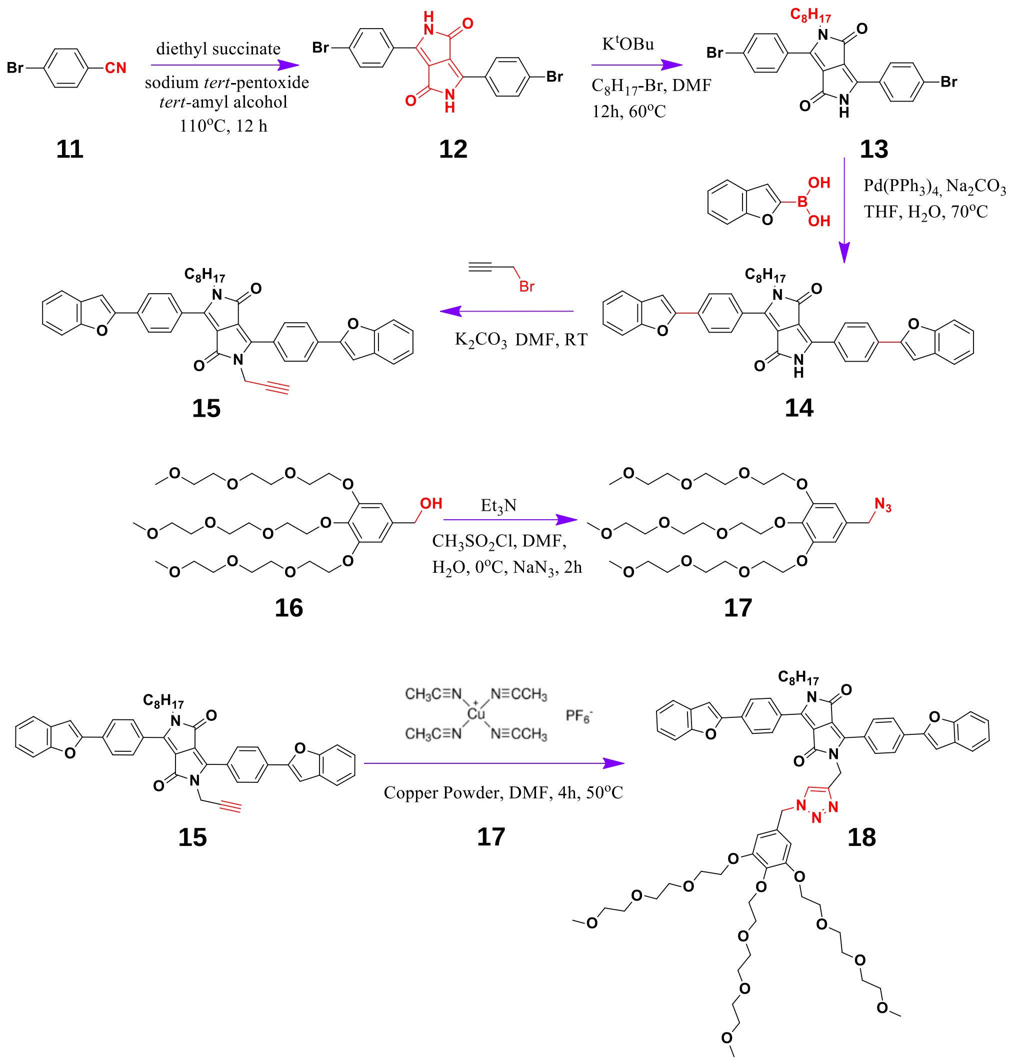

**Scheme. 4.1.** Synthetic protocol adopted for the synthesis of the amphiphile **18**.

## 4.3.2. Thermal Characterization

The thermal properties of **PDPP–Amphi** (**18**) was investigated by differential scanning calorimetry (DSC) and thermogravimetric analysis (TGA). DSC study revealed that the compound **18** does not show any phase transition except melting (167°C) and crystallization (107°C) (**Figure 4.6a**). **PDPP–Amphi** exhibited good thermal stability up to 260°C and 50% decomposition was observed above 400°C under $N_2$ atmosphere which is probably due to the thermal degradation of the soft hydrophilic fragment as shown in **Figure 4.6b, c**.

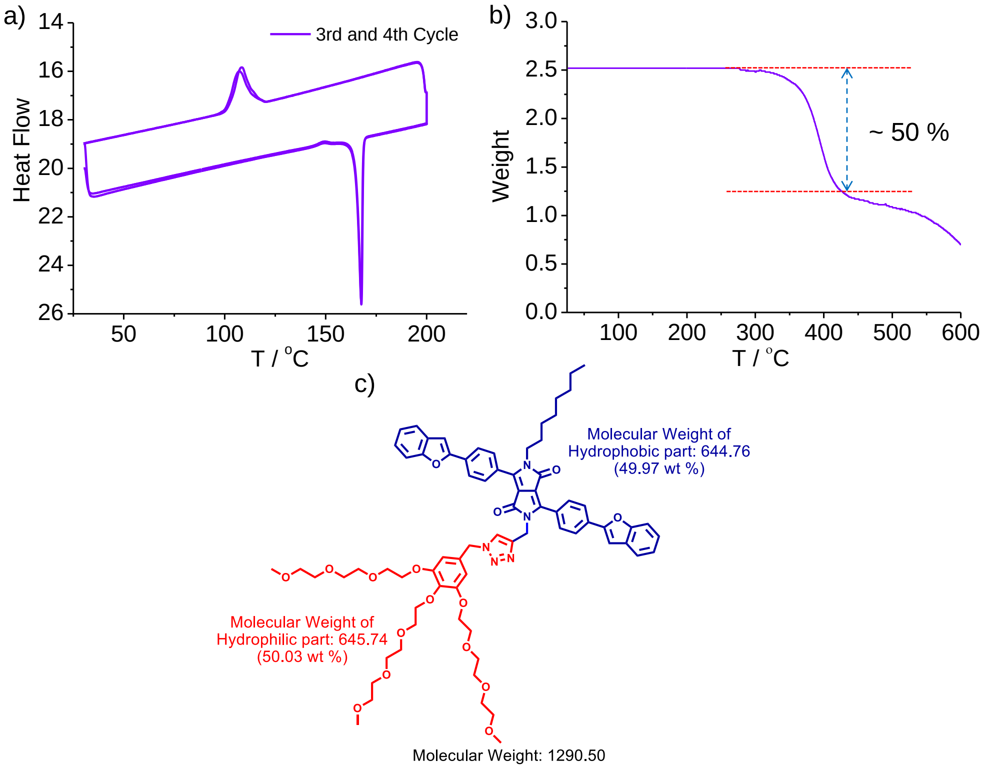

**Figure 4.6.** The **a)** DSC and **b)** TGA profiles of **PDPP–Amphi**. **c)** The chemical structure of **PDPP–Amphi** showing the molecular weight of hydrophilic and hydrophobic part, justifying the weight loss in TGA.

## 4.3.3. Photophysical Characterization

In chloroform, **PDPP–Amphi** ($c = 5 \times 10^{-5}$ M) exhibited an absorption maximum in the range of 300–420 nm corresponding to the π–π* transition of the monomer while the intramolecular charge transfer (ICT) band appeared at $\lambda_{\mathrm{max}}$ = 508 nm. The broadness of the ICT band confirmed the extended orbital overlap between the donor (benzofuran) and the acceptor (DPP) units. However, in methylcyclohexane (MCH) and water, **PDPP–Amphi** ($c = 5 \times 10^{-5}$ M) exhibited structured red shifted absorption having a maximum at 576 nm ($\Delta\lambda = 2323.9$ cm$^{-1}$) with a shoulder band at 540 nm, probably due to planarization and J–type aggregation of the molecule (**Figure 4.7b**).[38] Similarly, the fluorescence spectra in MCH and water showed red shifted structured emission maximum at 609 nm ($\lambda_{\mathrm{ex}}$ = 480 nm) having a lesser Stokes shift (940.7 cm$^{-1}$) as compared to the monomeric emission maximum at 576 nm with a larger Stokes shift (2323.9 cm$^{-1}$) that supports the existence of J–type aggregation (**Figure 4.7c**).

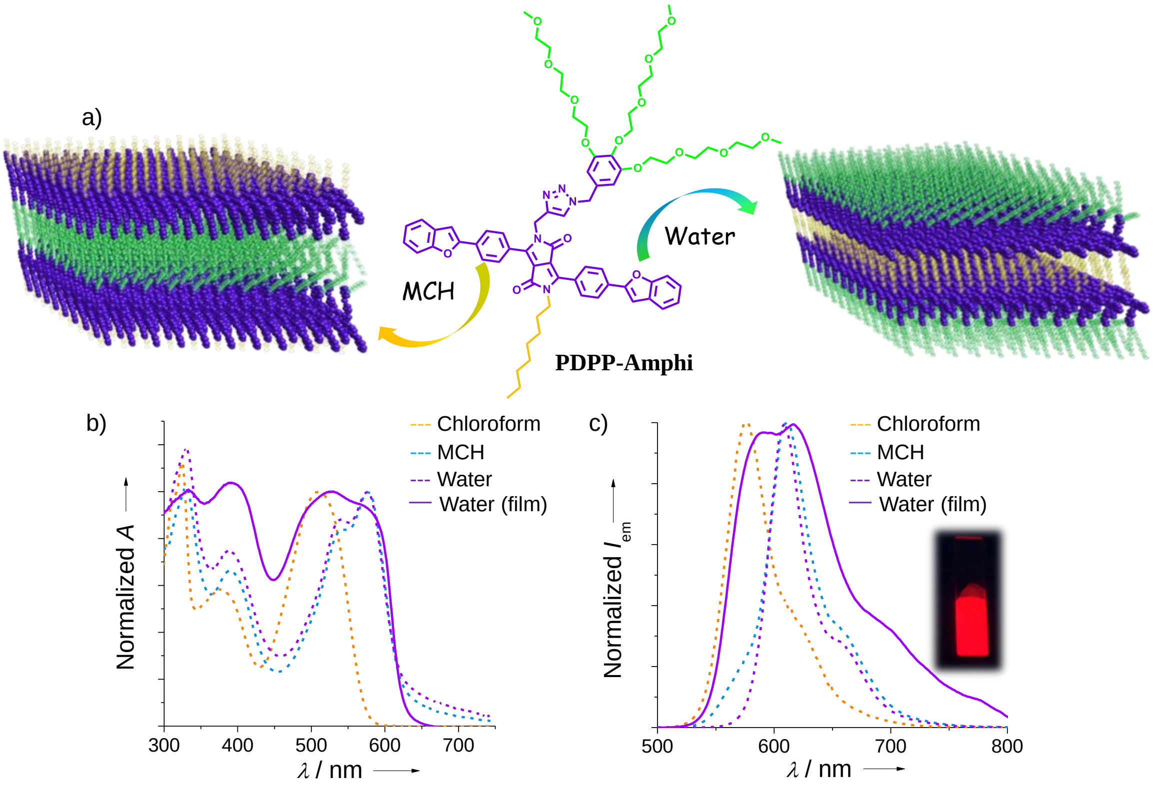

**Figure 4.7. a)** Chemical structure of **PDPP–Amphi** and the schematic illustration of its assembly in methylcyclohexane (MCH, nonpolar, left) and water (polar, right). **b)** Normalized absorption **c**) and emission of the monomer, aggregates (from MCH and water) and water–processed films. The inset shows high fluorescence of the film processed from water under UV light.

Although DPP based D–A–D systems are known to form both H– and J–type aggregates,[39] **PDPP–Amphi** exclusively formed J–aggregates in the solid state as evident from the absorption and the emission spectra. According to the exciton theory, for J–aggregates, transitions from lower energy levels (0–0) are considered to be allowed.[40] As a result, highly emissive monomer ($\Phi_f$ = 0.91 in chloroform, Rhodamine B in water as standard) of **PDPP–Amphi** retained its emission even in the self–assembled and solid states ($\Phi_f$ = 0.54 measured with integrated sphere spectrophotometer of a film processed from water) with reduced Stokes losses (**Figure 4.7c** inset).[41] The high fluorescence emission in the solid–state with a red shift can be attributed to the formation of J–aggregates and also due to the planarization of the molecule.

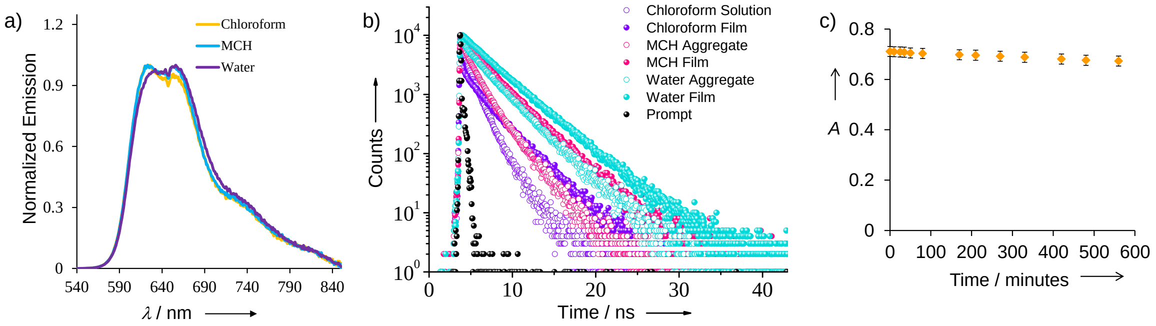

**Figure 4.8. a)** Solid state fluorescence spectra of **PDPP–Amphi** films upon excitation with 500 nm. **b)** Emission decay of **PDPP–Amphi** monomer, aggregates and films upon 375 nm excitation, monitored at 580 nm (monomer) and 625 nm (aggregates and films); **c)** Photostability of **PDPP–Amphi** in chloroform upon irradiation with a focused oriel lamp (white light).

The emission lifetime of the molecule was recorded in monomeric, self–assembled, and film states (**Figure 4.8a**). The **PDPP–Amphi** monomer exhibited a monoexponential decay with a fluorescence lifetime of 3.2 ns (monitored at 576 nm, $\lambda_{ex}$ = 375 nm) whereas the water processed film showed a biexponential decay indicating the existence of two species having lifetime of 2.7 and 4.4 ns (monitored at 609 nm, $\lambda_{ex}$ = 375 nm). The photophysical properties of the molecule under different conditions are summarized in the **Table 4.1**. **Figure 4.9** shows the bright fluorescence in monomeric and self–assembled states.

| PDPP-Amphi | Absorption (nm) | | Emission (nm) | | Quantum Yield (%) | | Lifetime (ns) | |
|---|---|---|---|---|---|---|---|---|
| | Solution | Solid (Film) | Solution | Solid (Film) | Solution | Solid (Film) | Solution | Solid (Film) |
| Chloroform | 319, 370, 502 | 518, 383, 339 | 577, 621, 683 | 620, 648, 727 | 91 | 41 | 3.6 ns | 3.27 ns (5%)<br>4.61 ns (95%) |
| Methylcyclohexane (MCH) | 327, 383, 533, 572 | 574, 527, 381, 337 | 632, 680 | 619, 649,727 | NA | 44 | 1.42 ns (31%)<br>3.9 ns (69%) | 1.69 ns (20%)<br>3.71 ns (80%) |
| Water | 326, 381, 534, 570 | 584, 518, 386, 339 | 632, 680 | 625, 649, 727 | NA | 54 | 2.48 ns (12%)<br>3.7 ns (88%) | 2.72 ns (21%)<br>4.39 ns (79%) |

**Table 4.1.** Summary of the photophysical properties of **PDPP–Amphi** in monomer, aggregated and solid states.

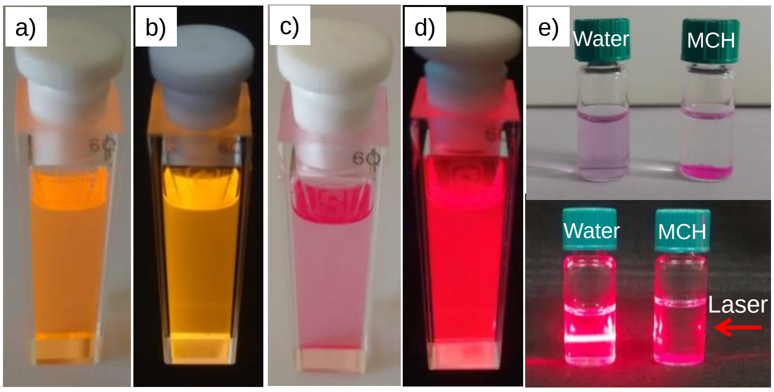

**Figure 4.9.** Photographs of **PDPP–Amphi** monomer in ACN **a)** under ambient light and **b)** under UV light (365 nm). Photograph of **PDPP–Amphi** aggregate in water: ACN (90:10) **c)** under ambient light and **d)** under UV light (365 nm). **e)** Photograph of **PDPP–Amphi** aggregate in water and MCH after two months (Top) and corresponding Tyndall effect suggesting the aggregates are highly dispersed in water as compared to that in MCH when flashed with a red laser ( $\lambda$ = 650 nm).

Unlike in MCH, **PDPP–Amphi** formed well dispersed aggregates in water that are stable over several months without any sign of precipitation, as evident from the observed Tyndall effect (**Figure 4.9e**). Due to the amphiphilic nature of **PDPP–Amphi**, two different molecular assemblies are expected to form as shown in

Figure **4.7a**. In MCH, the alkyl chains are exposed towards the solvent, whereas in water, the hydrophilic chains are exposed out.

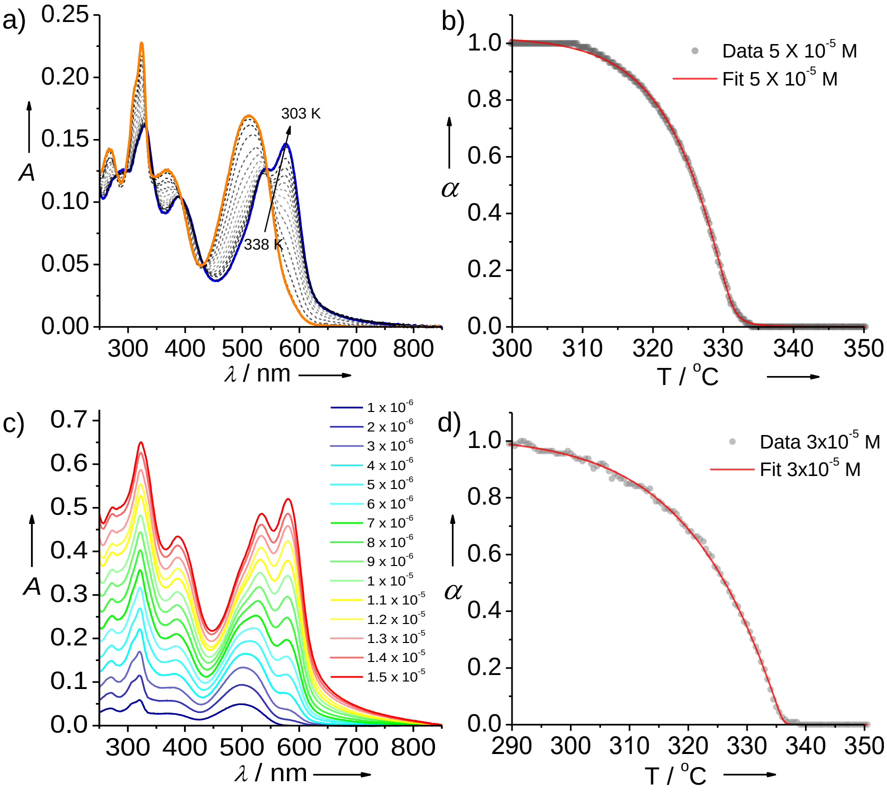

**Figure 4.10. a)** Temperature dependent absorption studies of **PDPP–Amphi** in MCH : $CHCl_3$ (95:5) at a concentration of $5 \times 10^{-5}$ M. **b)** Corresponding cooling curve and fitting using a cooperative model. **c)** Concentration dependent absorption in water: ACN (90:10). **d)** Cooling curve of a $3 \times 10^{-5}$ M solution of **PDPP–Amphi** in water: ACN (90:10) and the corresponding fitting using a cooperative model.

Insight on the molecular assembly was obtained by temperature dependent UV–Vis absorption spectral studies performed in MCH: $CHCl_3$ (95:5) at a concentration of $5 \times 10^{-5}$ M. On cooling the solution from 330 K at a rate of 1 K $min^{-1}$, intensity of the absorption maximum at 508 nm was decreased with the formation of a new red–shifted band at 576 nm along with a shoulder at 540 nm (**Figure 4.10.a**). Equilibrium existence of the monomer and the self–assembled states was confirmed by the presence of three prominent isosbestic points at 542, 431 and 391 nm in the absorption spectra.[42] A plot of the fraction of aggregates

($\alpha_{agg}$) against temperature at 576 nm showed a nonsigmoidal profile corresponding to a cooperative supramolecular polymerization (**Figure 4.10.b**).[43] The spectral changes were fitted with a nucleation elongation model.[44] To probe the aggregation of **PDPP–Amphi** in water, a concentration dependent absorption measurement was performed in water: ACN (90:10) (**Figure 4.10c**). The J–aggregate formation involving **PDPP–Amphi** was observed in water as well as in MCH with structured red shifted absorption. The temperature dependent UV–vis absorption study performed in water: acetonitrile (ACN) (90:10) at a concentration of $3 \times 10^{-5}$ M revealed a cooperative pathway (**Figure 4.10d**). Thus, **PDPP–Amphi** formed J–aggregates in both MCH and water through a cooperative self–assembly mechanism.

## 4.3.4. Contact Angle Measurements

As mentioned earlier, alkyl chains are exposed towards the solvent in MCH, whereas in water, the hydrophilic chains are projected outward. In such cases, one can expect a film of **PDPP–Amphi** prepared from MCH to be hydrophobic in nature and that from water to be hydrophilic in nature. To support our assumption, we measured the water contact angle (CA) of these films. Interestingly, the contact angle exhibited by the water processed film was relatively smaller (CA = 72.7° ± 2°) than that observed for a film processed from MCH (CA = 91.7° ± 2°) (**Figure 4.11a,c**), confirming the hydrophilic and hydrophobic nature, respectively, due to the difference in the exposure of the side chains (**Figure 4.11b,d**).

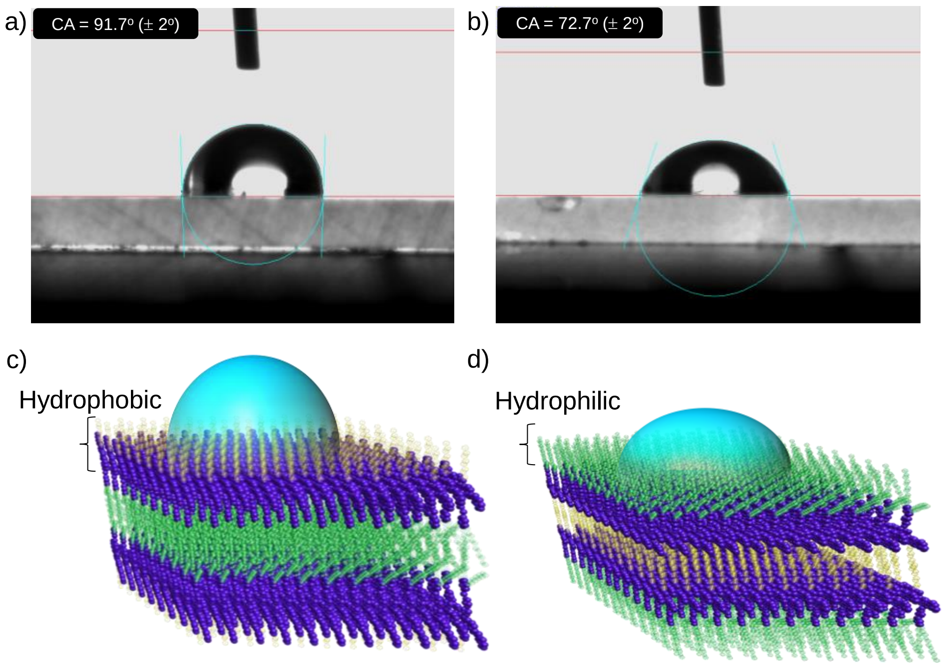

**Figure 4.11.** Contact angle of water droplets over the film of **PDPP–Amphi** processed from **a)** MCH and **b)** water and their corresponding schematic representation showing **c)** hydrophobic or **d)** hydrophilic nature of the films.

## 4.3.5. Morphological Analyses

The transmission electron microscopy (TEM) images of **PDPP–Amphi** aggregates in MCH: chloroform (95:5) as well as in water: ACN (90:10) mixtures ($5 \times 10^{-5}$ M) obtained upon drop casting over carbon coated copper grids are shown in **Figure 4.12c**. Formation of thin nanosheets in different size up to a few square micrometers was observed for the assembly in water (**Figure 4.12.c**) whereas the assembly in MCH showed agglomerated sheets (**Figure 4.12.e**). The circular spot pattern in selected area electron diffraction (SAED) of the former (**Figure 4.12.d**) suggests better crystallinity of **PDPP–Amphi** aggregates in water when compared to that in MCH (**Figure 4.12.f**).[45] Clear lattice planes were observed for the assembly in water with a *d*–spacing of 3.6 Å under high resolution TEM (inset **Figure 4.12.c**). This polycrystallinity probably arises from the increased π–stacking in water, accelerated by solvophobic interactions. The thickness of these nanosheets were estimated from the atomic force microscopy (AFM) images of **PDPP–Amphi** assembly obtained in water ($c = 5 \times 10^{-5}$ M). These nanosheets were found to have an average height of 2.8 ± 0.4 nm (**Figure 4.12a, b**) which can be correlated with a bilayer assembly as depicted in **Figure 4.12b** inset.[31] AFM height profile of these nanosheets revealed a uniform height with less surface roughness, a prerequisite for device applications.

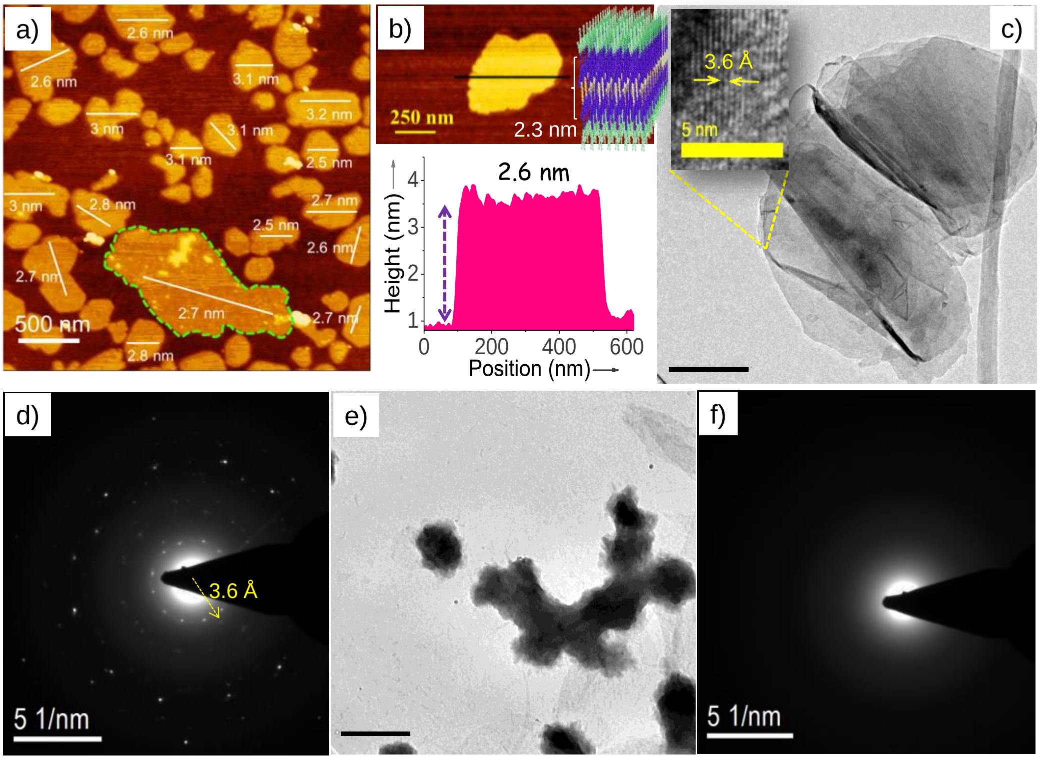

**Figure 4.12. a)** AFM image with height of the individual nanosheets and **b)** a representative height profile of the nanosheets of **PDPP–Amphi** in water ($c = 5 \times 10^{-5}$ M) over a silicon wafer and **c)** TEM image of the same. The inset shows the crystalline lattice planes depicting π stacking, **d)** corresponding SAED pattern over a carbon coated copper grid. **e)** TEM image and **f)** the corresponding SAED pattern of **PDPP–Amphi** prepared from MCH.

### 4.3.6. Linear Dichroism (LD)

Linear dichroism (LD) is a useful technique to monitor intrinsic or induced alignment of chromophores in a molecular assembly.[46] The solution state LD measurements of **PDPP–Amphi** in water ($c = 3 \times 10^{-4}$ M) exhibited significant negative LD signal indicating greater perpendicular ($A\perp$) absorption of the polarized light than parallel ($A\|$) due to predominant perpendicular orientation of the transition dipole moment with respect to the sheet direction.[47] Thus, the nanosheets obtained from water medium showed anisotropic behavior due to the well–defined alignment of the chromophores (**Figure 4.13**).[48]

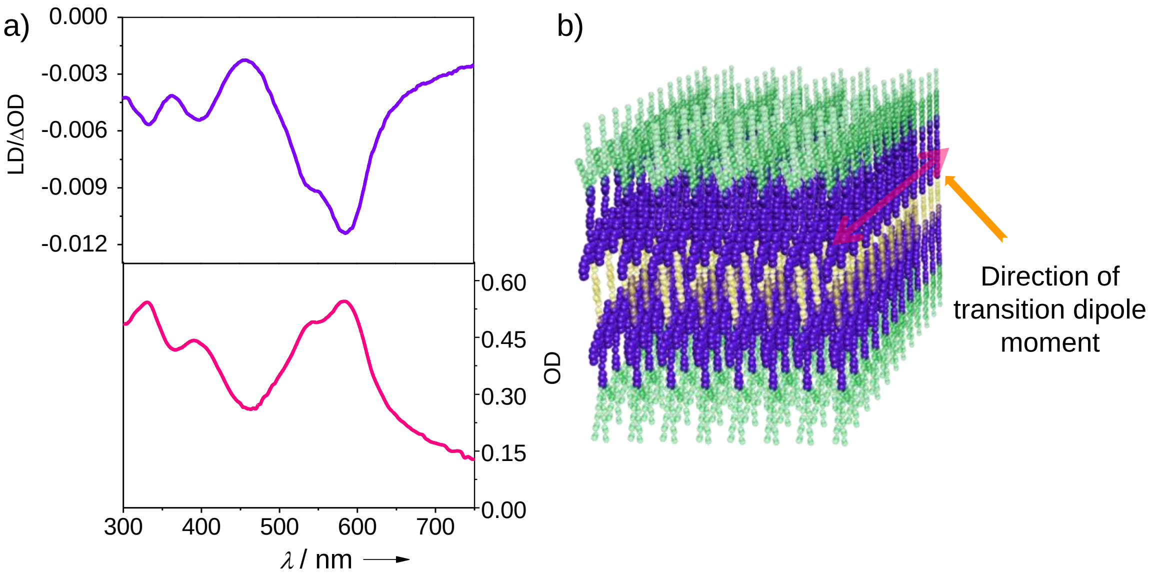

**Figure 4.13. a)** LD (top) and UV–Vis spectra (bottom) of **PDPP–Amphi** aggregates in water: ACN (90:10) ($3 \times 10^{-4}$ M) in a 1 mm path length cuvette. **b)** Plausible arrangement of **PDPP–Amphi** chromophores within nanosheet, with the direction of transition dipole moment.

### 4.3.7. Frontier Molecular Orbitals (FMO)

Density functional theory (DFT) calculations have been performed to understand the molecular conformation and the frontier molecular orbitals (FMOs). For simplicity, alkyl chains and glycol chains were replaced by $-CH_3$ groups. The ground state optimization of **PDPP–Amphi** was done at the B3LYP/6–31G* level, which showed a slight twist in the aromatic back bone. The electron density was equally delocalized over highest occupied molecular orbital (HOMO) and lowest unoccupied molecular orbital (LUMO) (**Figure 4.14c, d**). HOMO of the molecule was calculated as –5.8 eV by using photoelectron yield spectroscopy (**Figure 4.14a**). The optical band gap determined from the onset of solid–state absorption profile was 2.0 eV. Hence, the LUMO level stayed at –3.8 eV. **PDPP–Amphi** can, therefore, act as a donor as well as an acceptor for **$PC_{71}BM$** and **P3HT** respectively, due to the suitably placed energy levels and the equally delocalized HOMO and LUMO (**Figure 4.14b**).

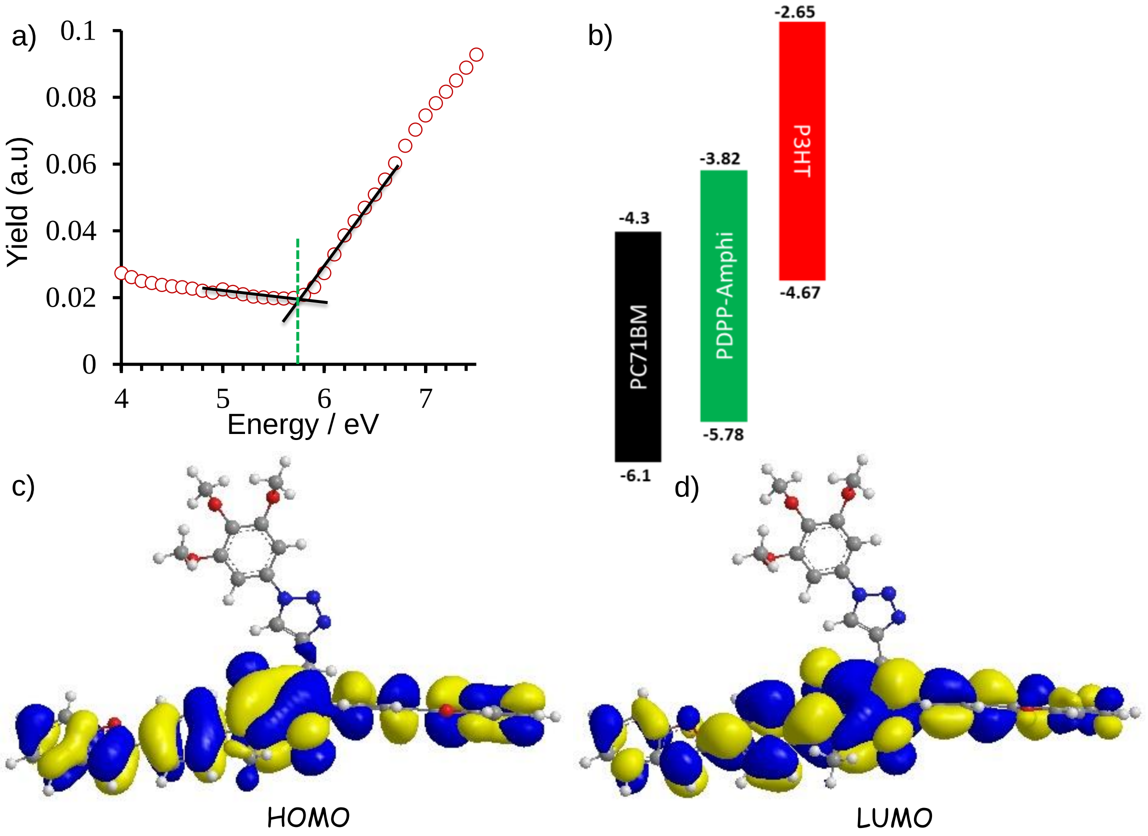

**Figure 4.14. a)** Photo Yield Spectra (PYS) of **PDPP–Amphi**. **b)** Comparative HOMO and LUMO energy levels of **$PC_{71}BM$**, **PDPP–Amphi** and **P3HT**. **c)** HOMO and **d)** LUMO of **PDPP–Amphi** calculated by using B3LYP/ 6–31G* (TD–DFT).

### 4.3.8. Conductivity Measurements by Flash Photolysis Time Resolved Microwave Conductivity (FP–TRMC)

To evaluate the intrinsic charge–carrier mobility of the nanosheets of **PDPP–Amphi**, films were processed from different solvents and subjected to FP–TRMC and TPC measurements.[49] Intrinsic photoconductivity of a system can be quantified from the $\varphi\Sigma\mu$ value, where $\varphi$ and $\Sigma\mu$ ($\mu_e$ + $\mu_h$) are charge–carrier generation quantum yields upon photoexcitation and the sum of charge–carrier mobilities, respectively.[50] **PDPP–Amphi** was drop cast over a clean quartz slide having a concentration of ≈ 8 mg $mL^{-1}$ from chloroform, MCH: chloroform (80:20) (in short, MCH processed **PDPP–Amphi**), and water: ACN (70:30) (in short, water processed **PDPP–Amphi**). Films were subjected to 355 nm laser excitation parallel (||) to the microwave electric–field vector giving the rise and decay profile in TRMC (**Figure 4.15a**). More than two–fold increase in $\varphi\Sigma\mu_{\parallel}$ was observed for self–assembled film of **PDPP–Amphi** processed from water than that of chloroform, while a 1.4–fold enhancement was exhibited by film processed from MCH. Since, the molecule is the same in both cases, the enhanced $\varphi\Sigma\mu_{\parallel}$ could be attributed to the enhancement in $\mu$ rather than $\varphi$, reflecting a greater molecular ordering and π–stacking in the order water > MCH >> chloroform. Also, significant increase in the half–life of the charge carriers was observed for the aggregates prepared in MCH and water.

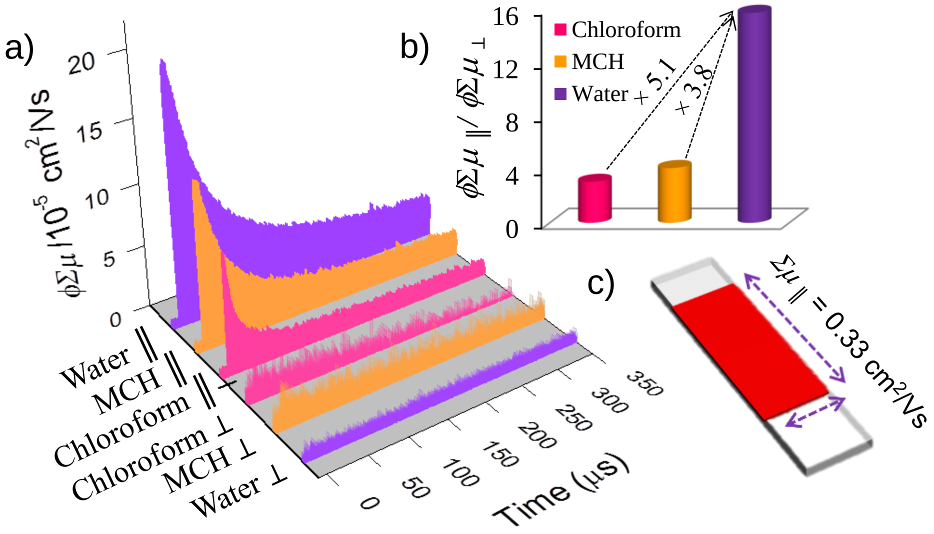

**Figure 4.15. a)** Transient photoconductivity (FP–TRMC) profile of **PDPP–Amphi** films processed from different solvents; chloroform, methylcyclohexane (MCH), and water over quartz slides and measured parallel (||) and perpendicular (⊥) to the microwave electric–field vector upon excitation with $\lambda$ = 355 nm laser having 10 mW power (10 Hz). **b)** Anisotropic photoconductivity of the films ($\varphi\Sigma\mu_{\parallel}$:$\varphi\Sigma\mu_{\perp}$) processed from various solvents. **c)** Pictorial representation of anisotropic charge carrier mobility of water processed **PDPP–Amphi** evaluated by combination of FP–TRMC and TPC.

In order to investigate the role of molecular orientation on charge–carrier mobility, the photoconductivity ($\varphi\Sigma\mu_{\perp}$) of the films was measured in the perpendicular direction by placing the sample perpendicular ($\perp$) to the microwave electric field vector.[51] Interestingly, very less $\varphi\Sigma\mu_{\perp}$ was observed for the water processed film when compared to the chloroform or MCH processed films. About 16–fold increment in anisotropic charge–carrier mobility ($\varphi\Sigma\mu_{\parallel}$:$\varphi\Sigma\mu_{\perp}$) (**Figure 4.15b**) was observed for the film processed from water, indicating the role of the solvent in organizing the chromophores without providing any external stimulus such as heating, scratching, electric, or magnetic fields.[52]

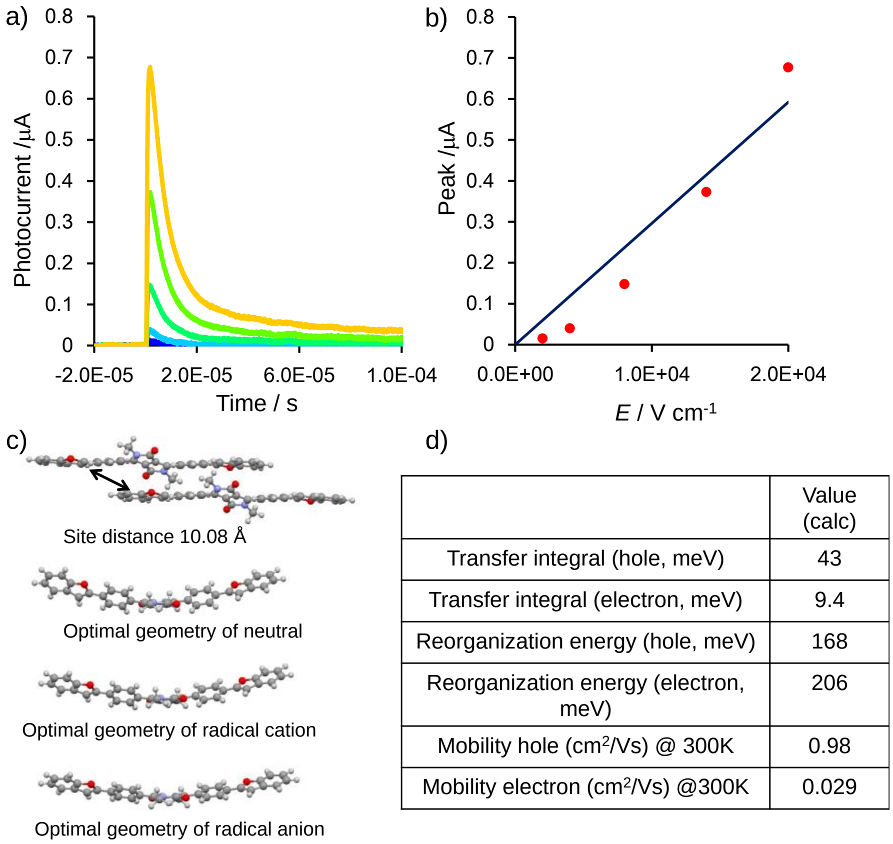

| | Value (calc) |
|---|---|
| Transfer integral (hole, meV) | 43 |
| Transfer integral (electron, meV) | 9.4 |
| Reorganization energy (hole, meV) | 168 |
| Reorganization energy (electron, meV) | 206 |
| Mobility hole (cm$^2$/Vs) @ 300K | 0.98 |
| Mobility electron (cm$^2$/Vs) @300K | 0.029 |

**Figure 4.16. a)** Photocurrent transients of **PDPP–Amphi** films processed from water : ACN (70:30) upon exposure to a 355 nm laser and **b)** corresponding plot of transient photocurrent intensity *vs* electric field. Amsterdam density functional (ADF) calculation of **c) PDPP–Amphi** and **d)** data summarised in a table.

For determining the maximum charge–carrier mobility of the 2D sheets processed from water, $\varphi$ was estimated by a direct current mode photocurrent measurement by placing the sample over a comb–type interdigitated gold electrode on a glass substrate, using transient photocurrent measurement (TPC).[53] Poly(9,9′–dioctylfluorene) film obtained from chlorobenzene solution was used as the standard. In presence of a bias voltage, both the prepared films were excited with a 355 nm laser having a power of 5 mW. Linear relationship between photocurrent and bias voltage was found for both the films (**Figure 4.16a**, **b**) and the $\varphi$ value was estimated as $4.8 \times 10^{-4}$ for the film processed from water. The maximum intrinsic 2D charge–carrier mobility was then estimated by dividing with $\varphi$ for the film of **PDPP–Amphi** processed from water and was found as $\Sigma\mu_{\parallel} = 0.33$ cm$^{2}$V$^{-1}$s$^{-1}$ (**Figure 4.15c**).

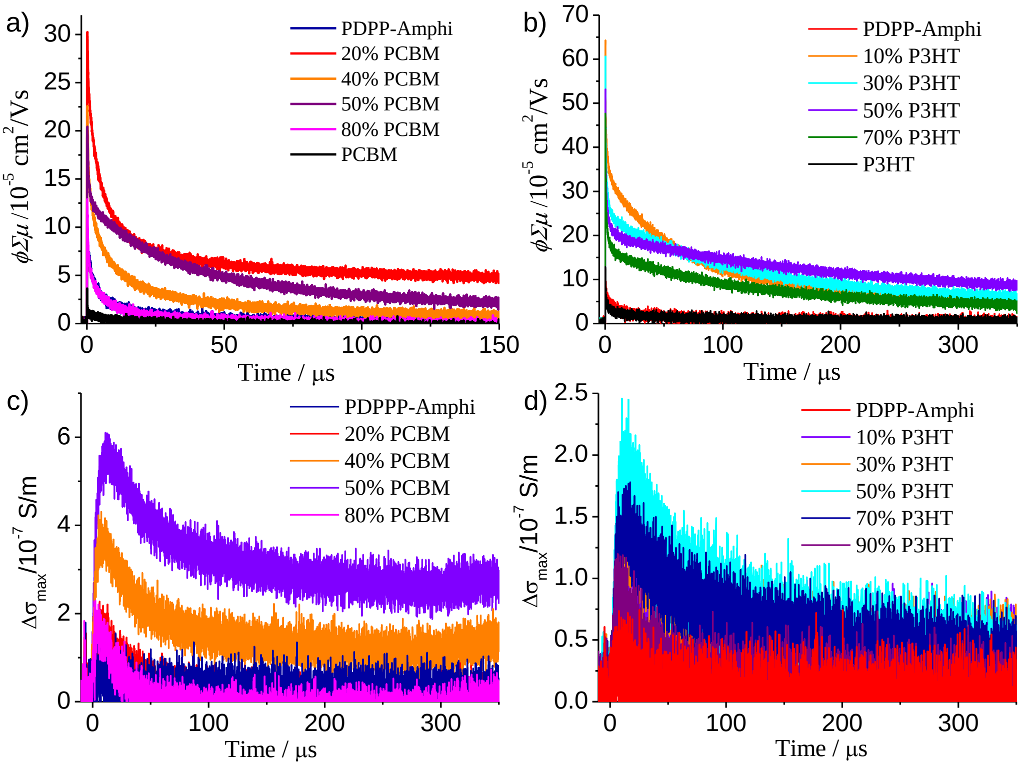

**Figure 4.17.** FP–TRMC transients of **PDPP–Amphi** films upon mixing with different weight % of **a**), **c**) acceptor **PC$_{71}$BM** and **b**), **d**) donor **P3HT** drop–casted from the corresponding chloroform solutions over a quartz slide. The excitation pulse was $\lambda = 355$ nm for **a**), **b**) and white light continuum for **c**), **d**).

The observed anisotropic mobility of **PDPP–Amphi** is high for a supramolecular D–A–D nanosheet processed from water, measured by FP–TRMC and TPC. We performed Amsterdam Density Functional (ADF) calculation with Marcus theory to predict the charge–carrier mobility of the self–assembled aggregates from water.[55] Since, **PDPP–Amphi** preferentially formed J–aggregates, we used a J–type dimer model considering the ease of calculation. The ADF calculation confirmed the high charge–carrier mobility of **PDPP–Amphi** aggregates in water (**Figure 4.16c**, **d**). In order to find the ambipolar nature and optimal blend ratio for maximum photovoltaic performance, FP–TRMC is a quick electrode less technique. **PDPP–Amphi** was mixed with different wt% of **P3HT** (donor) or **PC$_{71}$BM** (acceptor) and the photoconductivity was recorded upon 355 nm ($\varphi\Sigma\mu$) as well as under white light excitation ($\Delta\sigma$). Enhancement in transient photoconductivity ($\Delta\sigma$) with the addition of donor or acceptor manifests the ambipolar nature of **PDPP–Amphi** as predicted from FMO and DFT calculations (**Figure 4.17**).

## 4.3.9. Molecular Organization

To explain the contrasting anisotropic charge–carrier mobility of the films processed from different solvents, a grazing incidence X–ray diffraction (GIXD) experiment was performed. Molecular organization over a substrate can be categorized into edge–on (||) or face–on (⊥) by virtue of their $\pi$–stacking directions.[54] Edge–on or face–on or bimodal molecular orientation can be assessed by in–plane ($q_{xy}$) or out–of–plane ($q_z$) diffraction.[55]

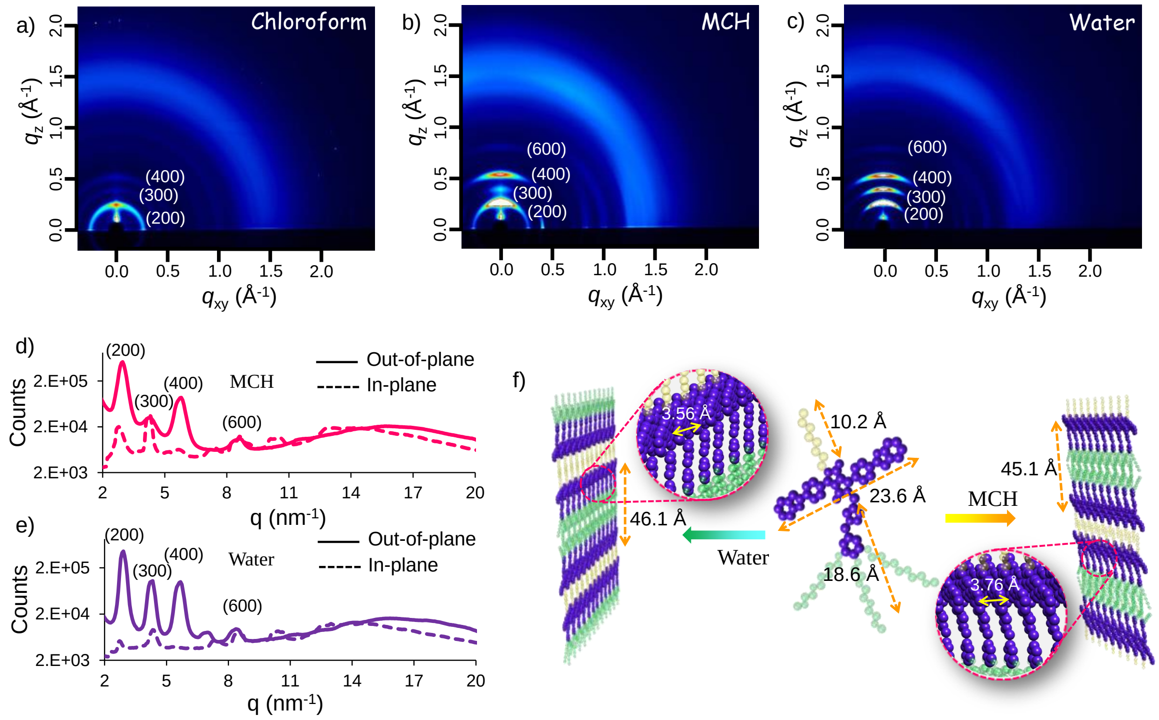

**Figure 4.18.** 2D Grazing–incidence X–ray diffraction (GIXD) profile of **PDPP–Amphi** films processed from **a**) chloroform, **b**) methylcyclohexane (MCH), and **c**) water. Out–of–plane and in–plane profile of **d)** MCH (–) and **e)** Water (–) aggregates. **f)** A schematic representation of two different aggregates of **PDPP–Amphi** formulated on the basis of the GIXD and their π–stacking distance.

Different films of **PDPP–Amphi** processed from chloroform, MCH, and water, prepared over quartz slides (same used for FP–TRMC) exhibited very distinct GIXD profiles as represented in Figure **4.18a–c**. Amorphous nature of the chloroform processed film of **PDPP–Amphi** was confirmed from the equal intensity distribution of diffractions in the $q_{xy}$ and $q_z$ axes (**Figure 4.18a**), whereas MCH processed film showed diffractions of relatively higher intensity along the $q_z$ axis when compared to $q_{xy}$ (**Figure 4.18b** and **d**). However, the intensity of the out–of–plane diffractions of the water processed film is much more prominent than in–plane diffractions, indicating preferred edge–on orientation (**Figure 4.18c** and **e**). Further, to estimate the degree of anisotropy, we have calculated the intensity ratio of the out–of–plane to in–plane peaks ($I_{op}/I_{ip}$).[55] The highest value was obtained for the film processed from water (84.7) when compared to that of the films obtained from MCH (23.6) and chloroform (2.5), pointing toward higher anisotropy of the film obtained under aqueous condition. **Figure 4.18c** underlines that although both MCH and water aggregates of **PDPP–Amphi** differ in their diffraction intensities, they exhibit similar reflections with a reciprocal *d*–spacing ratio of 1:2:3:4:6 corresponding to the multilamellar packing (**Figure 4.18d** and **e**),[56] which in turn is supported by the wide–angle X–ray diffraction measurements (**Figure 4.19**).

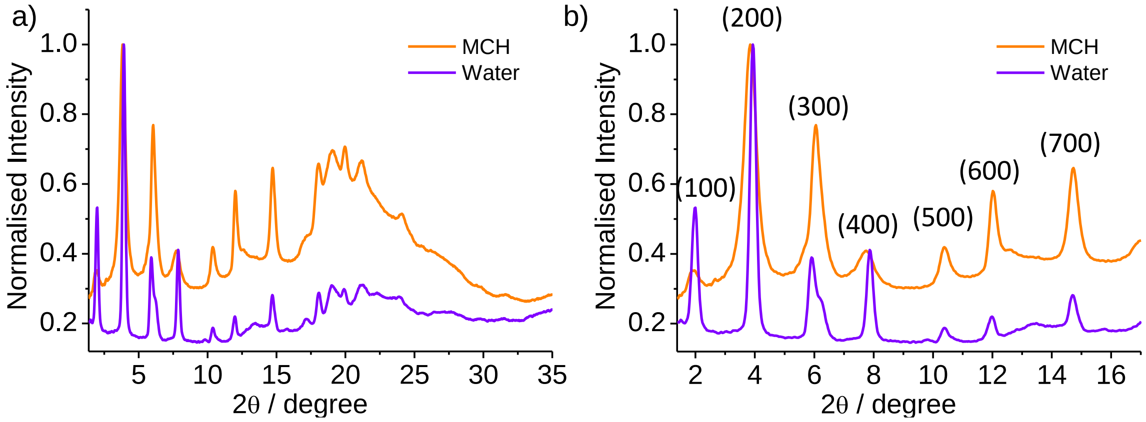

**Figure 4.19. a)** Wide angle X–ray scattering (WAXS) of **PDPP–Amphi** aggregates processed from water and MCH and **b)** the corresponding zoomed portion ($2\theta = 1.5$–17°).

Thus, while **PDPP–Amphi** is forced to hide its hydrophilic and hydrophobic part in MCH and water, respectively, it preserves a lamellar packing in either solvents. Moreover, the presence of clear interlamellar stacking peaks up to six orders (from 100 to 600) along the $q_z$ axis in the 2D diffractogram of the aggregates from water confirms better long range ordering when compared to that of the aggregates formed from MCH. The first–order interlamellar distance *d* (100) was determined to be 46.1 Å for the aggregates from water and 45.1 Å for the aggregates from MCH whereas, the π–stacking distance *d* (010), for water aggregates was observed at 3.56 Å (supported by HR–TEM, **Figure 4.12d** and inset of **Figure 4.12c**) and at 3.76 Å for MCH aggregates (**Figure 4.18.d** and **e**). The lower π–stacking distance confirms stronger π–π interactions in the former, pointing toward a strong effect of the solvent on crystalline self–assembly. These results complement the observed high photoconductivity ($\varphi\Sigma\mu_{\parallel}$) for water processed film in FP–TRMC measurements. After considering the various data obtained for **PDPP–Amphi**, a probable pathway of the multilamellar organization of the molecule is represented in **Figure 4.18f**.

## 4.4. Conclusion

In summary, two different types of assemblies were formed by the D–A–D type amphiphile (**PDPP–Amphi**) in polar as well as nonpolar solvents. J–type aggregation resulted in high fluorescence quantum yield for both the assemblies in solution as well as in solid state. Although, both the aggregates exhibited similar optical properties in solution and solid states, a few layered crystalline supramolecular nanosheets were obtained only under aqueous conditions. The nanosheets obtained under aqueous condition exhibited high anisotropic charge–carrier mobility of 0.33 $cm^2V^{-1}s^{-1}$, which is high among the various supramolecular assemblies reported till date. The observed anisotropy is attributed to the preferential edge–on orientation of the molecule as concluded from the LD and GIXD measurements. Also, moderate Fermi energy levels and equally delocalized HOMO and LUMO manifest **PDPP–Amphi** as a suitable candidate to be explored both as an electron donor as well as an acceptor in organic photovoltaic devices. The ability to develop highly fluorescent and crystalline 2D nanosheets with high anisotropic charge–carrier mobility is expected to be useful in designing molecular systems for device applications.

## 4.5. Experimental Section

### 4.5.1. Materials and Methods

### Linear Dichroism (LD) Measurement

LD experiments were performed on JASCO 810 spectrometer using a quartz cuvette of 1 mm path length. The LD spectra were recorded as ΔOD ($A_{\parallel} - A_{\perp}$) at room temperature and were processed by subtraction of non–rotating baseline spectra.

### Two–Dimensional Grazing Incidence X–ray Diffraction (2D–GIXD) Measurements

Grazing incidence X–ray diffraction (GIXD) measurements were conducted at the SPring–8, Japan on beamline BL46XU. The sample was irradiated at a fixed incident angle on the order of 0.12° with an X–ray energy of 12.39 keV ($\lambda$ = 1 Å). The GIXD patterns were recorded with a 2–D image detector (Pilatus 300K). Samples for the X–ray measurements were prepared *via* drop casting from respective solvents.

### Transient Photocurrent (TPC) Measurements

For TPC measurements poly(9,9′–dioctylfluorene) (PDOF) film was prepared from chlorobenzene. The solutions of **PDPP–Amphi** were prepared in acetonitrile (ACN) : water (Milli–Q deionised water) (30:70). The films were excited with 355 nm pulsed laser (5 mW) from the bottom of the sample to generate the charge carriers. The bias voltage was tuned from 0 to $2.5 \times 10^4$ $\mathrm{Vcm^{-1}}$ for all the films to measure the photocurrent transients of PDOF, and **PDPP–Amphi**. The corresponding peak current intensity was plotted against the applied voltage.

### Contact Angle (CA) Measurements

CAs of all the fims were measured by a contact angle goniometer (Kernco Instrument Inc.) under ambient conditions. Water droplets (about 3 μL) were placed over the films by a sessile drop method.

### General Procedure to Prepare Nanosheet for TEM and AFM Analyses

From a monomeric stock solution of **PDPP–Amphi** in acetonitrile ($c = 9.3 \times 10^{-4}$ M), 160 μL was slowly transferred into a vial containing 3 mL Milli–Q deionised water to achieve a final concentration of $5 \times 10^{-5}$ M. The solution containing the supramolecular nanosheets was then drop–cast over the respective substrate.

### General Procedure of Film Preparation for FP–TRMC, GIXD and CA Measurements

**PDPP–Amphi** was taken in a 5 mL glass vial with the required amount of solvent, so that the final concentration was 8 mg/mL. Samples were prepared in chloroform ($CHCl_3$), chloroform: methylcyclohexane (MCH) (20:80), and acetonitrile (ACN) : water (Milli–Q deionised water) (30:70). Samples prepared in the respective solvents were drop cast over a quartz slide inside a vaccum oven at 40°C.

## 4.5.2. Synthesis and Characterization

### Synthesis of 3,6–bis(4–bromophenyl)pyrrolo[3,4–c]pyrrole 1,4(2H,5H)–dione (12)

A dried 250 mL two–neck flask connected to a condenser and a vacuum adapter was charged with sodium *tert*–pentoxide (5.14 g, 46.67 mmol) and anhydrous *tert*–amyl alcohol (30 mL) under argon atmosphere. The reaction mixture was heated at 100 °C until it became homogeneous (~1 h). The mixture was then cooled to 60°C and 4–bromobenzonitrile, **11** (5 g, 27.46 mmol) was added into it. In a pressure equalizer, diethyl succinate (2.4 g, 13.77 mmol) mixed with *tert*–amyl alcohol (10 mL) was taken and added drop wise to the reaction mixture over a time period of 2 h till the solution turned dark purple. The reaction mixture was vigorously stirred at 110 °C for 10 h, and then acidic MeOH (40 mL MeOH and 10 mL glacial acetic acid) was added at room temperature to neutralize the reaction mixture. Again the reaction mixture was heated at 70°C and filtered hot through a Buchner funnel (Whatman filter paper) under vacuum. A dark purple solid cake of **12** (6g) was obtained and dried inside a vacuum oven at 110°C, which was used in subsequent reactions without further characterization or purification.

### Synthesis of 3,6–bis(4–bromophenyl)–2–octylpyrrolo[3,4–c] pyrrole 1,4(2H,5H)–dione (13)

To a dried two–neck 250 mL round bottom flask, **12** (1.5 g, 3.36 mmol) and 50 mL of degassed anhydrous *N,N*–dimethylformamide (DMF) were taken and stirred till dissolution (30 min) under an inert atmosphere. Subsequently, potassium *tert*–butoxide (1.32 g, 11.76 mmol) was added resulting in an immediate blue coloration due to anion generation. The reaction mixture was stirred for 30 min. 1–Bromooctane (1.0 gm, 5.17 mmol) was added dropwise over a period of 1 h into the reaction mixture using a syringe, and kept for 3 h at 60°C. The reaction mixture was allowed to cool down to room temperature, poured into ice cold water (150 mL) and stirred for another 2 h. The mixture was extracted by $CHCl_3$ and dried over $Na_2SO_4$. Then the solvent was removed under reduced pressure and the residue was purified by column chromatography using hexane/chloroform (1:1) as eluent. An orange powder was obtained. Yield: 300 mg (16%). $^1$H–NMR (500 MHz, chloroform–*d* ($CDCl_3$), δ): 10.18 (s, 1H, N–H), 8.17–8.15 (d, *J* = 3.5 Hz, 2H, Ar–H), 7.69–7.67 (d, *J* = 8.5 Hz, 2H, Ar–H), 7.65–7.63 (d, *J* = 8.5 Hz, 2H, Ar–H), 7.57–7.55 (d, *J* = 8 Hz, 2H, Ar–H), 3.79–3.76 (t, *J* = 7.5 Hz, *J* = 7.5 Hz, 2H, $–N–CH_2–$), 1.24–1.23 (m, 12H, $–CH_2–CH_2–$), 0.89–0.86 (t, *J* = 7.5 Hz, *J* = 7.5 Hz, 3H, $–CH_3$). $^{13}$C–NMR (125 MHz, $CDCl_3$, δ): 168.1, 165.3, 142.6, 137.1, 137.5, 133.4, 131.3, 128.6, 122.5, 107.4, 45.6, 31.4, 29.3, 27.1, 22.7, 14.1. HRMS: m/z 557.5 (100%). Calculated Mass: 556.04.

## Synthesis of 3,6–bis(4–(benzofuran–2–yl)phenyl)–2 octylpyrrolo [3,4–c]pyrrole–1,4(2H,5H)–dione (14)

In a dried 100 mL two–neck round bottom flask, **13** (0.1 g, 0.179 mmol) and $Na_2CO_3$ (0.2 g, 1.88 mol) was mixed and fitted with a condenser and vacuum adapter under inert atmosphere (Ar). Then deoxygenated THF (10 mL), deoxygenated $H_2O$ (5 mL) and $Pd^0(PPh_3)_4$ (30 mg, 0.01 mmol) as a catalyst were added into the mixture and heated to 45°C under an argon atmosphere for 30 min. A solution of 2–benzofuranylboronic acid (0.1 g, 0.6 mmol) in deoxygenated THF (5 mL) was added slowly to the reaction mixture, and refluxed at $70^oC$ for another 12 h. Yellowish green to orange color change was observed with progress of the reaction. After cooling to room temperature, the mixture was extracted with $CHCl_3$ (100 mL) and dried over $Na_2SO_4$. The solvent was removed under reduced pressure. The residue was purified by column chromatography on silica ($CHCl_3$/MeOH 95:5, v/v) to give a purple solid (80 mg, yield = 72%). $^1$H–NMR (500 MHz, $CDCl_3$, $\delta$): 10.23 (s, 1H, N–H), 8.21–8.19 (d, $J$ = 8.5Hz, 2H, Ar–H), 8.06–8.04 (d, $J$ = 8.5Hz, 2H, Ar–H), 8.04–8.02 (d, $J$ = 8.5Hz, 2H, Ar–H), 7.97–7.95 (d, $J$ = 8Hz, 2H, Ar–H), 7.63–7.62 (d, $J$ = 8.5Hz, 2H, Ar–H), 7.56–7.55 (m, 2H, Ar–H), 7.35–7.32 (m, $J$ = 8Hz, $J$ = 7.5Hz 2H, Ar–H), 7.28–7.26 (d, 2H, Ar–H), 7.184 (s, 2H, Ar–H), 3.86–3.83 (t, 2H, –N–$CH_2$–), 1.44–1.13 (m, 36H), 1.67–1.64 (t, 2H, N–$CH_2$– $CH_2$–), 1.25–1.21 (m, 11H, –$CH_2$–$CH_2$–$CH_2$), 0.85–0.82 (s, 3H, –O–$CH_3$). $^{13}$C–NMR (125 MHz, $CDCl_3$, $\delta$): 168.1, 165.3, 157.2, 155.3, 142.8, 138.5, 137.5, 129.3, 123.3, 120.9, 111.5, 107.6, 102.7, 45.4, 31.1, 27.1, 29.3, 22.7, 14.1. HRMS: m/z 634.5 (100%). Exact Mass: 632.27.

## Synthesis of 3,6–bis(4–(benzofuran–2–yl)phenyl)–2–octyl–5–(prop–2–ynyl)pyrrolo[3,4–c]pyrrole–1,4(2H,5H)–dione (15)

Under an inert atmosphere, **14** (0.1 g, 0.158 mmol) was taken in a dried two–neck 50 mL round bottom flask and degassed anhydrous *N,N*–dimethylformamide (DMF, 10 mL) was injected and stirred until complete dissolution (10 min). After complete dissolution, $K_2CO_3$ (0.11 g, 11.76 mmol) was added and stirred further for 30 min. Subsequently, 3–bromo–1–propyne (0.06 gm, 0.5 mmol) was added dropwise into the reaction mixture using a syringe, and kept at room temperature for 3 h. The reaction mixture was poured into ice cold water and stirred for 1 h to quench the reaction. The reaction mixture was then extracted with chloroform and dried over $Na_2SO_4$. The filtrate obtained was concentrated and purified by column chromatography on silica gel (Hexane/$CHCl_3$ 50:50, v/v) (82 mg, yield = 78%). $^1$H–NMR (500 MHz, $CDCl_3$, δ): 8.21–8.19 (d, *J* = 8.5Hz, 2H, Ar–H), 8.06–8.04 (d, *J* = 8.5Hz, 2H, Ar–H), 8.04–8.02 (d, *J* = 8.5Hz, 2H, Ar–H), 7.97–7.95 (d, *J* = 8Hz, 2H, Ar–H), 7.63–7.62 (d, *J* = 8.5Hz, 2H, Ar–H), 7.56–7.55 (m, 2H, Ar–H), 7.35–7.32 (m, 2H, Ar–H), 7.28–7.26 (d, 2H, Ar–H), 7.18 (s, 2H, Ar–H), 4.55 (s, 2H, –N–$CH_2$–), 3.86–3.83 (t, 2H, –N–$CH_2$–), 2.36 (s, 2H, –C≡CH) 1.44–1.13 (m, 36H), 1.67–1.64 (t, 2H, N–$CH_2$– $CH_2$–), 1.25–1.21 (m, 11H, –$CH_2$–$CH_2$–$CH_2$), 0.85–0.82 (s, 3H, –O–$CH_3$). $^{13}$C–NMR (125 MHz, $CDCl_3$, δ): 165.3, 157.0, 155.5, 142.5, 138.4, 134.7, 129.3, 123.3, 120.9, 111.5, 107.6, 102.7, 78.0, 73.1, 45.4, 33.4, 31.1, 29.3, 27.1, 22.7, 14.1. HRMS: m/z 672.4 (100%) Calculated Mass: 670.28.

### Synthesis of 5–(azidomethyl)–1,2,3–tris(2–(2–(2 methoxyethoxy )ethoxy)ethoxy)benzene (17)

A 50 mL round bottom flask containing triethylamine (760 μL, 5.64 mmol) and **16** (2 gm, 3.6 mmol) was placed in an ice bath and stirred for 10 min. Then methanesulfonyl chloride (430 μL, 5.43 mmol) in DMF was added drop wise into this mixture at 0°C and it was stirred for 1 h at room temperature. Subsequently, $NaN_3$ (0.15 mL, 4.5 mmol) and 2–3 drops of water were added and the reaction mixture was stirred for additional 2 h at room temperature. The reaction mixture was poured into brine (100 mL) and extracted with EtOAc (200 mL). The extract was washed with saturated aqueous $Na_2CO_3$ solution, dried over $Na_2SO_4$, filtered and the filtrate was concentrated to provide the analytically pure product. $^1$H–NMR (500 MHz, $CDCl_3$, δ): 6.62 (s, 2H, Ar–H), 4.08–4.10 (m, 6H, –O–$CH_2$), 3.86–3.82 (t, 6H, –O–$CH_2$–), 3.80–3.74 (m, 6H, –O–$CH_2$–$CH_2$–O), 3.70–3.66 (m, 6H, –O–$CH_2$–$CH_2$–O), 3.36–3.59 (m, 12H, –O–$CH_2$–$CH_2$–O), 3.54–3.46 (m, 6H, –O–$CH_2$–$CH_2$–O), 3.35–3.33 (d, 9H, –O–$CH_3$). ESI–MS 619.7 Calculated Mass: 619.3.

### Synthesis of 3,6–bis(4–(benzofuran–2–yl)phenyl)–2–octyl–5–((1–(3,4,5–tris(2–(2–(2 methoxyethoxy)ethoxy)ethoxy)benzyl)–1H–1,2,3–triazol–4–yl)methyl)pyrrolo[3,4–c]pyrrole–1,4(2H,5H)–dione (PDPP–Amphi, 18)

**15** (35 mg, 0.0522 mmol), **17** (50mg, 0.08 mmol) and tetrakis(acetonitrile)copper (I) hexafluorophosphate (1 mg, 0.002 mmol) were taken in 50 mL round bottom flask. Dry DMF (15 mL) was added to the mixture and bubbled with $N_2$ for 20 min. Copper powder (4 mg, 0.062 mmol) was then added and the mixture was stirred for 6 h at 50ºC. The reaction mixture was then poured into ice cold water (150 mL) and stirred for 1 h to quench the reaction, extracted with chloroform and dried over $Na_2SO_4$. The filtrate was concentrated and purified by column chromatography on silica ($CHCl_3$/MeOH 95: 5, v/v). A highly fluorescent red solid was obtained by precipitation using $CHCl_3$/Hexane 5: 95, v/v (60 mg, yield = 87 %). $^1$H–NMR (500 MHz, $CDCl_3$, δ): 8.30–8.28 (d, *J* = 8.5Hz, 2H, Ar–H), 8.07–8.05 (d, *J* = 8.5Hz, 2H, Ar–H), 8.04–8.03 (d, *J* = 8.5Hz, 2H, Ar–H), 7.92–7.91 (d, *J* = 8Hz, 2H, Ar–H), 7.70 (s, 1H, $R_2C$=CH), 7.64–7.62 (d, *J* = 8.5Hz, 2H, Ar–H), 7.56–7.55 (m, 2H, Ar–H), 7.36–7.31 (m, *J* = 8Hz, *J* = 7.5Hz 2H, Ar–H), 7.28–7.27 (d, 2H, Ar–H), 7.18 (s, 2H, Ar–H), 6.49 (s, 2H, Ar–H), 5.35 (s, 2H, N–$CH_2$) 5.02 (s, 2H, N–$CH_2$), 4.08–4.10 (m, 6H, –O–$CH_2$), 3.86–3.82 (t, 6H, –O–$CH_2$–), 3.80–3.74 (m, 6H, –O–$CH_2$–$CH_2$–O), 3.70–3.66 (m, 6H, –O–$CH_2$–$CH_2$–O), 3.36–3.59 (m, 12H, –O–$CH_2$–$CH_2$–O), 3.54–3.46 (m, 6H, –O–$CH_2$–$CH_2$–O), 3.35–3.33 (d, 9H, –O–$CH_3$), 1.64 (s, 2H, N–$CH_2$– $CH_2$–), 1.25–1.21 (m, 11H, –$CH_2$–$CH_2$–$CH_2$), 0.85–0.82 (s, 3H, –$CH_3$). $^{13}$C–NMR (125 MHz, chloroform–*d*, δ): 165.3, 157.0, 155.5, 142.5, 138.4, 134.7, 129.3, 123.3, 120.9, 111.5, 107.6, 102.7, 71.0, 69.1, 59.4, 45.4, 33.4, 31.1, 29.3, 27.1, 22.7, 14.1. Calculated Mass: 1289.61 HRMS: 1290.6.

## 4.6. References

[1] S. J. Kim, K. Choi, B. Lee, Y. Kim, B. H. Hong, *Annu. Rev. Mater. Res.* **2015**, *45*, 63.

[2] X. Huang, C. Tan, Z. Yin, H. Zhang, *Adv. Mater.* **2014**, *26*, 2185.

[3] J. W. Colson, W. R. Dichtel, *Nat. Chem.* **2013**, *5*, 453.

[4] K. Ariga, Q. M. Ji, J. P. Hill, Y. Bando, M. Aono, *NPG Asia Mater.* **2012**, *4*, 17.

[5] S. Z. Butler, S. M. Hollen, L. Cao, Y. Cui, J. A. Gupta, H. R. Gutiérrez, T. F. Heinz, S. S. Hong, J. Huangz, A. F. Ismach, E. Johnston-Halperin, M. Kuno, V. V. Plashnitsa, R. D. Robinson, R. S. Ruoff, S. Salahuddin, J. Shan, L. Shi, M. G. Spencer, M. Terrones, W. Windl, J. E. Goldberger, *ACS Nano.* **2013**, *7*, 2898.

[6] D. Chimene, D. L. Alge, A. K. Gaharwar, *Adv. Mater.* **2015**, *27*, 7261.

[7] K. Ariga, J. P. Hill, M. V. Lee, A. Vinu, R. Charvet, S. Acharya, *Sci. Technol. Adv. Mater.* **2008**, *9*, 014109.

[8] H-J. Kim, T. Kim, M. Lee, *Acc. Chem. Res.* **2010**, *44*, 72.

[9] S. S. Babu, V. K. Praveen, A. Ajayaghosh, *Chem. Rev.* **2014**, *114*, 1973.

[10] E. Busseron, Y. Ruff, E. Moulin, N. Giuseppone, *Nanoscale* **2013**, *5*, 7098.

[11] T. Marangoni, S. A. Mezzasalma, A. Llanes-Pallas, K. Yoosaf, N. Armaroli, D. Bonifazi, *Langmuir* **2011**, *27*, 1513.

[12] K. Yoosaf, A. Llanes-Pallas, T. Marangoni, A. Belbakra, R. Marega, E. Botek, B. Champagne, D. Bonifazi, N. Armaroli, *Chem. Eur. J.* **2011**, *17*, 3262.

[13] J. Puigmartí-Luis, A. P. del Pino, V. Laukhin, L. N. Feldborg, C. Rovira, E. Laukhinaac, D. B. Amabilino, *J. Mater. Chem.* **2010**, *20*, 466.

[14] R. Pfukwa, P. H. J. Kouwer, A. E. Rowan, B. Klumperman, *Angew. Chem. Int. Ed.* **2013**, *52*, 11040 .

[15] M. A. J. Gillissen, M. M. E. Koenigs, J. J. H. Spiering, J. A. J. M. Vekemans, A. R. A. Palmans, I. K. Voets, E. W. Meijer, *J. Am. Chem. Soc.* **2014**, *136*, 336.

[16] C. E. Boott, A. Nazemi, I. Manners, *Angew. Chem. Int. Ed.* **2015**, *54*, 13876.

[17] X. Zhuang, Y. Mai, D. Wu, F. Zhang, X. Feng, *Adv. Mater.* **2015**, *27*, 403.

[18] S. L. Cai, W. G. Zhang, R. N. Zuckermann, Z. T. Li, X. Zhao, Y. Liu, *Adv. Mater.* **2015**, *27*, 5762.

[19] L. Đorđevića , N. Demitrib, D. Bonifazi, *Supramol. Chem.* **2016**, *28*, 753.

[20] P. Anees, S. Sreejith, A. Ajayaghosh, *J. Am. Chem. Soc.* **2014**, *136*, 13233.

[21] V. K. Praveen, C. Ranjith, N. Armaroli, *Angew. Chem. Int. Ed.* **2014**, *53*, 365.

[22] R. Li, L. Jiang, Q. Meng, J. Gao, H. Li, Q. Tang, M. He, W. Hu, Y. Liu, D. Zhu, *Adv. Mater.* **2009**, *21*, 4492.

[23] T. He, X. Zhang, J. Jia, Y. Li, X. Tao, *Adv. Mater.* **2012**, *24*, 2171.

[24] E. Krieg, M. M. C. Bastings, P. Besenius, B. Rybtchinski, *Chem. Rev.* **2016**, *116*, 2414.

[25] T. Aida, E. W. Meijer, S. I. Stupp, *Science* **2012**, *335*, 813.

[26] D. Görl, X. Zhang, F. Würthner, *Angew. Chem. Int . Ed.* **2012**, *51*, 6328.

[27] M. R. Molla, S. Ghosh, *Phys. Chem. Chem. Phys.* **2014**, *16*, 26672.

[28] L. Đorđević, T. Marangoni, T. Miletić, J. R–Magnieto, J. Mohanraj, H. Amenitsch, D. Pasini, N. Liaros, S. Couris, N. Armaroli, M. Surin, D. Bonifazi, *J. Am. Chem. Soc.* **2015**, *137*, 8150.

[29] E. Lee, J–K Kim, M. Lee, *Angew. Chem., Int. Ed.* **2009**, *48*, 3657.

[30] B. Narayan, S. P. Senanayak, A. Jain, K. S. Narayan, S. J. George, *Adv. Funct. Mater.* **2013**, *23*, 3053.

[31] Y. Zheng, H. Zhou, D. Liu, G. Floudas, M. Wagner, K. Koynov, M. Mezger, H. J. Butt, T. Ikeda, *Angew. Chem. Int. Ed.* **2013**, *52*, 4845.

[32] T. Ikeda, H. Tamura, T. Sakurai, S. Seki, *Nanoscale* **2016**, *8*, 14673.

[33] M. Vybornyi, A. V. Rudnev, S. M. Langenegger, T. Wandlowski, G. Calzaferri, R. Häner, *Angew. Chem., Int. Ed.* **2013**, *52*, 11488.

[34] M. Vybornyi, A. Rudnev, R. Häner, *Chem. Mater.* **2015**, *27*, 1426.

[35] C. Shahar, J. Baram, Y. Tidhar, H. Weissman, S. R. Cohen, I. Pinkas, B. Rybtchinski, *ACS Nano* **2013**, *7*, 3547.

[36] C. Kim, J. Liu, J. Lin, A. B. Tamayo, B. Walker, G. Wu, T.–Q. Nguyen, *Chem. Mater.* **2012**, *24*, 1699.

[37] J. Dhar, D. P. Karothu, S. Patil, *Chem. Commun.* **2015**, *51*, 97.

[38] F. Wurthner, T. E. Kaiser, C. R. Saha–Moller, *Angew. Chem. Int. Ed.* **2011**, *50*, 3376.

[39] M. Kirkus, L. Wang, S. Mothy, D. Beljonne, J. Cornil, R. A. J. Janssen, S. C. J. Meskers *J. Phys. Chem. A* **2012**, *116*, 7927−7936.

[40] F. C. Spano, C. Silva, *Annu. Rev. Phys. Chem.* **2014**, *65*, 477.

[41] J. R. Lakowicz, *Principles of Fluorescence Spectroscopy*, Springer, Baltimore, Maryland, USA **2006**.

[42] M. J. Mayoral, C. Rest, V. Stepanenko, J. Schellheimer, R. Q. Albuquerque, G. Fernández, *J. Am. Chem. Soc.* **2013**, *135*, 2148.

[43] M. M. Smulders, M. M. Nieuwenhuizen, T. F. de Greef, P. van der Schoot, A. P. Schenning, E. W. Meijer, *Chemistry* **2010**, *16*, 362.

[44] H. M. ten Eikelder, A. J. Markvoort, T. F. de Greef, P. A. Hilbers, *J. Phys. Chem. B* **2012**, *116*, 5291.

[45] A. Ustinov, H. Weissman, E. Shirman, I. Pinkas, X. Zuo, B. Rybtchinski, *J. Am. Chem. Soc.* **2011**, *133*, 16201.

[46] M. R. Hicks, J. Kowałski, A. Rodger, *Chem. Soc. Rev.* **2010**, *39*, 3380.

[47] O. A. Bell, G. Wu, J. S. Haataja, F. Brömmel, N. Fey, A. M. Seddon, R. L. Harniman, R. M. Richardson, O. Ikkala, X. Zhang, C. F. J. Faul, *J. Am. Chem. Soc.* **2015**, *137*, 142.

[48] K. Sakakibara, P. Chithra, B. Das, T. Mori, M. Akada, J. Labuta, T. Tsuruoka, S. Maji, S. Furumi, L. K. Shrestha, J. P. Hill, S. Acharya, K. Ariga, A. Ajayaghosh, *J. Am. Chem. Soc.* **2014**, *136*, 8548.

[49] S. Seki, A. Saeki, T. Sakurai, D. Sakamaki, *Phys. Chem. Chem. Phys.* **2014**, *16*, 11093.

[50] A. Saeki, S.-i. Ohsaki, S. Seki, S. Tagawa, *J. Phys. Chem. C* **2008**, *112*, 16643.

[51] S. Prasanthkumar, A. Saeki, S. Seki, A. Ajayaghosh, *J. Am. Chem. Soc.* **2010**, *132*, 8866.

[52] L. Shaw, P. Hayoz, Y. Diao, J. A. Reinspach, J. W. F. To, M. F. Toney, R. T. Weitz, Z. Bao, *ACS Appl. Mater. Interfaces* **2016**, *8*, 9285.

[53] Y. Yasutani, A. Saeki, T. Fukumatsu, Y. Koizumi, S. Seki, *Chem. Lett.* **2013**, *42*, 19.

[54] J. Rivnay, S. C. Mannsfeld, C. E. Miller, A. Salleo, M. F. Toney, *Chem. Rev.* **2012**, *112*, 5488.

[55] I. Osaka , M. Saito , T. Koganezawa , K. Takimiya, *Adv. Mater.* **2014**, *26*, 331.

[56] S. Yagai, S. Okamura, Y. Nakano, M. Yamauchi, K. Kishikawa, T. Karatsu, A. Kitamura, A. Ueno, D. Kuzuhara, H. Yamada, T. Seki, H. Ito, *Nat. Commun.* **2014**, *5*, 4013.

# Papers Presented at Conferences (Posters/Oral)

1. Coaxial p–n Heterojunctions of Organic Donor–Acceptor Assemblies with High Photoconductivity. S. Prasanthkumar, **S. Ghosh**, V. C. Nair, A. Saeki, S. Seki and A. Ajayaghosh*
   Poster presented at 9th CRSI-RSC Symposium organized by National Chemical Laboratory (NCL) on February 5-8, 2015, Pune, India.

2. A Low Band Gap π-Gelator with Enhanced Intrinsic Photoconductivity. **S. Ghosh** and A. Ajayaghosh*
   Oral and Poster presented at 11th JNC Research Conference on Chemistry of Materials organized by Jawaharlal Nehru Centre for Advanced Scientific Research on October 2-4, 2015, Alleppey, Kerala, India.

3. Nanosheets of a Diketopyrrolopyrrole (DPP) Derived Functional Dye with High Solid-State Emission and Anisotropic Charge-Carrier Mobility. **S. Ghosh** and A. Ajayaghosh*
   Poster presented at 8th East Asia Symposium on Functional Dyes and Advanced Materials by CSIR- National Institute for Interdisciplinary Science and Technology on September 20-22, 2017, Trivandrum, Kerala, India.

4. A Diketopyrrolopyrrole Based Supramolecular Nanocomposite as Near Infrared Transmitting Optical Filter. **S. Ghosh** and A. Ajayaghosh*
   at 13th JNC Research Conference on Chemistry Of Materials organized by Jawaharlal Nehru Centre for Advanced Scientific Research on October 1-3, 2017, Trivandrum, Kerala, India.

## List of Publications and Patents from the Thesis

1. Nanosheets of Organic Molecular Assembly from Aqueous Medium Exhibit High Solid-State Emission and Anisotropic Charge-Carrier Mobility. **S. Ghosh**, D. S. Philips, A. Saeki, A. Ajayaghosh.
   *Adv. Mater.* **2017**, *29*, 1605408.

2. A Supramolecular Nanocomposite as Near Infrared Transmitting Optical Filter for Security and Forensic Applications. **S. Ghosh**, S. Cherumukkil, C. H. Suresh, A. Ajayaghosh.
   *Adv. Mater*. **2017**, 1703783.

3. Composite of a Supramolecular Black dye and Elastomer as a Near Infrared (NIR) Filter for Photography, Security and Forensic Related Applications. **S. Ghosh**, A. Ajayaghosh.
   *Patent number*: 201711002216.

4. Modulating Charge Carrier Polarity of Diketopyrrolopyrrole–based Low Band Gap Semiconductors by Terminal Functionalization. **S. Ghosh**, R. Raveendran, M. Namboothiry, A. Saeki, S. Seki, A. Ajayaghosh.
   (Manuscript under preparation)

## List of Publications from Other Related Works

5. Luminescent and Conductive Supramolecular Polymers from an *N*-annulated Perylenedicarboxamide. F. García, J. Buendía, **S. Ghosh**, A. Ajayaghosh, L. Sánchez.
   *Chem. Commun.* **2013**, *49, 9278.*

6. Organic Donor–Acceptor Assemblies form Coaxial p–n Heterojunctions with High Photoconductivity. S. Prasanthkumar, **S. Ghosh**, V. C Nair, A. Saeki, S. Seki, A. Ajayaghosh.
   *Angew. Chem. Int. Ed.* **2015**, *54, 946.*

7. The Chemistry and Applications of π-Gels. **S. Ghosh**, V. K Praveen, A. Ajayaghosh.
   *Annu. Rev. Mater. Res.* **2016**, *46*, 235.

8. Unprecedented Charge-Transfer Complex of Fused Diporphyrin as Near-Infrared Absorption-Induced High-Aspect-Ratio Nanorods. B S. Achary, S. Gokulnath, **S. Ghosh**, M. Mrinalini, S. Prasanthkumar, L. Giribabu.
   *Chem. Asian J.* **2016**, *11*, 3498.

9. An Unprecedented Amplification of Near-Infrared Emission in a Bodipy Derived π-System by Stress or Gelation. S. Cherumukkil, **S. Ghosh**, V. K Praveen, A. Ajayaghosh.
   *Chem. Sci.* **2017**, *8,* 5644.

10. An Unsymmetrical Squaraine Dye based Chemical Platform for Multiple Analyte Recognition. D. S. Philips, **S. Ghosh**, K. V. Sudheesh, C. H. Suresh, A. Ajayaghosh.
    *Chem.-Eur. J.* **2017** DOI: *10.1002/chem.201703645.*